The Dissertation Committee for Dalin Zhu
certifies that this is the approved version of the following dissertation:

Millimeter Wave MIMO Communications: High-Resolution Angle Acquisition and Low-Resolution Time-Frequency Synchronization

Committee:

_____
Robert W. Heath, Jr., Supervisor

_____
Jeffrey G. Andrews

_____
Junil Choi

_____
Nuria González-Prelcic

_____
Haris Vikalo

Millimeter Wave MIMO Communications: High-Resolution Angle Acquisition and Low-Resolution Time-Frequency Synchronization

by

Dalin Zhu

DISSERTATION

Presented to the Faculty of the Graduate School of

The University of Texas at Austin

in Partial Fulfillment

of the Requirements

for the Degree of

DOCTOR OF PHILOSOPHY

THE UNIVERSITY OF TEXAS AT AUSTIN

May 2019

Dedicated to my wife, Yuanyuan Hu, and my son, Tianpei.

Acknowledgments

I would like to express my sincere gratitude to my advisor, Professor Robert W. Heath, Jr., for his support, guidance and friendship through each stage of my Ph.D. studies at UT. I thank him for giving me a large amount of freedom to select my own research topics. I will always appreciate his high standards of technical excellence and professionalism, which were fundamental to all my accomplishments. I feel very grateful to him for sharing his invaluable insights into research, experiences and lessons with me, which I am sure to cherish for the rest of my journey that I call life. I also feel fortunate to have the opportunity to closely work with Professor Junil Choi during my first two years at UT. I thank him for his patience in reviewing my ideas and revising my papers, and generosity of sharing his response letter template with me. I appreciate his commitment to high quality research. I would like to extend my gratitude to Professor Jeffrey G. Andrews, Professor Nuria González-Prelcic and Professor Haris Vikalo for serving as my committee members and reviewing my dissertation.

I thank former WSIL members and visitors, Tianyang Bai, Ahmed Alkhateeb, Jianhua Mo, Kiran Venugopal, Jeonghun Park, Talha Khan, Andrew Thornburg, Christopher Mollen, Vutha Va and Sungwoo Park, for fun times at Karaoke and passing down their experiences. I also thank current

Millimeter Wave MIMO Communications: High-Resolution Angle Acquisition and Low-Resolution Time-Frequency Synchronization

Publication No. _____

Dalin Zhu, Ph.D.
The University of Texas at Austin, 2019

Supervisor: Robert W. Heath, Jr.

Knowledge of the propagation channel is critical to exploit the full benefit of multiple-input multiple-output (MIMO) techniques in millimeter wave (mmWave) cellular systems. Obtaining accurate channel state information in mmWave systems, however, is challenging due to high estimation overhead, high computational complexity and on-grid setting. It is also desirable to reduce the analog-to-digital converters (ADCs) resolution at mmWave frequencies to reduce power consumption and implementation costs. The use of low-precision ADCs, though, brings new design challenges to practical cellular networks.

In the first part of this dissertation, we develop several new methods to estimate and track the mmWave channel's angle-of-departure and angle-of-arrival with high accuracy and low overhead. The key ingredient of the

proposed strategies is custom designed beam pairs, from which there exists an invertible function of the angle to be estimated. We further extend the proposed algorithms to dual-polarized MIMO in wideband channels, and angle tracking design for fast-varying environments. We derive analytical angle estimation error performance of the proposed methods in single-path channels. We also use numerical examples to characterize the robustness of the proposed approaches to various transceiver settings and channel conditions.

In the second part of this dissertation, we focus on improving the low-resolution time-frequency synchronization performance for mmWave cellular systems. In our system model, the base station uses analog beams to send the synchronization signal with infinite-resolution digital-to-analog converters (DACs). The user equipment employs a fully digital front end to detect the synchronization signal with low-resolution ADCs. For low-resolution timing synchronization, we propose a new multi-beam probing based strategy, targeting at maximizing the minimum received synchronization signal-to-quantization-plus-noise ratio among all serving users. Regarding low-resolution frequency synchronization, we construct new sequences for carrier frequency offset (CFO) estimation and compensation. We use both analytical and numerical examples to show that the proposed sequences and the corresponding metrics used for retrieving the CFOs are robust to the quantization distortion.

Table of Contents

List of Tables

List of Figures

xviii

xxii

Chapter 1

Introduction

The millimeter wave (mmWave) band holds promise for providing high data rates in wireless local area network and fifth generation (5G) cellular network [1]-[3]. The small carrier wavelengths at mmWave frequencies enable synthesis of compact antenna arrays, providing additional array gain and a reduction in mean interference levels [1]-[4]. Dual-polarized antenna systems, discussed in [5]-[7], can also be incorporated into mmWave systems allowing a large number of antennas to be deployed with a small form factor. In addition to space efficiency, high rank data streams can be multiplexed across the polarizations by taking advantage of dual-pole decoupling in the channel. In this dissertation, we focus on two critical issues of implementing mmWave multiple-input multiple-output (MIMO) systems in practice, which are: (i) high-resolution channel estimation to enable high-rate data communications, and (ii) low-resolution quantization to reduce power consumption.

In this chapter, we explain the motivation of the research problems addressed in this dissertation and give a summary of our contributions. In Section 1.1, we illustrate the transceiver architecture of mmWave systems. In Section 1.2, we point out some challenges of estimating the channel state infor-
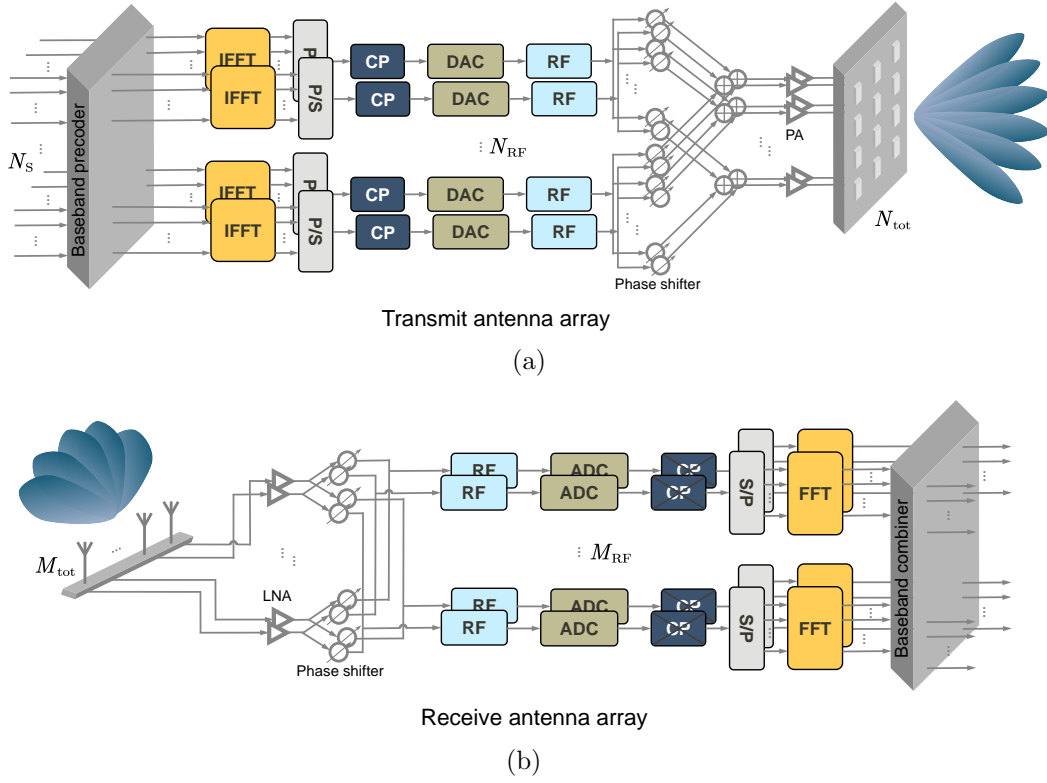
Figure 1.1: One example of transceiver structure for mmWave systems. (a) Shared transmit array architecture with N_{RF} radio frequency (RF) chains and N_{tot} transmit antenna elements. (b) Shared receive array architecture with M_{RF} RF chains and M_{tot} receive antenna elements.

mation in mmWave systems. We highlight the necessity and opportunities of employing low-resolution quantization at mmWave frequencies in Section 1.3. In Section 1.4, we summarize our contributions. We conclude this chapter with a summary of the organization of this dissertation and a list of abbreviations in Sections 1.5 and 1.6.

1.1 Transceiver Structure of MmWave Systems

Different from a fully digital architecture employed in traditional lower-frequency MIMO systems, hybrid analog and digital precoding has become a means of exploiting both beamforming and spatial multiplexing gains in hardware constrained mmWave cellular systems. In Figure 1.1, we present a precoded MIMO-orthogonal frequency division multiplexing (OFDM) system with N subcarriers and a hybrid precoding transceiver structure. A base station (BS) or a transmitter is equipped with N_{tot} transmit antennas and N_{RF} radio frequency (RF) chains. A user equipment (UE) or a receiver uses M_{tot} receive antennas and M_{RF} RF chains. As can be seen from Figure 1.1, in a shared-array architecture, all antenna elements are jointly controlled by all RF chains sharing the same network of phase shifters. In this example, a uniform planar array (UPA) is adopted at the BS, and a uniform linear array (ULA) is employed at the UE. Other array geometries (e.g., non-uniform linear arrays), array architectures (e.g., array-of-subarray architecture) and polarization configurations are also possible.

In the hybrid transceiver structure, the number of RF chains is usually much smaller than the number of antennas. This divides mmWave precoding into the analog and digital domains. The analog precoding/beamforming is subject to the constant modulus constraint because only the phases of the phase-shifters are configured. The digital precoding/beamforming, however, is not limited by the constant modulus constraint and can be optimized by leveraging the available channel state information.

In this dissertation, we develop high-resolution angle acquisition strategies via the analog precoding/beamforming. We therefore set the digital baseband precoding matrix as identity matrix. In some deployment scenarios, we simply assume single-stream analog-only beamforming, resulting in $N_{\mathrm{RF}} = 1$ in Figure 1.1(a). For low-resolution time-frequency synchronization design, we assume fully digital baseband processing at the UE, i.e., $M_{\mathrm{tot}} = M_{\mathrm{RF}}$ in Figure 1.1(b), equipped with few-bit analog-to-digital converters (ADCs).

1.2   Channel Estimation in MmWave Systems

Knowledge of the wireless propagation channel is critical to exploit the full benefit of MIMO techniques, such as hybrid precoding, in mmWave cellular systems. Classical channel estimation techniques developed for lower-frequency MIMO systems, however, are not applicable for mmWave MIMO due to the use of large antenna arrays and hybrid precoding [2]. MmWave specific channel estimation techniques have been proposed in [8]-[15]. In [8], channel estimation algorithms that exploit mmWave channel sparsity were developed by assuming that the channel directions lie on a specific grid. An open-loop channel estimation strategy was proposed in [9], in which the estimation algorithm is independent of the hardware constraints and applies to either phase shifter or switching networks. In [10], compressed measurements obtained from the mmWave channels were exploited to estimate the second order statistics of the channel to enable adaptive multi-user hybrid precoding. In [11], a support (the index set of non-zero entries in a sparse vector)

4

detection based channel estimation algorithm was developed for mmWave systems with lens antennas. In [12], a minimum-mean-squared-error (MMSE) hybrid analog and digital channel estimator was developed without exploiting channel sparsity and directional beamforming. In [13], a grid-of-beams (GoBs) based approach was proposed to obtain the channel's angle of departures (AoDs) and angle of arrivals (AoAs). In the GoBs based method, a set of narrow quasi-non-overlapping beams are established to cover a given angular range. The transmitter/receiver selects the transmit/receive beams that optimize given performance metric(s) for control/data channel communications. The steering directions of the selected transmit/receive beams are treated as the estimated AoDs/AoAs. Similar ideas of forming beams grid were also investigated in [14, 15], though these two papers mainly focused on the hierarchical beam codebook design. Most of the prior work in [8]-[15], however, focuses on narrowband channels, while the mmWave channel is indeed frequency selective.

Channel estimation methods for wideband frequency-selective mmWave channels have been proposed in [16]-[24]. In [16], a time-domain channel estimation approach was developed for wideband mmWave systems assuming a hybrid MIMO architecture; the proposed strategy exploited the sparsity in both the angular and delay domains to formulate the estimation problem, but the computational complexity of the algorithm is high. A frequency-domain wideband channel estimation method was proposed in [17]; a sparse reconstruction problem was formulated to estimate the channel independently for

each subcarrier. In [18], another frequency-domain approach was developed by exploiting the congruence between subcarriers; only the information from a reduced number of subcarriers was used, which reduces the estimation overhead and complexity. Spatially common sparsity of the channels across different subcarriers was exploited in [20], and the structured SAMP algorithm initially proposed in [19] was employed to reconstruct the channel in the frequency-domain. A similar idea to leverage the common sparsity in the frequency-domain to estimate the wideband channels was also proposed in [21]. The prior work in [20,21], however, assumed Gaussian measurements and high SNR regimes (above 10 dB), which are unrealistic for mmWave communications. These limitations were overcome by the methods developed in [22], which also leveraged the spatially common sparsity within the system bandwidth to estimate the wideband channels. In [23], the authors focused on joint estimation of the multi-user frequency selective channels and the hybrid precoder/combiner optimization according to various design criteria. In [24], a third-order tensor was employed to model the received signals for wideband channel parameters estimation; via low-rank decomposition, the wideband channel parameters were extracted from the corresponding factor matrices.

The concept of the GoBs and its variants have been exploited in the 5G NR for the beam management. The performance of the GoBs based strategies is limited by the grid resolution. In Figure 1.2, we provide a conceptual example of the GoBs. As can be seen from Figure 1.2, there exists quantization error between the estimated angle and the exact angle of the channel even
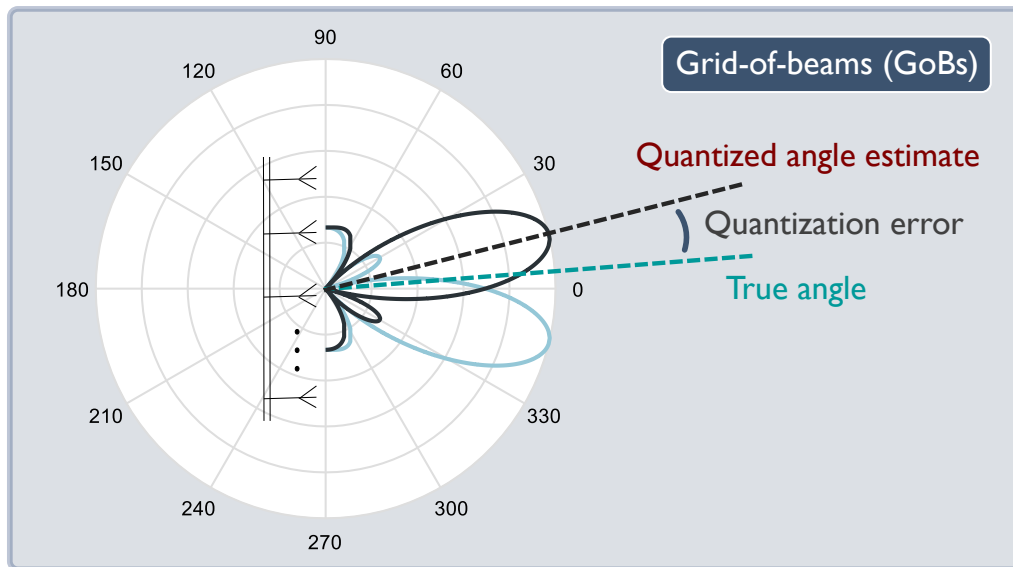
Figure 1.2: A conceptual example of grid-of-beams based angle estimation approach. The steering direction of the selected beam is considered as the estimated angle of the channel. There exists quantization error between the estimated angle and the true angle of the channel even without noise.

without incorporating noise and other impairments. A smaller beam codebook will result in larger quantization error. To minimize the quantization error, a high-resolution beam codebook with many beam codewords is needed, leading to prohibitive complexity, estimation/tracking overhead, and access delay. It is therefore desirable to design mmWave specific channel estimation that does not require an on-grid assumption.

1.3 Low-Resolution ADCs in MmWave Systems

As mmWave makes use of large available bandwidths, the corresponding sampling rate of the ADCs scales up, which results in high power con-

sumption and hardware implementation complexity. For instance, for an ideal b-bit ADC with flash architecture, a total of $2^b - 1$ comparators are required, which causes exponentially increased power consumption with respect to the resolution. For example, the power consumption of a 1-bit ADC operating at 1 GHz is only 0.01 mW. The power consumption of a 12-bit ADC operating at 1 GHz, however, is more than 20 mW (sometimes up to 120 mW), which is impractical for current wireless communications systems. It is therefore desirable to reduce the ADC resolution in mmWave systems to reduce the power consumption [25]. In Figure 1.3, we provide an illustrative example of a MIMO receiver equipped with 1-bit ADCs. As can be seen from Figure 1.3, each receive RF chain corresponds to a pair of ADCs, separately quantizing the real and imaginary parts of the input signal samples to the quantizer. For 1-bit quantization, the output of the ADC is either 1 or -1, depending on the sign of the input sample.

The use of low-resolution ADCs in wireless communications systems has been investigated in various aspects, e.g, input signal optimization in [26]-[28], mutual information analysis in [29]-[31], channel estimation techniques in [32]-[36], and uplink multiuser detection algorithms in [37]-[39]. Most of the prior work on low-resolution ADCs, however, focused on analytical performance assessment rather than practical implementation issues such as time and frequency synchronization designs. In this dissertation, for both the time and frequency synchronization designs, we assume that the corresponding synchronization signals are sent by the transmitter via analog beamforming, which is

8
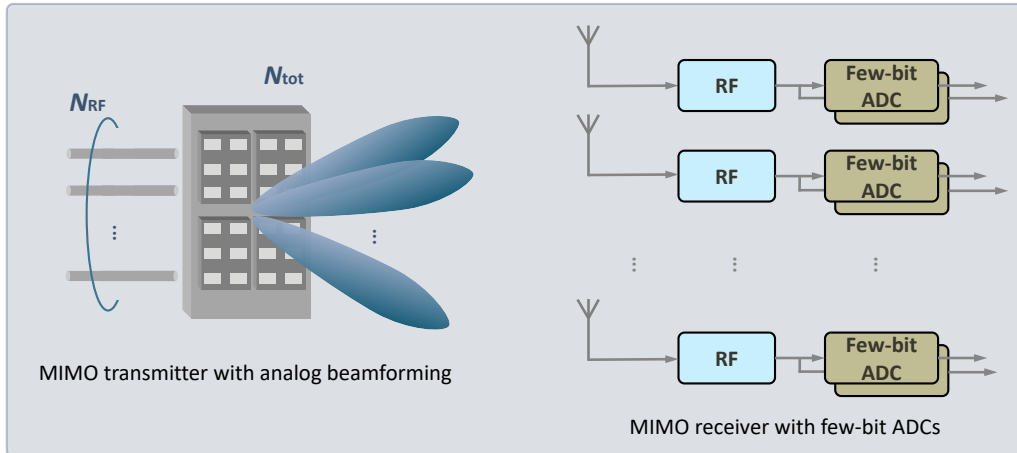
Figure 1.3: Conceptual examples of a MIMO transmitter with analog beamforming and a MIMO receiver equipped with few-bit ADCs. Each receive RF chain corresponds to a pair of ADCs, separately quantizing the real and imaginary parts of the received signal samples.

depicted by a conceptual example on the left-hand-side in Figure 1.3. We will elaborate on our proposed directional time-frequency synchronization strategies under few-bit ADCs in Chapters 5 and 6.

1.4 Summary of Contributions

In the first part of this dissertation, we first propose an algorithm to estimate the channel's AoDs and AoAs with high accuracy and low training overhead. The key ingredient of the proposed method is custom designed pairs of auxiliary beams, from which there exists an invertible function of the channel's AoDs and AoAs. Further, we develop two quantization and feedback strategies to support the proposed method in Frequency Division Duplex (FDD) systems. The proposed two quantization methods are different

in terms of the quantization resolution and feedback overhead. To better reveal the achievable performance of the proposed strategy, we derive the variance of the angle estimate in single-path channels. We extend the auxiliary beam pair design to dual-polarized mmWave MIMO systems, estimating the channel's two-dimensional (azimuth and elevation) AoDs and AoAs.

By leveraging the fact that the AoD/AoA is identical for both vertical and horizontal polarization domains, we develop various auxiliary beam pair and polarization domain mapping strategies, and evaluate their impact on the two-dimensional angle estimation performance. Assuming mobility, we propose to use the auxiliary beams as the tracking beams to capture the angle variations, towards which the steering directions of the data beams are adjusted. We custom design two receive combining based array calibration methods to better support the proposed angle acquisition (estimation and tracking) strategies.

In the second part of this dissertation, we focus on the time-frequency synchronization in mmWave systems equipped with low-resolution ADCs. For frame timing synchronization under few-bit ADCs, we develop a new multi-beam probing based directional synchronization strategy, targeting at maximizing the minimum received synchronization signal-to-quantization-plus-noise ratio (SQNR) of the whole network. Leveraging a common synchronization signal structure design, the proposed approach synthesizes an effective composite beam from the simultaneously probed beams to better trade off the beamforming gain and the quantization distortion. For frequency synchro-

nization under few-bit ADCs, we develop two double-sequence structures, i.e., auxiliary sequences and sum-difference sequences, to estimate the carrier frequency offset (CFO) in mmWave systems. We optimize the double-sequence design parameters such that: (i) for each individual user, the impact of the quantization distortion on the CFO estimation accuracy is minimized, and (ii) the resulting frequency range of estimation can capture as many users' CFOs as possible.

We summarize our contributions in this dissertation as follows.

⋆ Chapter 2: Auxiliary beam pair angle estimation in mmWave MIMO

1. We construct pairs of auxiliary beams and derive a set of ratio measures by performing amplitude comparison on the auxiliary beam pairs. The derived ratio metrics characterize the channel's AoDs and AoAs, and can be inverted to retrieve the corresponding angle information. We introduce two quantization and feedback options for implementing the proposed strategy in FDD systems.

2. We derive the variance of the angle estimate obtained by the proposed method. The derived variance characterizes the achievable angle estimation performance of the proposed method.

3. We extend the proposed single-path solution to estimate multipath's angle information. We provide and discuss potential deployment scenarios of the proposed approach, including control channels beamforming and multi-user scenario.

- This work was published in [40, 41].

★ Chapter 3: Angle estimation in dual-polarized mmWave MIMO

1. We propose a two-dimensional angle estimation algorithm via the auxiliary beam pair design. We develop a multi-layer pilot structure to better support the implementation of the proposed algorithm in wideband channels with multi-carrier transmission. By judiciously exploiting the auxiliary beam pair structure, we present a differential quantization strategy to reduce the feedback overhead.

2. We extend the proposed algorithm to dual-polarized MIMO structure. We develop various mapping strategies between auxiliary beams and polarization domains (vertical and horizontal). The obtained results show that the proposed technique is robust to the angle mismatch and power imbalance in dual-polarized MIMO.

- This work was published in [42, 43].

★ Chapter 4: Angle tracking in mmWave MIMO with array calibration

1. We develop several auxiliary beam pair-assisted high-resolution angle tracking strategies for wideband mmWave systems in fast-varying environments. We differentiate the proposed strategies in terms of tracking triggering device, information required at the UE side,

and other design parameters. We propose a beam-specific pilot signal structure for tracking and several feedback strategies to better adopt the proposed methods in different deployment scenarios.

2. We evaluate the impact of the impaired radiation pattern with phase and amplitude errors on the proposed designs. We custom design two antenna array calibration methods for the employed hybrid MIMO architecture, and characterize the impact of the calibrated radiation pattern on the proposed methods.

- This work was published in [44].

⋆ Chapter 5: Timing synchronization under low-resolution ADCs

1. We show that optimizing the received synchronization SQNR at zero-lag correlation is a viable solution to improve the overall frame timing synchronization performance under low-resolution ADCs. We use analytical and numerical examples to exhibit that for well-structured synchronization signals, the non-zero-lag correlation values are small and barely affected by the quantization, while the zero-lag peak correlation value is significantly distorted by the quantization.

2. We formulate the corresponding optimization problem as maximizing the minimum received synchronization SQNR at zero-lag correlation among all serving UEs. We solve the formulated problem

13

by optimizing the combination of the synchronization beams such that the resulted composite beam maximizes the received synchronization SQNR at zero-lag correlation, and at the same time characterizes the worst-case scenario of the network.

- This work has been submitted for possible publication [45], and part of this work was published in [46].

⋆ Chapter 6: Frequency synchronization under low-resolution ADCs

1. We develop two double-sequence high-resolution CFO estimation methods for mmWave systems operating with low-resolution ADCs. In each method, we custom design two sequences (i.e., a sequence pair) for frequency synchronization. The key ingredient of the custom designed double-sequence structure (both auxiliary and sum-difference) is a ratio measure derived from the sequence pair, which is an invertible function of the CFO to be estimated and robust to the quantization distortion.

2. We derive the Cramer-Rao lower bound (CRLB) of frequency estimation assuming 1-bit ADCs. We show that the mean squared errors (MSEs) of our estimated CFOs using 1-bit ADCs are close to the derived 1-bit CRLB.

3. We propose to fine tune the double-sequence design parameters such that the CFO estimation accuracy and the frequency range

14

of estimation are jointly optimized. To better realize our proposed algorithms in practical systems, we implement additional signaling support and procedure at both the BS and UE sides.

- This work has been submitted for possible publication [47].

1.5 Thesis Organization

We organize the remainder of this dissertation as follows. In Chapter 2, we present the design principle of the proposed auxiliary beam pair-assisted high-resolution angle estimation in mmWave systems. In Chapter 3, we explain the proposed two-dimensional angle estimation design in dual-polarized mmWave MIMO along with discussion on several practical implementation issues. In Chapter 4, we describe the proposed angle tracking designs for mmWave systems with high mobility and array calibration. In Chapter 5, we illustrate our proposed multi-beam probing based low-resolution timing synchronization strategy for mmWave initial access. We introduce the double-sequence structure and the corresponding low-resolution frequency synchronization procedure in Chapter 6. Finally, we conclude this dissertation and summarize potential future research directions in Chapter 7.

1.6 Abbreviations

5G   Fifth generation

ABP   Auxiliary beam pair

ADC   Analog-to-digital converter

AoA   Angle of arrival

AoD   Angle of departure

BS   Base station

CDF   Cumulative density function

CDM   Code division multiplexing

CFO   Carrier frequency offset

CP   Cyclic prefix

CRLB   Cramer-Rao lower bound

CRS   Cell-specific reference signal

CS   Compressed sensing

DAC   Digital-to-analog converter

DC   Direct current

DDC   Dedicated data channel

DTC   Dedicated tracking channel

FDD   Frequency division duplex

FDM   Frequency division multiplexing

FER   Frame error rate

GoB   Grid-of-beam

IBI   Inter-beam interference

LOS   Line-of-sight

LTE   Long Term Evolution

MAEE   Mean angle estimation error

MAQE	Mean angle quantization error
MATE	Mean angle tracking error
MCS	Modulation and coding scheme
MIMO	Multiple-input multiple-output
MMSE	Minimum mean squared error
MSE	Mean squared error
MUI	Multi-user interference
NLOS	Non-line-of-sight
NMSE	Normalized mean squared error
NR	New radio
OFDM	Orthogonal frequency division multiplexing
PCI	Physical cell identity
PSS	Primary synchronization sequence
RF	Radio frequency
RS	Reference signal
SINR	Signal-to-interference-plus-noise ratio
SNR	Signal-to-noise ratio
SQNR	Signal-to-quantization-plus-noise ratio
TDL	Tapped delay line
TDM	Time division multiplexing
UE	User equipment
ULA	Uniform linear array
UMi	Urban micro

UPA   Uniform planar array

XPD   Cross-polar discrimination

ZC   Zadoff-Chu

Chapter 2

Auxiliary Beam Pair Enabled Angle Estimation in MmWave MIMO Systems

In this chapter, we propose and evaluate a new angle estimation algorithm for mmWave MIMO systems. Pairs of auxiliary beams are formed by the BS to cover the angular range of interest, and are used to estimate the corresponding AoDs and AoAs. By performing amplitude comparison on the pairs of auxiliary beams, a set of ratio metrics, which are invertible with respect to the AoDs and AoAs of interest, are obtained. By directly inverting the ratio metrics, high-resolution angle estimates are retrieved, towards which highly directional narrow beams can be formed for high-rate data communications. Unlike prior work that requires a large number of training samples to obtain the high-resolution results, the proposed approach can be executed with low training overhead by judiciously exploiting the custom designed auxiliary beam pair structure. We present the detailed design principle and procedure of the proposed approach along with discussion on feedback options and deployment scenarios. This work was published in [40, 41].

2.1 Prior Work and Motivation

Many high-resolution subspace based angle estimation algorithms such as MUSIC [48], ESPRIT [49] and their variants [50] have been of interest to the array processing community for decades. Their applications to massive MIMO or full-dimension MIMO to estimate the two-dimensional angles were extensively investigated in [51]-[55]. In [56], the MUSIC algorithm was employed to support directional initial user discovery in mmWave systems. A relatively large number of snap-shots (samples) are required in the subspace based angle estimation algorithms employed in [51]-[56] to obtain accurate received signal covariance matrix, which in turn, results in high training overhead. Further, it is difficult to directly extend the MUSIC and ESPRIT-type estimators to mmWave systems with the hybrid architecture. This is because with the hybrid architecture, only a reduced-dimension channel matrix can be accessed after the analog combining, which makes the estimation of the full MIMO channel matrix difficult.

Construction of pairs of beams was previously employed in monopulse radar systems to improve the AoA estimation accuracy [57]. In amplitude monopulse radar, a sum beam and a difference beam form a pair such that the difference beam steers a null towards the boresight angle of the sum beam. By comparing the relative amplitude of the pulse in the pair of two beams, the direction of the target can be determined with accuracy dependent on the received signal-to-noise ratio (SNR). Directly applying the technique for monopulse radar to communications systems will yield large overhead as the

difference beams are only used for assisting the sum beams to conduct the angle estimation, not providing any angular coverage. This is because the angular coverage provided by the monopulse beam pair is approximately the same as the half-power beamwidth of the corresponding sum beam.

It is therefore necessary to develop high-resolution angle estimation methods that not only require low training overheads, but also are compatible with the hybrid MIMO architecture.

2.2 Contributions

The main objective of this chapter is to explain the key idea of implementing the well structured beam pairs to help acquire high-resolution AoD and AoA estimates under various channel conditions. We summarize our main contributions in this chapter as follows:

- We illustrate detailed design principle and procedure of the proposed auxiliary beam pair enabled angle estimation method. We use both analytical and numerical examples to show that there is no grid quantization error with the proposed approach.

- We define various quantization and feedback methods for the proposed algorithm in closed-loop systems. We show that quantizing the ratio measure gives better quantization performance than quantizing the estimated transmit spatial frequency, although the difference is marginal.

- Building on the single-path solution, we propose an algorithm for multi-path AoD and AoA estimation employing multiple transmit and receive radio frequency (RF) chains. We specifically design the associated auxiliary beam pair based channel probing matrix for the multi-path angle estimation.

We organize the rest of this chapter as follows. In Section 2.3, we describe the system model, channel model along with a brief discussion on the basic auxiliary beam pair setup. In Section 2.4, we specify the design principle of the proposed auxiliary beam pair in estimating both single-path and multi-path channels. We explain the application of the proposed design approach to control channel beamforming and multi-user scenario in Section 2.5. In Section 2.6, we provide numerical results to validate the effectiveness of the proposed technique. We conclude this chapter in Section 2.7.

2.3   Models and Assumptions

In this section, we first present the employed system and channel models. Then, we introduce basic setup of the auxiliary beam pair.

2.3.1   System Model

We consider a narrowband MIMO system with a hybrid transceiver structure. A transmitter equipped with N_{tot} transmit antennas and N_{RF} RF chains transmits N_{S} data streams to a receiver equipped with M_{tot} receive antennas and M_{RF} RF chains. Here, $N_{\text{S}} \leq M_{\text{RF}} \leq N_{\text{RF}}$, and both the transmitter

and receiver are equipped with shared-array antenna architectures. Note that the proposed approach can be applied to a sub-array antenna architecture, with some modifications. In a shared-array architecture, all antenna elements are jointly controlled by all RF chains sharing the same network of phase shifters. Denote by $\boldsymbol{x} = [x_1, \cdots, x_{N_\mathrm{S}}]^\mathrm{T}$ an $N_\mathrm{S} \times 1$ vector of symbols such that $\mathbb{E}\left[|x_k|^2\right] = 1$ for $k = 1, \cdots, N_\mathrm{S}$, and denote by $\boldsymbol{y} = [y_1, \cdots, y_{N_\mathrm{S}}]^\mathrm{T}$ an $N_\mathrm{S} \times 1$ vector of symbols received across the receive antennas after analog and baseband combining, then:

$$\boldsymbol{y} = \boldsymbol{W}_{\mathrm{BB}}^* \boldsymbol{W}_{\mathrm{RF}}^* \boldsymbol{H} \boldsymbol{F}_{\mathrm{RF}} \boldsymbol{F}_{\mathrm{BB}} \boldsymbol{x} + \boldsymbol{W}_{\mathrm{BB}}^* \boldsymbol{W}_{\mathrm{RF}}^* \boldsymbol{n}, \tag{2.1}$$

where $\boldsymbol{n} \sim \mathcal{N}_\mathrm{c}(\boldsymbol{0}_{M_\mathrm{tot}}, \sigma^2 \boldsymbol{I}_{M_\mathrm{tot}})$ is a noise vector, $\sigma^2 = 1/\gamma$, and γ represents the target SNR, which is obtained without beamforming and combining; $\boldsymbol{F}_{\mathrm{RF}}$ is an $N_\mathrm{tot} \times N_\mathrm{RF}$ analog precoding matrix at the transmitter, satisfying the constant amplitude constraint $\left[[\boldsymbol{F}_{\mathrm{RF}}]_{:,\jmath} [\boldsymbol{F}_{\mathrm{RF}}]_{:,\jmath}^*\right]_{i,i} = \frac{1}{N_\mathrm{tot}}$ with $\jmath = 1, \cdots, N_\mathrm{RF}$ and $i = 1, \cdots, N_\mathrm{tot}$; $\boldsymbol{F}_{\mathrm{BB}}$ is an $N_\mathrm{RF} \times N_\mathrm{S}$ digital baseband precoding matrix at the transmitter such that $\|\boldsymbol{F}_{\mathrm{RF}} \boldsymbol{F}_{\mathrm{BB}}\|_\mathrm{F}^2 = 1$; $\boldsymbol{W}_{\mathrm{BB}}$ and $\boldsymbol{W}_{\mathrm{RF}}$ denote $M_\mathrm{RF} \times N_\mathrm{S}$ and $M_\mathrm{tot} \times M_\mathrm{RF}$ baseband and analog combining matrices; $\boldsymbol{H}$ represents an $M_\mathrm{tot} \times N_\mathrm{tot}$ narrowband MIMO channel matrix.

2.3.2   Channel Model

In this part, we employ a ray-cluster based spatial channel model. Denote by g_ℓ, ϕ_ℓ and θ_ℓ the complex path gain, AoA and AoD of path-ℓ, N_p the total number of paths in the channel, and $\boldsymbol{a}_\mathrm{r}(\cdot)$ and $\boldsymbol{a}_\mathrm{t}(\cdot)$ the array response vectors for the receive and transmit antenna arrays. The narrowband channel

is therefore represented as

$$\boldsymbol{H} = \sum_{\ell=1}^{N_\mathrm{p}} g_\ell \boldsymbol{a}_\mathrm{r}(\phi_\ell) \boldsymbol{a}_\mathrm{t}^*(\theta_\ell). \tag{2.2}$$

We employ a ULA at both the transmitter and receiver to explain the key idea of auxiliary beam pair design. Denoting by λ the wavelength corresponding to the operating carrier frequency, and d_t the inter-element distance of the transmit antenna elements, we express the transmit array response vector as

$$\boldsymbol{a}_\mathrm{t}(\theta_\ell) = \frac{1}{\sqrt{N_\mathrm{tot}}} \left[1, e^{\mathrm{j}\frac{2\pi}{\lambda} d_\mathrm{t} \sin(\theta_\ell)}, \cdots, e^{\mathrm{j}\frac{2\pi}{\lambda}(N_\mathrm{tot}-1)d_\mathrm{t}\sin(\theta_\ell)} \right]^\mathrm{T}. \tag{2.3}$$

Similarly, assuming d_r as the inter-element distance of the receive antenna elements,

$$\boldsymbol{a}_\mathrm{r}(\phi_\ell) = \frac{1}{\sqrt{M_\mathrm{tot}}} \left[1, e^{\mathrm{j}\frac{2\pi}{\lambda} d_\mathrm{r} \sin(\phi_\ell)}, \cdots, e^{\mathrm{j}\frac{2\pi}{\lambda}(M_\mathrm{tot}-1)d_\mathrm{r}\sin(\phi_\ell)} \right]^\mathrm{T}. \tag{2.4}$$

We can further express the channel model in (2.2) as $\boldsymbol{H} = \boldsymbol{A}_\mathrm{r}\mathrm{diag}(\boldsymbol{g})\boldsymbol{A}_\mathrm{t}^*$, where $\boldsymbol{g} = \left[g_1, g_2, \cdots, g_{N_\mathrm{p}} \right]^\mathrm{T}$, $\boldsymbol{A}_\mathrm{t} = \left[\boldsymbol{a}_\mathrm{t}(\theta_1), \boldsymbol{a}_\mathrm{t}(\theta_2), \cdots, \boldsymbol{a}_\mathrm{t}(\theta_{N_\mathrm{p}}) \right]$ and $\boldsymbol{A}_\mathrm{r} = \left[\boldsymbol{a}_\mathrm{r}(\phi_1), \boldsymbol{a}_\mathrm{r}(\phi_2), \cdots, \boldsymbol{a}_\mathrm{r}(\phi_{N_\mathrm{p}}) \right]$ contain the transmit and receive array response vectors.

For single-path channels, we can rewrite the channel matrix in (2.2) as $\boldsymbol{H} = g\boldsymbol{a}_\mathrm{r}(\phi)\boldsymbol{a}_\mathrm{t}^*(\theta)$, where the path index is dropped. Denote by $\mu = \frac{2\pi}{\lambda} d_\mathrm{t} \sin(\theta)$ and $\psi = \frac{2\pi}{\lambda} d_\mathrm{r} \sin(\phi)$ the transmit and receive spatial frequencies. We can rewrite the array response vectors for the transmitter and receiver as $\boldsymbol{a}_\mathrm{t}(\mu) = \frac{1}{\sqrt{N_\mathrm{tot}}} \left[1, e^{\mathrm{j}\mu}, \cdots, e^{\mathrm{j}(N_\mathrm{tot}-1)\mu} \right]^\mathrm{T}$ and $\boldsymbol{a}_\mathrm{r}(\psi) = \frac{1}{\sqrt{M_\mathrm{tot}}} \left[1, e^{\mathrm{j}\psi}, \cdots, e^{\mathrm{j}(M_\mathrm{tot}-1)\psi} \right]^\mathrm{T}$.
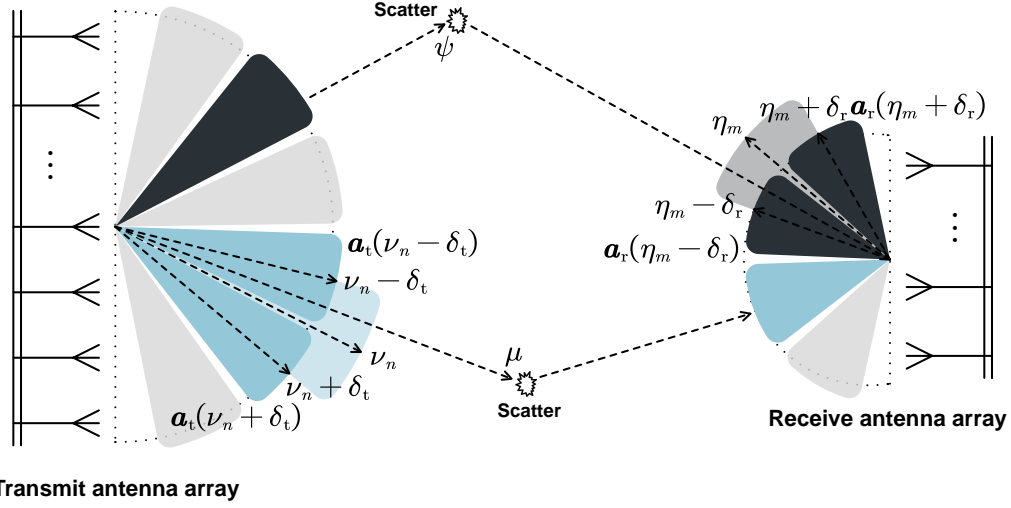
Figure 2.1: A conceptual example of transmit and receive auxiliary beam pairs design. The two beams in the transmit auxiliary beam pair steer towards $\nu_n - \delta_{\mathrm{t}}$ and $\nu_n + \delta_{\mathrm{t}}$. In the receive auxiliary beam pair, the two beams are steered towards $\eta_m - \delta_{\mathrm{r}}$ and $\eta_m + \delta_{\mathrm{r}}$. Further, ν_n and η_m represent the boresights of the corresponding transmit and receive auxiliary beam pairs. For the transmit/receive auxiliary beam pair in this figure, the dark colored regime denotes the half-power beamwidth of the beam in the auxiliary beam pair, while the light colored regime represents the probing range of the corresponding beam pair.

2.3.3 Auxiliary Beam Pair Setup

Denote by N_{K} and M_{K} the total numbers of auxiliary beam pairs sent from the transmitter and receiver. As shown in Figure 2.1, each auxiliary beam pair contains two consecutive analog beams in the angular domain. The total numbers of analog transmit and receive beams are therefore $N_{\mathrm{K}} + 1$ and $M_{\mathrm{K}} + 1$. That is, every two consecutive auxiliary beam pairs share one common analog beam. Consider the n-th ($n = 1, \cdots, N_{\mathrm{K}}$) auxiliary beam pair formed by the transmitter as $\boldsymbol{a}_{\mathrm{t}}(\nu_n - \delta_{\mathrm{t}})$ and $\boldsymbol{a}_{\mathrm{t}}(\nu_n + \delta_{\mathrm{t}})$, where ν_n is the boresight

25

angle of the n-th transmit auxiliary beam pair, and δ_t approximates the half of half-power beamwidth for the transmitter. Similarly, consider the m-th $(m = 1, \cdots, M_\mathrm{K})$ auxiliary beam pair formed by the receiver as $\boldsymbol{a}_\mathrm{r}(\eta_m - \delta_\mathrm{r})$ and $\boldsymbol{a}_\mathrm{r}(\eta_m + \delta_\mathrm{r})$, where η_m and δ_r are similarly defined to ν_n and δ_t. Denote by $\mathcal{A}_n^\mathrm{t} = [\nu_n - \delta_\mathrm{t}, \nu_n + \delta_\mathrm{t}]$ and $\mathcal{A}_m^\mathrm{r} = [\eta_m - \delta_\mathrm{r}, \eta_m + \delta_\mathrm{r}]$ the main probing ranges of the n-th and m-th transmit and receive auxiliary beam pairs. We further assume that the main probing ranges of auxiliary beam pairs are disjoint, i.e., $\cap_{n=1}^{N_\mathrm{K}} \mathcal{A}_n^\mathrm{t} = \emptyset$ and $\cap_{m=1}^{M_\mathrm{K}} \mathcal{A}_m^\mathrm{r} = \emptyset$. For given angular ranges Ω_t and Ω_r for the transmitter and receiver, $\cup_{n=1}^{N_\mathrm{K}} \mathcal{A}_n^\mathrm{t} = \Omega_\mathrm{t}$ and $\cup_{m=1}^{M_\mathrm{K}} \mathcal{A}_m^\mathrm{r} = \Omega_\mathrm{r}$. We assume that the transmit and receive beams are transmitted in a time division multiplexing (TDM) manner. For a given analog receive beam, all analog transmit beams are successively sent by the transmitter. This process continues until all $M_\mathrm{K}+1$ analog receive beams have been formed.

2.4   Auxiliary Beam Pair Enabled Angle Estimation

In this section, we describe the basic design principle of using an auxiliary beam pair to estimate the AoD and AoA in both single-path and multi-path channels.

2.4.1   Single-path AoD/AoA estimation

To estimate the transmit spatial frequency μ, for a given analog receive beam, say, $\boldsymbol{a}_\mathrm{r}(\eta_m + \delta_\mathrm{r})$ and $\boldsymbol{a}_\mathrm{t}(\nu_n - \delta_\mathrm{t})$ in the n-th transmit auxiliary beam

pair, we express the received signal as

$$y_{n,m}^{\Delta} = \alpha \boldsymbol{a}_r^*(\eta_m + \delta_r)\boldsymbol{a}_r(\psi)\boldsymbol{a}_t^*(\mu)\boldsymbol{a}_t(\nu_n - \delta_t)x_1 + \boldsymbol{a}_r^*(\eta_m + \delta_r)\boldsymbol{n}. \qquad (2.5)$$

Assume that μ is within the half-power beamwidth of $\boldsymbol{a}_t(\nu_n - \delta_t)$. We can therefore calculate the corresponding received signal strength as (assuming $|x_1|^2 = 1$ because of the single RF assumption)

$$\chi_{n,m}^{\Delta} = \left(y_{n,m}^{\Delta}\right)^* y_{n,m}^{\Delta} \qquad (2.6)$$

$$\leq \underbrace{|\alpha|^2 \boldsymbol{a}_t^*(\nu_n - \delta_t)\boldsymbol{a}_t(\mu)\boldsymbol{a}_t^*(\mu)\boldsymbol{a}_t(\nu_n - \delta_t)}_{I_1} \qquad (2.7)$$

$$+ \underbrace{\boldsymbol{n}^* \boldsymbol{a}_r(\eta_m + \delta_r)\boldsymbol{a}_r^*(\eta_m + \delta_r)\boldsymbol{n}}_{I_2}$$

$$+ \underbrace{\alpha \boldsymbol{a}_t^*(\nu_n - \delta_t)\boldsymbol{a}_t(\mu)\boldsymbol{a}_r^*(\eta_m + \delta_r)\boldsymbol{n}}_{I_3}$$

$$+ \underbrace{\alpha \boldsymbol{n}^* \boldsymbol{a}_r(\eta_m + \delta_r)\boldsymbol{a}_t^*(\mu)\boldsymbol{a}_t(\nu_n - \delta_t)}_{I_4}$$

$$\approx |\alpha|^2 \boldsymbol{a}_t^*(\nu_n - \delta_t)\boldsymbol{a}_t(\mu)\boldsymbol{a}_t^*(\mu)\boldsymbol{a}_t(\nu_n - \delta_t). \qquad (2.8)$$

The equality in (2.7) is achieved if $\boldsymbol{a}_r(\eta_m + \delta_r) = \boldsymbol{a}_r(\psi)$. To approach $\boldsymbol{a}_r(\eta_m + \delta_r) = \boldsymbol{a}_r(\psi)$, i.e., to minimize the gap with the upper bound in (2.7), the receiver calculates the received signal strength for every combination between analog transmit and receive beams. The analog receive beam that yields the highest received signal strength is then used in (3.12). Because μ is within the half-power beamwidth of $\boldsymbol{a}_t(\nu_n - \delta_t)$, by assuming large $N_{tot}M_{tot}$, $|I_1| \gg |I_2|, |I_3|, |I_4|$, which results in the approximation in (2.8). In this chapter, we employ (2.8) to derive the following results and denote $\chi_n^{\Delta} = |\alpha|^2 \boldsymbol{a}_t^*(\nu_n - \delta_t)\boldsymbol{a}_t(\mu)\boldsymbol{a}_t^*(\mu)\boldsymbol{a}_t(\nu_n - \delta_t)$.

Similarly, using $\boldsymbol{a}_{\mathrm{t}}(\nu_n + \delta_{\mathrm{t}})$ in the n-th transmit auxiliary beam pair, the received signal after combining with $\boldsymbol{a}_{\mathrm{r}}(\eta_m + \delta_{\mathrm{r}})$ is

$$y_{n,m}^{\Sigma} = \alpha \boldsymbol{a}_{\mathrm{r}}^*(\eta_m + \delta_{\mathrm{r}})\boldsymbol{a}_{\mathrm{r}}(\psi)\boldsymbol{a}_{\mathrm{t}}^*(\mu)\boldsymbol{a}_{\mathrm{t}}(\nu_n + \delta_{\mathrm{t}})x_1 + \boldsymbol{a}_{\mathrm{r}}^*(\eta_m + \delta_{\mathrm{r}})\boldsymbol{n}. \tag{2.9}$$

We can calculate the corresponding received signal strength as $\chi_{n,m}^{\Sigma} = \left(y_{n,m}^{\Sigma}\right)^* y_{n,m}^{\Sigma}$. Similar to (2.8) and the definition of χ_n^{Δ}, by assuming that μ is within the half-power beamwidth of $\boldsymbol{a}_{\mathrm{t}}(\nu_n + \delta_{\mathrm{t}})$, we can obtain $\chi_n^{\Sigma} = |\alpha|^2 \boldsymbol{a}_{\mathrm{t}}^*(\nu_n + \delta_{\mathrm{t}})\boldsymbol{a}_{\mathrm{t}}(\mu)\boldsymbol{a}_{\mathrm{t}}^*(\mu)\boldsymbol{a}_{\mathrm{t}}(\nu_n + \delta_{\mathrm{t}})$. Further, we set $\delta_{\mathrm{t}} = \pi/N_{\mathrm{tot}}$ to approximate the half of half-power beamwidth for a ULA [58]. Hence, we have

$$\chi_n^{\Delta} \overset{(a)}{=} |\alpha|^2 \frac{\sin^2\left(\frac{N_{\mathrm{tot}}(\mu - \nu_n + \delta_{\mathrm{t}})}{2}\right)}{\sin^2\left(\frac{\mu - \nu_n + \delta_{\mathrm{t}}}{2}\right)} \overset{(b)}{=} |\alpha|^2 \frac{\cos^2\left(\frac{N_{\mathrm{tot}}(\mu - \nu_n)}{2}\right)}{\sin^2\left(\frac{\mu - \nu_n + \delta_{\mathrm{t}}}{2}\right)}, \tag{2.10}$$

where (a) is obtained via $\left|\sum_{\bar{m}=1}^{M} e^{-j(\bar{m}-1)\bar{x}}\right|^2 = \frac{\sin^2\left(\frac{M\bar{x}}{2}\right)}{\sin^2\left(\frac{\bar{x}}{2}\right)}$ and (b) is by assuming $\delta_{\mathrm{t}} = \pi/N_{\mathrm{tot}}$. Similarly,

$$\chi_n^{\Sigma} = |\alpha|^2 \frac{\cos^2\left(\frac{N_{\mathrm{tot}}(\mu - \nu_n)}{2}\right)}{\sin^2\left(\frac{\mu - \nu_n - \delta_{\mathrm{t}}}{2}\right)}. \tag{2.11}$$

We define a ratio metric ζ_n^{AoD} as

$$\zeta_n^{\mathrm{AoD}} = \frac{\chi_n^{\Delta} - \chi_n^{\Sigma}}{\chi_n^{\Delta} + \chi_n^{\Sigma}} = \frac{\sin^2\left(\frac{\mu - \nu_n - \delta_{\mathrm{t}}}{2}\right) - \sin^2\left(\frac{\mu - \nu_n + \delta_{\mathrm{t}}}{2}\right)}{\sin^2\left(\frac{\mu - \nu_n - \delta_{\mathrm{t}}}{2}\right) + \sin^2\left(\frac{\mu - \nu_n + \delta_{\mathrm{t}}}{2}\right)} \tag{2.12}$$

$$= -\frac{\sin\left(\mu - \nu_n\right)\sin(\delta_{\mathrm{t}})}{1 - \cos\left(\mu - \nu_n\right)\cos(\delta_{\mathrm{t}})}. \tag{2.13}$$

It can be seen from the last equality in (2.13) that $\zeta_n^{\mathrm{AoD}} \in [-1, 1]$. As the beam pattern designed in this chapter is different from that in the monopulse radar systems, we present the following lemma to illustrate the monotonicity of the ratio metric for a given interval.

Lemma 2.1. If $|\mu - \nu_n| < \delta_t$, i.e., the transmit spatial frequency μ is within the range of $(\nu_n - \delta_t, \nu_n + \delta_t)$, ζ_n^{AoD} is a monotonically decreasing function of $\mu - \nu_n$ and invertible with respect to $\mu - \nu_n$.

Proof. Denote by $z = \mu - \nu_n$,

$$\frac{d}{dz} \frac{\sin(z)\sin(\delta_t)}{\cos(z)\cos(\delta_t) - 1} = \frac{\sin(\delta_t)\left[\cos(\delta_t) - \cos(z)\right]}{\left[\cos(z)\cos(\delta_t) - 1\right]^2}. \tag{2.14}$$

According to the definition, $\delta_t \in [0, \pi]$, and $\sin(\delta_t) \geq 0$. As $|\mu - \nu_n| < \delta_t$, $\cos(\delta_t) - \cos(z) < 0$ for every $z \in [-\pi, \pi]$. This leads to (3.16) being nonnegative for every z. $\qquad\square$

By using the ratio metric ζ_n^{AoD} and based on Lemma 2.1, we can therefore derive the estimated value of μ via the inverse function as

$$\hat{\mu}_n = \nu_n - \arcsin\left(\frac{\zeta_n^{\mathrm{AoD}}\sin(\delta_t) - \zeta_n^{\mathrm{AoD}}\sqrt{1 - (\zeta_n^{\mathrm{AoD}})^2}\sin(\delta_t)\cos(\delta_t)}{\sin^2(\delta_t) + (\zeta_n^{\mathrm{AoD}})^2\cos^2(\delta_t)}\right). \tag{2.15}$$

Note that if ζ_n^{AoD} is perfect, i.e., not impaired by noise, the transmit spatial frequency can be perfectly recovered, i.e., $\mu = \hat{\mu}_n$. The corresponding array response vector for the transmitter can then be constructed as $\boldsymbol{a}_t(\hat{\theta})$ with the estimated AoD $\hat{\theta} = \arcsin(\lambda\hat{\mu}_n/2\pi d_t)$.

So far, we illustrate the estimation of single-path AoD using the ratio metric calculated from the n-th auxiliary beam pair because we assume $|\mu - \nu_n| < \delta_t$. In practice, however, it is not possible to know which auxiliary beam pair covers the AoD *a prior* at either the transmitter or receiver. It is therefore necessary to form multiple auxiliary beam pairs to cover a given

29

angular range and determine a performance metric that helps the receiver to identify the transmit auxiliary beam pair whose main probing range most likely covers the AoD. For all transmit auxiliary beam pairs with a given analog combining vector, a set of ratio metrics $\left\{\zeta_1^{\text{AoD}}, \cdots, \zeta_n^{\text{AoD}}, \cdots, \zeta_{N_{\text{K}}}^{\text{AoD}}\right\}$ are determined according to (2.13). If the receiver does not have any knowledge of ν_n's and δ_{t}, it can select the ratio metric that characterizes the AoD the best using the following lemma.

Lemma 2.2. If $|\mu - \nu_n| < \delta_{\text{t}}$, i.e., the transmit spatial frequency μ is within the main probing range of the n-th auxiliary beam pair, and $|\mu - (\nu_n - \delta_{\text{t}})| \leq |\mu - (\nu_n + \delta_{\text{t}})|$,

$$\chi_n^{\Delta} = \max_{n'=1,\cdots,N_{\text{K}}} \left\{\chi_{n'}^{\Delta}, \chi_{n'}^{\Sigma}\right\}, \tag{2.16}$$

for a given analog receive combining vector assuming no noise. Similarly, if $|\mu - \nu_n| < \delta_{\text{t}}$ and $|\mu - (\nu_n + \delta_{\text{t}})| \leq |\mu - (\nu_n - \delta_{\text{t}})|$,

$$\chi_n^{\Sigma} = \max_{n'=1,\cdots,N_{\text{K}}} \left\{\chi_{n'}^{\Delta}, \chi_{n'}^{\Sigma}\right\}, \tag{2.17}$$

for a given analog receive combining vector assuming no noise.

Proof. Assume $|\mu - (\nu_n - \delta_{\text{t}})| \leq |\mu - (\nu_n + \delta_{\text{t}})|$. As $|\mu - \nu_n| < \delta_{\text{t}}$, μ is within the half-power beamwidth of $\boldsymbol{a}_{\text{t}}(\nu_n - \delta_{\text{t}})$ because δ_{t} is set as the half of half-power beamwidth for the given antenna array. Denote by

$$\chi_{\max} = |\alpha|^2 \left|\boldsymbol{a}_{\text{t}}^*(\mu)\boldsymbol{a}_{\text{t}}(\mu)\right|^2, \tag{2.18}$$

we have $\chi_n^{\Delta} \in \left[\frac{1}{2}\chi_{\max}, \chi_{\max}\right]$ and $\chi_n^{\Sigma} \in \left[0, \frac{1}{2}\chi_{\max}\right]$. Note that $\chi_n^{\Delta} = \chi_n^{\Sigma} = \frac{1}{2}\chi_{\max}$ only occurs when $\mu = \nu_n$. According to the design principle of the auxiliary

30

beam pairs, the main probing ranges of auxiliary beam pairs are disjoint. We therefore have $\chi_{n'}^{\Delta}, \chi_{n'}^{\Sigma} \in [0, \frac{1}{2}\chi_{\max})$ for $n' = 1, \cdots, N_{\mathrm{K}}$, $n' \neq n$. Hence, $\chi_n^{\Delta} = \max_{n'=1,\cdots,N_{\mathrm{K}}} \{\chi_{n'}^{\Delta}, \chi_{n'}^{\Sigma}\}$. For $|\mu - (\nu_n + \delta_{\mathrm{t}})| \leq |\mu - (\nu_n - \delta_{\mathrm{t}})|$, we obtain (2.17) in a similar fashion. $\qquad\square$

Lemma 2.2 implies that if we select the beam with the highest received signal strength, the probing range of the corresponding auxiliary beam pair covers the transmit spatial frequency to be estimated. To choose the paired beam with respect to the beam selected using Lemma 2.2, we can test the received signal strengths of its two adjacent beams. We can then select the adjacent beam with the highest received signal strength among the two.

To estimate the receive spatial frequency ψ, we can similarly compute the ratio metric as

$$\zeta_m^{\mathrm{AoA}} = -\frac{\sin\left(\psi - \eta_m\right)\sin(\delta_{\mathrm{r}})}{1 - \cos\left(\psi - \eta_m\right)\cos(\delta_{\mathrm{r}})}. \tag{2.19}$$

If $|\psi - \eta_m| < \delta_{\mathrm{r}}$, ζ_m^{AoA} is invertible with respect to $\psi - \eta_m$, and we can obtain the estimated value of ψ via the inverse function as

$$\hat{\psi}_m = \eta_m - \arcsin\left(\frac{\zeta_m^{\mathrm{AoA}}\sin(\delta_{\mathrm{r}}) - \zeta_m^{\mathrm{AoA}}\sqrt{1 - \left(\zeta_m^{\mathrm{AoA}}\right)^2}\sin(\delta_{\mathrm{r}})\cos(\delta_{\mathrm{r}})}{\sin^2(\delta_{\mathrm{r}}) + \left(\zeta_m^{\mathrm{AoA}}\right)^2\cos^2(\delta_{\mathrm{r}})}\right). \tag{2.20}$$

The corresponding receive array response vector can be constructed as $\boldsymbol{a}_{\mathrm{r}}(\hat{\phi})$ with the estimated AoA $\hat{\phi} = \arcsin\left(\lambda\hat{\psi}_m/2\pi d_{\mathrm{r}}\right)$. According to (2.19) and (2.20), for all receive auxiliary beam pairs with a given transmit beamforming vector, a set of ratio metrics $\{\zeta_1^{\mathrm{AoA}}, \cdots, \zeta_m^{\mathrm{AoA}}, \cdots, \zeta_{M_{\mathrm{K}}}^{\mathrm{AoA}}\}$ and a set of estimated

receive spatial frequencies $\{\hat{\psi}_1, \cdots, \hat{\psi}_m, \cdots, \hat{\psi}_{M_K}\}$ are obtained by the receiver. The receive spatial frequency, and therefore, the AoA estimated from the receive auxiliary beam pair determined using Lemma 2.2 is then selected.

If multiple paths exist in the propagation channel, the proposed algorithm would estimate the dominant path's AoD and AoA with the highest path gain with high probability. Consider $\boldsymbol{a}_{\mathrm{t}}(\nu_n - \delta_{\mathrm{t}})$ and $\boldsymbol{a}_{\mathrm{r}}(\eta_m + \delta_{\mathrm{r}})$, we can rewrite (3.12) as

$$\acute{y}_{n,m}^{\Delta} = \sum_{\ell'=1}^{N_{\mathrm{p}}} \alpha_{\ell'} \boldsymbol{a}_{\mathrm{r}}^*(\eta_m + \delta_{\mathrm{r}}) \boldsymbol{a}_{\mathrm{r}}(\psi_{\ell'}) \boldsymbol{a}_{\mathrm{t}}^*(\mu_{\ell'}) \boldsymbol{a}_{\mathrm{t}}(\nu_n - \delta_{\mathrm{t}}) x_1 + \boldsymbol{a}_{\mathrm{r}}^*(\eta_m + \delta_{\mathrm{r}}) \boldsymbol{n}, \quad (2.21)$$

where $\alpha_{\ell'} = g_{\ell'} \sqrt{N_{\mathrm{tot}} M_{\mathrm{tot}}}$. In the absence of noise, we calculate the corresponding received signal strength as

$$\begin{aligned}
\acute{\chi}_{n,m}^{\Delta} &= |\alpha_{\ell}|^2 \left|\boldsymbol{a}_{\mathrm{t}}^*(\mu_\ell) \boldsymbol{a}_{\mathrm{t}}(\nu_n + \delta_{\mathrm{t}})\right|^2 \left|\boldsymbol{a}^*(\psi_\ell) \boldsymbol{a}_{\mathrm{r}}(\eta_m + \delta_{\mathrm{r}})\right|^2 \\
&\quad + \alpha_\ell \boldsymbol{a}^*(\psi_\ell) \boldsymbol{a}_{\mathrm{r}}(\eta_m + \delta_{\mathrm{r}}) \boldsymbol{a}_{\mathrm{t}}^*(\mu_\ell) \boldsymbol{a}_{\mathrm{t}}(\nu_n + \delta_{\mathrm{t}}) \\
&\quad\quad \times \sum_{\ell'=1, \ell' \neq \ell}^{N_{\mathrm{p}}} \alpha_{\ell'} \boldsymbol{a}_{\mathrm{t}}^*(\nu_n + \delta_{\mathrm{t}}) \boldsymbol{a}_{\mathrm{t}}(\mu_{\ell'}) \boldsymbol{a}_{\mathrm{r}}^*(\psi_{\ell'}) \boldsymbol{a}_{\mathrm{r}}(\eta_m + \delta_{\mathrm{r}}) \\
&\quad + \alpha_\ell \boldsymbol{a}_{\mathrm{t}}^*(\nu_n + \delta_{\mathrm{t}}) \boldsymbol{a}_{\mathrm{t}}(\mu_\ell) \boldsymbol{a}_{\mathrm{r}}^*(\psi_\ell) \boldsymbol{a}_{\mathrm{r}}(\eta_m + \delta_{\mathrm{r}}) \\
&\quad\quad \times \sum_{\ell'=1, \ell' \neq \ell}^{N_{\mathrm{p}}} \alpha_{\ell'} \boldsymbol{a}^*(\psi_{\ell'}) \boldsymbol{a}_{\mathrm{r}}(\eta_m + \delta_{\mathrm{r}}) \boldsymbol{a}_{\mathrm{t}}^*(\mu_{\ell'}) \boldsymbol{a}_{\mathrm{t}}(\nu_n + \delta_{\mathrm{t}}) \\
&\quad + \sum_{\ell'=1, \ell' \neq \ell}^{N_{\mathrm{p}}} |\alpha_{\ell'}|^2 \left|\boldsymbol{a}_{\mathrm{t}}^*(\mu_{\ell'}) \boldsymbol{a}_{\mathrm{t}}(\nu_n + \delta_{\mathrm{t}})\right|^2 \left|\boldsymbol{a}^*(\psi_{\ell'}) \boldsymbol{a}_{\mathrm{r}}(\eta_m + \delta_{\mathrm{r}})\right|^2 \quad (2.22) \\
&\xrightarrow[N_{\mathrm{tot}} M_{\mathrm{tot}} \to \infty]{\text{a.s.}} |\alpha_\ell|^2 \left|\boldsymbol{a}_{\mathrm{t}}^*(\mu_\ell) \boldsymbol{a}_{\mathrm{t}}(\nu_n + \delta_{\mathrm{t}})\right|^2 \left|\boldsymbol{a}^*(\psi_\ell) \boldsymbol{a}_{\mathrm{r}}(\eta_m + \delta_{\mathrm{r}})\right|^2. \quad (2.23)
\end{aligned}$$

Assuming $\mu_\ell \in (\nu_n - \delta_{\mathrm{t}}, \nu_n + \delta_{\mathrm{t}})$ and $\psi_\ell \in (\eta_m - \delta_{\mathrm{r}}, \eta_m + \delta_{\mathrm{r}})$, as mmWave channels generally exhibit sparse structure in the angular domain such that

32

the number of multi-path components is limited with relatively small angular spreads [59, 60], by jointly employing directional transmit beamforming and receive combining with $N_{\mathrm{tot}} M_{\mathrm{tot}} \to \infty$, the last three terms, in particular, the sum terms in (2.22) converge to zeros, and (2.23) is achieved. Similar to (2.23), we can obtain $\acute{\chi}_{n,m}^{\Sigma}$. Using the asymptotic results of $\acute{\chi}_{n,m}^{\Delta}$ and $\acute{\chi}_{n,m}^{\Sigma}$ to calculate (2.13), we can obtain the same ratio metric. If $\ell = \underset{\ell'=1,\cdots,N_{\mathrm{p}}}{\mathrm{argmax}}\ \alpha_{\ell'}$, we can identify the dominant path ℓ almost surely (a.s.) via simple power comparison [61]. In the proposed method, a total number of $(N_{\mathrm{K}} + 1) \times (M_{\mathrm{K}} + 1)$ attempts are required by the receiver to simultaneously estimate the single-path AoD and AoA. In Section 2.4.3, we describe how to exploit the proposed algorithm to estimate the multi-path components with multiple RF chains.

2.4.2 Performance analysis and comparison with other angle estimation methods

In this subsection, we first present the analytical estimation error variance performance of our proposed strategy in both single-path and multi-path channels. We then compare our derived variance of angle estimate with those obtained from the GoB and compressed sensing based designs. We conclude from the comparison that they converge to the same result when applying the large system analysis.

2.4.2.1 Angle estimation error variance analysis

Consider a given transmit beamforming vector $\boldsymbol{a}_{\mathrm{t}}(\nu_n + \delta_{\mathrm{t}})$, and assume that $\boldsymbol{a}_{\mathrm{t}}^*(\nu_n + \delta_{\mathrm{t}})\boldsymbol{a}_{\mathrm{t}}(\mu) = \beta$, where $0 \le |\beta| \le 1$ represents the amount of transmit

beamforming mismatch. Further, we assume that the receive spatial frequency satisfies $|\psi - \eta_m| < \delta_r$. To derive the following lemma that characterizes the receive spatial frequency estimation performance of the proposed approach, $\psi = 0$ is assumed.

Lemma 2.3. In a single-path channel, the variance of receive spatial frequency estimate, i.e., $\mathbb{E}\left[\hat{\psi}^2\right]$, using the proposed auxiliary beam pair design is approximated as

$$\sigma_{\hat{\psi}}^2 \approx \frac{(1 - \cos(\delta_r))^2 |\Upsilon_\Sigma|}{2|\alpha|^2|\beta|^2\gamma \sin^2(\delta_r)\, |\boldsymbol{a}_r^*(\psi)\boldsymbol{\Lambda}_\Delta \boldsymbol{a}_r(\psi)|} \left[1 + \left(\zeta_m^{\mathrm{AoA}}\right)^2\right], \qquad (2.24)$$

where $\boldsymbol{\Lambda}_\Delta = \boldsymbol{a}_r(\eta_m - \delta_r)\boldsymbol{a}_r^*(\eta_m - \delta_r) - \boldsymbol{a}_r(\eta_m + \delta_r)\boldsymbol{a}_r^*(\eta_m + \delta_r)$ and $\Upsilon_\Sigma = \boldsymbol{a}_r^*(\eta_m - \delta_r)\boldsymbol{a}_r(\eta_m - \delta_r) + \boldsymbol{a}_r^*(\eta_m + \delta_r)\boldsymbol{a}_r(\eta_m + \delta_r)$.

Proof. For a given analog transmit beam $\boldsymbol{a}_t(\nu_n + \delta_t)$, the received signals after analog combining with $\boldsymbol{a}_r(\eta_m - \delta_r)$ and $\boldsymbol{a}_r(\eta_m + \delta_r)$ are given as

$$v_{n,m}^\Delta = \alpha\boldsymbol{a}_r^*(\eta_m - \delta_r)\boldsymbol{a}_r(\psi)\boldsymbol{a}_t^*(\mu)\boldsymbol{a}_t(\nu_n + \delta_t)x_1 + \boldsymbol{a}_r^*(\eta_m - \delta_r)\boldsymbol{n}, \quad (2.25)$$

$$v_{n,m}^\Sigma = \alpha\boldsymbol{a}_r^*(\eta_m + \delta_r)\boldsymbol{a}_r(\psi)\boldsymbol{a}_t^*(\mu)\boldsymbol{a}_t(\nu_n + \delta_t)x_1 + \boldsymbol{a}_r^*(\eta_m + \delta_r)\boldsymbol{n}. \quad (2.26)$$

Assume $\boldsymbol{a}_t^*(\nu_n + \delta_t)\boldsymbol{a}_t(\mu) = \beta$, the corresponding received signal strength of combining with $\boldsymbol{a}_r(\eta_m - \delta_r)$ is calculated as

$$\rho_m^\Delta = \left(v_{n,m}^\Delta\right)^* v_{n,m}^\Delta \qquad (2.27)$$

$$= |\alpha|^2|\beta|^2\boldsymbol{a}_r^*(\eta_m - \delta_r)\boldsymbol{a}_r(\psi)\boldsymbol{a}_r^*(\psi)\boldsymbol{a}_r(\eta_m - \delta_r)$$

$$+ \boldsymbol{a}_r^*(\eta_m - \delta_r)\boldsymbol{n}\boldsymbol{n}^*\boldsymbol{a}_r(\eta_m - \delta_r)$$

$$+ \alpha\beta\boldsymbol{a}_r^*(\eta_m - \delta_r)\boldsymbol{a}_r(\psi)\boldsymbol{n}^*\boldsymbol{a}_r(\eta_m - \delta_r)$$

$$+ \alpha\beta\boldsymbol{a}_r^*(\eta_m - \delta_r)\boldsymbol{n}\boldsymbol{a}_r^*(\psi)\boldsymbol{a}_r(\eta_m - \delta_r), \qquad (2.28)$$

34

and the received signal strength of combining with $\boldsymbol{a}_\mathrm{r}(\eta_m+\delta_\mathrm{r})$ can be similarly obtained via $\rho_m^\Sigma = \left(v_{n,m}^\Sigma\right)^* v_{n,m}^\Sigma$. Regard $\rho_m^\Delta - \rho_m^\Sigma$ and $\rho_m^\Delta + \rho_m^\Sigma$ as difference and sum channel outputs. Denote by S_Δ the signal power of the difference channel output as

$$S_\Delta = |\alpha|^2 |\beta|^2 \left| \boldsymbol{a}_\mathrm{r}^*(\psi)\boldsymbol{\Lambda}_\Delta\boldsymbol{a}_\mathrm{r}(\psi) \right|. \tag{2.29}$$

Denote by N_Σ the noise power of the sum channel output such that

$$N_\Sigma = \sigma^2 \left| \Upsilon_\Sigma \right|. \tag{2.30}$$

For unbiased estimator, i.e., $\mathbb{E}\left[\hat{\psi}_m \right] = 0$, a reasonable approximation to the variance of angle estimation is expressed as

$$\sigma_\psi^2 = \mathbb{E}\left[\hat{\psi}_m^2 \right] \approx \frac{1}{2k_\mathrm{m}^2 S_\Delta/N_\Sigma} \left[1 + \mathcal{M}^2(\psi) \right], \tag{2.31}$$

where in this paper, $\mathcal{M}(\psi) = \zeta_m^{\mathrm{AoA}}$, and $k_\mathrm{m} = \mathcal{M}'(\eta_m)$ is the slope of $\mathcal{M}(\cdot)$ at boresight of the corresponding auxiliary beam pair. According to (2.13),

$$k_\mathrm{m} = \mathcal{M}'(\eta_m) = -\frac{\sin(\delta_\mathrm{r})}{1 - \cos(\delta_\mathrm{r})}. \tag{2.32}$$

By plugging (2.29), (2.30) and (2.32) into (2.31), (2.24) is obtained, which completes the proof. $\qquad\square$

For a multi-path channel and a given transmit beamforming vector $\boldsymbol{a}_\mathrm{t}(\nu_n + \delta_\mathrm{t})$, let the dominant path's transmit spatial frequency μ_ℓ satisfy $\boldsymbol{a}_\mathrm{t}^*(\nu_n + \delta_\mathrm{t})\boldsymbol{a}_\mathrm{t}(\mu_\ell) = \beta$. The corresponding receive spatial frequency satisfies $|\psi_\ell - \eta_m| < \delta_\mathrm{r}$. Assuming $\psi_\ell = 0$, the following corollary characterizes the dominant path's receive spatial frequency estimation performance.

35

Corollary 2.1. For a given multi-path channel, the variance of dominant path's receive spatial frequency estimate, i.e., $\mathbb{E}\left[\hat{\psi}_\ell^2\right]$, using the proposed auxiliary beam pair design is approximated as

$$\sigma_{\hat{\psi}_\ell}^2 \approx \frac{(1-\cos(\delta_{\mathrm{r}}))^2 \left(\sigma^2 |\Upsilon_\Sigma| + \sum_{\ell'=1,\ell'\neq\ell}^{N_{\mathrm{p}}} |\boldsymbol{a}_{\mathrm{t}}^*(\nu_n+\delta_{\mathrm{t}})\boldsymbol{G}_{\ell'}^*\boldsymbol{\Lambda}_\Sigma\boldsymbol{G}_{\ell'}\boldsymbol{a}_{\mathrm{t}}(\nu_n+\delta_{\mathrm{t}})|\right)}{2|\alpha|^2|\beta|^2\sin^2(\delta_{\mathrm{r}})\,|\boldsymbol{a}_{\mathrm{r}}^*(\psi_\ell)\boldsymbol{\Lambda}_\Delta\boldsymbol{a}_{\mathrm{r}}(\psi_\ell)|}$$

$$\times \left[1 + \left(\zeta_{m,\ell}^{\mathrm{AoA}}\right)^2\right], \tag{2.33}$$

where $\boldsymbol{G}_{\ell'} = \alpha_{\ell'}\boldsymbol{a}_{\mathrm{r}}(\psi_{\ell'})\boldsymbol{a}_{\mathrm{t}}^*(\mu_{\ell'})$, $\zeta_{m,\ell}^{\mathrm{AoA}} = -\frac{\sin(\psi_\ell-\eta_m)\sin(\delta_{\mathrm{r}})}{1-\cos(\psi_\ell-\eta_m)\cos(\delta_{\mathrm{r}})}$, and $\boldsymbol{\Lambda}_\Sigma = \boldsymbol{a}_{\mathrm{r}}(\eta_m - \delta_{\mathrm{r}})\boldsymbol{a}_{\mathrm{r}}^*(\eta_m - \delta_{\mathrm{r}}) + \boldsymbol{a}_{\mathrm{r}}(\eta_m + \delta_{\mathrm{r}})\boldsymbol{a}_{\mathrm{r}}^*(\eta_m + \delta_{\mathrm{r}})$.

The approximated result in Corollary 2.1 is obtained by treating N_Σ in (2.30) as the multi-path interference plus noise power of the sum channel output, which is computed as

$$N_\Sigma = \sigma^2 |\Upsilon_\Sigma| + \sum_{\ell'=1,\ell'\neq\ell}^{N_{\mathrm{p}}} |\boldsymbol{a}_{\mathrm{t}}^*(\nu_n+\delta_{\mathrm{t}})\boldsymbol{G}_{\ell'}^*\boldsymbol{\Lambda}_\Sigma\boldsymbol{G}_{\ell'}\boldsymbol{a}_{\mathrm{t}}(\nu_n+\delta_{\mathrm{t}})|. \tag{2.34}$$

2.4.2.2   Large system analysis

We can conclude from Lemma 2.3 that if the angular spacing between the two beams in the same auxiliary beam pair is zero, i.e., $\delta_{\mathrm{r}} = 0$, we have $\cos(\delta_{\mathrm{r}}) = 1$, and therefore $\sigma_{\hat{\psi}}^2 = 0$. As we assume $\psi = 0$ in our derivation, we can obtain $\hat{\psi} = \psi = 0$. Assuming infinite number of receive antennas, i.e., $M_{\mathrm{tot}} \to \infty$, we can first asymptotically compute the sum and difference channel outputs as $|\Upsilon_\Sigma| \to 2$ and $|\boldsymbol{a}_{\mathrm{r}}^*(\psi)\boldsymbol{\Lambda}_\Delta\boldsymbol{a}_{\mathrm{r}}(\psi)| \to 0$. Note that $M_{\mathrm{tot}} \to \infty$ also implies that extremely narrow receive beams are used by the receiver to

conduct the angle estimation with DFT-type beam codebook. Further, we assume that a total of M_{tot} receive beams are probed to cover the given angular range. Intuitively, under this large system assumption, we have $\delta_{\text{r}} \to 0$. Based on our previous analysis, we can therefore obtain $\sigma_{\hat{\psi}}^2 \to 0$ regardless of the receive spatial frequency to be estimated. We can derive similar results for the multi-path channel, where the estimation of dominant path's spatial frequency is the design focus. From the above analysis, we can see that our proposed off-grid auxiliary beam pair structure is still subject to the beam grid resolution assuming noise, multi-path interference and other types of impairments. From the design principle of the on-grid GoB based method (uniform quantization), it is straightforward that the corresponding angle estimation error variance also converges to zero if the number of employed antennas is very large. For the on-grid compressed sensing based strategy, it is reported in [62] that the asymptotic error variance of orthogonal matching pursuit (OMP) can be expressed as $\sigma_{\text{OMP}}^2 = \frac{2\mathbb{E}[L]}{N_{\text{D}}}\sigma^2$, where N_{D} corresponds to the dictionary size and L is the number of iterations required by the OMP. Assuming $N_{\text{D}} \to \infty$, this error variance converges to those derived from the auxiliary beam pair and GoB based methods.

2.4.3 Multi-path AoD/AoA estimation

If the transmitter and receiver have N_{RF} and M_{RF} RF chains, we propose to simultaneously form N_{RF} and M_{RF} analog transmit and receive beams for a given time instant. This is more efficient than forming one beam at a

time using a single RF chain to cover a given angular range. By selecting the best transmit and receive auxiliary beam pairs from all beamforming and combining vectors, we can obtain high-resolution multi-path AoD and AoA estimates. To facilitate the selection of the best transmit and receive auxiliary beam pairs, the simultaneously formed analog transmit and receive beams are sent towards random directions. Pseudo-random sequence (e.g., m-sequence) scrambled with the beam specific identity (ID) is transmitted along with the analog transmit beam. By detecting the pseudo-random sequence, the receiver is able to differentiate the simultaneously probed analog transmit beams.

Denote by N_T and M_T the total numbers of probings performed by the transmitter and receiver. Denote by $\mathcal{F}_\mathrm{T} = \{\boldsymbol{a}_\mathrm{t}(\nu_n \pm \delta_\mathrm{t}), n = 1, \cdots, N_\mathrm{K}\}$ and $\mathcal{W}_\mathrm{T} = \{\boldsymbol{a}_\mathrm{r}(\eta_m \pm \delta_\mathrm{r}), m = 1, \cdots, M_\mathrm{K}\}$ the codebooks of analog transmit and receive steering vectors. The analog transmit and receive probing matrices are constructed by concatenating all successively probed analog transmit precoding and receive combining matrices. For instance, denote by $\boldsymbol{F}_\mathrm{T}$ and $\boldsymbol{W}_\mathrm{T}$ the analog transmit and receive probing matrices, we have $\boldsymbol{F}_\mathrm{T} = [\boldsymbol{F}_1, \cdots, \boldsymbol{F}_{n_\mathrm{t}}, \cdots, \boldsymbol{F}_{N_\mathrm{T}}]$ and $\boldsymbol{W}_\mathrm{T} = [\boldsymbol{W}_1, \cdots, \boldsymbol{W}_{m_\mathrm{t}}, \cdots, \boldsymbol{W}_{M_\mathrm{T}}]$, where $\boldsymbol{F}_{n_\mathrm{t}} \in \mathbb{C}^{N_\mathrm{tot} \times N_\mathrm{RF}}$ represents the n_t-th probing formed by the transmitter, $\boldsymbol{W}_{m_\mathrm{t}} \in \mathbb{C}^{M_\mathrm{tot} \times M_\mathrm{RF}}$ is the m_t-th probing at the receiver. Each column in $\boldsymbol{F}_{n_\mathrm{t}}$ and $\boldsymbol{W}_{m_\mathrm{t}}$ is randomly chosen from $\mathcal{F}_\mathrm{T}$ and $\mathcal{W}_\mathrm{T}$. We will elaborate the reason for simultaneously steering the transmit and receive beams towards random directions other than successive or predefined directions later. The transmit and receive probings are conducted in a TDM manner. That is, for a given probing at the

38

receiver, e.g., $\boldsymbol{W}_{m_{\mathrm{t}}}$, N_{T} consecutive probings $\boldsymbol{F}_1, \cdots, \boldsymbol{F}_{N_{\mathrm{T}}}$ are performed at the transmitter. This process iterates until all M_{T} probings have been executed by the receiver. As each beam in $\mathcal{F}_{\mathrm{T}}$ is associated with a distinct beam ID, the receiver can identify a specific beam in $\boldsymbol{F}_{\mathrm{T}}$, and therefore, a specific transmit auxiliary beam pair.

Assume that $\mu_\ell \in (\nu_n - \delta_{\mathrm{t}}, \nu_n + \delta_{\mathrm{t}})$ and $\psi_\ell \in (\eta_m - \delta_{\mathrm{r}}, \eta_m + \delta_{\mathrm{r}})$ for a given $\ell \in \{1, \cdots, N_{\mathrm{p}}\}$ where N_{p} is the total number of paths. To estimate path-ℓ's transmit spatial frequency μ_ℓ, considering a given probing at the receiver, e.g., $\boldsymbol{W}_{m_{\mathrm{t}}}$, we obtain the resultant matrix by concatenating the $N_{\mathrm{T}} N_{\mathrm{RF}}$ transmit beamforming vectors in the absence of noise as

$$\boldsymbol{Y}_{m_{\mathrm{t}}} \;=\; \boldsymbol{W}_{m_{\mathrm{t}}}^* \boldsymbol{H} \boldsymbol{F}_{\mathrm{T}} \boldsymbol{X}, \tag{2.35}$$

where $\boldsymbol{X}$ is a diagonal matrix carrying $N_{\mathrm{T}} N_{\mathrm{RF}}$ training symbols on its diagonal. For simplicity, we set $\boldsymbol{X} = \boldsymbol{I}_{N_{\mathrm{T}} N_{\mathrm{RF}}}$. By detecting the beam ID, the receiver is able to locate a specific transmit auxiliary beam pair in $\boldsymbol{F}_{\mathrm{T}}$. For instance, $[\boldsymbol{F}_{\mathrm{T}}]_{:,u} = \boldsymbol{a}_{\mathrm{t}}(\nu_n - \delta_{\mathrm{t}})$, and $[\boldsymbol{F}_{\mathrm{T}}]_{:,v} = \boldsymbol{a}_{\mathrm{t}}(\nu_n + \delta_{\mathrm{t}})$, $u, v \in \{1, \cdots, N_{\mathrm{T}} N_{\mathrm{RF}}\}$. Consider path-$\ell$ and $\boldsymbol{a}_{\mathrm{t}}(\nu_n - \delta_{\mathrm{t}})$, we have

$$\left| [\boldsymbol{Y}_{m_{\mathrm{t}}}]_{\ell,u} \right|^2 \;=\; \chi_{n,m_{\mathrm{t}},\ell}^{\Delta} + \sum_{\ell'=1, \ell' \neq \ell}^{N_{\mathrm{p}}} |\alpha_{\ell'}|^2 \Bigg[[\boldsymbol{W}_{m_{\mathrm{t}}}]_{:,\ell}^* \boldsymbol{a}_{\mathrm{r}}(\psi_{\ell'}) \boldsymbol{a}_{\mathrm{t}}^*(\mu_{\ell'}) \boldsymbol{a}_{\mathrm{t}}(\nu_n - \delta_{\mathrm{t}})$$
$$\times \;\; \boldsymbol{a}_{\mathrm{t}}^*(\nu_n - \delta_{\mathrm{t}}) \boldsymbol{a}_{\mathrm{t}}(\mu_{\ell'}) \boldsymbol{a}_{\mathrm{r}}^*(\psi_{\ell'}) \, [\boldsymbol{W}_{m_{\mathrm{t}}}]_{:,\ell} \Bigg], \tag{2.36}$$

where $\chi_{n,m_{\mathrm{t}},\ell}^{\Delta} = |\alpha_\ell|^2 \left| [\boldsymbol{W}_{m_{\mathrm{t}}}]_{:,\ell}^* \boldsymbol{a}_{\mathrm{r}}(\psi_\ell) \right|^2 |\boldsymbol{a}_{\mathrm{t}}^*(\mu_\ell) \boldsymbol{a}_{\mathrm{t}}(\nu_n - \delta_{\mathrm{t}})|^2$. Exploiting the sparse nature of mmWave channels, if $N_{\mathrm{tot}} M_{\mathrm{tot}} \to \infty$, the second term in

39

(2.36) converges to zero [61], resulting in $\left|[\boldsymbol{Y}_{m_t}]_{\ell,u}\right|^2 \overset{\text{a.s.}}{\to} \chi^{\Delta}_{n,m_t,\ell}$. Similarly, with respect to $\boldsymbol{a}_t(\nu_n + \delta_t)$, we have

$$\left|[\boldsymbol{Y}_{m_t}]_{\ell,v}\right|^2 \overset{\text{a.s.}}{\to} \chi^{\Sigma}_{n,m_t,\ell} = |\alpha_\ell|^2 \left|[\boldsymbol{W}_{m_t}]^*_{:,\ell}\, \boldsymbol{a}_r(\psi_\ell)\right|^2 |\boldsymbol{a}^*_t(\mu_\ell)\boldsymbol{a}_t(\nu_n + \delta_t)|^2. \quad (2.37)$$

Using the asymptotic results to estimate μ_ℓ, we calculate the ratio metric as

$$
\begin{aligned}
\zeta^{\text{AoD}}_{n,\ell} &= \frac{\left|[\boldsymbol{Y}_{m_t}]_{\ell,u}\right|^2 - \left|[\boldsymbol{Y}_{m_t}]_{\ell,v}\right|^2}{\left|[\boldsymbol{Y}_{m_t}]_{\ell,u}\right|^2 + \left|[\boldsymbol{Y}_{m_t}]_{\ell,v}\right|^2} = \frac{\chi^{\Delta}_{n,m_t,\ell} - \chi^{\Sigma}_{n,m_t,\ell}}{\chi^{\Delta}_{n,m_t,\ell} + \chi^{\Sigma}_{n,m_t,\ell}} &&(2.38)\\
&= \frac{|\boldsymbol{a}^*_t(\mu_\ell)\boldsymbol{a}_t(\nu_n - \delta_t)|^2 - |\boldsymbol{a}^*_t(\mu_\ell)\boldsymbol{a}_t(\nu_n + \delta_t)|^2}{|\boldsymbol{a}^*_t(\mu_\ell)\boldsymbol{a}_t(\nu_n - \delta_t)|^2 + |\boldsymbol{a}^*_t(\mu_\ell)\boldsymbol{a}_t(\nu_n + \delta_t)|^2}. &&(2.39)
\end{aligned}
$$

According to Lemma 2.2 and $\mu_\ell \in (\nu_n - \delta_t, \nu_n + \delta_t)$, $\chi^{\Delta}_{n,m_t,\ell}$ and $\chi^{\Sigma}_{n,m_t,\ell}$ are determined as the auxiliary beam pair of interest. The quantized version of $\zeta^{\text{AoD}}_{n,\ell}$ is fed back to the transmitter. Upon receiving the feedback information, the transmitter estimates μ_ℓ via (similar to (2.20))

$$\hat{\mu}_{n,\ell} = \nu_n - \arcsin\left(\frac{\zeta^{\text{AoD}}_{n,\ell}\sin(\delta_t) - \zeta^{\text{AoD}}_{n,\ell}\sqrt{1 - \left(\zeta^{\text{AoD}}_{n,\ell}\right)^2}\sin(\delta_t)\cos(\delta_t)}{\sin^2(\delta_t) + \left(\zeta^{\text{AoD}}_{n,\ell}\right)^2\cos^2(\delta_t)}\right). \quad (2.40)$$

The corresponding transmit array response vector can be constructed as $\boldsymbol{a}_t(\hat{\theta}_\ell)$ with $\hat{\theta}_\ell = \arcsin\left(\lambda\hat{\mu}_{n,\ell}/2\pi d_t\right)$. The above process is conducted with respect to each path ℓ, and finally, $\hat{\boldsymbol{A}}_t = \left[\boldsymbol{a}_t(\hat{\theta}_1), \cdots, \boldsymbol{a}_t(\hat{\theta}_{N_p})\right]$ is constructed accounting for all estimated AoDs.

To estimate path-ℓ's AoA ψ_ℓ, a given probing at the transmitter $\boldsymbol{F}_{n_t}$ is considered by concatenating all M_T receive probings in the absence of noise, i.e.,

$$\boldsymbol{Y}_{n_t} = \boldsymbol{W}^*_T\boldsymbol{H}\boldsymbol{F}_{n_t}\boldsymbol{X}, \quad (2.41)$$

where $\boldsymbol{Y}_{n_t}$ has dimension of $M_T M_{RF} \times N_{RF}$, and $\boldsymbol{X} = \boldsymbol{I}_{N_{RF}}$. Different from the AoD estimation, the receiver has full knowledge of the position of a specific receive auxiliary beam pair in $\boldsymbol{W}_T$, e.g., $[\boldsymbol{W}_T]_{:,p} = \boldsymbol{a}_r(\eta_m - \delta_r)$, and $[\boldsymbol{W}_T]_{:,q} = \boldsymbol{a}_r(\eta_m + \delta_r)$, $p, q \in \{1, \cdots, M_T M_{RF}\}$. We can therefore compute the corresponding ratio metric as

$$\zeta_{m,\ell}^{AoA} = \frac{\left|[\boldsymbol{Y}_{n_t}]_{p,\ell}\right|^2 - \left|[\boldsymbol{Y}_{n_t}]_{q,\ell}\right|^2}{\left|[\boldsymbol{Y}_{n_t}]_{p,\ell}\right|^2 + \left|[\boldsymbol{Y}_{n_t}]_{q,\ell}\right|^2} \tag{2.42}$$

$$= \frac{\left|\boldsymbol{a}_r^*(\psi_\ell)\boldsymbol{a}_r(\eta_m - \delta_r)\right|^2 - \left|\boldsymbol{a}_r^*(\psi_\ell)\boldsymbol{a}_r(\eta_m + \delta_r)\right|^2}{\left|\boldsymbol{a}_r^*(\psi_\ell)\boldsymbol{a}_r(\eta_m - \delta_r)\right|^2 + \left|\boldsymbol{a}_r^*(\psi_\ell)\boldsymbol{a}_r(\eta_m + \delta_r)\right|^2} \tag{2.43}$$

assuming $N_{tot} M_{tot} \to \infty$. We can obtain the estimation of the associated receive spatial frequency as

$$\hat{\psi}_{m,\ell} = \eta_m - \arcsin\left(\frac{\zeta_{m,\ell}^{AoA} \sin(\delta_t) - \zeta_{m,\ell}^{AoA}\sqrt{1 - \left(\zeta_{m,\ell}^{AoA}\right)^2}\sin(\delta_r)\cos(\delta_r)}{\sin^2(\delta_r) + \left(\zeta_{m,\ell}^{AoA}\right)^2\cos^2(\delta_r)}\right). \tag{2.44}$$

The corresponding receive array response vector can be constructed as $\boldsymbol{a}_r(\hat{\phi}_\ell)$ with $\hat{\phi}_\ell = \arcsin\left(\lambda\hat{\psi}_{m,\ell}/2\pi d_r\right)$. Finally, the receive array response matrix is constructed as $\hat{\boldsymbol{A}}_r = \left[\boldsymbol{a}_r(\hat{\phi}_1), \cdots, \boldsymbol{a}_r(\hat{\phi}_{N_p})\right]$ accounting for all estimated AoAs.

In the absence of noise, the estimation performance of the proposed algorithm is only subject to the multi-path interference (see e.g., the second term in (2.36)). By leveraging the high-power regime and channel sparsity, the multi-path interference can be minimized, and the corresponding ratio metric in (2.38) (or (2.42)) is independent of the analog receive (or transmit)

41

processing. If the noise impairment is accounted for, (3.25) and (2.41) become

$$\boldsymbol{Y}_{m_t} = \boldsymbol{W}_{m_t}^* \boldsymbol{H} \boldsymbol{F}_T \boldsymbol{X} + \boldsymbol{W}_{m_t}^* \boldsymbol{P}, \tag{2.45}$$

$$\boldsymbol{Y}_{n_t} = \boldsymbol{W}_T^* \boldsymbol{H} \boldsymbol{F}_{n_t} \boldsymbol{X} + \boldsymbol{W}_T^* \boldsymbol{Q}, \tag{2.46}$$

where $\boldsymbol{P}$ ($\boldsymbol{Q}$) is an $M_{RF} \times N_T N_{RF}$ ($N_T M_{RF} \times N_{RF}$) noise matrix given by concatenating $N_T N_{RF}$ (N_{RF}) noise vectors. To estimate multi-path's AoD and AoA using (2.45) and (2.46), the receive and transmit probing matrices $\boldsymbol{W}_{m_t'}$ and $\boldsymbol{F}_{n_t'}$ that satisfy $m_t' = \underset{m_t=1,\cdots,M_T}{\operatorname{argmax}} \operatorname{tr}\left(\boldsymbol{Y}_{m_t}^* \boldsymbol{Y}_{m_t}\right)$ and $n_t' = \underset{n_t=1,\cdots,N_T}{\operatorname{argmax}} \operatorname{tr}\left(\boldsymbol{Y}_{n_t}^* \boldsymbol{Y}_{n_t}\right)$ are first selected. By plugging $\boldsymbol{W}_{m_t'}$ and $\boldsymbol{F}_{n_t'}$ into (2.45) and (2.46), the resulted $\boldsymbol{Y}_{m_t'}$ and $\boldsymbol{Y}_{n_t'}$ are then employed in (2.38) and (2.42) to determine the ratio metrics. To efficiently execute this selection process, the steering angles of simultaneously probed beams should match the distribution of AoD/AoA, which are unknown to the transmitter and receiver in prior, as much as possible. Hence, with finite N_T and M_T, we propose to steer the analog beams in one probing matrix to random angular directions. Using multiple transmit and receive RF chains, the number of attempts of the proposed algorithm then becomes $N_T N_{RF} \times M_T M_{RF}$.

We provide the pseudo-code of the proposed auxiliary beam pair enabled multi-path AoD estimation in Algorithm 2.1.

Algorithm 2.1 Multi-path AoD estimation via auxiliary beam pair design

---

Initialization

1: Set the transmit and receive beam codebooks $\mathcal{F}_\mathrm{T}$ and $\mathcal{W}_\mathrm{T}$

2: Set the total numbers of transmit and receive probings N_T and M_T

3: Set $\boldsymbol{F}_{n_\mathrm{t}} \in \mathbb{C}^{N_\mathrm{tot} \times N_\mathrm{RF}}$ $(n_\mathrm{t} = 1, \cdots, N_\mathrm{T})$ such that $[\boldsymbol{F}_{n_\mathrm{t}}]_{:,i}$ $(i = 1, \cdots, N_\mathrm{RF})$ is randomly chosen from $\mathcal{F}_\mathrm{T}$

4: Set $\boldsymbol{W}_{m_\mathrm{t}} \in \mathbb{C}^{M_\mathrm{tot} \times M_\mathrm{RF}}$ $(m_\mathrm{t} = 1, \cdots, M_\mathrm{T})$ such that $[\boldsymbol{W}_{m_\mathrm{t}}]_{:,\kappa}$ $(\kappa = 1, \cdots, M_\mathrm{RF})$ is randomly chosen from $\mathcal{W}_\mathrm{T}$

5: Set $\boldsymbol{F}_\mathrm{T} = [\boldsymbol{F}_1, \cdots, \boldsymbol{F}_{n_\mathrm{t}}, \cdots, \boldsymbol{F}_{N_\mathrm{T}}]$ and $\boldsymbol{W}_\mathrm{T} = [\boldsymbol{W}_1, \cdots, \boldsymbol{W}_{m_\mathrm{t}}, \cdots, \boldsymbol{W}_{M_\mathrm{T}}]$

Find the best receive combining matrix

6: **For** $m_\mathrm{t} = 1, \cdots, M_\mathrm{T}$

7:    **For** $n_\mathrm{t} = 1, \cdots, N_\mathrm{T}$

8:       $[\boldsymbol{Y}_{m_\mathrm{t}}]_{:,N_\mathrm{RF}(n_\mathrm{t}-1)+1:N_\mathrm{RF}n_\mathrm{t}} = \boldsymbol{W}_{m_\mathrm{t}}^* \boldsymbol{H} \boldsymbol{F}_{n_\mathrm{t}} \boldsymbol{X} + \boldsymbol{W}_{m_\mathrm{t}}^* [\boldsymbol{P}]_{:,N_\mathrm{RF}(n_\mathrm{t}-1)+1:N_\mathrm{RF}n_\mathrm{t}}$

9:    **end For**

10: **end For**

11: $m_\mathrm{t}' = \underset{m_\mathrm{t}=1,\cdots,M_\mathrm{T}}{\mathrm{argmax}} \; \mathrm{tr}\left(\boldsymbol{Y}_{m_\mathrm{t}}^* \boldsymbol{Y}_{m_\mathrm{t}}\right) \Rightarrow \boldsymbol{W}_{m_\mathrm{t}'}$ is selected for the rest of the procedure

Find the best transmit auxiliary beam pair for path-ℓ, $\ell = 1, \cdots, N_\mathrm{p}$

12: **For** $n' = 1, \cdots, N_\mathrm{K}$

13:    Determine u' and v' $(u', v' \in \{1, \cdots, N_\mathrm{T}N_\mathrm{RF}\})$ such that $[\boldsymbol{F}_\mathrm{T}]_{:,u'} = \boldsymbol{a}_\mathrm{t}(\nu_{n'} - \delta_\mathrm{t})$, and $[\boldsymbol{F}_\mathrm{T}]_{:,v'} = \boldsymbol{a}_\mathrm{t}(\nu_{n'} + \delta_\mathrm{t})$ by detecting the beam ID

14:    Calculate $\left|[\boldsymbol{Y}_{m_\mathrm{t}'}]_{\ell,u'}\right|^2$ and $\left|[\boldsymbol{Y}_{m_\mathrm{t}'}]_{\ell,v'}\right|^2$

15: **end For**

16: $[\boldsymbol{F}_\mathrm{T}]_{:,u}$ and $[\boldsymbol{F}_\mathrm{T}]_{:,v}$ are chosen as the auxiliary beam pair of interest using Lemma 2.2

17: Determine $n \in \{1, \cdots, N_\mathrm{K}\}$ such that $[\boldsymbol{F}_\mathrm{T}]_{:,u} = \boldsymbol{a}_\mathrm{t}(\nu_n - \delta_\mathrm{t})$, and $[\boldsymbol{F}_\mathrm{T}]_{:,v} = \boldsymbol{a}_\mathrm{t}(\nu_n + \delta_\mathrm{t})$

Estimate path-ℓ's AoD

18: Compute $\zeta_{n,\ell}^{\mathrm{AoD}}$ following (2.38) and $\hat{\mu}_{n,\ell}$ using (2.40)

2.5 Applications and Implementation Issues of Auxiliary Beam Pair in MmWave Cellular Systems

In this section, we first address potential deployment scenarios of the proposed design approach in mmWave cellular systems, including control chan-

nel beamforming and hybrid precoding for data channel communications. We then discuss two important issues of implementing our proposed method in practical systems, including extension to the multi-user scenario and the scalability to different antenna array architectures.

2.5.1 Analog-only beamforming for control channel

To achieve sufficiently high received signal quality, we believe that the control channel will be beamformed in mmWave cellular systems. We classify the control channel as system-specific, cell-specific and user-specific control channel due to their different purposes and link-budget requirements. For instance, the system-specific control channel carries basic network information such as operating carrier frequency, bandwidth, and etc., which needs a wide coverage. The cell-specific control channel conveys the signals that help the UE to discover, synchronize and access the cell, which requires not only a certain level of coverage, but also relatively high received signal strength. For user-specific control channel, which embeds reference signals for channel information acquisition for a specific UE, *pencil* beams are employed to ensure high received signal quality. We propose a multi-layer structure in this chapter for control channel beamforming such that analog transmit beams in different layers are associated with different types of control channel. In Figure 2.2, conceptual examples of the multi-layer control channel beamforming are presented. Layer-1, 2 and 3 transmit system-specific, cell-specific and user-specific control channels using coarse and fine-grained beams.
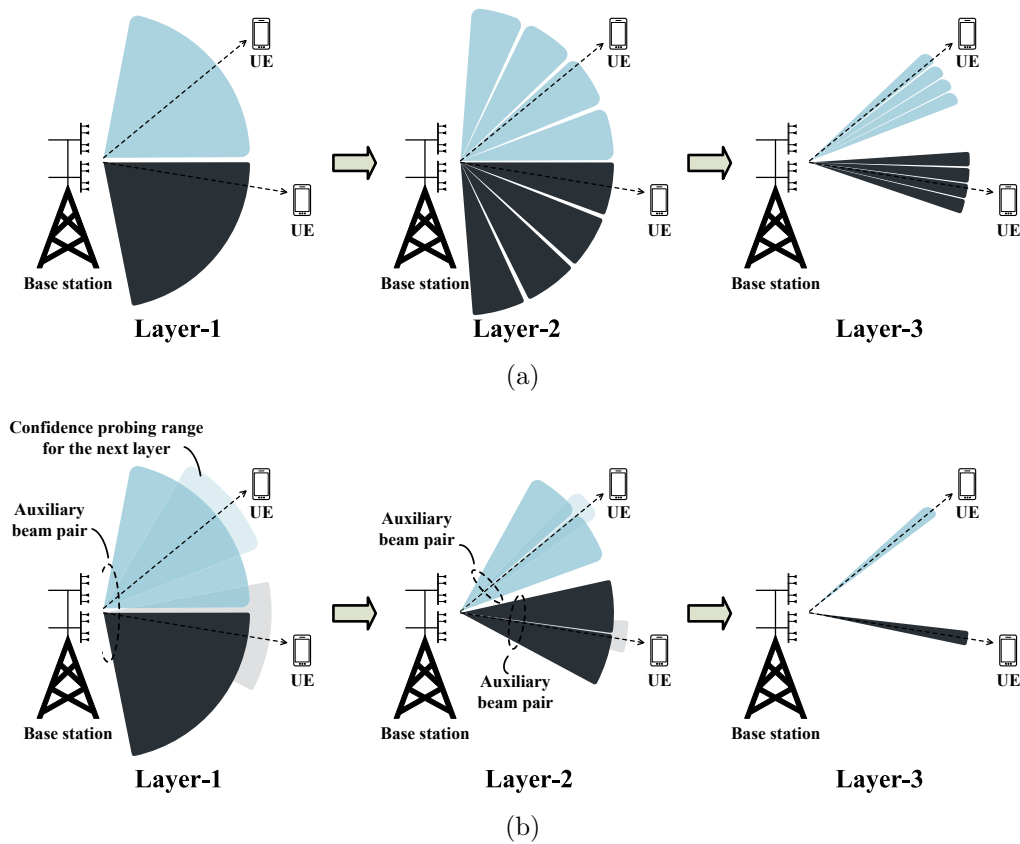
Figure 2.2: (a) A conceptual example of multi-layer grid-of-beams based control channel beamforming in mmWave cellular systems. (b) A conceptual example of multi-layer auxiliary beam pair based control channel beamforming in mmWave cellular systems.

We provide one conceptual example of a grid-of-beams based multi-layer control channel beamforming design in Figure 2.2(a). As the grid-of-beams based approach is not able to provide high-resolution estimates of channel's AoD and AoA, each UE in a given layer searches over all analog transmit beams within the probing range of interest, and selects the one with the highest received signal strength. Using the example shown in Figure 2.2(a), the total

45

number of attempts for a given UE to finally select the user-specific control channel beam is $2 + 4 + 4 = 10$.

In Figure 2.2(b), we exhibit one conceptual example of employing auxiliary beam pairs in the multi-layer beamformed control channel design. In each layer, the analog transmit beams not only carry necessary control signals, but also act as auxiliary beam pair to help acquire channel information. For instance, in Layer-1, one auxiliary beam pair is formed, in which two $60°$ analog transmit beams are contained covering a $120°$ sector. Upon receiving the analog transmit beams, each UE not only decodes the system-specific information from the beam that yields the highest received signal strength, but also calculates the ratio metric corresponding to the auxiliary beam pair. The ratio metric is then quantized and sent back to the BS. According to the ratio metric feedback, the BS estimates the AoD and determines the confidence probing range for the next layer beamforming. For instance, assume that $\hat{\mu}_{\ell_1}$ is the estimated transmit spatial frequency obtained via Layer-1 beamforming, and δ_{ℓ_2} approximates the half of half-power beamwidth of the analog transmit beam used for Layer-2 beamforming. The confidence probing range for Layer-2 is then determined as $[\hat{\mu}_{\ell_1} - \delta_{\ell_2}, \hat{\mu}_{\ell_1} + \delta_{\ell_2}]$. The above process repeats until the final layer beamforming has been executed. Using the example shown in Figure 2.2(b), the total number of attempts for a given UE to finally select the user-specific control channel beam becomes $2 + 2 + 2 = 6$. In contrast to the grid-of-beams based approach, the beam finding overhead is reduced by 40%.

2.5.2 Hybrid analog and digital precoding for data channel

Using the high-resolution angle estimates, both the transmitter and receiver can first build their own array response matrices, i.e., $\hat{A}_t = \left[a_t(\hat{\theta}_1), \cdots, a_t(\hat{\theta}_{N_p}) \right]$ and $\hat{A}_r = \left[a_r(\hat{\phi}_1), \cdots, a_r(\hat{\phi}_{N_p}) \right]$. Both the transmit precoder and receive combiner can then be constructed as matched filters to the transmit and receive array response matrices, i.e., $F_{RF} = \hat{A}_t$ and $W_{RF} = \hat{A}_r$. Note that if the channel reciprocity can be exploited to provide more accurate angle estimates, F_{RF} and W_{RF} can be further optimized. To properly configure the digital baseband precoder, F_{RF} and W_{RF} are first formed by the transmitter and receiver. The transmit-receive beam-space channel can therefore be obtained by the receiver as $H_{TR} = W_{RF}^* H F_{RF}$, by using predetermined reference signals/pilots sent through the analog beamforming vectors in F_{RF}. Using H_{TR}, the digital baseband precoder is then chosen by the receiver from a predefined codebook $\mathcal{F} = \{ F_1, F_2, \cdots, F_{N_B} \}$. In closed-loop systems, the receiver searches for the baseband codebook and finds the codeword that maximizes/minimizes a given performance metric. For instance, if the system targets at maximizing the spectral efficiency, we can express the corresponding optimization problem as

$$F^* = \underset{F \in \mathcal{F}}{\mathrm{argmax}} \ \log_2 \det \left(I_{N_S} + \frac{1}{N_S} R_n^{-1} H_{TR} F F^* H_{TR}^* \right), \tag{2.47}$$

where $R_n = \sigma^2 W_{RF}^* W_{RF}$. The receiver then sends the index of the selected codeword in the codebook back to the transmitter, based on which the transmitter could build the baseband precoder as $F_{BB} = F^*$. If the receiver has the knowledge of F_{BB} via necessary control signaling from the transmitter, the

receiver can also construct the baseband combiner $\boldsymbol{W}_{\mathrm{BB}} = \boldsymbol{H}_{\mathrm{TR}}\boldsymbol{F}_{\mathrm{BB}}$, to better support the multi-stream data channel communications.

2.5.3   Extension to multi-user scenario

In previous sections, we specifically illustrate the proposed AoD/AoA estimation algorithm for a single-user scenario. In this part, we discuss extension of the proposed approach to a multi-user setup as this application scenario is important for practical cellular systems.

Assume perfect synchronization between the BS and UEs, we can directly extend the algorithms proposed for the single-user case to the multi-user scenario with appropriate frame structure design that can better support the communications between the BS and UEs through auxiliary beam pairs. We therefore define a probing frame, which includes a predetermined number of probing slots. From the perspective of each UE, the same receive probing is performed for all probing slots. The receive probing can be either single receive beam if the UE is equipped with a single RF chain, or receive combining matrix if multiple RF chains are employed. For a given probing frame, all transmit probings are conducted by the BS across all probing slots in the probing frame. That is, in a given probing frame, the UE uses the same receive probing to combine all transmit probings across all probing slots, and this procedure continues until all receive probings are executed by the UE across all probing frames. Following steps 6∼18 in Algorithm 2.1, each UE then estimates the desired AoDs/AoAs. Note that for the multi-user scenario, the auxiliary beam
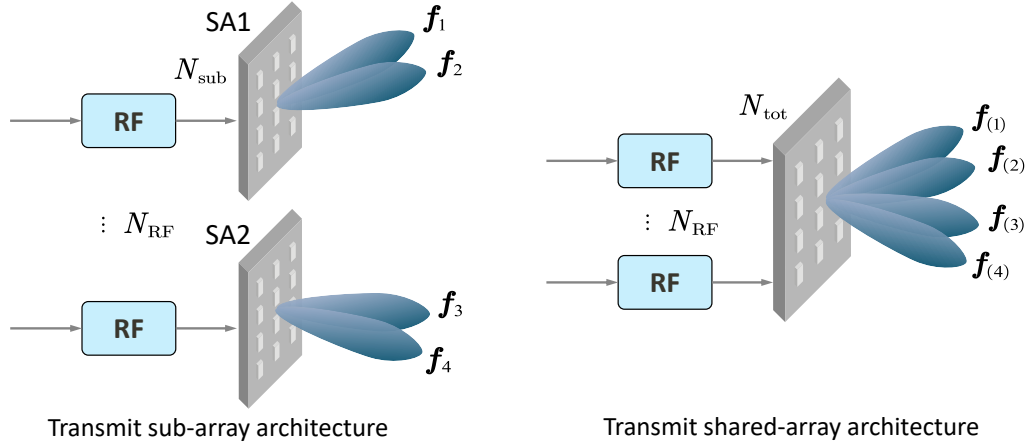
Figure 2.3: Conceptual examples of transmit subarray and shared-array architectures in forming the auxiliary beams.

pair for angle estimation plays a similar role to the common reference signal (CRS) in LTE for channel estimation such that the transmitted beam-specific signals are common for all active users.

2.5.4 Sub-array architecture versus shared-array architecture

In Figure 2.3, we present conceptual examples of both the transmit shared-array and sub-array antenna architectures. In the sub-array architecture, we assume two sub-arrays (i.e., SA1 and SA2) equipped at the transmitter, i.e., $N_{\mathrm{RF}} = 2$. Denote the number of transmit antennas at each transmit sub-array by N_{sub}, the total number of antennas are then calculated as $N_{\mathrm{ant}} = N_{\mathrm{RF}}N_{\mathrm{sub}}$. A total number of M_{tot} receive antennas are assumed at the receiver with a single receive RF chain. Further, the two analog transmit beams used to form one auxiliary beam pair are restricted from the same sub-

array. For instance, in the example shown on the left-hand-side of Figure 2.3, the analog transmit beams $\boldsymbol{f}_1$ and $\boldsymbol{f}_2$ from SA1 form one auxiliary beam pair, and $\boldsymbol{f}_3$, $\boldsymbol{f}_4$ from SA 2 form another auxiliary beam pair. In the shared-array architecture presented on the right-hand-side of Figure 2.3, a total number of N_{tot} transmit antennas are deployed and jointly controlled by $N_{\text{RF}} = 2$ RF chains. In the shared-array example, we consider $\boldsymbol{f}_{(1)}$ and $\boldsymbol{f}_{(2)}$ form one auxiliary beam pair, and $\boldsymbol{f}_{(3)}$ and $\boldsymbol{f}_{(4)}$ form another auxiliary beam pair. We highlight here that $\boldsymbol{f}_1, \cdots, \boldsymbol{f}_4$ are $N_{\text{sub}} \times 1$ vectors, while $\boldsymbol{f}_{(1)}, \cdots, \boldsymbol{f}_{(4)}$ are $N_{\text{tot}} \times 1$ vectors.

The probing strategies of the auxiliary beam pairs are different between the two array architectures. For instance, regarding the sub-array example shown in Figure 2.3, as two RF chains are assumed, two analog transmit beams can be probed simultaneously. In the first time-slot, if $\boldsymbol{f}_1$ and $\boldsymbol{f}_3$ are transmitted, $\boldsymbol{f}_2$ and $\boldsymbol{f}_4$ would be probed during the second time-slot. That is, for a given time-slot, only one of the two beams in the same auxiliary beam pair can be probed for the sub-array architecture. On the contrary, the probing strategy of the auxiliary beam pairs is more flexible in the shared-array structure shown in Figure 2.3.

We consider a single-path channel with the transmit spatial frequency μ and receive spatial frequency ψ. Denote the channel matrix between SA1 at the transmitter and receiver by $\boldsymbol{H}_1$,

$$\boldsymbol{H}_1 = \alpha \boldsymbol{a}_{\text{r}}(\psi) \boldsymbol{a}_{\text{t}}^*(\mu), \tag{2.48}$$

where α is the path gain, $\boldsymbol{a}_\mathrm{r}(\psi)$ denotes the $M_\mathrm{tot} \times 1$ receive array response vector in this example, and $\boldsymbol{a}_\mathrm{t}(\mu)$ represents the $N_\mathrm{sub} \times 1$ transmit array response vector. The full channel matrix between the transmitter and receiver in the sub-array example shown in Figure 2.3 is then constructed as $\boldsymbol{H}_\mathrm{SA} = \begin{bmatrix} \boldsymbol{H}_1 & e^{-\mathrm{j}(N_\mathrm{sub}-1)\mu}\boldsymbol{H}_1 \end{bmatrix}$. In the absence of noise, the concatenated received signal is expressed as

$$\boldsymbol{y} = \boldsymbol{w}^*\boldsymbol{H}_\mathrm{SA} \begin{bmatrix} \boldsymbol{f}_1 & \boldsymbol{0}_{N_\mathrm{sub}} & \boldsymbol{f}_2 & \boldsymbol{0}_{N_\mathrm{sub}} \\ \boldsymbol{0}_{N_\mathrm{sub}} & \boldsymbol{f}_3 & \boldsymbol{0}_{N_\mathrm{sub}} & \boldsymbol{f}_4 \end{bmatrix}, \tag{2.49}$$

following the probing order stated above, and $\boldsymbol{w}$ denotes the $M_\mathrm{tot} \times 1$ receive combining vector.

With respect to $\boldsymbol{f}_1$ and $\boldsymbol{f}_2$ from SA1, the corresponding ratio metric can therefore be calculated as

$$\zeta_\mathrm{SA1} = \frac{|\boldsymbol{w}^*\boldsymbol{H}_1\boldsymbol{f}_1|^2 - |\boldsymbol{w}^*\boldsymbol{H}_1\boldsymbol{f}_2|^2}{|\boldsymbol{w}^*\boldsymbol{H}_1\boldsymbol{f}_1|^2 + |\boldsymbol{w}^*\boldsymbol{H}_1\boldsymbol{f}_2|^2}. \tag{2.50}$$

If the transmit spatial frequency μ is within the probing range of $\boldsymbol{f}_1$ and $\boldsymbol{f}_2$, it can be estimated by directly inverting ζ_SA1 due to the monotonicity. Similarly, regarding $\boldsymbol{f}_3$ and $\boldsymbol{f}_4$ from SA2, the ratio metric can be derived as

$$\zeta_\mathrm{SA2} = \frac{|\boldsymbol{w}^*\boldsymbol{H}_1\boldsymbol{f}_3|^2 - |\boldsymbol{w}^*\boldsymbol{H}_1\boldsymbol{f}_4|^2}{|\boldsymbol{w}^*\boldsymbol{H}_1\boldsymbol{f}_3|^2 + |\boldsymbol{w}^*\boldsymbol{H}_1\boldsymbol{f}_4|^2}. \tag{2.51}$$

Note that the term $e^{-\mathrm{j}(N_\mathrm{sub}-1)}$ is simply cancelled out from both the numerator and the denominator in (2.51). If the transmit spatial frequency μ is within the probing range of $\boldsymbol{f}_3$ and $\boldsymbol{f}_4$, it can be estimated by inverting ζ_SA2.

For the shared-array example shown on the right-hand-side of Figure 2.3, the corresponding ratio metrics derived from the auxiliary beam pairs

$\{\boldsymbol{f}_{(1)}, \boldsymbol{f}_{(2)}\}$ and $\{\boldsymbol{f}_{(3)}, \boldsymbol{f}_{(4)}\}$ are

$$
\begin{aligned}
\zeta_{\mathrm{SH1}} &= \frac{\left|\boldsymbol{w}^*\boldsymbol{H}_{\mathrm{SH}}\boldsymbol{f}_{(1)}\right|^2 - \left|\boldsymbol{w}^*\boldsymbol{H}_{\mathrm{SH}}\boldsymbol{f}_{(2)}\right|^2}{\left|\boldsymbol{w}^*\boldsymbol{H}_{\mathrm{SH}}\boldsymbol{f}_{(1)}\right|^2 + \left|\boldsymbol{w}^*\boldsymbol{H}_{\mathrm{SH}}\boldsymbol{f}_{(2)}\right|^2}, \\
\zeta_{\mathrm{SH2}} &= \frac{\left|\boldsymbol{w}^*\boldsymbol{H}_{\mathrm{SH}}\boldsymbol{f}_{(3)}\right|^2 - \left|\boldsymbol{w}^*\boldsymbol{H}_{\mathrm{SH}}\boldsymbol{f}_{(4)}\right|^2}{\left|\boldsymbol{w}^*\boldsymbol{H}_{\mathrm{SH}}\boldsymbol{f}_{(3)}\right|^2 + \left|\boldsymbol{w}^*\boldsymbol{H}_{\mathrm{SH}}\boldsymbol{f}_{(4)}\right|^2},
\end{aligned} \tag{2.52}
$$

where $\boldsymbol{H}_{\mathrm{SH}} = \alpha\boldsymbol{a}_{\mathrm{r}}(\psi)\boldsymbol{a}_{\mathrm{t}}^*(\mu)$ and now $\boldsymbol{a}_{\mathrm{t}}(\mu)$ becomes a $N_{\mathrm{tot}} \times 1$ transmit array response vector. If μ is within the range of $\boldsymbol{f}_{(1)}$ and $\boldsymbol{f}_{(2)}$, it can be estimated by inverting ζ_{SH1}. Similarly, if μ is in the probing range of $\boldsymbol{f}_{(3)}$ and $\boldsymbol{f}_{(4)}$, it can be estimated by inverting ζ_{SH2}.

We can conclude from the above derivations the difference between the shared-array and sub-array antenna architectures in supporting our proposed auxiliary beam pair based angle estimation method. For given numbers of total transmit antennas and RF chains, i.e., $N_{\mathrm{ant}} = N_{\mathrm{tot}}$ and $N_{\mathrm{sub}} = N_{\mathrm{tot}}/N_{\mathrm{RF}}$, the beamforming gain provided by the sub-array based approach is smaller than that in the shared-array architecture when deriving the ratio metrics. This is mainly because $\boldsymbol{f}_1, \cdots, \boldsymbol{f}_4$ are N_{sub}-dimensional, while $\boldsymbol{f}_{(1)}, \cdots, \boldsymbol{f}_{(4)}$ are N_{tot}-dimensional. If the noise impairment is accounted for, the angle estimation performance in the sub-array based design is expected to be worse than that in the shared-array architecture. We note though the the total number of beams required by the sub-array architecture to cover a given angular range becomes smaller than that in the shared-array architecture. This is because wider beams are formed in the sub-array architecture due to the smaller beamforming vectors dimensions. Smaller number of required beams

implies reduced estimation overhead and computational complexity. To ensure the same beamforming gain and estimation overhead, the total number of antennas required by the sub-array architecture is N_{RF} times of that in the shared-array based structure.

2.6 Numerical Results

In this section, we evaluate the performance of the proposed auxiliary beam pair enabled channel estimation technique. Both the transmitter and receiver employ a ULA with inter-element spacing $\lambda/2$, and $180°$ boresight. The codebook for quantizing the ratio measure in the proposed method has non-uniformly distributed codewords within the interval of $[-1, 1]$. Denote by $N_{\mathrm{ant}} = N_{\mathrm{tot}}$ (or M_{tot}), and $\delta = \delta_{\mathrm{t}}$ (or δ_{r}) for AoD (or AoA) estimation. In the simulation, we set $\delta = \pi/N_{\mathrm{ant}}$.

In Figure 2.4(a), we evaluate the spectral efficiency performance of analog-only beamforming and combining under single-path channel conditions. Both the AoD and AoA are uniformly distributed in the interval of $[-\pi/2, \pi/2]$ for each channel use. The transmit beamforming and receive combining vectors are constructed using (i) perfect channel knowledge of AoD and AoA, and (ii) estimated AoD and AoA via auxiliary beam pair design. The ratio measure that characterizes the AoD for each channel use is quantized using 4 bits. It can be observed from Figure 2.4(a) that the spectral efficiency performance of employing the proposed channel estimation method approaches that with perfect channel knowledge, for different numbers of employed trans-

53

mit antennas. We provide the MSE performance of the single-path's AoD and AoA estimation in Figure 2.4(b) under various SNR levels. We define the SNR here as the target SNR γ before the analog beamforming and combining. It is observed from Figure 2.4(b) that promising MSE performance of AoD and AoA estimation can be achieved even in a relatively low SNR regime. With an increase in the number of employed antennas, the AoD and AoA estimation performance is further improved.

We plot the corresponding MSE performance of AoD and AoA estimation in Figure 2.5(a) under multi-path channel condition and 10 dB SNR. In this example, we assume a Rician channel model, with various Rician K-factor values,

$$\boldsymbol{H} = \sqrt{\frac{\mathsf{K}}{1+\mathsf{K}}} \underbrace{\alpha_\ell \boldsymbol{a}_\mathrm{r}(\phi_\ell) \boldsymbol{a}_\mathrm{t}^*(\theta_\ell)}_{\boldsymbol{H}_{\mathrm{LOS}}} + \sqrt{\frac{1}{1+\mathsf{K}}} \underbrace{\sum_{\ell'=1, r' \neq r}^{N_\mathrm{p}} \alpha_{\ell'} \boldsymbol{a}_\mathrm{r}(\phi_{\ell'}) \boldsymbol{a}_\mathrm{t}^*(\theta_{\ell'})}_{\boldsymbol{H}_{\mathrm{NLOS}}}, \qquad (2.53)$$

where $\boldsymbol{H}_{\mathrm{LOS}}$ and $\boldsymbol{H}_{\mathrm{NLOS}}$ represent line-of-sight (LOS) and non-LOS (NLOS) channel components. The number of NLOS channel components is 5. The objective is to estimate the dominant path's AoD and AoA, and steer the analog transmit and receive beams towards the estimated angles. From the channel observation in [63], 13.2 dB Rician K-factor characterizes the mmWave channels' conditions the best in an urban wireless channel topography. The reason for evaluating various Rician K-factor values is to validate the capability of the proposed algorithm in estimating the dominant path's AoD/AoA when NLOS components have relatively strong power. With directional analog beamforming and combining, the MSE performance of AoD and AoA estimation is still

promising even in the small K-factor regime (e.g., 2 dB). In Figure 2.5(b), the effective channel gain $|\boldsymbol{w}^*\boldsymbol{H}\boldsymbol{f}|^2$ is evaluated, where $\boldsymbol{f}$ and $\boldsymbol{w}$ are analog transmit and receive steering vectors obtained using perfect channel information and estimated AoD and AoA via auxiliary beam pair design. It can be observed from Figure 2.5(b) that the proposed technique approaches that with perfect channel knowledge.

With large δ_t (implying wide transmit beams), the angle estimation performance would be degraded due to the low received SNR. With small δ_t, the angle estimation performance would be improved as narrow beams are used and the received SNR is increased. In Figure 2.6, we examine the "sensitivity" of the estimated angle information to the number of transmit antennas and δ_t. It can be observed from Figure 2.6(a) that with relatively small N_tot (e.g., 8), the MAEE performance gap between the proposed algorithm and that without any estimation error is relatively large. That is, the angle estimation performance of the auxiliary beam pair design is more "sensitive" if relatively wide beams are employed. With an increase in the number of transmit antennas, the corresponding transmit beams become narrower, resulting in better angle estimation performance due to the improved received SNR.

It can also be observed from Figure 2.6(b) that with relatively small δ_t, the MAEE performance of the proposed method approaches the case without any estimation error. For instance, with $\delta_\mathrm{t} = 3°$, the MAEE of the proposed approach is less than $8°$. With an increase in δ_t, the MAEE performance gap between the proposed method and that without any estimation error becomes

large, implying that the algorithm now becomes more "sensitive" in terms of the angle estimation performance.

In Figures 2.5 and 2.7, we evaluate the performance of the proposed design approach assuming relatively small numbers of transmit and receive antennas, and a wide range of target SNRs. The mmWave systems, however, are expected to deploy a large number of antennas to provide sufficient link margin via directional beamforming. In Figure 2.7(a), we evaluate the mean angle estimation error (MAEE) performance for the proposed algorithm using different numbers of transmit antennas in the single-path channel. Here, we define the MAEE as $\mathbb{E}\left[|v_{\text{true}} - v_{\text{est}}|\right]$, where v_{true} represents the exact angle in degree, and v_{est} is its estimated counterpart in degree. From Figure 2.7(a), it can be observed that with an increase in the number of transmit antennas, the MAEE is reduced for both -10 dB and -30 dB SNRs. For large $N_{\text{tot}}M_{\text{tot}}$, e.g., 128×8 in this example, the MAEE is close to $0°$ for different SNR levels. The estimation performance improvements, however, are brought by increased estimation overhead. In Figure 2.7(b), we evaluate the trade-off performance between the estimation overhead in terms of the total number of iterations between the transmitter and receiver, and the angle estimation performance determined by δ. For instance, $\delta = 11.25°$ corresponds to $N_{\text{ant}} = 16$, and eight beams are formed to cover the $180°$ angular range. That is, for $\delta_{\text{t}} = 11.25°$ and $\delta_{\text{r}} = 22.5°$, we calculate the total number of iterations as $4 \times 8 = 32$, and we obtain the MAEE performance by setting $N_{\text{tot}} = 16$ and $M_{\text{tot}} = 8$ for a given target SNR (as shown in Figure 2.7(a)).

In Figure 2.8, we evaluate our proposed method in single-path channels, assuming both shared-array and sub-array architectures. For the shared-array architecture, a total number of $N_{\text{tot}} = 8$ transmit antennas are employed with one transmit RF chain. For the sub-array architecture, two cases are considered: (i) $N_{\text{sub}} = 4$ with $N_{\text{RF}} = 2$, and (ii) $N_{\text{sub}} = 8$ with $N_{\text{RF}} = 2$. For case (i), a total number of $N_{\text{sub}}N_{\text{RF}} = 8$ transmit antennas are employed for the sub-array architecture, which are the same as in the shared-array architecture. In case (ii), a total of $N_{\text{sub}}N_{\text{RF}} = 16$ transmit antennas are used, which double the number of employed transmit antennas in the shared-array scenario. It is evident from Figure 2.8 that case (i) sub-array architecture exhibits worse MAEE performance than the shared-array architecture though the total number of transmit antennas are the same for both scenarios. Further, case (ii) sub-array architecture shows similar MAEE performance relative to the shared-array architecture.

In Figure 2.9, we evaluate the MSE performance of transmit array response matrix estimation using the proposed design approach, adaptive compressed sensing (CS) technology developed in [8] and modified GoB based approach in [13] using the proposed probing strategy in Section 2.4.3. We define the performance metric as $\mathbb{E}\left[\text{tr}\left(\mathbf{\Gamma}^*\mathbf{\Gamma}\right)\right]$, where $\mathbf{\Gamma} = \boldsymbol{A}_{\text{t}} - \hat{\boldsymbol{A}}_{\text{t}}$, and $\hat{\boldsymbol{A}}_{\text{t}}$ contains the estimated transmit array response vectors. Here, $N_{\text{p}} = N_{\text{RF}} = M_{\text{RF}} = 3$. We interpret the total number of *training steps* Ω_{tr} defined in [8] as the total number of probings in the proposed approach and modified GoB. For fair comparison, we set $\Omega_{\text{tr}} = 96, 196$ and 400. These correspond to $N_{\text{T}} \times M_{\text{T}} =$

57

12×8, 14×14 and 20×20. From Figure 2.9, it is observed that with $M_{\text{tot}} = 4$, the adaptive CS approach exhibits better MSE performance than the proposed approach. The reason is that with relatively small set of candidate receive combining vectors and M_{T}, the proposed approach is not able to provide sufficient receive array gain to achieve high-resolution angle estimate. With an increase in the number of receive antennas and total number of probings, however, the proposed design approach outperforms the adaptive CS and GoB based methods. The reason is that the performance of the adaptive CS and GoB is limited by the codebook resolution, while the proposed approach is able to provide super-resolution AoD estimate as long as multi-path components can be resolved. It can also be observed from Figure 2.9 that, the auxiliary beam pair based design with $N_{\text{tot}} = 8$ and $M_{\text{tot}} = 8$ exhibits similar angle estimation performance to the grid-of-beams based method with $N_{\text{tot}} = 16$ and $M_{\text{tot}} = 8$ for various SNR values.

2.7   Conclusion

In this chapter, we proposed and evaluated a novel auxiliary beam pair based angle estimation strategy in closed-loop mmWave systems with large number of deployed antennas. We showed that by leveraging well structured pairs of custom designed analog beams, we can obtain high-resolution estimates of channel's AoD and AoA via amplitude comparison. By using the estimated AoD and AoA, we can better facilitate the directional initial access process, and enable data channel spatial multiplexing via hybrid precoding.

We employed several numerical examples to reveal that by using the proposed algorithm, promising channel estimation performance was achieved with significantly reduced training overhead under a moderate amount of feedback.
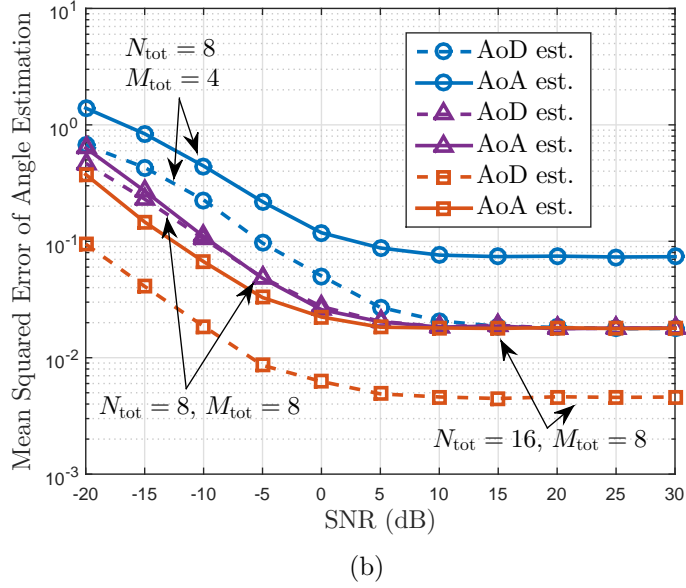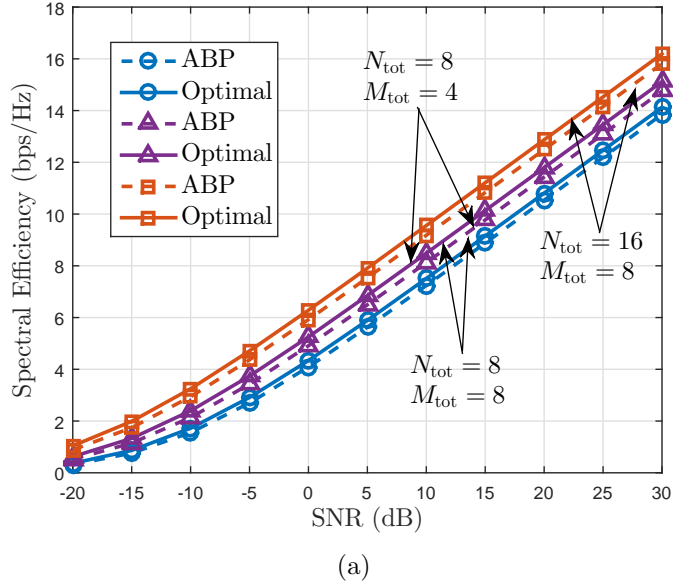
Figure 2.4: (a) Spectral efficiency of analog-only beamforming and combining using perfect channel information and estimated AoD and AoA via auxiliary beam pair design in a single-path channel. (b) Mean squared error performance of AoD and AoA estimation using the proposed approach under various SNR levels.

(a)

(b)
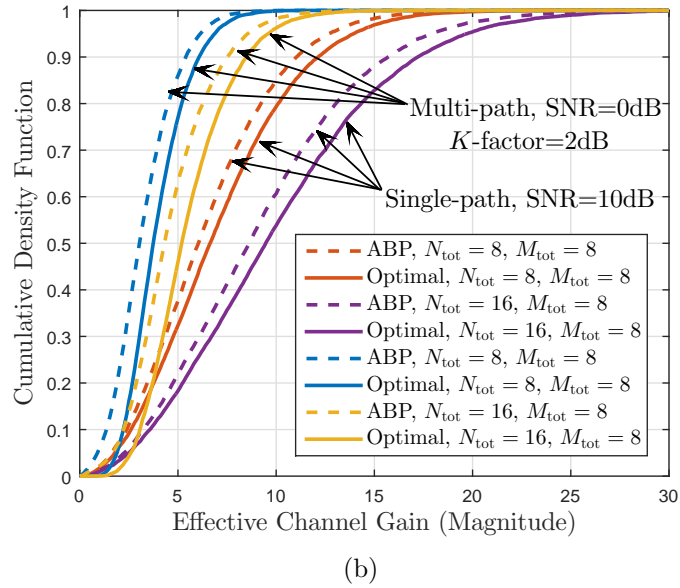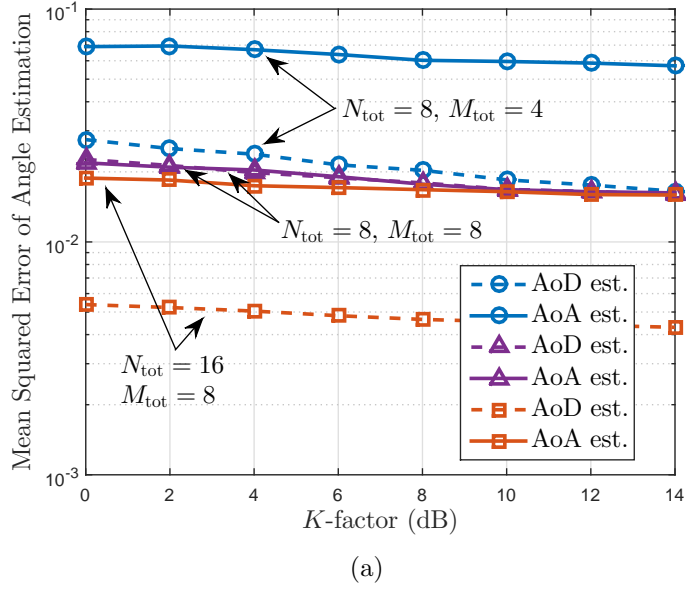
Figure 2.5: (a) Mean squared error performance of AoD and AoA estimation using the proposed approach under various K-factor values. (b) Cumulative density function of effective channel gain of analog-only beamforming and combing using perfect channel information and estimated AoD and AoA via auxiliary beam pair design.

Figure 2.6: (a) Mean angle estimation error (MAEE) of AoD estimation using the proposed approach with different number of transmit antennas. (b) Mean angle estimation error (MAEE) of AoD estimation using the proposed approach with different values of δ_t.

62
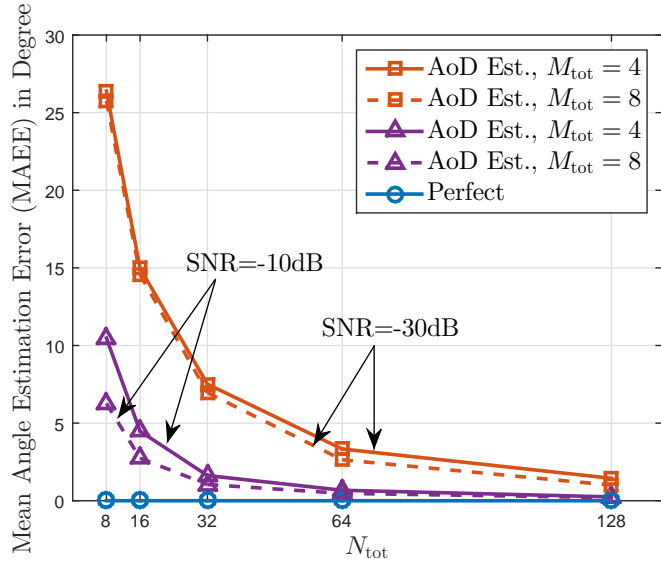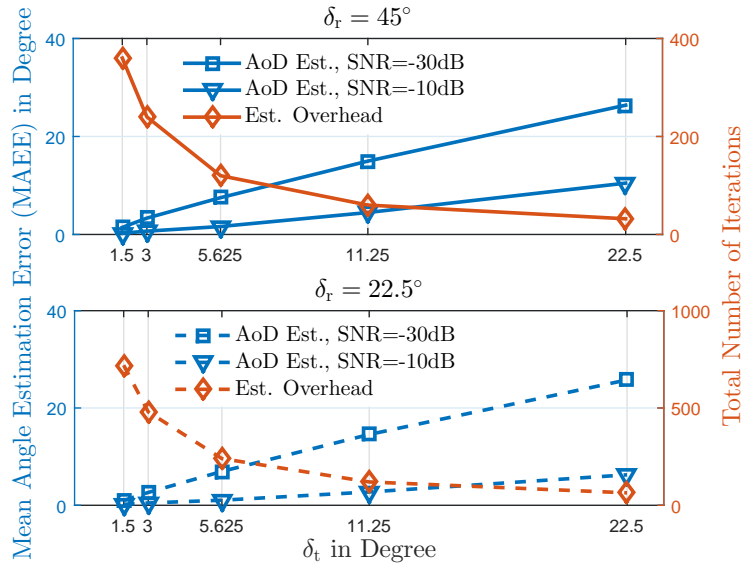
Figure 2.7: (a) Mean angle estimation error (MAEE) of AoD estimation using the proposed approach with different numbers of transmit antennas. (b) Trade-off performance between the angle estimation and the total number of iterations between the transmitter and receiver.
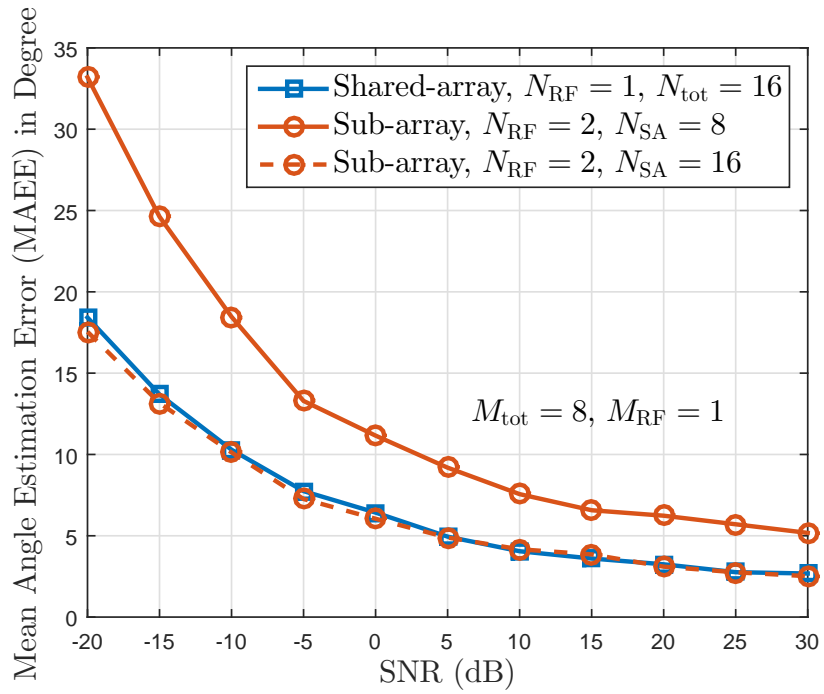
Figure 2.8: Mean angle estimation error (MAEE) performance of the AoD estimation using the proposed approach under shared-array and sub-array architectures.
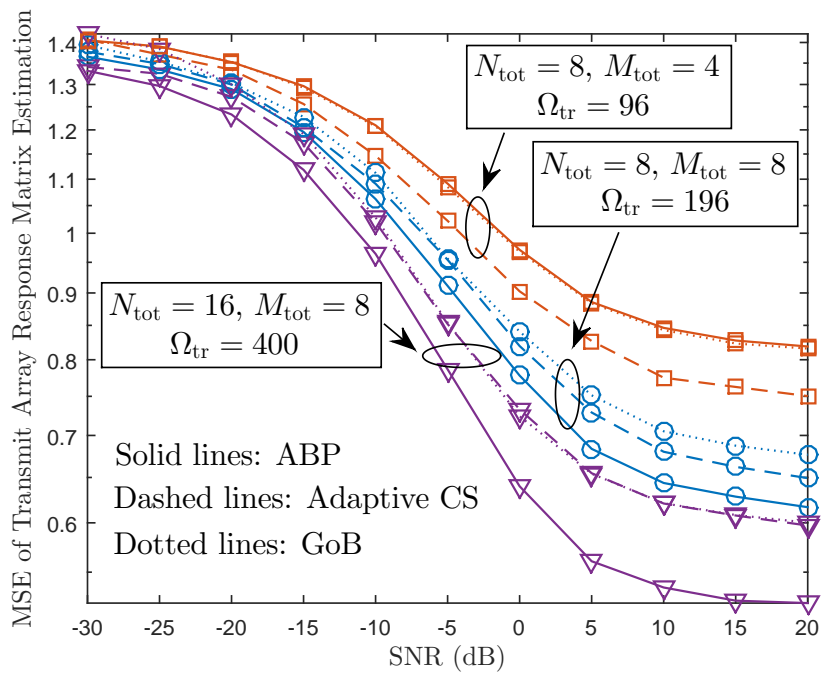
Figure 2.9: MSE performance of transmit array response matrix estimation using the proposed approach, adaptive CS and modified GoB versus various SNR values.

Chapter 3

Two-Dimensional Angle Estimation in MmWave Systems with Dual-Polarization

In this chapter, we propose a two-dimensional high-resolution angle estimation algorithm for mmWave MIMO systems. Different from our prior work in Chapter 2 and [40, 41], we focus on wideband channels with dual-polarized array structure, and leverage the fact that the AoDs and AoAs are the same for both vertical an horizontal polarization domains. We also develop and evaluate various auxiliary beam pair and polarization domain mapping strategies for the proposed method. Further, we design a new multi-layer pilot signal structure and a differential quantization strategy for the proposed approach. The design target here is to reduce the reference signal and feedback overheads. This work was published in [42, 43].

3.1 Prior Work and Motivation

Dual-polarized antenna systems, discussed in [5], can also be incorporated into mmWave systems allowing a large number of antennas to be deployed with a small form factor. In addition to space efficiency, high-rank data streams can be multiplexed across the polarizations by taking advantage

of dual-pole decoupling in the channel. In a dual-polarized mmWave MIMO system, it is useful to acquire accurate AoDs and AoAs of the channels, with which highly directional beams can be formed for data communications. To develop practical angle estimation algorithms, the fact that the AoDs and AoAs are the same for both polarization domains can be leveraged, while at the same time recognizing that wideband channels should also be frequency selective.

None of the existing wideband mmWave channel estimation approaches in [16]-[24] considered the polarization. An analytical framework of dual-polarized multi-antenna wireless systems was presented in [5]. In [64], dual-polarization was used for beam training in narrowband mmWave systems. In summary, the channel estimation techniques proposed in [16]-[24] and [64] focused on either the wideband channels or dual-polarization, but not both.

3.2   Contributions

In this chapter, we propose to estimate the channel's azimuth/elevation AoD and AoA through auxiliary beam pair design for dual-polarized MIMO in wideband mmWave systems. To facilitate practical realization of the proposed design, we provide several feedback options and guidelines on pilot designs. We summarize the main contributions of this chapter as follows:

- The BS forms elevation (azimuth) transmit auxiliary beam pairs and steers them towards successive angular directions in the elevation (az-

imuth) domain. We employ the formed elevation and azimuth transmit auxiliary beam pairs to estimate the elevation and azimuth transmit spatial frequencies, and therefore, the corresponding AoDs. We can similarly estimate the AoAs by forming receive auxiliary beam pairs.

- We propose to form the analog beams within each auxiliary beam pair across both vertical and horizontal polarization domains to leverage the fact that the AoD/AoA is identical for both polarization domains. We discuss various auxiliary beam pair and polarization mapping strategies, and evaluate their impact on the system design.

- For FDD systems, we develop a new differential feedback option for the proposed auxiliary beam pair design, in which the relative position of the estimated angle with respect to the boresight of the corresponding auxiliary beam pair is quantized. In contrast to the direct quantization we used in Chapter 2, the proposed differential quantization method is able to reduce the feedback overhead for two-dimensional angle acquisition.

- Building on the single-path solution, to facilitate the multi-path angle acquisition, we employ multiple RF chains to form multiple auxiliary beam pairs simultaneously. Accordingly, we develop a new multi-layer pilot structure. In the first-layer, we use the auxiliary beam pair specific pilot to distinguish among simultaneously probed auxiliary beam pairs. In the second-layer, we use the paired-beam specific pilot to independently decouple the beams in the same auxiliary beam pair.

We evaluate our proposed angle estimation algorithm by simulations under realistic assumptions. The numerical results reveal that the proposed design approach is capable of providing high-resolution azimuth/elevation AoD and AoA estimation under various SNR levels and channel conditions subject to moderate amounts of feedback and training overheads.

We organize the rest of this chapter as follows. In Section 3.3, we specify the system and channel models. In Section 3.4, we describe the principle and procedure of the proposed auxiliary beam pair design in estimating the two-dimensional angles using the multi-layer pilot structure. We illustrate several practical issues of implementing the proposed algorithm, including duplexing, feedback options, and codebook design in Section 3.5. In Section 3.6, we show numerical results to validate the effectiveness of the proposed technique. Finally, we draw our conclusions in Section 3.7.

3.3   Models and Assumptions

In this section, we first present the transceiver architecture and the signal model. We then describe the employed channel model with dual-polarized antenna arrays.

3.3.1   System Model

We consider a precoded MIMO-OFDM system with N subcarriers and a hybrid precoding transceiver structure as shown in Figures 3.1(a) and 3.1(b). Both the BS and UE are equipped with partially shared-array antenna archi-
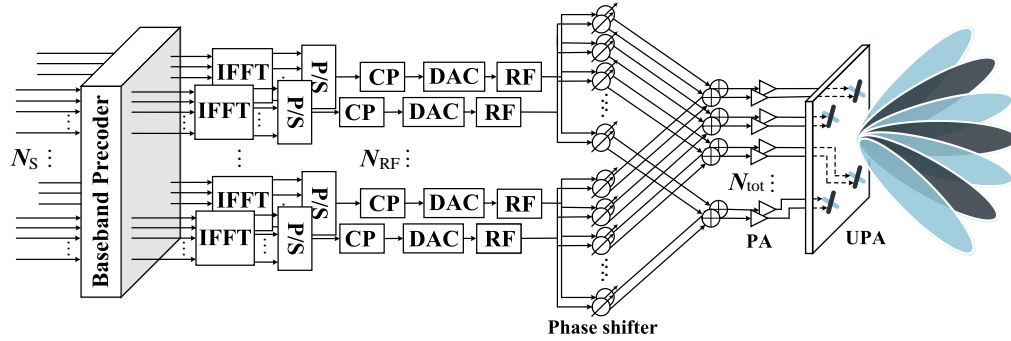
(a)
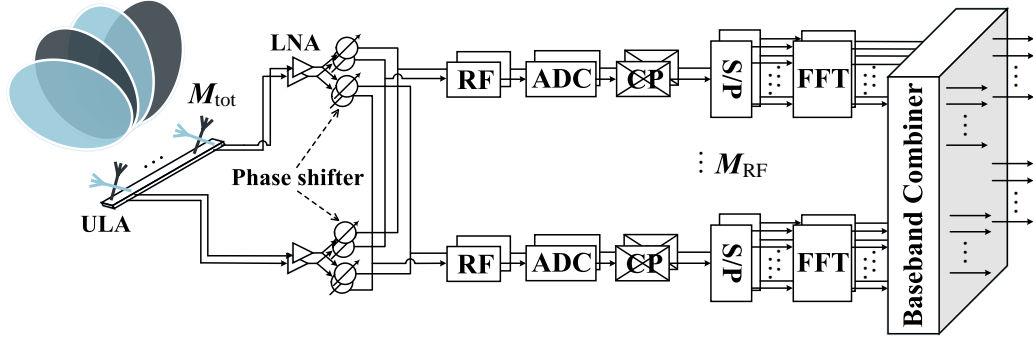
(b)

Figure 3.1: Structures of the transmit and receive arrays with dual-polarized antenna elements are presented in this figure. (a) A partially shared-array architecture is employed at the BS with N_{RF} RF chains and a total number of N_{tot} dual-polarized antenna elements. N_{S} data streams are transmitted. (b) A partially shared-array architecture is employed at the UE with M_{RF} RF chains and a total number of M_{tot} dual-polarized antenna elements.

tectures. In Figure 3.2(a), we present the exact mapping between the RF chains and the dual-polarized antenna elements for the developed partially shared-array architecture. All RF chains are first evenly grouped into sets of vertical and horizontal RF chains, denoted as vRF and hRF in Figure 3.2(a). All vertically (horizontally) polarized antenna elements are jointly controlled

(a)

ς_t

BS

ς_r

UE

$\varsigma = \varsigma_t - \varsigma_r$

(b)
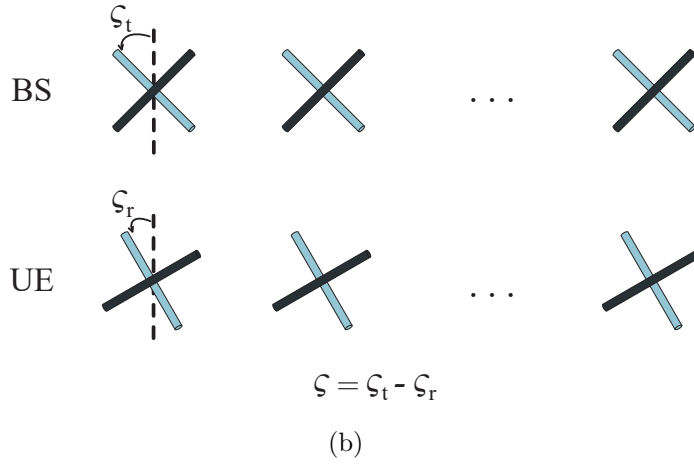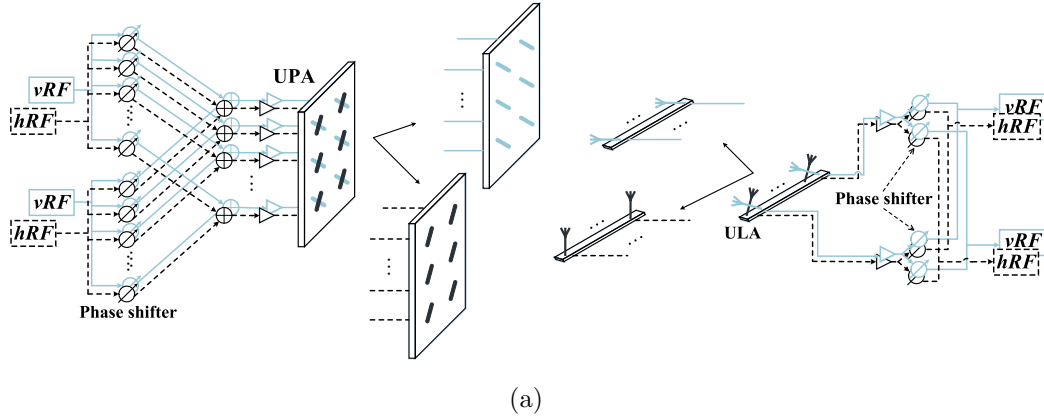
Figure 3.2: (a) Detailed polarization and RF chain mapping for the proposed partially shared-array architecture. (b) Illustrative example of angle mismatch in dual-polarized MIMO. The angle mismatch ς is determined as $\varsigma = \varsigma_t - \varsigma_t$, where ς_t and ς_r represent the orientation angles of the BS and UE.

by all corresponding vertical (horizontal) RF chains sharing the same network of phase shifters. Analog beamforming is independently performed from each polarization domain via the corresponding vertical or horizontal RF chain. In addition, a UPA is equipped at the BS. For simplicity, a ULA is assumed at the UE side.

Based on the employed transceiver architecture, we now develop the baseband received signal model after beamforming and combining. Let $\boldsymbol{s}[k]$ denote an $N_{\mathrm{S}} \times 1$ baseband transmit symbol vector such that $\mathbb{E}\left[\boldsymbol{s}[k]\boldsymbol{s}^*[k]\right] = \boldsymbol{I}_{N_{\mathrm{S}}}$, $k = 0, \cdots, N - 1$. The data symbol vector $\boldsymbol{s}[k]$ is first precoded using an $N_{\mathrm{RF}} \times N_{\mathrm{S}}$ digital baseband precoding matrix $\boldsymbol{F}_{\mathrm{BB}}[k]$, resulting in $\boldsymbol{d}[k] = [d_1[k], \cdots, d_{N_{\mathrm{RF}}}[k]]^{\mathrm{T}} = \boldsymbol{F}_{\mathrm{BB}}[k]\boldsymbol{s}[k]$. The data symbol blocks are then transformed to the time-domain via N_{RF}, N-point IFFTs, generating discrete-time signal as $\boldsymbol{x}_{n_{\mathrm{R}}}[k] = \sum_{n=0}^{N-1} d_{n_{\mathrm{R}}}[n]e^{\mathrm{j}\frac{2\pi n}{N}k}$, where $n_{\mathrm{R}} = 1, \cdots, N_{\mathrm{RF}}$ and $k = 0, \cdots, N - 1$. Before applying an $N_{\mathrm{tot}} \times N_{\mathrm{RF}}$ wideband analog precoding matrix $\boldsymbol{F}_{\mathrm{RF}}$, a cyclic prefix (CP) with length D is added to the data symbol blocks such that D is greater than or equal to the maximum delay spread of the multi-path channel. Denote by $\boldsymbol{x}[k_{\mathrm{c}}] = [\boldsymbol{x}_1[k_{\mathrm{c}}], \cdots, \boldsymbol{x}_{N_{\mathrm{RF}}}[k_{\mathrm{c}}]]^{\mathrm{T}}$, where $k_{\mathrm{c}} = N - D, \cdots, N - 1, 0, \cdots, N - 1$ due to the insertion of the CP. The discrete-time transmit signal model is then expressed as $\boldsymbol{x}_{\mathrm{cp}}[k_{\mathrm{c}}] = \boldsymbol{F}_{\mathrm{RF}}\boldsymbol{x}[k_{\mathrm{c}}]$. As the analog precoder is implemented using analog phase shifters, $\left[[\boldsymbol{F}_{\mathrm{RF}}]_{:,n_{\mathrm{R}}}[\boldsymbol{F}_{\mathrm{RF}}]_{:,n_{\mathrm{R}}}^*\right]_{i,i} = \frac{1}{N_{\mathrm{tot}}}$ is satisfied, where $n_{\mathrm{R}} = 1, \cdots, N_{\mathrm{RF}}$ and $i = 1, \cdots, N_{\mathrm{tot}}$. To further ensure the total power constraint, $\sum_{k=1}^{N} \|\boldsymbol{F}_{\mathrm{RF}}\boldsymbol{F}_{\mathrm{BB}}[k]\|_{\mathrm{F}}^2 = N_{\mathrm{S}}$ is required.

At the UE side, after combining with an $M_{\mathrm{tot}} \times M_{\mathrm{RF}}$ analog combining matrix $\boldsymbol{W}_{\mathrm{RF}}$, the CP is removed. After transforming the received data symbols from time-domain to frequency-domain via M_{RF}, N-point FFTs, an $M_{\mathrm{RF}} \times N_{\mathrm{S}}$ digital baseband combining matrix $\boldsymbol{W}_{\mathrm{BB}}[k]$ is applied on subcarrier k. The discrete-time received signal can then be expressed as

$$\boldsymbol{y}[k] = \boldsymbol{W}_{\mathrm{BB}}^*[k]\boldsymbol{W}_{\mathrm{RF}}^*\boldsymbol{H}[k]\boldsymbol{F}_{\mathrm{RF}}\boldsymbol{F}_{\mathrm{BB}}[k]\boldsymbol{s}[k] + \boldsymbol{W}_{\mathrm{BB}}^*[k]\boldsymbol{W}_{\mathrm{RF}}^*\boldsymbol{n}[k]. \tag{3.1}$$

Here, $\boldsymbol{n} \sim \mathcal{N}_{\mathrm{c}}(\boldsymbol{0}_{M_{\mathrm{tot}}}, \sigma^2 \boldsymbol{I}_{M_{\mathrm{tot}}})$ and $\sigma^2 = 1/\gamma$, where γ represents the target SNR.

3.3.2 Channel Model

We first express the basic two-dimensional wideband MIMO channel model with co-polarized antenna elements. We then construct the dual-pol channel model by accounting for the effects of power imbalance and angle mismatch. Similar to the channel model used in Chapter 2, we assume that the channel has N_{r} paths, and each path r has azimuth and elevation AoDs ϕ_r, θ_r, and AoA ψ_r. Let $p(\tau)$ denote the combined effect of filtering and pulse-shaping for T_{s}-spaced signaling at τ seconds. Assuming only co-polarized antenna elements at both the BS and UE, the time-domain delay-d MIMO channel matrix can be expressed as

$$\boldsymbol{G}[d] = \sum_{r=1}^{N_{\mathrm{r}}} g_r p\left(dT_{\mathrm{s}} - \tau_r\right) \boldsymbol{a}_{\mathrm{r}}(\psi_r) \boldsymbol{a}_{\mathrm{t}}^*(\theta_r, \phi_r), \tag{3.2}$$

where g_r represents the complex path gain of path-r, $\boldsymbol{a}_{\mathrm{r}}(\cdot) \in \mathbb{C}^{M_{\mathrm{tot}} \times 1}$ and $\boldsymbol{a}_{\mathrm{t}}(\cdot) \in \mathbb{C}^{N_{\mathrm{tot}} \times 1}$ correspond to the receive and transmit array response vectors. Assuming that the UPA is employed by the BS in the xy-plane with N_{x} and N_{y} elements on the x and y axes,

$$\begin{aligned}
\boldsymbol{a}_{\mathrm{t}}(\theta_r, \phi_r) = \frac{1}{\sqrt{N_{\mathrm{tot}}}} \Big[& 1, e^{\mathrm{j}\frac{2\pi}{\lambda} d_{\mathrm{tx}} \sin(\theta_r)\cos(\phi_r)}, \cdots, \\
& e^{\mathrm{j}\frac{2\pi}{\lambda}(N_{\mathrm{x}}-1)d_{\mathrm{tx}}\sin(\theta_r)\cos(\phi_r)}, e^{\mathrm{j}\frac{2\pi}{\lambda}d_{\mathrm{tx}}\sin(\theta_r)\sin(\phi_r)}, \cdots, \\
& e^{\mathrm{j}\frac{2\pi}{\lambda}((N_{\mathrm{x}}-1)d_{\mathrm{tx}}\sin(\theta_r)\cos(\phi_r)+(N_{\mathrm{y}}-1)d_{\mathrm{ty}}\sin(\theta_r)\sin(\phi_r))} \Big]^{\mathrm{T}},
\end{aligned} \tag{3.3}$$

73

where $N_{\text{tot}} = N_{\text{x}}N_{\text{y}}$, λ represents the wavelength corresponding to the operating carrier frequency, d_{tx} and d_{ty} are the inter-element distances of the co-polarized antenna elements on the x and y axes. Further, since the ULA is employed by the UE, we can express the receive array response vector as

$$\boldsymbol{a}_{\text{r}}(\psi_r) = \frac{1}{\sqrt{M_{\text{tot}}}}\left[1, e^{\text{j}\frac{2\pi}{\lambda}d_{\text{r}}\sin(\psi_r)}, \cdots, e^{\text{j}\frac{2\pi}{\lambda}d_{\text{r}}(M_{\text{tot}}-1)\sin(\psi_r)}\right]^{\text{T}}, \qquad (3.4)$$

where d_{r} denotes the inter-element distance of the co-polarized receive antenna elements. The channel frequency response matrix on subcarrier k is the Fourier transform of $\boldsymbol{G}[d]$, i.e.,

$$\boldsymbol{H}[k] = \sum_{r=1}^{N_{\text{r}}} g_r \rho_{\tau_r}[k]\boldsymbol{a}_{\text{r}}(\psi_r)\boldsymbol{a}_{\text{t}}^*(\theta_r, \phi_r), \qquad (3.5)$$

where $\rho_{\tau_r}[k] = \sum_{d=0}^{D-1} p\left(dT_{\text{s}} - \tau_r\right)e^{-\text{j}\frac{2\pi kd}{N}}$.

The basic model in (3.5) needs further modification to account for the use of dual-polarized antennas. Assuming perfect polarized transmit and receive systems, therefore all polarized coupling effects are due to dual-polarized design in the channel. A cross polar discrimination (XPD) value is incorporated, which implies the ability to distinguish among different polarized antennas [65, 66]. The difference in orientation of the polarized antenna groups is further characterized by a Givens rotation matrix. To be more specific, denoting by g_r^{ab} the complex path gain from polarization a to b for path-r, the channel model in (3.5) can be rewritten as

$$\boldsymbol{H}[k] = \sum_{r=1}^{N_{\text{r}}} \rho_{\tau_r}[k]\left(\boldsymbol{X}_\chi \odot \left(\begin{bmatrix} g_r^{\text{vv}} & g_r^{\text{vh}} \\ g_r^{\text{hv}} & g_r^{\text{hh}} \end{bmatrix} \otimes \left(\boldsymbol{a}_{\text{r}}(\psi_r)\boldsymbol{a}_{\text{t}}^*(\theta_r, \phi_r)\right)\right)\right)\boldsymbol{R}_\varsigma, \quad (3.6)$$

where

$$\boldsymbol{X}_\chi = \sqrt{\frac{1}{1+\chi}} \left[\begin{array}{cc} 1 & \sqrt{\chi} \\ \sqrt{\chi} & 1 \end{array} \right] \otimes \boldsymbol{1}_{\frac{M_{\text{tot}}}{2} \times \frac{N_{\text{tot}}}{2}}, \qquad (3.7)$$

represents the power imbalance between the polarizations with the parameter χ, defining the reciprocal of the XPD, and

$$\boldsymbol{R}_\varsigma = \left[\begin{array}{cc} \cos(\varsigma) & -\sin(\varsigma) \\ \sin(\varsigma) & \cos(\varsigma) \end{array} \right] \otimes \boldsymbol{I}_{\frac{N_{\text{tot}}}{2}}, \qquad (3.8)$$

denotes the Givens rotation matrix for a mismatch angle of ς. We provide one conceptual example of the mismatch angle in dual-polarized MIMO in Figure 3.2(b). Denoting the orientation angles of the BS and UE by ς_{t} and ς_{r}, we have $\varsigma = \varsigma_{\text{t}} - \varsigma_{\text{r}}$. For co-polarized MIMO, $\varsigma = 0$, and for orthogonally dual-polarized MIMO, $\varsigma = \pi/2$. Assuming $N_{\text{tot}} = N_{\text{x}}N_{\text{y}}$, we have $\boldsymbol{a}_{\text{t}}(\cdot) \in \mathbb{C}^{\frac{N_{\text{tot}}}{2} \times 1}$ and $\boldsymbol{a}_{\text{r}}(\cdot) \in \mathbb{C}^{\frac{M_{\text{tot}}}{2} \times 1}$. That is, the dimensionality of the array response vector for the dual-polarized antenna array is one half of that for the co-polarized antenna array.

3.4   Auxiliary Beam Pair Enabled Two-Dimensional Angle Estimation in Dual-Polarized MIMO

In this section, we first describe our proposed two-dimensional angle estimation design assuming a simple narrowband single-path channel using a single RF chain without considering dual-polarization. Afterwards, we present a means of estimating wideband multi-path angle components assuming multiple RF chains and dual-polarized antenna elements.

3.4.1 Narrowband angle estimation using single RF chain with co-polarized UPA

For narrowband single-path channels with UPA equipped at the BS and co-polarized antenna elements, the channel model can be simplified as $\boldsymbol{H} = g\boldsymbol{a}_\mathrm{r}(\psi)\boldsymbol{a}_\mathrm{t}^*(\theta, \phi)$. As only co-polarized antenna setup is assumed in this subsection, $\boldsymbol{a}_\mathrm{r}(\psi) \in \mathbb{C}^{M_\mathrm{tot} \times 1}$ and $\boldsymbol{a}_\mathrm{t}(\theta, \phi) \in \mathbb{C}^{N_\mathrm{tot} \times 1}$. Denote by $\mu_\mathrm{x} = \frac{2\pi}{\lambda}d_\mathrm{tx}\sin(\theta)\cos(\phi)$ and $\mu_\mathrm{y} = \frac{2\pi}{\lambda}d_\mathrm{ty}\sin(\theta)\sin(\phi)$, which can be interpreted as the elevation and azimuth transmit spatial frequencies. We further define two vectors $\boldsymbol{a}_\mathrm{tx}(\mu_\mathrm{x}) \in \mathbb{C}^{N_\mathrm{x} \times 1}$ and $\boldsymbol{a}_\mathrm{ty}(\mu_\mathrm{y}) \in \mathbb{C}^{N_\mathrm{y} \times 1}$ as

$$
\begin{aligned}
\boldsymbol{a}_\mathrm{tx}(\mu_\mathrm{x}) &= \frac{1}{\sqrt{N_\mathrm{x}}}\left[1, e^{j\mu_\mathrm{x}}, \cdots, e^{j(N_\mathrm{x}-1)\mu_\mathrm{x}}\right]^\mathrm{T}, \\
\boldsymbol{a}_\mathrm{ty}(\mu_\mathrm{y}) &= \frac{1}{\sqrt{N_\mathrm{y}}}\left[1, e^{j\mu_\mathrm{y}}, \cdots, e^{j(N_\mathrm{y}-1)\mu_\mathrm{y}}\right]^\mathrm{T},
\end{aligned}
\tag{3.9}
$$

which can be viewed as the transmit steering vectors in the elevation and azimuth domains. We therefore have $\boldsymbol{a}_\mathrm{t}(\theta, \phi) = \boldsymbol{a}_\mathrm{tx}(\mu_\mathrm{x}) \otimes \boldsymbol{a}_\mathrm{ty}(\mu_\mathrm{y})$.

3.4.1.1 General setup for analog transmit beamforming and receive combining

Two analog transmit beams form an elevation transmit auxiliary beam pair, and they steer towards $\mu_\mathrm{el} - \delta_\mathrm{x}$ and $\mu_\mathrm{el} + \delta_\mathrm{x}$ in the elevation domain for a given azimuth transmit direction μ'_az, i.e., the two transmit array response vectors become

$$
\begin{aligned}
\boldsymbol{a}_\mathrm{t}(\mu_\mathrm{el} - \delta_\mathrm{x}, \mu'_\mathrm{az}) &= \boldsymbol{a}_\mathrm{tx}(\mu_\mathrm{el} - \delta_\mathrm{x}) \otimes \boldsymbol{a}_\mathrm{ty}(\mu'_\mathrm{az}), \\
\boldsymbol{a}_\mathrm{t}(\mu_\mathrm{el} + \delta_\mathrm{x}, \mu'_\mathrm{az}) &= \boldsymbol{a}_\mathrm{tx}(\mu_\mathrm{el} + \delta_\mathrm{x}) \otimes \boldsymbol{a}_\mathrm{ty}(\mu'_\mathrm{az}).
\end{aligned}
\tag{3.10}
$$

Here, $\delta_x = \frac{2\ell_x \pi}{N_x}$ where $\ell_x = 1, \cdots, \frac{N_x}{4}$. To form an azimuth transmit auxiliary beam pair, two analog transmit beams are formed, and they steer towards $\mu_{az} - \delta_y$ and $\mu_{az} + \delta_y$ respectively in the azimuth domain for a given elevation transmit direction μ'_{el}:

$$
\begin{aligned}
\boldsymbol{a}_t(\mu'_{el}, \mu_{az} - \delta_y) &= \boldsymbol{a}_{tx}(\mu'_{el}) \otimes \boldsymbol{a}_{ty}(\mu_{az} - \delta_y), \\
\boldsymbol{a}_t(\mu'_{el}, \mu_{az} + \delta_y) &= \boldsymbol{a}_{tx}(\mu'_{el}) \otimes \boldsymbol{a}_{ty}(\mu_{az} + \delta_y).
\end{aligned}
\tag{3.11}
$$

Here, $\delta_y = \frac{2\ell_y \pi}{N_y}$ where $\ell_y = 1, \cdots, \frac{N_y}{4}$.

3.4.1.2 Auxiliary beam pair enabled azimuth/elevation AoD and AoA estimation

We first demonstrate the estimation of azimuth/elevation AoD. Using the analog transmit beam $\boldsymbol{a}_t(\mu_{el} - \delta_x, \mu'_{az})$ and the receive beam $\boldsymbol{a}_r(\eta - \delta_r)$, we express the received signal on subcarrier $k \in \{0, \cdots, N-1\}$ as

$$
\boldsymbol{y}[k] = g\boldsymbol{a}_r^*(\eta - \delta_r)\boldsymbol{a}_r(\nu)\boldsymbol{a}_t^*(\theta, \phi)\boldsymbol{a}_t(\mu_{el} - \delta_x, \mu'_{az})\boldsymbol{s}[k].
\tag{3.12}
$$

Note that we neglect noise in (3.12). Assuming $|\boldsymbol{s}[k]|^2 = 1$, we calculate the corresponding received signal strength as

$$
\chi_{el}^{\Delta} = |g|^2 \left|\boldsymbol{a}_r^*(\eta - \delta_r)\boldsymbol{a}_r(\nu)\boldsymbol{a}_t^*(\theta, \phi)\boldsymbol{a}_t(\mu_{el} - \delta_x, \mu'_{az})\right|^2
\tag{3.13}
$$

$$
= |g|^2 |\boldsymbol{a}_r^*(\eta - \delta_r)\boldsymbol{a}_r(\nu)|^2 \left|\frac{\sin\left(N_x\left(\frac{\mu_x - \mu_{el}}{2}\right)\right)}{N_x \sin\left(\frac{\mu_x - \mu_{el} + \delta_x}{2}\right)}\right|^2
$$

$$
\times \left|\frac{\sin\left(N_y\left(\frac{\mu_y - \mu'_{az}}{2}\right)\right)}{N_y \sin\left(\frac{\mu_y - \mu'_{az}}{2}\right)}\right|^2.
\tag{3.14}
$$

Similarly, for $\boldsymbol{a}_{\mathrm{t}}(\mu_{\mathrm{el}}+\delta_{\mathrm{x}}, \mu'_{\mathrm{az}})$ and $\boldsymbol{a}_{\mathrm{r}}(\eta - \delta_{\mathrm{r}})$, the corresponding received signal strength is

$$
\begin{aligned}
\chi_{\mathrm{el}}^{\Sigma} &= |g|^2 \, |\boldsymbol{a}_{\mathrm{r}}^*(\eta - \delta_{\mathrm{r}})\boldsymbol{a}_{\mathrm{r}}(\nu)|^2 \left| \frac{\sin\left(N_{\mathrm{x}}\left(\frac{\mu_{\mathrm{x}}-\mu_{\mathrm{el}}}{2}\right)\right)}{N_{\mathrm{x}} \sin\left(\frac{\mu_{\mathrm{x}}-\mu_{\mathrm{el}}-\delta_{\mathrm{x}}}{2}\right)} \right|^2 \\
&\quad \times \left| \frac{\sin\left(N_{\mathrm{y}}\left(\frac{\mu_{\mathrm{y}}-\mu'_{\mathrm{az}}}{2}\right)\right)}{N_{\mathrm{y}} \sin\left(\frac{\mu_{\mathrm{y}}-\mu'_{\mathrm{az}}}{2}\right)} \right|^2 .
\end{aligned} \tag{3.15}
$$

We can obtain the ratio metric as

$$
\begin{aligned}
\zeta_{\mathrm{el}} &= \frac{\chi_{\mathrm{el}}^{\Delta} - \chi_{\mathrm{el}}^{\Sigma}}{\chi_{\mathrm{el}}^{\Delta} + \chi_{\mathrm{el}}^{\Sigma}} \\
&= \frac{\left| \frac{\sin\left(N_{\mathrm{x}}\left(\frac{\mu_{\mathrm{x}}-\mu_{\mathrm{el}}}{2}\right)\right)}{N_{\mathrm{x}} \sin\left(\frac{\mu_{\mathrm{x}}-\mu_{\mathrm{el}}+\delta_{\mathrm{x}}}{2}\right)} \right|^2 - \left| \frac{\sin\left(N_{\mathrm{x}}\left(\frac{\mu_{\mathrm{x}}-\mu_{\mathrm{el}}}{2}\right)\right)}{N_{\mathrm{x}} \sin\left(\frac{\mu_{\mathrm{x}}-\mu_{\mathrm{el}}-\delta_{\mathrm{x}}}{2}\right)} \right|^2}{\left| \frac{\sin\left(N_{\mathrm{x}}\left(\frac{\mu_{\mathrm{x}}-\mu_{\mathrm{el}}}{2}\right)\right)}{N_{\mathrm{x}} \sin\left(\frac{\mu_{\mathrm{x}}-\mu_{\mathrm{el}}+\delta_{\mathrm{x}}}{2}\right)} \right|^2 + \left| \frac{\sin\left(N_{\mathrm{x}}\left(\frac{\mu_{\mathrm{x}}-\mu_{\mathrm{el}}}{2}\right)\right)}{N_{\mathrm{x}} \sin\left(\frac{\mu_{\mathrm{x}}-\mu_{\mathrm{el}}-\delta_{\mathrm{x}}}{2}\right)} \right|^2} \\
&= -\frac{\sin\left(\frac{\mu_{\mathrm{x}}-\mu_{\mathrm{el}}}{2}\right)\sin(\delta_{\mathrm{x}})}{1 - \cos\left(\mu_{\mathrm{x}} - \mu_{\mathrm{el}}\right)\cos(\delta_{\mathrm{x}})},
\end{aligned} \tag{3.16}
$$

which does not depend on the path gain, analog receive combining and azimuth transmit beamforming, in the absence of noise. If $|\mu_{\mathrm{x}} - \mu_{\mathrm{el}}| < \delta_{\mathrm{x}}$, i.e., μ_{x} is within the range of $(\mu_{\mathrm{el}} - \delta_{\mathrm{x}}, \mu_{\mathrm{el}} + \delta_{\mathrm{x}})$, ζ_{el} is a monotonically decreasing function of $\mu_{\mathrm{x}} - \mu_{\mathrm{el}}$ and invertible with respect to $\mu_{\mathrm{x}} - \mu_{\mathrm{el}}$. Hence, by solving (3.16), we have

$$
\hat{\mu}_{\mathrm{x}} = \mu_{\mathrm{el}} - \arcsin\left(\frac{\zeta_{\mathrm{el}} \sin(\delta_{\mathrm{x}}) - \zeta_{\mathrm{el}}\sqrt{1 - \zeta_{\mathrm{el}}^2}\sin(\delta_{\mathrm{x}})\cos(\delta_{\mathrm{x}})}{\sin^2(\delta_{\mathrm{x}}) + \zeta_{\mathrm{el}}^2 \cos^2(\delta_{\mathrm{x}})} \right). \tag{3.17}
$$

Similarly, neglecting noise and assuming $\boldsymbol{a}_{\mathrm{r}}(\eta + \delta_{\mathrm{r}})$ as the analog combining vector formed by the UE, for the azimuth transmit auxiliary beam pair

containing $\boldsymbol{a}_\text{t}(\mu'_\text{el}, \mu_\text{az} - \delta_\text{y})$ and $\boldsymbol{a}_\text{t}(\mu'_\text{el}, \mu_\text{az} + \delta_\text{y})$, we can obtain

$$\zeta_\text{az} = -\frac{\sin\left(\frac{\mu_\text{y} - \mu_\text{az}}{2}\right) \sin(\delta_\text{y})}{1 - \cos(\mu_\text{y} - \mu_\text{az}) \cos(\delta_\text{y})}, \tag{3.18}$$

and therefore, if $|\mu_\text{y} - \mu_\text{az}| < \delta_\text{y}$,

$$\hat{\mu}_\text{y} = \mu_\text{az} - \arcsin\left(\frac{\zeta_\text{az} \sin(\delta_\text{y}) - \zeta_\text{az}\sqrt{1 - \zeta_\text{az}^2}\sin(\delta_\text{y})\cos(\delta_\text{y})}{\sin^2(\delta_\text{y}) + \zeta_\text{az}^2\cos^2(\delta_\text{y})}\right). \tag{3.19}$$

Using $\hat{\mu}_\text{x}$ and $\hat{\mu}_\text{y}$, we obtain the estimated azimuth and elevation AoDs as

$$\hat{\phi} = \arctan\left(\frac{d_\text{tx}\hat{\mu}_\text{y}}{d_\text{ty}\hat{\mu}_\text{x}}\right),$$

$$\hat{\theta} = \arcsin\left(\frac{\lambda\hat{\mu}_\text{y}}{2\pi d_\text{ty}}\left(\sin\left(\arctan\left(\frac{d_\text{tx}\hat{\mu}_\text{y}}{d_\text{ty}\hat{\mu}_\text{x}}\right)\right)\right)^{-1}\right). \tag{3.20}$$

The estimation of receive spatial frequency and AoA via the receive auxiliary beam pair can be conducted in a similar fashion.

3.4.2 Wideband angle estimation using multiple RF chains with dual-polarized UPA

To facilitate multi-path angle estimation for wideband channels, multiple RF chains can be employed by both the BS and UE such that multiple auxiliary beam pairs can be sent simultaneously. To distinguish among simultaneously probed auxiliary beam pairs, we design a first-layer auxiliary beam pair specific pilot structure.

In the proposed design approach, the two beams in one auxiliary beam pair are generated from the same polarization domain. We present a conceptual example illustrating this in Figure 3.3, in which the beams formed

79
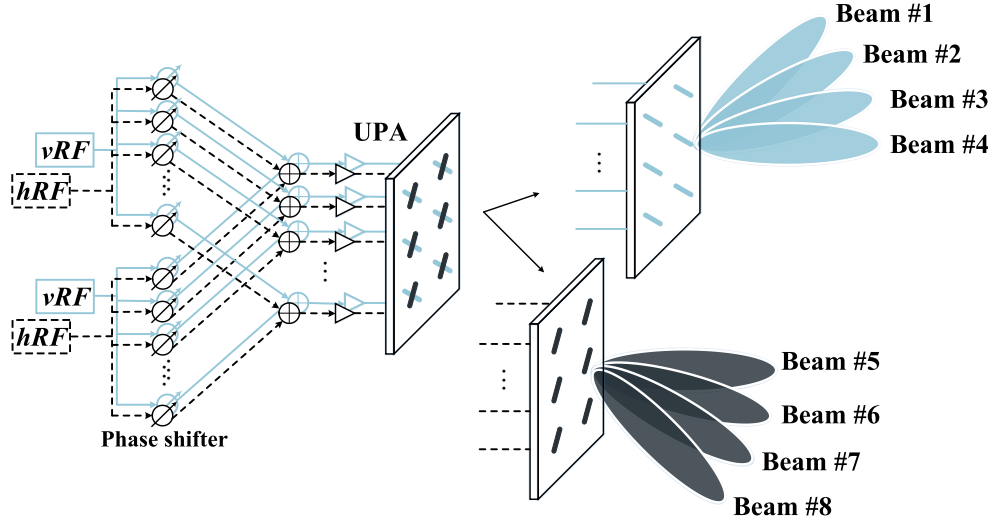
Figure 3.3: A conceptual example of the mapping between the polarization domain and auxiliary beam pair. In this example, every two beams with consecutive indices probed from the same polarization domain form an auxiliary beam pair. For instance, Beams #1 and #2 form an auxiliary beam pair, while Beams #1 and #4 or Beams #4 and #5 are not paired.

from the vertically polarized antennas are indexed from $1 \sim 4$, and the beams probed from the horizontal domain are indexed from $5 \sim 8$. Denote the vertical and horizontal beam index sets by $\Upsilon_{\mathrm{v}} = \{\#1, \#2, \#3, \#4\}$ and $\Upsilon_{\mathrm{h}} = \{\#5, \#6, \#7, \#8\}$. Only the beams that are chosen from the same set (either Υ_{v} or Υ_{h}) can be paired. For instance, the two beams with beam indices #4 and #5 selected from Υ_{v} and Υ_{h} are not allowed to form an auxiliary beam pair. As will be discussed later, by pairing beams only from the same polarization domain, the corresponding ratio metrics derived assuming high-power regime will exhibit similar forms to those using co-polarized antennas, i.e., (3.16) and (3.18).

We therefore develop a second-layer paired-beam specific pilot and apply it to distinguish between the two beams in the same auxiliary beam pair. Note that different from the conventional beam-specific pilot design, in which, each beam is associated with a distinct pilot sequence, the second-layer paired-beam specific pilot signals can be reused among the beams in simultaneously probed auxiliary beam pairs. This is because the first-layer auxiliary beam pair specific pilot signals serve as the cover codes for the second-layer paired-beam specific pilot signals. For illustration, the estimation of azimuth transmit spatial frequency is of our design focus throughout this part, while the estimation of elevation transmit spatial frequency and receive spatial frequency can be derived in a similar fashion.

3.4.2.1 General setup for analog transmit beamforming and receive combining

For a given elevation transmit direction μ'_{el}, denoting by $\mathcal{F}_{\text{T}}^{\text{v}}$ and $\mathcal{F}_{\text{T}}^{\text{h}}$ the codebooks of azimuth analog transmit steering vectors for the vertical and horizontal transmit RF chains, we have

$$\mathcal{F}_{\text{T}}^{\text{v}} = \left\{ \left[\boldsymbol{a}_{\text{t}}^{\text{T}} \left(\mu'_{\text{el}}, \mu_{\text{az}}^{0} \right) \ \boldsymbol{0}_{N_{\text{tot}}/2}^{\text{T}} \right]^{\text{T}}, \cdots, \left[\boldsymbol{a}_{\text{t}}^{\text{T}} \left(\mu'_{\text{el}}, \mu_{\text{az}}^{N_{\text{az}}/2-1} \right) \ \boldsymbol{0}_{N_{\text{tot}}/2}^{\text{T}} \right]^{\text{T}} \right\}, \quad (3.21)$$

$$\mathcal{F}_{\text{T}}^{\text{h}} = \left\{ \left[\boldsymbol{0}_{N_{\text{tot}}/2}^{\text{T}} \ \boldsymbol{a}_{\text{t}}^{\text{T}} \left(\mu'_{\text{el}}, \mu_{\text{az}}^{N_{\text{az}}/2} \right) \right]^{\text{T}}, \cdots, \left[\boldsymbol{0}_{N_{\text{tot}}/2}^{\text{T}} \ \boldsymbol{a}_{\text{t}}^{\text{T}} \left(\mu'_{\text{el}}, \mu_{\text{az}}^{N_{\text{az}}-1} \right) \right]^{\text{T}} \right\}, \quad (3.22)$$

where $\left\{ \mu_{\text{az}}^{0}, \cdots, \mu_{\text{az}}^{N_{\text{az}}-1} \right\}$ is the set of candidate azimuth transmit directions. Similarly,

$$\mathcal{W}_{\text{T}}^{\text{v}} = \left\{ \left[\boldsymbol{a}_{\text{r}}^{\text{T}} \left(\nu^{0} \right) \ \boldsymbol{0}_{M_{\text{tot}}/2}^{\text{T}} \right]^{\text{T}}, \cdots, \left[\boldsymbol{a}_{\text{r}}^{\text{T}} \left(\nu^{N_{\text{rx}}/2-1} \right) \ \boldsymbol{0}_{M_{\text{tot}}/2}^{\text{T}} \right]^{\text{T}} \right\}, \quad (3.23)$$

$$\mathcal{W}_{\mathrm{T}}^{\mathrm{h}} = \left\{ \left[\mathbf{0}_{M_{\mathrm{tot}}/2}^{\mathrm{T}} \ \boldsymbol{a}_{\mathrm{r}}^{\mathrm{T}} \left(\nu^{N_{\mathrm{rx}}/2} \right) \right]^{\mathrm{T}}, \cdots, \left[\mathbf{0}_{M_{\mathrm{tot}}/2}^{\mathrm{T}} \ \boldsymbol{a}_{\mathrm{r}}^{\mathrm{T}} \left(\nu^{N_{\mathrm{rx}}-1} \right) \right]^{\mathrm{T}} \right\}, \qquad (3.24)$$

denote the codebooks of analog receive steering vectors for the vertical and horizontal receive RF chains, where $\left\{ \nu^0, \cdots, \nu^{N_{\mathrm{rx}}-1} \right\}$ is the set of candidate receive directions. Note that here, $\boldsymbol{a}_{\mathrm{t}} \left(\mu_{\mathrm{el}}', \mu_{\mathrm{az}}^n \right) \in \mathbb{C}^{\frac{N_{\mathrm{tot}}}{2} \times 1}$ and $\boldsymbol{a}_{\mathrm{r}} \left(\nu^{\acute{n}} \right) \in \mathbb{C}^{\frac{M_{\mathrm{tot}}}{2} \times 1}$ due to the cross-polarization assumption, where $n \in \{0, \cdots, N_{\mathrm{az}} - 1\}$ and $\acute{n} \in \{0, \cdots, N_{\mathrm{rx}} - 1\}$.

The constructions of the transmit and receive beam codebooks in (3.21)-(3.24) leverage the fact that the AoD and AoA are the same for both vertical and horizontal polarization domains. It is therefore feasible to form vertical beams to cover one half of the probing range, and horizontal beams to cover the other half. By doing so, the number of required beams to cover a given angular range is minimized, which in turn, reduces the estimation overhead.

The analog transmit and receive probing matrices are constructed by concatenating all successively probed azimuth analog transmit precoding and receive combining matrices. Denote by N_{T} and M_{T} the total numbers of probings performed by the BS in the azimuth domain for a given elevation steering direction and UE. Further, denoting by $\boldsymbol{F}_{\mathrm{T}}$ and $\boldsymbol{W}_{\mathrm{T}}$ the analog azimuth transmit and receive probing matrices, we have $\boldsymbol{F}_{\mathrm{T}} = [\boldsymbol{F}_1, \cdots, \boldsymbol{F}_{n_{\mathrm{t}}}, \cdots, \boldsymbol{F}_{N_{\mathrm{T}}}]$ and $\boldsymbol{W}_{\mathrm{T}} = [\boldsymbol{W}_1, \cdots, \boldsymbol{W}_{m_{\mathrm{t}}}, \cdots, \boldsymbol{W}_{M_{\mathrm{T}}}]$, where $\boldsymbol{F}_{n_{\mathrm{t}}} \in \mathbb{C}^{N_{\mathrm{tot}} \times N_{\mathrm{RF}}}$ represents the n_{t}-th azimuth transmit probing, $\boldsymbol{W}_{m_{\mathrm{t}}} \in \mathbb{C}^{M_{\mathrm{tot}} \times M_{\mathrm{RF}}}$ is the m_{t}-th receive probing.

To facilitate the selection of the best pairs of azimuth transmit auxiliary beam pairs and receive beams with noise impairment and various interference

sources, the steering angles of simultaneously probed beams should match the distribution of azimuth AoD and AoA, which are unknown to the BS and UE a prior, as much as possible. With finite N_T and M_T, the analog beams in one probing matrix are steered towards random angular directions. That is, each column in $\boldsymbol{F}_{n_\mathrm{t}}$ is randomly chosen from $\mathcal{F}_\mathrm{T}^\mathrm{v}$ and $\mathcal{F}_\mathrm{T}^\mathrm{h}$, and each column in $\boldsymbol{W}_{m_\mathrm{t}}$ is randomly chosen from $\mathcal{W}_\mathrm{T}^\mathrm{v}$ and $\mathcal{W}_\mathrm{T}^\mathrm{h}$. Note that from (3.21)-(3.24), it can be observed that since the vertical and horizontal beams cover the first and second half of the probing range, the transmit and receive beams can be randomly selected from the same polarization domain for a given probing to facilitate the whole process. The transmit and receive probings are conducted in a TDM manner. For a given probing at the UE, N_T consecutive probings $\boldsymbol{F}_1, \cdots, \boldsymbol{F}_{N_\mathrm{T}}$ are performed at the BS. This process iterates until all M_T probings have been executed by the UE.

Considering a given probing at the UE, e.g., $\boldsymbol{W}_{m_\mathrm{t}}$, we obtain the resultant matrix by concatenating the $N_\mathrm{T} N_\mathrm{RF}$ azimuth transmit beamforming vectors in the absence of noise as

$$\boldsymbol{Y}_{m_\mathrm{t}}[k] \;=\; \boldsymbol{W}_{m_\mathrm{t}}^* \boldsymbol{H}[k] \boldsymbol{F}_\mathrm{T} \boldsymbol{X}[k], \tag{3.25}$$

where $\boldsymbol{X}[k]$ carries the $N_\mathrm{T} N_\mathrm{RF}$ multi-layer pilot symbols such that

$$[\boldsymbol{X}[k]]_{i,q} = \begin{cases} 0, & 0 < i \le N_\mathrm{RF}(q-1) \text{ or } N_\mathrm{RF}q < i \le N_\mathrm{T} N_\mathrm{RF}, \ q = 1, \cdots, N_\mathrm{T}, \\ \ne 0, & \text{otherwise.} \end{cases}$$

$$\tag{3.26}$$

3.4.2.2 Design principle and procedure for the proposed approach

We use the Zadoff-Chu (ZC) sequences for designing the multi-layer pilot due to their constant amplitude and zero autocorrelation properties in both time and frequency domains [67]. In this chapter, the multi-layer pilot consists of a first-layer auxiliary beam pair specific pilot and a second-layer paired-beam specific pilot. Denote by a_ℓ and b_m the auxiliary beam pair identity (ID) and paired-beam ID. Denoting by N_a the total number of possible azimuth transmit auxiliary beam pairs that can be constructed via the azimuth transmit steering vectors in $\mathcal{F}_\mathrm{T}^\mathrm{v}$ and $\mathcal{F}_\mathrm{T}^\mathrm{h}$, we have $\ell \in \{0, \cdots, N_\mathrm{a} - 1\}$ and $m \in \{0, \cdots, N_\mathrm{az} - 1\}$. Note that as one auxiliary beam pair consists of two beams, $\mathrm{b}_m \in \{0, 1\}$. By mapping the proposed multi-layer pilot to one OFDM symbol, we have

$$x^{\mathrm{a}_\ell, \mathrm{b}_m}[k] = e^{\frac{j\pi r^{(\mathrm{a}_\ell)}(k+p\mathrm{b}_m)(k+p\mathrm{b}_m+1)}{N}}, \tag{3.27}$$

where $r^{(\mathrm{a}_\ell)}$ denotes the root index associated with the auxiliary beam pair ID a_ℓ, and p is a prime number representing the circular shift spacing in the frequency domain. Further, $\gcd(r^{(\mathrm{a}_\ell)}, N) = 1$ is satisfied. Assuming that the azimuth transmit beamforming vector $[\boldsymbol{F}_\mathrm{T}]_{:,q}$ corresponds to the auxiliary beam pair ID a_ℓ and the paired-beam ID b_m, we have $[\boldsymbol{X}[k]]_{q, \lceil q/N_\mathrm{RF} \rceil} = x^{\mathrm{a}_\ell, \mathrm{b}_m}[k]$. Note that as can be seen from (3.27), we reuse the ZC sequence structure as in [67], but with custom designed mapping between the root indices, frequency domain circular shifts and auxiliary beams.

Consider the n_t-th azimuth probing $\boldsymbol{F}_{n_\mathrm{t}}$ at the BS. For simplicity, we make the following assumptions: (i) $N_\mathrm{r} = M_\mathrm{RF}$, and (ii) the first $N_\mathrm{RF}/2$

columns in $\boldsymbol{F}_{n_\mathrm{t}}$ are chosen from $\mathcal{F}_\mathrm{T}^\mathrm{v}$, while its last $N_\mathrm{RF}/2$ columns are selected from $\mathcal{F}_\mathrm{T}^\mathrm{h}$ assuming that N_RF is an even number. Specifically,

$$
\boldsymbol{F}_{n_\mathrm{t}} = \Big[\ \big[\boldsymbol{a}_\mathrm{t}^\mathrm{T} \left(\mu_\mathrm{el}', \mu_\mathrm{az}^{n_0} \right) \ \boldsymbol{0}_{N_\mathrm{tot}/2}^\mathrm{T} \big]^\mathrm{T} \ \cdots \ \big[\boldsymbol{a}_\mathrm{t}^\mathrm{T} \left(\mu_\mathrm{el}', \mu_\mathrm{az}^{n_{N_\mathrm{RF}/2-1}} \right) \ \boldsymbol{0}_{N_\mathrm{tot}/2}^\mathrm{T} \big]^\mathrm{T}
$$
$$
\big[\boldsymbol{0}_{N_\mathrm{tot}/2}^\mathrm{T} \ \boldsymbol{a}_\mathrm{t}^\mathrm{T} \left(\mu_\mathrm{el}', \mu_\mathrm{az}^{n_{N_\mathrm{RF}/2}} \right) \big]^\mathrm{T} \ \cdots \ \big[\boldsymbol{0}_{N_\mathrm{tot}/2}^\mathrm{T} \ \boldsymbol{a}_\mathrm{t}^\mathrm{T} \left(\mu_\mathrm{el}', \mu_\mathrm{az}^{n_{N_\mathrm{RF}-1}} \right) \big]^\mathrm{T} \ \Big],
$$
$$(3.28)$$

where $n_0, \cdots, n_{N_\mathrm{RF}/2-1} \in \{0, \cdots, N_\mathrm{az}/2 - 1\}$ and

$$
n_{N_\mathrm{RF}/2}, \cdots, n_{N_\mathrm{RF}-1} \in \{N_\mathrm{az}/2, \cdots, N_\mathrm{az} - 1\}.
$$

Further, assume that the azimuth transmit beamforming vectors

$$
\boldsymbol{a}_\mathrm{t} \left(\mu_\mathrm{el}', \mu_\mathrm{az}^{n_0} \right), \cdots, \boldsymbol{a}_\mathrm{t} \left(\mu_\mathrm{el}', \mu_\mathrm{az}^{n_{N_\mathrm{RF}-1}} \right)
$$

correspond to the auxiliary beam pair IDs $\mathrm{a}_0, \cdots, \mathrm{a}_{N_\mathrm{RF}-1}$ and the paired-beam IDs $\mathrm{b}_0, \cdots, \mathrm{b}_{N_\mathrm{RF}-1}$.

Before proceeding with detailed design procedure, we first partition the channel model in (3.6) into a block matrix form as

$$
\boldsymbol{H}[k] = \begin{bmatrix} \boldsymbol{H}^\mathrm{vv}[k] & \boldsymbol{H}^\mathrm{vh}[k] \\ \boldsymbol{H}^\mathrm{hv}[k] & \boldsymbol{H}^\mathrm{hh}[k] \end{bmatrix}, \ \ \boldsymbol{H}^\mathrm{vv}[k], \boldsymbol{H}^\mathrm{vh}[k], \boldsymbol{H}^\mathrm{hv}[k], \boldsymbol{H}^\mathrm{vv}[k] \in \mathbb{C}^{\frac{M_\mathrm{tot}}{2} \times \frac{N_\mathrm{tot}}{2}}.
$$
$$(3.29)$$

Denoting by $\boldsymbol{A}_r^{\mathrm{TR}} = \mathbf{1}_{\frac{M_{\mathrm{tot}}}{2} \times \frac{N_{\mathrm{tot}}}{2}} \odot (\boldsymbol{a}_{\mathrm{r}}(\psi_r) \boldsymbol{a}_{\mathrm{t}}^*(\theta_r, \phi_r))$, we have

$$\boldsymbol{H}^{\mathrm{vv}}[k] = \sqrt{\frac{1}{1+\chi}} \sum_{r=1}^{N_{\mathrm{r}}} \rho_{\tau_r}[k] \left(g_r^{\mathrm{vv}} \cos(\varsigma) + \sqrt{\chi} g_r^{\mathrm{vh}} \sin(\varsigma) \right) \boldsymbol{A}_r^{\mathrm{TR}}, \quad (3.30)$$

$$\boldsymbol{H}^{\mathrm{vh}}[k] = \sqrt{\frac{1}{1+\chi}} \sum_{r=1}^{N_{\mathrm{r}}} \rho_{\tau_r}[k] \left(-g_r^{\mathrm{vv}} \sin(\varsigma) + \sqrt{\chi} g_r^{\mathrm{vh}} \cos(\varsigma) \right) \boldsymbol{A}_r^{\mathrm{TR}}, \quad (3.31)$$

$$\boldsymbol{H}^{\mathrm{hv}}[k] = \sqrt{\frac{1}{1+\chi}} \sum_{r=1}^{N_{\mathrm{r}}} \rho_{\tau_r}[k] \left(\sqrt{\chi} g_r^{\mathrm{hv}} \cos(\varsigma) + g_r^{\mathrm{hh}} \sin(\varsigma) \right) \boldsymbol{A}_r^{\mathrm{TR}}, \quad (3.32)$$

$$\boldsymbol{H}^{\mathrm{hh}}[k] = \sqrt{\frac{1}{1+\chi}} \sum_{r=1}^{N_{\mathrm{r}}} \rho_{\tau_r}[k] \left(-\sqrt{\chi} g_r^{\mathrm{hv}} \sin(\varsigma) + g_r^{\mathrm{hh}} \cos(\varsigma) \right) \boldsymbol{A}_r^{\mathrm{TR}}. \quad (3.33)$$

In the absence of noise and considering the r-th receive beam $[\boldsymbol{W}_{m_{\mathrm{t}}}]_{:,r}$ chosen from $\mathcal{W}_{\mathrm{T}}^{\mathrm{v}}$,

$$[\boldsymbol{Y}_{m_{\mathrm{t}}}[k]]_{r,n_{\mathrm{t}}} = \sum_{\imath=0}^{N_{\mathrm{RF}}/2-1} \boldsymbol{w}_{m_{\mathrm{t}},r}^* \boldsymbol{H}^{\mathrm{vv}}[k] \boldsymbol{a}_{\mathrm{t}}(\mu_{\mathrm{el}}', \mu_{\mathrm{az}}^{n_\imath}) x^{\mathrm{a}_\imath, \mathrm{b}_\imath}[k]$$

$$+ \sum_{\kappa=N_{\mathrm{RF}}/2}^{N_{\mathrm{RF}}-1} \boldsymbol{w}_{m_{\mathrm{t}},r}^* \boldsymbol{H}^{\mathrm{vh}}[k] \boldsymbol{a}_{\mathrm{t}}(\mu_{\mathrm{el}}', \mu_{\mathrm{az}}^{n_\kappa}) x^{\mathrm{a}_\kappa, \mathrm{b}_\kappa}[k], \quad (3.34)$$

where $\boldsymbol{w}_{m_{\mathrm{t}},r} = [\boldsymbol{W}_{m_{\mathrm{t}}}]_{1:\frac{M_{\mathrm{tot}}}{2},r}$. For $\imath \in \{0, \cdots, N_{\mathrm{RF}}/2-1\}$, we have

$$\boldsymbol{w}_{m_{\mathrm{t}},r}^* \boldsymbol{H}^{\mathrm{vv}}[k] \boldsymbol{a}_{\mathrm{t}}(\mu_{\mathrm{el}}', \mu_{\mathrm{az}}^{n_\imath})$$

$$= \sqrt{\frac{1}{1+\chi}} \sum_{r'=1}^{N_{\mathrm{r}}} \rho_{\tau_{r'}}[k] \left(g_{r'}^{\mathrm{vv}} \cos(\varsigma) + \sqrt{\chi} g_{r'}^{\mathrm{vh}} \sin(\varsigma) \right)$$

$$\times \left(\boldsymbol{w}_{m_{\mathrm{t}},r}^* \left(\mathbf{1}_{\frac{M_{\mathrm{tot}}}{2} \times \frac{N_{\mathrm{tot}}}{2}} \odot (\boldsymbol{a}_{\mathrm{r}}(\psi_{r'})) \boldsymbol{a}_{\mathrm{t}}^*(\theta_{r'}, \phi_{r'}) \right) \boldsymbol{a}_{\mathrm{t}}(\mu_{\mathrm{el}}', \mu_{\mathrm{az}}^{n_\imath}) \right) \quad (3.35)$$

$$= \boldsymbol{w}_{m_{\mathrm{t}},r}^* \sum_{r'=1}^{N_{\mathrm{r}}} \rho_{\tau_{r'}}[k] h_{r'}^{\mathrm{vv}} \boldsymbol{a}_{\mathrm{r}}(\psi_{r'}) \boldsymbol{a}_{\mathrm{t}}^*(\theta_{r'}, \phi_{r'}) \boldsymbol{a}_{\mathrm{t}}(\mu_{\mathrm{el}}', \mu_{\mathrm{az}}^{n_\imath}), \quad (3.36)$$

where $h_{r'}^{\mathrm{vv}} = \sqrt{\frac{1}{1+\chi}} \left(g_{r'}^{\mathrm{vv}} \cos(\varsigma) + \sqrt{\chi} g_{r'}^{\mathrm{vh}} \sin(\varsigma) \right)$. Similarly, for $\kappa \in \{N_{\mathrm{RF}}/2, \cdots,$

$N_{\mathrm{RF}} - 1\}$,

$$\boldsymbol{w}_{m_{\mathrm{t}},r}^{*}\boldsymbol{H}^{\mathrm{vh}}[k]\boldsymbol{a}_{\mathrm{t}}\left(\mu_{\mathrm{el}}^{\prime}, \mu_{\mathrm{az}}^{n_{\kappa}}\right) = \boldsymbol{w}_{m_{\mathrm{t}},r}^{*} \sum_{r'=1}^{N_{\mathrm{r}}} \rho_{\tau_{r'}}[k] h_{r'}^{\mathrm{vh}} \boldsymbol{a}_{\mathrm{r}}\left(\psi_{r'}\right) \boldsymbol{a}_{\mathrm{t}}^{*}\left(\theta_{r'}, \phi_{r'}\right) \boldsymbol{a}_{\mathrm{t}}\left(\mu_{\mathrm{el}}^{\prime}, \mu_{\mathrm{az}}^{n_{\kappa}}\right),$$

(3.37)

where $h_{r'}^{\mathrm{vh}} = \sqrt{\frac{1}{1+\chi}}\left(-g_{r'}^{\mathrm{vv}}\sin(\varsigma) + \sqrt{\chi}g_{r'}^{\mathrm{vh}}\cos(\varsigma)\right)$.

At the UE side, the received signal in the frequency domain is corre-
lated with the reference ZC sequence corresponding to the reference auxiliary
beam pair ID $a_{\bar{\ell}}$ and the reference paired-beam ID $b_{\bar{m}}$ ($\bar{\ell} \in \{0, \cdots, N_{\mathrm{a}} - 1\}$,
$\bar{m} \in \{0, \cdots, N_{\mathrm{az}} - 1\}$) at zero-lag. In the following, we will interpret the inter-
ference terms from the perspective of the vertical polarization domain, while
the same principles can be applied to the horizontal polarization domain as

well. Specifically,

$$y_{m_\mathrm{t},r,n_\mathrm{t}}^u = \sum_{k=0}^{N-1} [\boldsymbol{Y}_{m_\mathrm{t}}[k]]_{r,n_\mathrm{t}} \left(x^{\mathrm{a}_{\bar{\ell}},\mathrm{b}_{\bar{m}}}[k]\right)^* \tag{3.38}$$

$$= \sum_{k=0}^{N-1} \boldsymbol{w}_{m_\mathrm{t},r}^* \left(\sum_{r'=1}^{N_\mathrm{r}} \rho_{\tau_{r'}}[k] h_{r'}^{\mathrm{vv}} \boldsymbol{a}_\mathrm{r}(\psi_{r'}) \boldsymbol{a}_\mathrm{t}^*(\theta_{r'},\phi_{r'})\right)$$
$$\times \boldsymbol{a}_\mathrm{t}\left(\mu_\mathrm{el}',\mu_\mathrm{az}^{n_u}\right) x^{\mathrm{a}_u,\mathrm{b}_u}[k] \left(x^{\mathrm{a}_{\bar{\ell}},\mathrm{b}_{\bar{m}}}[k]\right)^* \tag{3.39}$$

$$+ \sum_{k=0}^{N-1} \boldsymbol{w}_{m_\mathrm{t},r}^* \left(\sum_{r'=1}^{N_\mathrm{r}} \rho_{\tau_{r'}}[k] h_{r'}^{\mathrm{vv}} \boldsymbol{a}_\mathrm{r}(\psi_{r'}) \boldsymbol{a}_\mathrm{t}^*(\theta_{r'},\phi_{r'})\right)$$
$$\times \boldsymbol{a}_\mathrm{t}\left(\mu_\mathrm{el}',\mu_\mathrm{az}^{n_{\bar{u}}}\right) x^{\mathrm{a}_{\bar{u}},\mathrm{b}_{\bar{u}}}[k] \left(x^{\mathrm{a}_{\bar{\ell}},\mathrm{b}_{\bar{m}}}[k]\right)^* \tag{3.40}$$

$$+ \sum_{k=0}^{N-1} \sum_{\breve{u}\neq\bar{\ell}} \boldsymbol{w}_{m_\mathrm{t},r}^* \left(\sum_{r'=1}^{N_\mathrm{r}} \rho_{\tau_{r'}}[k] h_{r'}^{\mathrm{vv}} \boldsymbol{a}_\mathrm{r}(\psi_{r'}) \boldsymbol{a}_\mathrm{t}^*(\theta_{r'},\phi_{r'})\right)$$
$$\times \boldsymbol{a}_\mathrm{t}\left(\mu_\mathrm{el}',\mu_\mathrm{az}^{n_{\breve{u}}}\right) x^{\mathrm{a}_{\breve{u}},\mathrm{b}_{\breve{u}}}[k] \left(x^{\mathrm{a}_{\bar{\ell}},\mathrm{b}_{\bar{m}}}[k]\right)^* \tag{3.41}$$

$$+ \sum_{k=0}^{N-1} \sum_{\iota'=N_\mathrm{RF}/2}^{N_\mathrm{RF}-1} \boldsymbol{w}_{m_\mathrm{t},r}^* \left(\sum_{r'=1}^{N_\mathrm{r}} \rho_{\tau_{r'}}[k] h_{r'}^{\mathrm{vh}} \boldsymbol{a}_\mathrm{r}(\psi_{r'}) \boldsymbol{a}_\mathrm{t}^*(\theta_{r'},\phi_{r'})\right)$$
$$\times \boldsymbol{a}_\mathrm{t}\left(\mu_\mathrm{el}',\mu_\mathrm{az}^{n_{\iota'}}\right) x^{\mathrm{a}_{\iota'},\mathrm{b}_{\iota'}}[k] \left(x^{\mathrm{a}_{\bar{\ell}},\mathrm{b}_{\bar{m}}}[k]\right)^*, \tag{3.42}$$

where $u,\bar{u},\breve{u} \in \{0,\cdots,N_\mathrm{RF}/2-1\}$; I_0 (i.e., (3.39)) denotes the correlation value if the azimuth transmit beamforming vector corresponds to the same auxiliary beam pair and paired-beam IDs as the reference ones, i.e., $\mathrm{a}_u = \mathrm{a}_{\bar{\ell}}$ and $\mathrm{b}_u = \mathrm{b}_{\bar{m}}$; the term I_1 (i.e., (3.40)) represents the interference caused by the correlation when the azimuth transmit beamforming vector having the same auxiliary beam pair ID but different paired-beam ID with respect to the reference ones, i.e., $\mathrm{a}_{\bar{u}} = \mathrm{a}_{\bar{\ell}}$ and $\mathrm{b}_{\bar{u}} \neq \mathrm{b}_{\bar{m}}$; the interference term I_2 (i.e., (3.41)) is obtained via the correlation when $\mathrm{a}_{\breve{u}} \neq \mathrm{a}_{\bar{\ell}}$ for either $\mathrm{b}_{\breve{u}} = \mathrm{b}_{\bar{m}}$ or $\mathrm{b}_{\breve{u}} \neq \mathrm{b}_{\bar{m}}$; the interference term I_3 (i.e., (3.42)) is resulted from the design principle that beams formed from different polarization domains do not share

88

the same auxiliary beam pair ID, i.e., $a_{i'} \neq a_u(a_{\bar{\ell}})$ for either $b_{i'} = b_u(b_{\bar{m}})$ or $b_{i'} \neq b_u(b_{\bar{m}})$.

To compare the amplitudes of I_0, I_1, I_2 and I_3, we first derive their upper bounds in the absence of frequency selectivity, i.e., $\rho_{\tau_r} \leq \rho_{\tau_r}[0] = \cdots = \rho_{\tau_r}[N-1]$ for $r = 1, \cdots, N_r$. It can therefore be observed from (3.39) that the amplitude of I_0 is upper bounded by $N\sqrt{\frac{1}{1+\chi}}\left|\sum_{r'=1}^{N_r} \rho_{\tau_{r'}} h_{r'}^{vv}\right|$. The amplitude of I_1 can be upper bounded as

$$|I_1| \leq \sqrt{\frac{1}{1+\chi}}\left|\sum_{r'=1}^{N_r}\rho_{\tau_{r'}}h_{r'}^{vv}\right|\left|\sum_{k=0}^{N-1}x^{a_{\bar{u}},b_{\bar{u}}}[k]\left(x^{a_{\bar{\ell}},b_{\bar{m}}}[k]\right)^*\right| \tag{3.43}$$

$$= \sqrt{\frac{1}{1+\chi}}\left|\sum_{r'=1}^{N_r}\rho_{\tau_{r'}}h_{r'}^{vv}\right|$$

$$\times \left|x^{a_{\bar{u}},b_{\bar{u}}}[0]\left(x^{a_{\bar{\ell}},b_{\bar{m}}}[0]\right)^*\sum_{k=0}^{N-1}e^{\frac{j2\pi k\left(r^{\left(a_{\bar{\ell}}\right)}p(b_{\bar{u}}-b_{\bar{m}})\right)}{N}}\right| \tag{3.44}$$

$$= \begin{cases} 0, & \text{if } r^{(a_{\bar{\ell}})}p\left(b_{\bar{u}}-b_{\bar{m}}\right) \neq \varrho N \\ N\sqrt{\frac{1}{1+\chi}}\left|\sum_{r'=1}^{N_r}\rho_{\tau_{r'}}h_{r'}^{vv}\right|\left|x^{a_{\bar{u}},b_{\bar{u}}}[0]\left(x^{a_{\bar{\ell}},b_{\bar{m}}}[0]\right)^*\right|, & \text{else,} \end{cases} \tag{3.45}$$

where ϱ is an arbitrary integer and p is an arbitrary prime number. To achieve zero correlation interference, we can adjust p such that $p \neq \frac{\varrho N}{r^{\left(a_{\bar{\ell}}\right)}(b_{\bar{u}}-b_{\bar{m}})}$ is achieved under the constraints of $p \leq p_{max}$ and $\varrho \leq \varrho_{max}$. Here, p_{max} denotes the maximum possible circular shift spacing in the frequency domain, i.e., $p_{max} = \lfloor N/N_p \rfloor$, where N_p represents the total number of possible paired-beam IDs. Further, denoting by $\triangle b_{max}$ the maximum possible paired-beam ID difference, we have $\varrho_{max} = \lceil r_{max}p_{max}\triangle b_{max}/N \rceil$ [67], where $r_{max} = \max\left\{r^{\left(a_{\ell}\right)}, \breve{\ell} = 0, \cdots, N_a - 1\right\}$. For our proposed multi-layer pilot

structure, as $b_m \in \{0, 1\}$ for $m \in \{0, \cdots, N_{az} - 1\}$, we therefore have $N_p = 2$ and $\triangle b_{max} = 1$ resulting in $p_{max} = N/2$ and $\varrho_{max} = r_{max}/2$.

Using the property of a Gauss sum [68], the amplitude of the correlation interference term I_2 is upper bounded as [69]

$$|I_2| \leq \sqrt{\frac{1}{1+\chi}} \left| \sum_{r'=1}^{N_r} \rho_{\tau_{r'}} h_{r'}^{vv} \right| \left| \sum_{\breve{u} \neq \bar{\ell}} \sum_{k=0}^{N-1} x^{a_{\breve{u}}, b_{\breve{u}}}[k] \left(x^{a_{\bar{\ell}}, b_{\bar{m}}}[k] \right)^* \right|. \quad (3.46)$$

The amplitude of I_2 can be further upper bounded by $\sqrt{\frac{1}{1+\chi}} \left| \sum_{r'=1}^{N_r} \rho_{\tau_{r'}} h_{r'}^{vv} \right| N_e$ $\sqrt{N}$ for either $b_{\breve{u}} = b_{\bar{m}}$ or $b_{\breve{u}} \neq b_{\bar{m}}$, where N_e denotes the total number of azimuth transmit steering vectors in $\boldsymbol{F}_{n_t}$ formed from the vertically polarized antenna elements that have different auxiliary beam pair IDs from the reference auxiliary beam pair ID $\bar{\ell}$. That is, denoting by $A = \{0, \cdots, N_{RF}/2 - 1\} \setminus \bar{\ell}$, we therefore have $N_e = \text{card}(A)$, where $\text{card}(\cdot)$ represents the cardinality of the set. Similarly, the amplitude of I_3 is upper bounded as

$$|I_3| \leq \sqrt{\frac{1}{1+\chi}} \left| \sum_{r'=1}^{N_r} \rho_{\tau_{r'}} h_{r'}^{vh} \right| \frac{N_{RF}}{2} \sqrt{N}, \quad (3.47)$$

for either $b_{\imath'} = b_{\bar{m}}$ or $b_{\imath'} \neq b_{\bar{m}}$, where $\frac{N_{RF}}{2}$ implies the total number of azimuth transmit steering vectors probed from the horizontally polarized antenna elements in $\boldsymbol{F}_{n_t}$ (see (3.28)). For large bandwidth at mmWave frequencies with large N and limited number of RF chains, $|I_0| \gg |I_2|$ and $|I_0| \gg |I_3|$. We therefore have $\left| y^u_{m_t, r, n_t} \right| \approx |I_0|$.

Denote by $\Omega_{r,u} = \sum_{k=0}^{N-1} \rho_{\tau_r} h_r^{vv}[k] x^{a_u, b_u}[k] \left(x^{a_u, b_u}[k] \right)^*$, and

$$\boldsymbol{\Lambda}_{r,u} = \sum_{k=0}^{N-1} \left(\sum_{r'=1, r' \neq r}^{N_r} \rho_{\tau_{r'}}[k] h_{r'}^{vv} \boldsymbol{a}_r \left(\psi_{r'} \right) \boldsymbol{a}_t^* \left(\theta_{r'}, \phi_{r'} \right) \right) \left(x^{a_u, b_u}[k] \right)^*, \quad (3.48)$$

90

where $u \in \{0, \cdots, N_{\mathrm{RF}}/2 - 1\}$. Further, we assume that the azimuth transmit spatial frequency $\mu_{\mathrm{y},r}$ for path-r ($\mu_{\mathrm{y},r} = \frac{2\pi}{\lambda} d_{\mathrm{tx}} \sin(\theta_r) \cos(\phi_r)$) is within the range of $(\mu_{\mathrm{az}}^{n_u}, \mu_{\mathrm{az}}^{n_v})$ where $v \in \{0, \cdots, N_{\mathrm{RF}}/2 - 1\}$. For a given elevation transmit direction μ_{el}', $\boldsymbol{a}_{\mathrm{t}}(\mu_{\mathrm{el}}', \mu_{\mathrm{az}}^{n_u})$ and $\boldsymbol{a}_{\mathrm{t}}(\mu_{\mathrm{el}}', \mu_{\mathrm{az}}^{n_v})$ form an azimuth transmit auxiliary beam pair, and they come from the n_{t}-th and s_{t}-th azimuth probings by the BS. With respect to $\boldsymbol{a}_{\mathrm{t}}(\mu_{\mathrm{el}}', \mu_{\mathrm{az}}^{n_u})$, we can therefore approximate the corresponding received signal strength as

$$\left| y_{m_{\mathrm{t}},r,n_{\mathrm{t}}}^{u} \right|^2 \approx |\Omega_{r,u}|^2 \left| \boldsymbol{w}_{m_{\mathrm{t}},r}^* \boldsymbol{a}_{\mathrm{r}}(\psi_r) \right| \left| \boldsymbol{a}_{\mathrm{t}}^*(\theta_r, \phi_r) \boldsymbol{a}_{\mathrm{t}}(\mu_{\mathrm{el}}', \mu_{\mathrm{az}}^{n_u}) \right| \tag{3.49}$$

$$+ \Omega_{r,u}^* \boldsymbol{w}_{m_{\mathrm{t}},r}^* \boldsymbol{\Lambda}_{r,u}^* \boldsymbol{a}_{\mathrm{t}}(\mu_{\mathrm{el}}', \mu_{\mathrm{az}}^{n_u}) \boldsymbol{a}_{\mathrm{t}}^*(\mu_{\mathrm{el}}', \mu_{\mathrm{az}}^{n_u}) \boldsymbol{a}_{\mathrm{t}}(\theta_r, \phi_r) \boldsymbol{a}_{\mathrm{r}}^*(\psi_r) \boldsymbol{w}_{m_{\mathrm{t}},r}$$

$$+ \Omega_{r,u} \boldsymbol{w}_{m_{\mathrm{t}},r}^* \boldsymbol{a}_{\mathrm{r}}(\psi_r) \boldsymbol{a}_{\mathrm{t}}^*(\theta_r, \phi_r) \boldsymbol{a}_{\mathrm{t}}(\mu_{\mathrm{el}}', \mu_{\mathrm{az}}^{n_u}) \boldsymbol{a}_{\mathrm{t}}^*(\mu_{\mathrm{el}}', \mu_{\mathrm{az}}^{n_u}) \boldsymbol{\Lambda}_{r,u}^* \boldsymbol{w}_{m_{\mathrm{t}},r}$$

$$+ \boldsymbol{w}_{m_{\mathrm{t}},r}^* \boldsymbol{\Lambda}_{r,u} \boldsymbol{a}_{\mathrm{t}}(\mu_{\mathrm{el}}', \mu_{\mathrm{az}}^{n_u}) \boldsymbol{a}_{\mathrm{t}}^*(\mu_{\mathrm{el}}', \mu_{\mathrm{az}}^{n_u}) \boldsymbol{\Lambda}_{r,u}^* \boldsymbol{w}_{m_{\mathrm{t}},r}$$

$$\xrightarrow[N_{\mathrm{tot}}M_{\mathrm{tot}} \to \infty]{\text{a.s.}} |\Omega_{r,u}|^2 \left| \boldsymbol{w}_{m_{\mathrm{t}},r}^* \boldsymbol{a}_{\mathrm{r}}(\psi_r) \right| \left| \boldsymbol{a}_{\mathrm{t}}^*(\theta_r, \phi_r) \boldsymbol{a}_{\mathrm{t}}(\mu_{\mathrm{el}}', \mu_{\mathrm{az}}^{n_u}) \right|. \tag{3.50}$$

Note that (3.50) is obtained by exploiting the sparse nature of the mmWave channels such that if $N_{\mathrm{tot}}M_{\mathrm{tot}} \to \infty$, the last three terms in (3.49) converge to zero since $\boldsymbol{w}_{m_{\mathrm{t}},r}^* \boldsymbol{\Lambda}_{r,u}^* \boldsymbol{a}_{\mathrm{t}}(\mu_{\mathrm{el}}', \mu_{\mathrm{az}}^{n_u})$ converges to zero [70]. This is because for large numbers of transmit and receive antennas with angular sparsity, the projection of path-r's beamforming and combining vectors $\boldsymbol{a}_{\mathrm{t}}(\mu_{\mathrm{el}}', \mu_{\mathrm{az}}^{n_u})$ and $\boldsymbol{w}_{m_{\mathrm{t}},r}$ on path-r''s ($r' \neq r$) channel $\boldsymbol{\Lambda}$ defined in (3.48) becomes arbitrarily small. Similarly, for $\boldsymbol{a}_{\mathrm{t}}(\mu_{\mathrm{el}}', \mu_{\mathrm{az}}^{n_v})$,

$$\left| y_{m_{\mathrm{t}},r,s_{\mathrm{t}}}^{v} \right|^2 \xrightarrow[N_{\mathrm{tot}}M_{\mathrm{tot}} \to \infty]{\text{a.s.}} |\Omega_{r,v}|^2 \left| \boldsymbol{w}_{m_{\mathrm{t}},r}^* \boldsymbol{a}_{\mathrm{r}}(\psi_r) \right| \left| \boldsymbol{a}_{\mathrm{t}}^*(\theta_r, \phi_r) \boldsymbol{a}_{\mathrm{t}}(\mu_{\mathrm{el}}', \mu_{\mathrm{az}}^{n_v}) \right|. \tag{3.51}$$

Using the asymptotical results provided in (3.50) and (3.51), we can

calculate the corresponding ratio metric as

$$
\zeta_{\text{az},r} = \frac{\left|y^u_{m_t,r,n_t}\right|^2 - \left|y^v_{m_t,r,s_t}\right|^2}{\left|y^u_{m_t,r,n_t}\right|^2 + \left|y^v_{m_t,r,s_t}\right|^2} \tag{3.52}
$$

$$
= \frac{|\Omega_{r,u}|^2 \left|\boldsymbol{a}^*_t(\theta_r,\phi_r)\,\boldsymbol{a}_t(\mu'_{\text{el}},\mu^{n_u}_{\text{az}})\right| - |\Omega_{r,v}|^2 \left|\boldsymbol{a}^*_t(\theta_r,\phi_r)\,\boldsymbol{a}_t(\mu'_{\text{el}},\mu^{n_v}_{\text{az}})\right|}{|\Omega_{r,u}|^2 \left|\boldsymbol{a}^*_t(\theta_r,\phi_r)\,\boldsymbol{a}_t(\mu'_{\text{el}},\mu^{n_u}_{\text{az}})\right| + |\Omega_{r,v}|^2 \left|\boldsymbol{a}^*_t(\theta_r,\phi_r)\,\boldsymbol{a}_t(\mu'_{\text{el}},\mu^{n_v}_{\text{az}})\right|} \tag{3.53}
$$

$$
= -\frac{\sin\left(\frac{\mu_{\text{y},r}-\mu_{\text{az}}}{2}\right)\sin(\delta_{\text{y}})}{1 - \cos(\mu_{\text{y},r}-\mu_{\text{az}})\cos(\delta_{\text{y}})}, \tag{3.54}
$$

where $\delta_{\text{y}} = |\mu^{n_v}_{\text{az}} - \mu^{n_u}_{\text{az}}|/2$, and $\mu_{\text{az}} = \mu^{n_v}_{\text{az}} - \delta_{\text{y}}$ or $\mu_{\text{az}} = \mu^{n_u}_{\text{az}} + \delta_{\text{y}}$. We can therefore obtain the estimate of the azimuth transmit spatial frequency for path-r as

$$
\hat{\mu}_{\text{y},r} = \mu_{\text{az}} - \arcsin\left(\frac{\zeta_{\text{az},r}\sin(\delta_{\text{y}}) - \zeta_{\text{az},r}\sqrt{1-\zeta^2_{\text{az},r}}\sin(\delta_{\text{y}})\cos(\delta_{\text{y}})}{\sin^2(\delta_{\text{y}}) + \zeta^2_{\text{az},r}\cos^2(\delta_{\text{y}})}\right). \tag{3.55}
$$

The custom designed multi-layer pilot structure is able to reduce pilot resource overhead. Here, we define the pilot resource as the required least number of ZC sequences that have different root indices. An alternative to the proposed multi-layer pilot design is the conventional single-layer pilot structure such that each beam is simply associated with a distinct ZC sequence with a unique root index. For the proposed multi-layer structure, however, only the auxiliary beam pair is associated with a distinct ZC sequence with two fixed shift spacing values corresponding to the two beams in the same pair. For instance, assume that N_{RF} transmit beams are simultaneously probed. For the single-layer pilot design, at least N_{RF} ZC sequences with different root indices are needed. Regarding the multi-layer structure, this number becomes $N_{\text{RF}}/2$,

which reduces the pilot resource overhead by 50%. Reducing the pilot resource overhead is beneficial such that appropriate ZC sequences (with different root indices) with good correlation properties such as those employed in LTE PSS (ZC sequences with root indices 25, 29 and 34) can be flexibly selected from the sequence pool to improve beam detection performance in wideband channels.

3.5 Practical Implementation Issues of Proposed Two-Dimensional Angle Estimation

In a closed-loop FDD system, the acquisition of the azimuth/elevation AoD at the BS requires information feedback from the UE via a feedback channel. In our prior work in Chapter 2, we discussed direct transmit spatial frequency and ratio metric quantization and feedback strategies. In this chapter, we custom design a differential quantization and feedback option for the proposed algorithm to reduce the feedback overhead in MIMO systems with two-dimensional phased array. For simplicity, we use the narrowband example employed in Section 3.4.1 throughout this section. In addition, we only consider transmit beamforming in the azimuth domain. For general wideband channels with multi-path angle components and two-dimensional phased array, both the estimated azimuth and elevation AoDs for each path are quantized and fed back.

In fact, the sign of the ratio metric implies the relative position of the AoD/AoA to the boresight of the corresponding auxiliary beam pair. We present a conceptual example showing the sign effect of the ratio metric in

Figure 3.4 using one azimuth transmit auxiliary beam pair. In Figure 3.4(a), the azimuth transmit spatial frequency μ_y is to the left of the boresight of the auxiliary beam pair μ_{az} such that $\mu_y \in (\mu_{az} - \delta_y, \mu_{az})$. In fact, it can be seen from (3.18) that, the sign of the azimuth ratio metric purely depends on the sign of $\sin\left(\frac{\mu_y - \mu_{az}}{2}\right)$. Since in this example $\mu_y \in (\mu_{az} - \delta_y, \mu_{az})$ and $0 \leq \delta_y < \pi/2$, ζ_{az} is therefore positive such that $\text{sign}(\zeta_{az}) = 1$. Similarly, in Figure 3.4(b), as $\mu_y \in (\mu_{az}, \mu_{az} + \delta_y)$, i.e., μ_y is to the right of μ_{az}, $\text{sign}(\zeta_{az}) = -1$.

With the knowledge of μ_{az} and δ_y, the UE can first obtain $\hat{\mu}_y$ according to (3.19). As μ_{az} and δ_y are predetermined semi-static parameters, they can be periodically broadcasted from the BS to the UE. The difference between the estimated azimuth transmit spatial frequency and the boresight of the corresponding azimuth transmit auxiliary beam pair can then be determined as $\triangle\hat{\mu}_y = |\hat{\mu}_y - \mu_{az}|$. Note that now $\triangle\hat{\mu}_y \in [-\delta_y, \delta_y]$. A relatively small codebook with codewords uniformly distributed within the interval of $[-\delta_y, \delta_y]$ can therefore be used to quantize $\triangle\hat{\mu}_y$. Along with the feedback of $\text{sign}(\zeta_{az})$ (1 bit indicating either "1" or "−1"), the BS can retrieve the azimuth transmit spatial frequency as $\hat{\mu}_y = \mu_{az} + \text{sign}(\zeta_{az})\triangle\hat{\mu}_y$.

3.6   Numerical Results

In this section, we evaluate the performance of the proposed auxiliary beam pair enabled two-dimensional angle estimation technique. The BS and UE employ the UPA and ULA with inter-element spacing of $\lambda/2$ between co-

Boresight of azimuth ABP μ_{az}

Boresight of left beam $\mu_{\mathrm{az}} - \delta_{\mathrm{y}}$ μ_{y} **Boresight of right beam** $\mu_{\mathrm{az}} + \delta_{\mathrm{y}}$

$\mathrm{sign}(\zeta_{\mathrm{az}}) = 1$

Left azimuth analog transmit beam **Right azimuth analog transmit beam**

Boresight of azimuth ABP μ_{az}

Boresight of left beam $\mu_{\mathrm{az}} - \delta_{\mathrm{y}}$ μ_{y} **Boresight of right beam** $\mu_{\mathrm{az}} + \delta_{\mathrm{y}}$

$\mathrm{sign}(\zeta_{\mathrm{az}}) = -1$

Left azimuth analog transmit beam **Right azimuth analog transmit beam**

(a) (b)
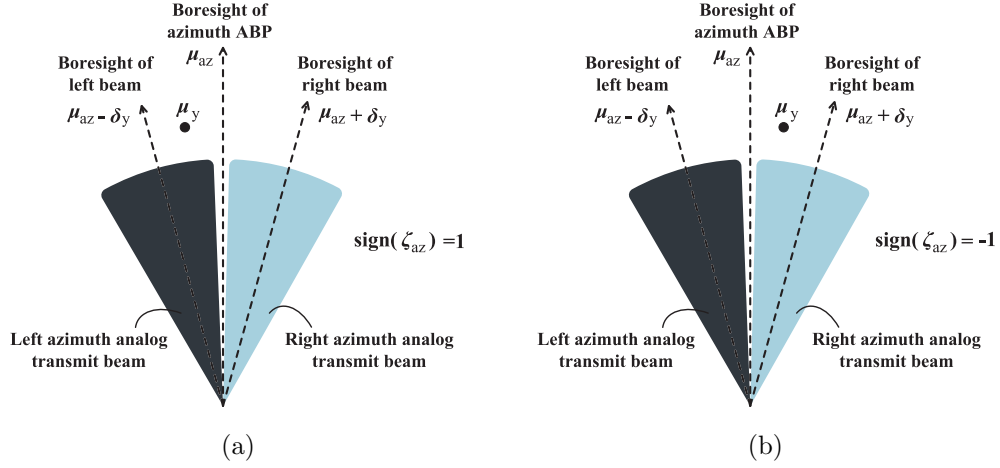
Figure 3.4: A conceptual example of the relationship between the relative position of the azimuth transmit spatial frequency to the boresight of the corresponding azimuth transmit auxiliary beam pair and the sign of the azimuth ratio metric: (a) $\mu_{\mathrm{y}} \in (\mu_{\mathrm{az}} - \delta_{\mathrm{y}}, \mu_{\mathrm{az}})$ implies that the azimuth transmit spatial frequency is within the probing range of the left azimuth analog transmit beam, $\mathrm{sign}(\zeta_{\mathrm{az}}) = 1$ indicates that the azimuth transmit spatial frequency is to the left of the boresight of the azimuth transmit auxiliary beam pair. (b) $\mu_{\mathrm{y}} \in (\mu_{\mathrm{az}}, \mu_{\mathrm{az}} + \delta_{\mathrm{y}})$ implies that the azimuth transmit spatial frequency is within the probing range of the right azimuth analog transmit beam, $\mathrm{sign}(\zeta_{\mathrm{az}}) = -1$ indicates that the azimuth transmit spatial frequency is to the right of the boresight of the azimuth transmit auxiliary beam pair.

polarized antennas. We set $\delta_{\mathrm{x}} = \frac{2\pi}{N_{\mathrm{x}}}$, $\delta_{\mathrm{y}} = \frac{2\pi}{N_{\mathrm{y}}}$ and $\delta_{\mathrm{r}} = \frac{2\pi}{M_{\mathrm{tot}}}$ to approximate the half-power beamwidth of the corresponding beamforming and combining vectors. The BS covers $120°$ angular range $[-60°, 60°]$ around azimuth boresight $(0°)$ and $90°$ angular range $[-45°, 45°]$ around elevation boresight $(0°)$. The UE monitors $180°$ angular region $[-90°, 90°]$ around boresight $(0°)$. We employ the differential transmit spatial frequency feedback strategy throughout this section unless otherwise specified. The codewords for quantizing the azimuth

95

and elevation AoDs are uniformly distributed within $[-\delta_{\mathrm{y}}, \delta_{\mathrm{y}}]$ and $[-\delta_{\mathrm{x}}, \delta_{\mathrm{x}}]$.

3.6.1 Narrowband single-path angle estimation using single RF chain without dual-polarization

The azimuth/elevation AoD and AoA are assumed to take continuous values, i.e., not quantized, and are uniformly distributed within the corresponding coverage ranges. The beam codebook size for the azimuth transmit domain, elevation transmit domain and receive domain is determined as $\lceil 120°/2\delta_{\mathrm{y}} \rceil$, $\lceil 90°/2\delta_{\mathrm{x}} \rceil$ and $\lceil 180°/2\delta_{\mathrm{r}} \rceil$ to avoid coverage holes. For instance, for $M_{\mathrm{tot}} = 8$, the codebook size for the UE is $\lceil 180°/2\delta_{\mathrm{r}} \rceil = \lceil 180°/45° \rceil = 4$. We employ the Rician channel model throughout this part without considering dual-polarization. We assume the number of NLOS channel components as 5. The objective is to estimate the dominant LOS path's AoD and AoA. From the channel measurements in [63], we set 13.2dB Rician K-factor that characterizes the mmWave channel in an urban wireless channel topography.

We plot the MAEE performance of the single-path's azimuth/elevation AoD and AoA acquisition in Figure 3.5(a) under various target SNR levels γ. We also evaluate the grid-of-beams based approach for comparison. Here, we define the MAEE as $\mathbb{E}\left[|v_{\mathrm{true}} - v_{\mathrm{est}}|\right]$, where v_{true} represents the exact angle in degree, and v_{est} is its estimated counterpart in degree. Further, we assume that $N_{\mathrm{x}} = 4, N_{\mathrm{y}} = 8$, and $M_{\mathrm{tot}} = 4$. It is observed from Figure 3.5(a) that promising MAEE performance of azimuth/elevation AoD and AoA estimation via the proposed auxiliary beam pair design can be achieved even at relatively

low SNR regime. It can also be observed from Figure 3.5(a) that the proposed technique outperforms the grid-of-beams based method for various target SNR levels.

In Figure 3.5(b), we compare the direct and differential AoD quantization and feedback strategies in terms of the mean angle quantization error (MAQE). We define the MAQE as $\mathbb{E}\left[\|v_{\mathrm{est}} - v_{\mathrm{quan}}\|\right]$, where v_{quan} represents the quantized version of the estimated value v_{est} in degree. We only examine the azimuth AoD quantization in this example assuming 10 dB SNR. For the direct quantization, the codewords are uniformly distributed within the interval of $[-60°, 60°]$. Regarding the proposed differential approach, the codewords are uniformly distributed within $[-\delta_{\mathrm{y}}, \delta_{\mathrm{y}}]$ where $\delta_{\mathrm{y}} = 22.5°$ and $\delta_{\mathrm{y}} = 11.25°$ for $N_{\mathrm{y}} = 8$ and $N_{\mathrm{y}} = 16$. Note that we add one extra bit indicating the sign to the number of feedback bits required by the differential approach. From Figure 3.5(b), it is observed that using the same amount of feedback bits, the proposed differential approach exhibits better MAQE performance than the direct quantization. That is, for a given target quantization error, the differential strategy requires less amount of feedback overhead than the direct quantization approach.

In Figure 3.6(a), we evaluate the MAEE performance with respect to different numbers of transmit antennas. For $N_{\mathrm{tot}} = 8, 16, 32, 64$, we correspondingly set $N_{\mathrm{x}} = 2, 4, 4, 8$ and $N_{\mathrm{y}} = 4, 4, 8, 8$. In this example, we provide the azimuth AoD estimation results for -10 and 10 dB SNRs. Other simulation assumptions are identical to those in Figure 3.6(a). As can be seen

from Figure 3.6(a), with an increase in the number of transmit antennas, the MAEE is significantly reduced for both the proposed method and the conventional grid-of-beams based approach. For large N_{tot}, e.g., 128, the mean azimuth AoD estimation error is close to 0° under various SNR levels. Further, with relatively small transmit antenna array, and therefore, relatively wide beam-widths, the performance gap between the proposed algorithm and the grid-of-beams based method is remarkable. This is mainly because the angle estimation performance of the grid-of-beams based method is subject to the grid resolution. For large transmit antenna array with fine grid resolution, the performance difference between the two methods vanishes. Note that we do not include the estimation overhead in evaluating the MAEE performance comparison between the proposed approach and the grid-of-beams based method. In Figure 3.7, however, we incorporate the estimation overhead when comparing the two angle estimation strategies in terms of the normalized average spectral efficiency.

In Figure 3.6(b), we evalaute the spectral efficiency performance under different mean azimuth AoD estimation errors in narrowband channels. Denoting by $\boldsymbol{H}_{\text{TR}}[k] = \boldsymbol{W}_{\text{RF}}^* \boldsymbol{H}[k] \boldsymbol{F}_{\text{RF}}$, the conventional spectral efficiency metric is

$$R_{\text{conv}} = \frac{1}{N} \sum_{k=0}^{N-1} \log_2 \det \left(\boldsymbol{I}_{N_{\text{S}}} + \frac{\gamma}{N_{\text{S}}} \boldsymbol{H}_{\text{TR}}[k] \boldsymbol{H}_{\text{TR}}^*[k] \right). \qquad (3.56)$$

The transmit and receive steering vectors in $\boldsymbol{F}_{\text{RF}}$ and $\boldsymbol{W}_{\text{RF}}$ exhibit the same structures as the transmit and receive array response vectors, and they steer towards the estimated angles acting as the spatial matched filters. In this

example, when constructing $\boldsymbol{F}_{\mathrm{RF}}$ and $\boldsymbol{W}_{\mathrm{RF}}$, the channel's elevation AoD and AoA are estimated via the proposed algorithm, while the azimuth AoD is selected to achieve the target mean azimuth AoD estimation error for a given channel realization. Here, $N_{\mathrm{RF}} = M_{\mathrm{RF}} = 1$ is assumed with single-stream transmission, i.e., $N_{\mathrm{S}} = 1$. Further $N = 1$ due to the narrowband assumption. It can be observed from Figure 3.6(b) that the angle estimation error has great impact on the spectral efficiency performance especially when large antenna arrays, and therefore, narrow beams are employed for data communications. For $0 \sim 5$ degrees mean angle estimation error, the performance degradation in contrast to 0 degree mean angle estimation error is negligible even with $N_{\mathrm{tot}} = 16$. With increase in the mean angle estimation error, the spectral efficiency performance is significantly degraded. For instance, with 20 degrees mean angle estimation error, the spectral efficiency drops from ~ 10 bps/Hz to ~ 3 bps/Hz with $N_{\mathrm{tot}} = 16$.

3.6.2 Wideband multi-path angle estimation using multiple RF chains with dual-polarization

In this part of simulation, we implement the statistical mmWave channel model developed in [71] using the NYUSIM open source platform V1.5. We consider the urban micro-cellular (UMi) scenario with NLOS components for the 28 GHz carrier frequency. We evaluate both 125 MHz and 250 MHz RF bandwidths with $N = 512$ and $N = 1024$ subcarriers. The corresponding CP lengths are $D = 64$ and $D = 256$. We set the subcarrier spacing and symbol duration as 270 KHz and 3.7 us following the numerology provided in [1].

One probing with N_{RF} simultaneously formed transmit beams corresponds to one OFDM symbol duration. We model the channel as a clustered channel where each cluster comprises several subpaths. Detailed channel modeling parameters including the distributions of clusters, subpaths in each cluster, azimuth/elevation AoD and AoA, the corresponding root-mean-square delay spreads and etc. are given in [71, TABLE III]. We use the ZC sequences for the construction of the multi-layer pilot signals. The root indices for generating the first-layer auxiliary beam pair specific ZC sequences are chosen from $\{1, 2, \cdots, N-1\}$, and they are pairwise primes with respect to $N-1$. We set the actual lengths of the ZC sequence as 511 and 1023 corresponding to the 125 MHz and 250 MHz bandwidths with the IFFT sizes of 512 and 1024, and the direct current (DC) subcarrier as zero. We configure the frequency circular shift spacing p as 6 for the construction of the second-layer ZC-based pilot signals.

In Figure 3.7(a), we evaluate the normalized average spectral efficiency performance for 125 MHz bandwidth with 512 subcarriers using both auxiliary beam pair and grid-of-beams based angle estimation methods. We set the angle mismatch and power imbalance as $\zeta = 20°$ and $\chi = 0.2$. Further, we assume $M_{\mathrm{tot}} = 8$ and $N_{\mathrm{tot}} = 64$ with $N_{\mathrm{x}} = 4$ and $N_{\mathrm{y}} = 8$ antenna elements on the x and y axes for each polarization domain. Denote the total number of coherence time slots for both the channel estimation and data communications by T_{tot}, and the numbers of time slots used for auxiliary beam pair and grid-of-beams based angle estimation methods by $T_{\mathrm{est}}^{\mathrm{ABP}}$ and $T_{\mathrm{est}}^{\mathrm{GoB}}$. We

100

then define the normalized average spectral efficiency as $(1 - T_{\mathrm{est}}^{\mathrm{ABP}}/T_{\mathrm{tot}})R_{\mathrm{conv}}$ and $(1 - T_{\mathrm{est}}^{\mathrm{GoB}}/T_{\mathrm{tot}})R_{\mathrm{conv}}$ for the proposed approach and grid-of-beams based design in wideband channels. Here, $\boldsymbol{F}_{\mathrm{RF}}$ and $\boldsymbol{W}_{\mathrm{RF}}$ in R_{conv} (i.e., (3.56)) are constructed using the exact azimuth/elevation AoD and AoA for the perfect case, and estimated ones for the proposed algorithm and grid-of-beams based method. Without estimating other channel parameters such as the path gain in this chapter, the constructions of the baseband precoding and combining matrices are not included in evaluating the normalized average spectral efficiency performance. With the complete channel information, the hybrid precoding/combining matrices can be further optimized using the proposed methods in [72]. We now interpret $T_{\mathrm{est}}^{\mathrm{ABP}}$ and $T_{\mathrm{est}}^{\mathrm{GoB}}$ using the number of iterations between the BS and UE for the proposed method and grid-of-beams based approach. As has been reported in [13], the computational complexity for the grid-of-beams based method is $E_{\mathrm{GoB}} = (N_{\mathrm{BM}})^{N_{\mathrm{RF}}} (M_{\mathrm{BM}})^{M_{\mathrm{RF}}}$, where N_{BM} and M_{BM} are the total numbers of candidate transmit and receive beams in the beam codebooks. Recall that for the proposed approach, the computational complexity is $E_{\mathrm{ABP}} = N_{\mathrm{RF}} N_{\mathrm{TX}} M_{\mathrm{RF}} M_{\mathrm{RX}}$ for the multi-RF case. Denote the maximum number of iterations between the BS and UE that can be supported in each time slot by ϵ_t. We then have $T_{\mathrm{est}}^{\mathrm{GoB}} = \lceil E_{\mathrm{GoB}}/\epsilon_t \rceil$ and $T_{\mathrm{est}}^{\mathrm{ABP}} = \lceil E_{\mathrm{ABP}}/\epsilon_t \rceil$. Here, we set $\epsilon_t = 1000$ and $T_{\mathrm{tot}} = 200$. Further, we set $N_{\mathrm{BM}} = 10$ and $M_{\mathrm{BM}} = 4$ for the array size assumed above to cover the given angular ranges. Regarding $N_{\mathrm{S}} = N_{\mathrm{RF}} = M_{\mathrm{RF}} = \{2, 3\}$, we set $N_{\mathrm{TX}} = \{20, 30\}$ and $M_{\mathrm{RX}} = \{20, 25\}$ for the proposed method. With different numbers of data

streams N_S, it can be observed from Figure 3.7(a) that the auxiliary beam pair based method shows superior performance relative to the grid-of-beams based approach in terms of the normalized average spectral efficiency performance especially with relatively large N_S.

We can obtain similar observations from Figure 3.7(b), in which we evaluate the normalized spectral efficiency performance for 250 MHz bandwidth with 1024 subcarriers and $N_\text{S} = 3$ under various values of T_tot. It can be observed from Figure 3.7(b) that for a relatively small T_tot, the performance gap between the grid-of-beams based approach and the proposed method is significant as a large portion of T_tot is occupied for angle estimation in the GoB based approach.

In Figure 3.8, we examine the effects of mismatched angle and power imbalance on the proposed design approach in terms of the spectral efficiency calculated using (3.56). The main focus of the simulation plots provided in Figures 3.8(a) and 3.8(b) is to verify the robustness of the proposed algorithm with respect to various mismatched angle and power imbalance assumptions. It can be observed from Figure 3.8(a) that for different mismatched angles between the BS and UE antenna arrays, the performance gap between applying the proposed approach and that with perfect channel directional information is marginal. In Figure 3.8(b), we plot the spectral efficiency versus various power imbalance values. Similar to Figure 3.8(a), the proposed auxiliary beam pair design is robust to variations in the power imbalance.

3.7 Conclusion

In this chapter, we developed and evaluated an auxiliary beam pair based two-dimensional AoD and AoA estimation algorithm for wideband channels with dual-polarization. In the proposed design approach, by leveraging the well structured pairs of transmit/receive analog beams, high-resolution estimates of channel directional information can be obtained. We exposed several tradeoffs in our design including the mapping between the auxiliary beam pair and polarization, pilot design and feedback strategy. To minimize the estimation overhead, we further proposed to form the vertical/horizontal auxiliary beams to cover one half of the entire probing range without exploiting the polarization diversity.

To evaluate our approach, we presented numerical results in a more elaborate clustered channel, in which each cluster comprises several paths and the path/sub-path parameters are specified for mmWave frequencies, though we developed the algorithm using a simplified spatial geometric channel model. As the main focus of the proposed method is to provide super-resolution angle estimates for mmWave communications, we first presented the MAEE performance under various system assumptions. At relatively high SNR, our proposed approach outperformed the conventional GoB based method by several orders of degree in terms of the MAEE. By accounting for the estimation overhead, we also provided the normalized spectral efficiency performance. It can be observed from the normalized spectral efficiency evaluation that the GoB assisted angle estimation exhibited significantly larger estimation overhead

than the proposed method, which in turn, degraded the normalized spectral efficiency performance.
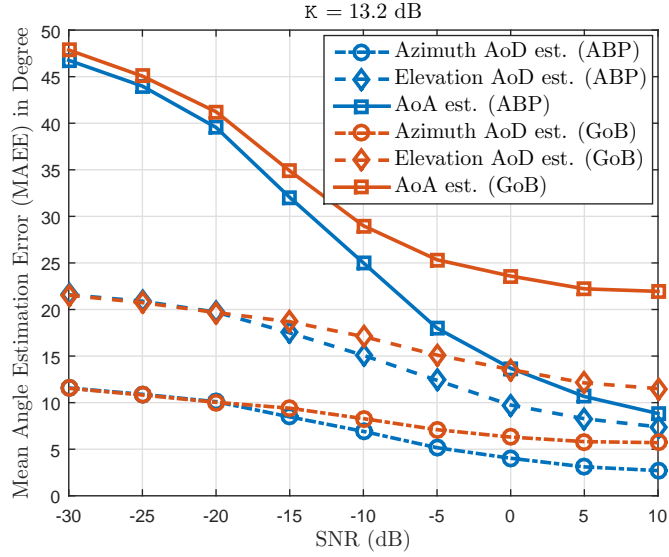
(a)
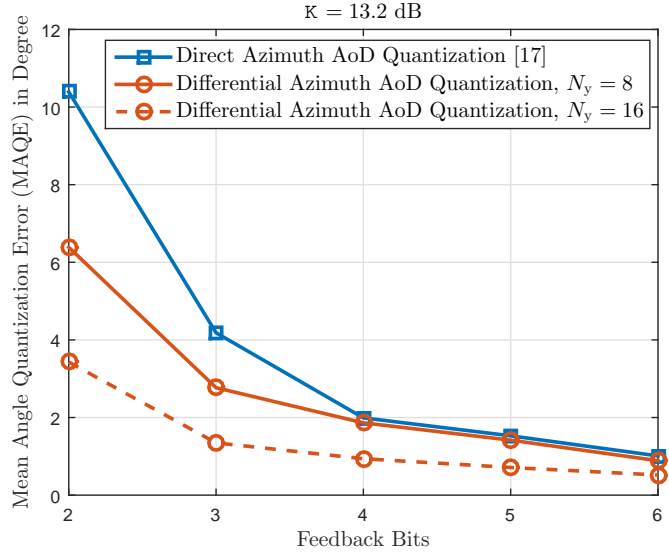
(b)

Figure 3.5: (a) MAEE performance of azimuth/elevation AoD and AoA estimation using the proposed auxiliary beam pair (ABP) and grid-of-beams (GoB) based methods. (b) Mean angle quantization error (MAQE) performance of quantizing the azimuth AoD using direct quantization in Chapter 2 and the newly proposed differential quantization.
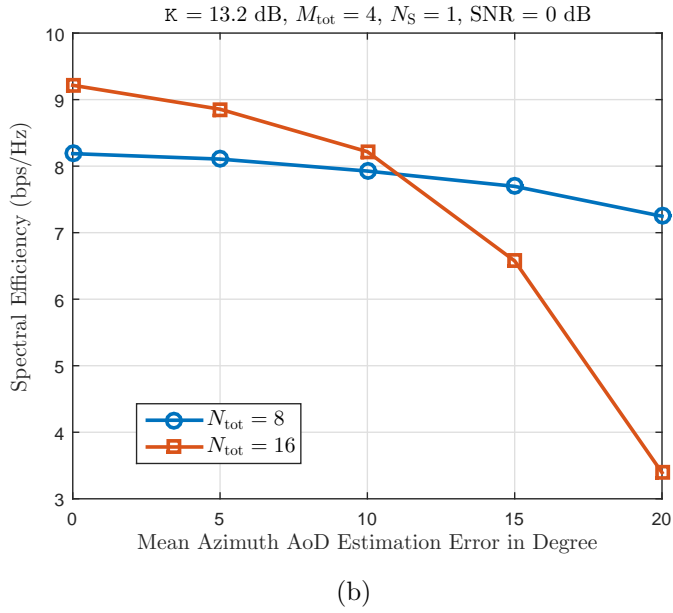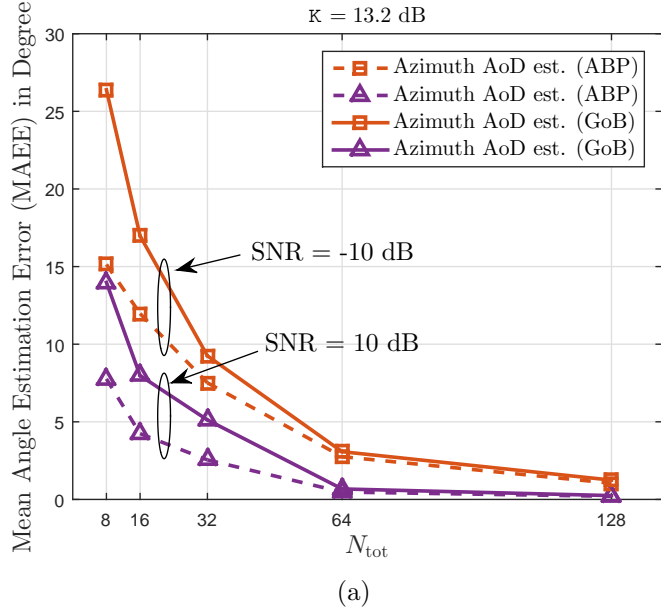
Figure 3.6: (a) Mean angle estimation error (MAEE) performance of azimuth AoD estimation using the proposed auxiliary beam pair (ABP) and grid-of-beams (GoB) based methods under different numbers of transmit antennas. (b) Spectral efficiency performance versus mean azimuth AoD estimation error.
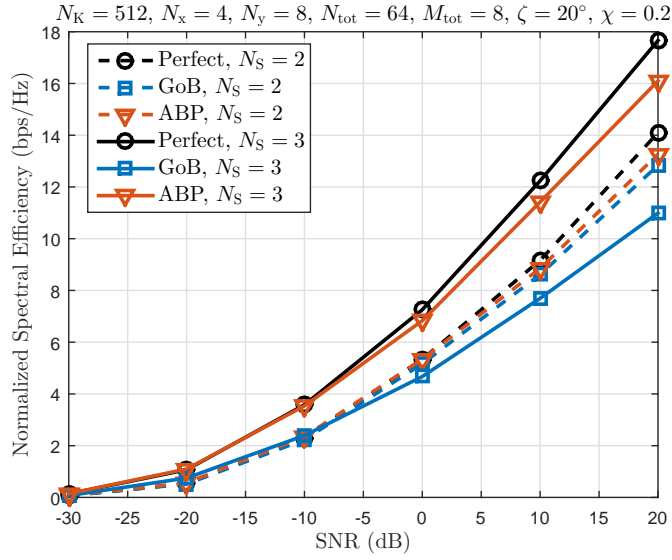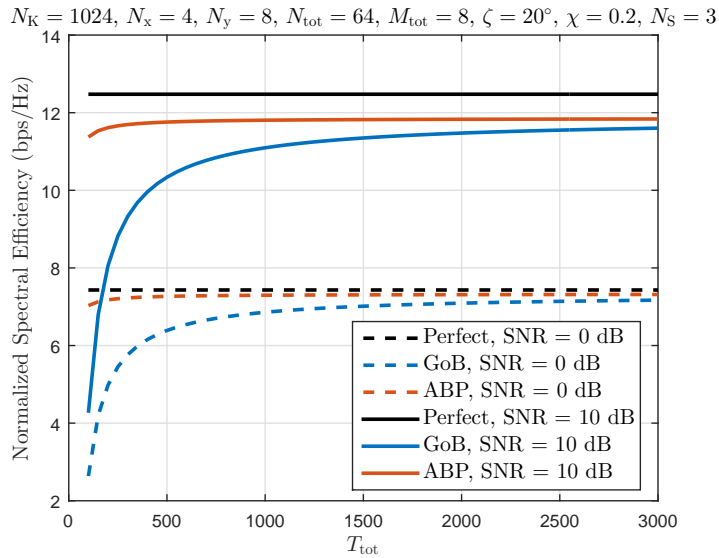
Figure 3.7: (a) Normalized average spectral efficiency of multi-layer transmission ($N_\mathrm{S} = 2, 3$) for 125 MHz bandwidth at various SNR levels. (b) Normalized average spectral efficiency of multi-layer transmission ($N_\mathrm{S} = 3$) for 250 MHz bandwidth at various SNR levels with different overheads.

$N_K = 512, N_x = 4, N_y = 8, N_{tot} = 64, M_{tot} = 8, \chi = 0.2$

(a)

$N_K = 512, N_x = 4, N_y = 8, N_{tot} = 64, M_{tot} = 8, \zeta = 20°$

(b)
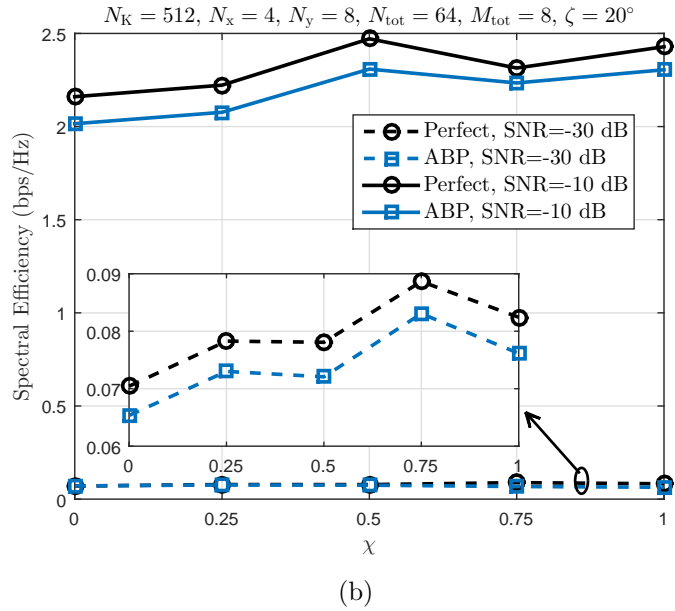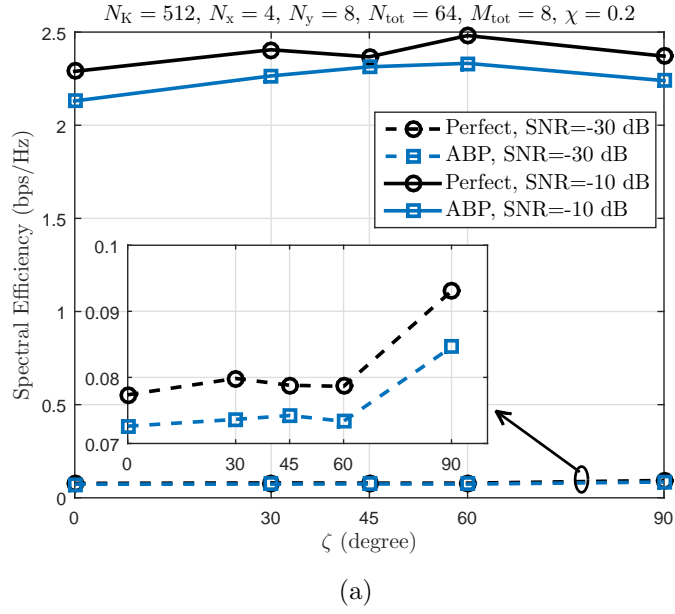
Figure 3.8: The robustness of the proposed technique to the angle mismatch and power imbalance in dual-polarized MIMO is examined in terms of the spectral efficiency performance. (a) Spectral efficiency for 125 MHz bandwidth regarding various mismatched angles. (b) Spectral efficiency for 125 MHz bandwidth regarding various power imbalance values.

Chapter 4

Angle Tracking in Mobile MmWave Systems with Antenna Array Calibration

In this chapter, we propose and evaluate several high-resolution angle tracking strategies for wideband mmWave systems with mobility. We custom design pairs of auxiliary beams as the tracking beams, and use them to capture fast angle variations, towards which the steering directions of the data beams are adjusted. We explain the detailed design procedure along with discussion on potential feedback strategies. We examine the impact of phase and amplitude errors on the proposed methods and show that the auxiliary beam pair structure is sensitive to these impairments. We also design a receive combining based array calibration method to compensate for the phase and amplitude errors. Via numerical examples, we show that the proposed angle tracking designs can still achieve promising tracking performances with calibrated radiation patterns. This work was published in [44].

4.1 Prior Work and Motivation

Grid-of-beams based beam training is the defacto approach for configuring transmit and receive beams; variations are used in IEEE 802.11ad

systems [14, 73] and will be used in 5G [74]. Beam tracking approaches that support grid-of-beams have been developed in [73], [14], [75] and [76], but the performance depends on the grid resolution, leading to high complexity, tracking overhead, and access delay. In [77, 78], a priori-aided angle tracking strategies were proposed. A temporal variation law of the AoD and AoA of the LOS path is first formed. By combining the temporal variation law with the sparse structure of the mmWave channels, the channels obtained during the previous time-slots are used to predict the support of the channel. The time-varying parameters corresponding to the support of the channel are then tracked for the subsequent time-slots. To track the NLOS paths, the classical Kalman filter can be employed by first eliminating the influence of the LOS path [79]. In [80], the idea of Kalman filter was exploited as well when designing the angle tracking and abrupt change detection algorithms. In [81], the extended Kalman filter was used to track the channel's AoDs and AoAs by only using the measurement of a single beam pair. The angle tracking algorithms developed in [77]-[81], however, depend on specific modeling of the geometric relationship between the BS and UE and the angle variations. Hence, there is a need for high-resolution angle/beam tracking designs that neither depend on any angle variation model nor require an on-grid assumption.

4.2 Contributions

In this chapter, we develop high-resolution angle tracking algorithms through the auxiliary beam pair design for mobile wideband mmWave systems

under the analog architecture. In the employed analog architecture, the BS uses a small number of RF chains to drive a large number of antenna elements, and forms the tracking beams in the analog domain. We propose and analyze new angle tracking procedure, where the basic principles follow those in Chapters 2 & 3 with moderate modifications based on the employed array configurations and pilot signal structures. In Chapters 2 & 3, we exploited the idea of auxiliary beam pair design to estimate both the narrowband and wideband mmWave channels with and without dual-polarization. The proposed approaches, however, were only applied to the angle estimation, and not specifically designed for the angle tracking. We summarize the main contributions of this chapter as follows:

- We provide detailed design procedure of the auxiliary beam pair-assisted angle tracking approaches in wideband mmWave systems. We propose several angle tracking design options and differentiate them in terms of triggering device, feedback information, and information required at the UE side.

- We reveal several important implementation aspects of deploying our proposed angle tracking algorithms in practical systems, including impacts of multi-user interference, multi-path interference and noise impairment on the tracking performances, and tracking sequences design for the auxiliary beam pair structure. We use conceptual and numerical examples to explain our proposed potential solutions in addressing these

issues. We also calculate the computational complexity and signaling overhead for the proposed designs.

- We characterize the impact of the radiation pattern impairments caused by the hardware flaw before and after the array calibration on our proposed methods. This hardware flaw is mainly brought by the antenna element tolerances and manufacturing inaccuracies, causing non-uniform amplitude and phase characteristics of the beam patterns. We first exhibit that relatively large phase and amplitude errors would contaminate the angle tracking performances of the proposed algorithms, resulting in increased tracking error probability and reduced spectral efficiency. We custom design a receive combining based array calibration method for the analog architecture. Note that since the radiation pattern impairments resulted from manufacturing inaccuracies/imperfections are long-term characteristics [82, Chapter 2], we focus on off-line array calibration in this chapter.

We organize the rest of this chapter as follows. In Section 4.3, we describe the employed frame structure and conventional grid-of-beams based beam tracking design for mmWave systems. In Section 4.4, we explain detailed design principles and procedures of the proposed high-resolution angle tracking strategies; we also address several important implementation issues of deploying the proposed algorithms in practice, such as computational complexity, signaling overhead, tracking sequence design and multi-user interference. In

Section 4.5, we discuss the developed array calibration method and its impact on the proposed angle tracking designs. In Section 4.6, we present numerical results to validate the effectiveness of the proposed techniques. Finally, we conclude this chapter in Section 4.7.

4.3   Frame Structure for Tracking

In Figure 4.1(a), we provide a potential frame structure. The time frame consists of three main components: channel estimation (ChEst), dedicated data channel (DDC), and dedicated tracking channel (DTC). The ChEst, DDC and DTC are composed of various numbers of time-slots. Here, we define the time-slot as the basic time unit, which is equivalent to, say, one OFDM symbol duration. We assume a total of T time-slots for one DTC. In the DDC, directional narrow beams are sent by the BS for high-rate data communications, while in the DTC, relatively wide beams are used to track the channel variations. In this chapter, the beams in the DTC and the DDC are multiplexed in the time-domain as shown in Figure 4.1(b). Further, the beam tracking in the DTC can be conducted in either a periodic or an aperiodic manner as shown in Figure 4.1(a). Based on the employed frame structure, we now illustrate the conventional grid-of-beams based beam tracking procedure for mmWave systems.

To reduce the computational complexity and tracking overhead, the beams in the DTC are formed surrounding the beam in the DDC in the angular domain. For simplicity, we first denote the beam in the DDC by anchor beam

113

and the beams in the DTC by backup beams. For a given DTC, the received signal strengths of the anchor and backup beams are measured by the UE and fed back to the BS. If the received signal strength of a backup beam is greater than that of the anchor beam by a certain threshold, the beam training is executed within the probing range of the backup beams to update the steering direction of the anchor beam. Otherwise, the current beam in the DDC is continuously used for data communications until the next DTC is triggered. If the received signal strengths of all the beams in the DTC and DDC are below a given threshold, the complete beam training process as in the channel estimation phase [13, 14] will be conducted.

4.4 Angle Tracking for Mobile MmWave Systems

In this section, we first illustrate the employed beam-specific pilot signal structure for the proposed tracking algorithms. Based on the employed shared-array architecture in Chapter 1, we then explain the design principles of the proposed high-resolution angle tracking approaches assuming the beam-specific pilot signal structure. Further, we present the detailed design procedure for the proposed algorithms along with the discussion of various feedback strategies. Further, we develop both code-division multiplexing (CDM) and TDM based methods to mitigate the multi-user interference in tracking channels. For practical implementation, we derive the computational complexity and signaling overhead for our proposed algorithms. Unless otherwise specified, we explain the proposed angle tracking strategies in the azimuth domain

assuming given elevation AoDs and AoAs. Note that the proposed algorithms can be directly extended to the tracking of the elevation directions.

4.4.1 Design principles of proposed angle tracking approaches

The design focus of the proposed angle tracking approaches is to first obtain high-resolution angle estimates, and then track the angle variations via the custom designed tracking beams. We employ the same frame structure as in Figure 4.1(a), where the tracking beams are sent during the DTC. In this part, we provide an overview of the auxiliary beam pair-assisted high-resolution angle estimation design for wideband mmWave systems. For simplicity, we focus on the estimation of the azimuth AoDs at the receiver.

Each auxiliary beam pair comprises two successively formed analog beams in the angular domain. Pairs of custom designed analog transmit and receive beams are probed to cover the given angular ranges. In this chapter, the two analog beams in the same auxiliary beam pair are formed simultaneously by the BS, and are differentiated by the beam-specific pilot signals at the UE side. For instance, to form an azimuth transmit auxiliary beam pair, the two analog beamforming vectors targeted at the directions of $\eta_{\mathrm{az}} - \delta_{\mathrm{y}}$ and $\eta_{\mathrm{az}} + \delta_{\mathrm{y}}$ in the azimuth domain are $\boldsymbol{a}_{\mathrm{t}}(\eta_{\mathrm{el}}, \eta_{\mathrm{az}} - \delta_{\mathrm{y}})$ and $\boldsymbol{a}_{\mathrm{t}}(\eta_{\mathrm{el}}, \eta_{\mathrm{az}} + \delta_{\mathrm{y}})$ respectively, where $\delta_{\mathrm{y}} = \frac{2\ell_{\mathrm{y}}\pi}{N_{\mathrm{y}}}$ with $\ell_{\mathrm{y}} = 1, \cdots, \frac{N_{\mathrm{y}}}{4}$ and η_{el} corresponds to a given elevation direction. Now, we illustrate the employed pilot signal structure.

Due to the constant amplitude and the robustness to the frequency selectivity, we use ZC-type sequences in this chapter as the pilot signals for

tracking. Denoting the sequence length by N_{ZC}, the employed ZC sequence with root index i_z is

$$s_{i_z}[m] = \exp\left(-\text{j}\frac{\pi m(m+1)i_z}{N_{\text{ZC}}}\right), \tag{4.1}$$

where $m = 0, \cdots, N_{\text{ZC}} - 1$. Here, we let $N_{\text{ZC}} = N$ (i.e., the total number of employed subcarriers) and $z = 0, 1$ such that i_0 and i_1 correspond to the two beams in the same auxiliary beam pair. By cross correlating two ZC sequences at zero-lag, we can obtain [67]

$$\sum_{k=0}^{N-1} s_{i_0}[k]s_{i_1}^*[k] = \begin{cases} 1, & \text{if } i_0 = i_1 \\ \beta_{i_0,i_1}, & \text{otherwise.} \end{cases} \tag{4.2}$$

Here, β_{i_0,i_1} is a constant, corresponding to $1/\sqrt{N_{\text{ZC}}}$. For relatively large sequence length N_{ZC}, $|\beta_{i_0,i_1}| \approx 0$. In this chapter, we assume $\beta_{i_0,i_1} = 0$ for better illustration of the proposed methods. For a relatively small sequence length N_{ZC}, this approximated code-domain orthogonality condition may not hold, resulting in significant inter-beam interference. To counter this challenge, the BS can send the two beams in the same auxiliary beam pair in a round-robin TDM manner. In contrast to simultaneous transmission, the TDM approach can eliminate the inter-beam interference, but may introduce extra access delay to the system. Note that the selection of appropriate sequence length N_{ZC} also depends on the channel condition, which will be elaborated later in this section. In practical systems, the RF impairments such as the I/Q imbalance and power amplifier nonlinearities would distort the received ZC sequence samples, resulting in degraded correlation performance. In this chapter, we ignore

these impairments in the employed system model as they do not affect the key design principles of our proposed tracking strategies.

Based on the employed pilot signal structure, we now explain the design principles of the auxiliary beam pair-assisted angle acquisition. Assume $M_{\mathrm{RF}} = 1$ and a given analog receive beam, say, $\boldsymbol{a}_{\mathrm{r}}(\vartheta)$. According to the employed array configurations and the pilot signal structure, we can then rewrite (3.1) in the absence of noise as

$$y[k] = \boldsymbol{a}_{\mathrm{r}}^*(\vartheta) \sum_{r=1}^{N_{\mathrm{r}}} g_r \rho_{\tau_r}[k] \boldsymbol{a}_{\mathrm{r}}(\nu_r) \boldsymbol{a}_{\mathrm{t}}^*(\theta_r, \psi_r) \left[\begin{array}{cc} \boldsymbol{a}_{\mathrm{t}}(\eta_{\mathrm{el}}, \eta_{\mathrm{az}} - \delta_{\mathrm{y}}) & \boldsymbol{a}_{\mathrm{t}}(\eta_{\mathrm{el}}, \eta_{\mathrm{az}} + \delta_{\mathrm{y}}) \end{array} \right]$$
$$\times \left[\begin{array}{c} s_{i_0}[k] \\ s_{i_1}[k] \end{array} \right]. \tag{4.3}$$

Our design focus here is to estimate the azimuth transmit spatial frequency $\psi_{r^\star}$ for path-$r^\star$ with $r^\star \in \{1, \cdots, N_{\mathrm{r}}\}$. We first assume that $\psi_{r^\star}$ falls into the probing range of the auxiliary beam pair such that $\psi_{r^\star} \in (\eta_{\mathrm{az}} - \delta_{\mathrm{y}}, \eta_{\mathrm{az}} + \delta_{\mathrm{y}})$. We can then rewrite (4.3) as

$$y[k] = \boldsymbol{a}_{\mathrm{r}}^*(\vartheta) g_{r^\star} \rho_{\tau_{r^\star}}[k] \boldsymbol{a}_{\mathrm{r}}(\nu_{r^\star}) \boldsymbol{a}_{\mathrm{t}}^*(\theta_{r^\star}, \psi_{r^\star}) \left[\begin{array}{cc} \boldsymbol{a}_{\mathrm{t}}(\eta_{\mathrm{el}}, \eta_{\mathrm{az}} - \delta_{\mathrm{y}}) & \boldsymbol{a}_{\mathrm{t}}(\eta_{\mathrm{el}}, \eta_{\mathrm{az}} + \delta_{\mathrm{y}}) \end{array} \right]$$
$$\times \left[\begin{array}{c} s_{i_0}[k] \\ s_{i_1}[k] \end{array} \right]$$
$$+ \boldsymbol{a}_{\mathrm{r}}^*(\vartheta) \sum_{\substack{r'=1, \\ r' \neq r^\star}}^{N_{\mathrm{r}}} g_{r'} \rho_{\tau_{r'}}[k] \boldsymbol{a}_{\mathrm{r}}(\nu_{r'}) \boldsymbol{a}_{\mathrm{t}}^*(\theta_{r'}, \psi_{r'})$$
$$\times \left[\begin{array}{cc} \boldsymbol{a}_{\mathrm{t}}(\eta_{\mathrm{el}}, \eta_{\mathrm{az}} - \delta_{\mathrm{y}}) & \boldsymbol{a}_{\mathrm{t}}(\eta_{\mathrm{el}}, \eta_{\mathrm{az}} + \delta_{\mathrm{y}}) \end{array} \right] \left[\begin{array}{c} s_{i_0}[k] \\ s_{i_1}[k] \end{array} \right]. \tag{4.4}$$

In this chapter, we focus on tracking the variations of the steering angle of the data beam, which is $\psi_{r^\star}$ in this example. To reduce the implementation

complexity and improve the tracking accuracy, narrow tracking beams are formed, closely surrounding the steering angle of the data beam. The resulted effective beam-space channels therefore contain few paths/clusters, though the general mmWave channels may have many rays in the entire angular domain according to the channel modeling progress in the 3GPP [83] and channel measurement campaigns [84, 85]. For instance, denote the angular coverage of the auxiliary beam pair $\{a_{\mathrm{t}}(\eta_{\mathrm{el}}, \eta_{\mathrm{az}} - \delta_{\mathrm{y}}), a_{\mathrm{t}}(\eta_{\mathrm{el}}, \eta_{\mathrm{az}} + \delta_{\mathrm{y}})\}$ in (4.4) by Ξ_{y}. For relatively large number of transmit antennas, it becomes highly likely that only the steering angle of the data beam, i.e., $\psi_{r^{\star}}$ is within Ξ_{y}, and other paths' spatial frequencies $\psi_{r'} \notin \Xi_{\mathrm{y}}$ for $r' \in \{1, \cdots, N_{\mathrm{r}}\}$ and $r' \neq r^{\star}$. In this case, the multi-path interference would become negligible, and the received signal in (4.4) can be approximated to

$$
\begin{aligned}
y[k] \approx & g_{r^{\star}} \rho_{\tau_{r^{\star}}}[k] a_{\mathrm{r}}^{*}(\vartheta) a_{\mathrm{r}}(\nu_{r^{\star}}) a_{\mathrm{t}}^{*}(\theta_{r^{\star}}, \psi_{r^{\star}}) \left[\begin{array}{cc} a_{\mathrm{t}}(\eta_{\mathrm{el}}, \eta_{\mathrm{az}} - \delta_{\mathrm{y}}) & a_{\mathrm{t}}(\eta_{\mathrm{el}}, \eta_{\mathrm{az}} + \delta_{\mathrm{y}}) \end{array} \right] \\
& \times \left[\begin{array}{c} s_{i_0}[k] \\ s_{i_1}[k] \end{array} \right] .
\end{aligned}
\tag{4.5}
$$

Note that we can extend the algorithm to separately estimate multiple paths in parallel.

Assuming perfect time-frequency synchronization, the UE employs locally stored reference beam-specific sequences to correlate the received signal samples. By using the reference ZC sequence with the sequence root index i_0,

we can first obtain

$$\Lambda_{\text{az}}^{\Delta} = \sum_{k=0}^{N-1} s_{i_0}^*[k]y[k] \tag{4.6}$$

$$= \sum_{k=0}^{N-1} g_{r^\star}\rho_{\tau_{r^\star}}[k]\boldsymbol{a}_{\text{r}}^*(\vartheta)\boldsymbol{a}_{\text{r}}(\nu_{r^\star})\boldsymbol{a}_{\text{t}}^*(\theta_{r^\star},\psi_{r^\star})\boldsymbol{a}_{\text{t}}(\eta_{\text{el}},\eta_{\text{az}}-\delta_{\text{y}})s_{i_0}^*[k]s_{i_0}[k]$$

$$+ \sum_{k=0}^{N-1} g_{r^\star}\rho_{\tau_{r^\star}}[k]\boldsymbol{a}_{\text{r}}^*(\vartheta)\boldsymbol{a}_{\text{r}}(\nu_{r^\star})\boldsymbol{a}_{\text{t}}^*(\theta_{r^\star},\psi_{r^\star})\boldsymbol{a}_{\text{t}}(\eta_{\text{el}},\eta_{\text{az}}+\delta_{\text{y}})s_{i_0}^*[k]s_{i_1}[k].$$

$$\tag{4.7}$$

We assume flat channels here such that $\bar{\rho}_{\tau_{r^\star}} = \rho_{\tau_{r^\star}}[0] = \cdots = \rho_{\tau_{r^\star}}[N-1]$ for better illustration of the design principles. The proposed design approach can still achieve promising angle estimation/tracking performance in wideband channels since the correlation properties of the ZC-type sequences are robust to the frequency selectivity (e.g., up to 8.6 MHz continuous bandwidth in LTE [86]). We can then rewrite (4.7) as

$$\Lambda_{\text{az}}^{\Delta} = g_{r^\star}\boldsymbol{a}_{\text{r}}^*(\vartheta)\boldsymbol{a}_{\text{r}}(\nu_{r^\star})\boldsymbol{a}_{\text{t}}^*(\theta_{r^\star},\psi_{r^\star})\boldsymbol{a}_{\text{t}}(\eta_{\text{el}},\eta_{\text{az}}-\delta_{\text{y}})\bar{\rho}_{\tau_{r^\star}}\sum_{k=0}^{N-1} s_{i_0}^*[k]s_{i_0}[k]$$

$$+ g_{r^\star}\boldsymbol{a}_{\text{r}}^*(\vartheta)\boldsymbol{a}_{\text{r}}(\nu_{r^\star})\boldsymbol{a}_{\text{t}}^*(\theta_{r^\star},\psi_{r^\star})\boldsymbol{a}_{\text{t}}(\eta_{\text{el}},\eta_{\text{az}}+\delta_{\text{y}})\bar{\rho}_{\tau_{r^\star}}\sum_{k=0}^{N-1} s_{i_0}^*[k]s_{i_1}[k]$$

$$\stackrel{(a)}{=} g_{r^\star}\bar{\rho}_{\tau_{r^\star}}\boldsymbol{a}_{\text{r}}^*(\vartheta)\boldsymbol{a}_{\text{r}}(\nu_{r^\star})\boldsymbol{a}_{\text{t}}^*(\theta_{r^\star},\psi_{r^\star})\boldsymbol{a}_{\text{t}}(\eta_{\text{el}},\eta_{\text{az}}-\delta_{\text{y}}), \tag{4.8}$$

where (a) is due to the employed beam-specific pilot signal structure in (5.2). We compute the corresponding received signal strength as $\chi_{\text{az}}^{\Delta} = \left(\Lambda_{\text{az}}^{\Delta}\right)^* \Lambda_{\text{az}}^{\Delta}$. Similarly, using the ZC sequence with the root index i_1 to correlate the received signal samples, we obtain

$$\Lambda_{\text{az}}^{\Sigma} = \sum_{k=0}^{N-1} s_{i_1}^*[k]y[k] = g_{r^\star}\bar{\rho}_{\tau_{r^\star}}\boldsymbol{a}_{\text{r}}^*(\vartheta)\boldsymbol{a}_{\text{r}}(\nu_{r^\star})\boldsymbol{a}_{\text{t}}^*(\theta_{r^\star},\psi_{r^\star})\boldsymbol{a}_{\text{t}}(\eta_{\text{el}},\eta_{\text{az}}+\delta_{\text{y}}). \tag{4.9}$$

119

We can calculate the corresponding received signal strength as $\chi^\Sigma_{\mathrm{az}} = \left(\Lambda^\Sigma_{\mathrm{az}}\right)^* \Lambda^\Sigma_{\mathrm{az}}$. We define the ratio metric as $\zeta_{\mathrm{az}} = (\chi^\Delta_{\mathrm{az}} - \chi^\Sigma_{\mathrm{az}})/(\chi^\Delta_{\mathrm{az}} + \chi^\Sigma_{\mathrm{az}})$. According to [41, Lemma 1], if $|\psi_{r^\star} - \eta_{\mathrm{az}}| < \delta_{\mathrm{y}}$, then the azimuth transmit spatial frequency $\psi_{r^\star}$ is within the range of $(\eta_{\mathrm{az}} - \delta_{\mathrm{y}}, \eta_{\mathrm{az}} + \delta_{\mathrm{y}})$, and ζ_{az} is a monotonically decreasing function of $\psi_{r^\star} - \eta_{\mathrm{az}}$ and invertible with respect to $\psi_{r^\star} - \eta_{\mathrm{az}}$. Via the inverse function, we can therefore derive the estimated value of $\psi_{r^\star}$ as

$$\hat{\psi}_{r^\star} = \eta_{\mathrm{az}} - \arcsin\left(\frac{\zeta_{\mathrm{az}}\sin(\delta_{\mathrm{y}}) - \zeta_{\mathrm{az}}\sqrt{1 - \zeta^2_{\mathrm{az}}}\sin(\delta_{\mathrm{y}})\cos(\delta_{\mathrm{y}})}{\sin^2(\delta_{\mathrm{y}}) + \zeta^2_{\mathrm{az}}\cos^2(\delta_{\mathrm{y}})}\right). \qquad (4.10)$$

If ζ_{az} is perfect, i.e., not impaired by noise and other types of interference, we can perfectly recover the azimuth transmit spatial frequency for path-$r^\star$, i.e., $\psi_{r^\star} = \hat{\psi}_{r^\star}$.

In Section 4.4.2, we restrict to the tracking of path-$r^\star$'s azimuth AoD. To better reveal the temporal evolution, we use $\psi_{r^\star,t}$ instead of $\psi_{r^\star}$ to represent path-$r^\star$'s azimuth transmit spatial frequency for a given time-slot $t \in \{0, \cdots, T-1\}$ in the DTC.

4.4.2 Design procedure of proposed angle tracking approaches

Leveraging the high-resolution angle estimates, we exploit the auxiliary beam pair design in forming tracking beams in the DTC. For example, we assume that one transmit auxiliary beam pair (e.g., $\boldsymbol{a}_{\mathrm{t}}(\eta_{\mathrm{el}}, \eta_{\mathrm{az}} - \delta_{\mathrm{y}})$ and $\boldsymbol{a}_{\mathrm{t}}(\eta_{\mathrm{el}}, \eta_{\mathrm{az}} + \delta_{\mathrm{y}})$) is formed during the DTC. The boresight angle of the auxiliary beam pair (e.g., η_{az}) is identical to the steering direction of the corresponding anchor beam in the DDC. In the following, we first illustrate the general framework of the proposed angle tracking designs.

In Figure 4.2, we provide the relationship between the UE's moving trajectory and the tracking beams in the DTC. At time-slot 0, the anchor beam in the DDC with the azimuth boresight angle $\eta_{\text{az},0}$ steers towards the UE of interest. One azimuth transmit auxiliary beam pair is formed as the tracking beams in the DTC. For a given elevation direction $\eta_{\text{el},0}$, the corresponding two beams steer towards $\eta_{\text{az},0} - \delta_{\text{y}}$ and $\eta_{\text{az},0} + \delta_{\text{y}}$ with the boresight angle $\eta_{\text{az},0}$ in the azimuth domain. As can be seen from the conceptual example shown in Figure 4.2, at time-slots $1, \cdots, T-1$, the UE of interest moves away from the original azimuth position $\psi_{r^\star,0}$ (or $\eta_{\text{az},0}$) to $\psi_{r^\star,1}, \cdots, \psi_{r^\star,T-1}$. Note that as long as $\psi_{r^\star,1}, \cdots, \psi_{r^\star,T-1}$ are in the probing range of the tracking beams, they are expected to be accurately tracked according to the design principles of the auxiliary beam pair.

In the proposed methods, either the BS or the UE can trigger the angle tracking process, which are referred to as BS-driven or UE-driven angle tracking methods. For both the BS-driven and UE-driven angle tracking strategies, either a periodic or aperiodic DTC design can be adopted. Further, for the proposed BS-driven angle tracking, no prior knowledge of the auxiliary beam pair setup is required at the UE side. In the following two parts, we first present the detailed design procedure of the proposed methods and illustrate the employed direct and differential feedback strategies; we then develop potential solutions to reduce the multi-user interference in tracking channels.

4.4.2.1 BS/UE-driven angle tracking design with direct and differential ratio metric feedback

We start by illustrating the BS-driven angle tracking strategy using the direct ratio metric feedback. For a given time-slot $t \in \{0, \cdots, T-1\}$ in the DTC, the corresponding ratio metric $\zeta_{\text{az},t}$ is calculated by the UE using the azimuth transmit auxiliary beam pair. First, we assume that the BS triggers the feedback of the derived ratio metric. For instance, considering a given DTC, if the BS requires the ratio metric feedback at time-slot $T-1$, $\zeta_{\text{az},T-1}$ is then quantized and sent back to the BS. In this case, time-slot $T-1$ is the last time-slot of a given DTC. Note that in practice, the BS may require the ratio metric feedback for multiple time-slots within the same DTC to track the fast-varying channels. It is therefore essential for the UE to keep computing the ratio metric for every time-slot in the DTC. Upon receiving the ratio metric feedback from the UE at time-slot t, the BS retrieves the corresponding angle estimate according to (4.10). Denoting the azimuth angle estimate at time-slot t by $\hat{\psi}_{r^\star,t}$, we have

$$\hat{\psi}_{r^\star,t} = \eta_{\text{az},0} - \arcsin\left(\frac{\zeta_{\text{az},t}\sin(\delta_{\text{y}}) - \zeta_{\text{az},t}\sqrt{1 - \zeta_{\text{az},t}^2}\sin(\delta_{\text{y}})\cos(\delta_{\text{y}})}{\sin^2(\delta_{\text{y}}) + \zeta_{\text{az},t}^2\cos^2(\delta_{\text{y}})} \right). \quad (4.11)$$

The angle difference $\Delta\psi_{r^\star,t} = \left| \psi_{r^\star,0} - \hat{\psi}_{r^\star,t} \right|$ is then calculated by the BS and compared with a predefined threshold ς_{az}. If $\Delta\psi_{r^\star,t} \geq \varsigma_{\text{az}}$, the azimuth steering direction of the anchor beam in the DDC is then updated from $\eta_{\text{az},0}$ to $\eta_{\text{az},t} = \hat{\psi}_{r^\star,t}$. Otherwise, the azimuth steering direction of the anchor beam in the DDC is kept unchanged from time-slot 0, i.e., $\eta_{\text{az},t} = \eta_{\text{az},0}$.

Different from the BS-driven strategy, the angle tracking process in the UE-driven method is triggered at the UE side. Here, the direct ratio metric feedback is still applied, but the feedback process is configured by the UE according to the received signal strength corresponding to the anchor beam in the DDC. We explain the design procedures of the UE-driven angle tracking approach with the direct ratio metric feedback in Algorithm 4.1. Note that in

---

Algorithm 4.1 UE-driven angle tracking design with direct feedback of the ratio metric

---

BS-side processing

1: For $t \in \{0, \cdots, T-1\}$, the BS forms the auxiliary beam pair(s) for angle tracking.

UE-side processing

2: The UE calculates the ratio metric $\zeta_{\mathrm{az},t}$, the received signal strengths γ_t and γ_0 of the DDCs at time-slots t and 0, and $\Delta\gamma_t = \gamma_t - \gamma_0$.

3: **If** $\Delta\gamma_t \geq \varrho_{\mathrm{az}}$

4:    The UE quantizes $\zeta_{\mathrm{az},t}$ and sends it back to the BS.

5: **Else**

6:    Start from step-1 for time-slot $t+1$.

7: **end If**

BS-side processing

8: The BS retrieves the channel's azimuth transmit spatial frequency $\hat{\psi}_{r^\star,t}$ according to (4.11).

9: The BS updates the azimuth steering direction of the data beam as $\eta_{\mathrm{az},t} = \hat{\psi}_{r^\star,t}$.

---

the proposed UE-driven angle tracking with the direct ratio metric feedback, no prior knowledge of the auxiliary beam pair setup is required at the UE side, while only the received signal strength of the anchor beam is deduced as the triggering performance metric. By exploiting the symmetric property of the ratio metric [43], the BS-driven and UE-driven differential ratio metric

feedback strategies can be similarly derived relative to the direct ratio metric feedback designs with moderate modifications on the tracking procedures.

Remark: Similar to the direct and differential ratio metric feedback methods, direct and differential angle feedback strategies can also be supported for the angle tracking designs, as long as necessary auxiliary beam pair setup is available at the UE side.

To compensate for the noise and other types of impairments, we can also form multiple identical auxiliary beam pairs to track a given angle's variations if the angle tracking is triggered. Upon receiving all the pilot signal samples, the UE can either average the received signal strengths or select the highest received signal strengths across all probings to derive the corresponding ratio metric. By exploiting this spreading gain from multiple probings/snapshots of the auxiliary beam pairs, we expect to improve the angle tracking performance especially with low SNR and high multi-path interference.

4.4.2.2   Multi-user interference between dedicated tracking channels (DTCs)

Having dedicated RFs for tracking reduces the spatial degrees-of-freedom to mitigate the multi-user interference (MUI) when different UEs share the same time and frequency resources. We consider a multi-user scenario, in which all UEs of interest are conducting angle tracking via the corresponding auxiliary beam pairs (dedicated tracking channels). We provide one conceptual example in Figure 4.3 to characterize this interference scenario and explain

124

our proposed solutions. As can be seen from Figure 4.3, if the UEs of interest are close to each other such that they are within the probing ranges of each other's auxiliary beam pairs, they would significantly interfere with each other if the same time-frequency resources are occupied and identical sequences are used. To mitigate the interference, we propose CDM and/or TDM based design approaches. We do not focus on frequency-division multiplexing (FDM) based strategy as the tracking beams are wideband and applied to all active subcarriers.

For CDM based design option, all simultaneously formed beams targeting for different UEs can embed distinct ZC sequences with different root indices. The number of such sequences, however, may not be enough to support a relatively large number of UEs in the network. To counter this problem, we develop an alternative CDM based approach by leveraging a custom designed hierarchical sequence structure. Here, we still employ the ZC-type sequences, and express the sequence structure as

$$s_{i_u,p_z}[m] = \exp\left(-\mathrm{j}\frac{\pi(m+p_z)(m+p_z+1)i_u}{N_{\mathrm{ZC}}}\right), \tag{4.12}$$

where $m = 0, \cdots, N_{\mathrm{ZC}} - 1$, i_u denotes the root index associated with a specific auxiliary beam pair that serves UE u, and p_z's ($z = 0, 1$) represent the circular shifts in the frequency domain, corresponding to the two beams in the same auxiliary beam pair. For instance, in Figure 4.3(a), the BS transmits the hierarchical sequences to the two UEs with the user indices, say #12 and #15 via the corresponding two auxiliary beam pairs. Assuming perfect time-frequency synchronization, UE #12 applies locally stored sequences $\boldsymbol{s}_{i_{12},p_0} =$

125

$\{s_{i_{12},p_0}[0], \cdots, s_{i_{12},p_0}[N_{\mathrm{ZC}} - 1]\}$ and $\boldsymbol{s}_{i_{12},p_1} = \{s_{i_{12},p_1}[0], \cdots, s_{i_{12},p_1}[N_{\mathrm{ZC}} - 1]\}$ to correlate the received signal samples and to derive the corresponding ratio metric. Similarly, UE #15 employs $\boldsymbol{s}_{i_{15},p_0} = \{s_{i_{15},p_0}[0], \cdots, s_{i_{15},p_0}[N_{\mathrm{ZC}} - 1]\}$ and $\boldsymbol{s}_{i_{15},p_1} = \{s_{i_{15},p_1}[0], \cdots, s_{i_{15},p_1}[N_{\mathrm{ZC}} - 1]\}$ to correlate the received signal samples. According to (5.2), the cross-correlation interference between UEs #12 and #15 can be minimized by choosing appropriate sequence length N_{ZC} and root indices i_{12} and i_{15}. For a given UE, the inter-beam interference (IBI) is subject to the correlation of two cyclically shifted ZC sequences with the same root index. This correlation is zero without incorporating noise and other impairments, but in practice it is subject to the maximum delay spread and Doppler shift of the channels [87].

In addition to the proposed CDM based design strategy, the MUI can also be mitigated if the BS performs angle tracking for different UEs in a TDM manner. We employ the example shown in Figure 4.3(b) to illustrate the procedure. As can be seen from Figure 4.3(b), the BS employs different time-slots to steer the auxiliary beam pairs towards UEs #12 and #15 for angle tracking. Obviously, there would be no interference between UE #12 and UE #15. The TDM strategy, however, would introduce extra access delay to the network in contrast to the code-domain approaches. For practical implementation, a hybrid approach of both CDM and TDM based strategies would be of design interest to mitigate the interference.

4.4.3 Computational complexity and signaling overhead

In this part, we first evaluate the implementation complexity of the proposed angle tracking algorithms. As the angle tracking does not involve extensive beam search as in the angle estimation phase, we focus on the number of complex arithmetic operations required at the UE. The complex arithmetic operation includes complex multiplication, division, addition and substraction. In the proposed angle tracking methods, the complex arithmetic operations are mainly resulted from correlating the received signal samples with reference ZC sequences. For a length-N_{ZC} ZC sequence, the number of complex arithmetic operations required to perform the zero-lag correlation is $2N_{ZC} - 1$. If a total of N_{ABP} auxiliary beam pairs are formed (we set $N_{ABP} = 1$ when deriving the design principle and procedure) in a DTC to enhance the angular coverage, this number becomes $2N_{ABP}(2N_{ZC} - 1)$. Further, assuming that a total of N_{DTC} DTCs are triggered for angle tracking, the number of complex arithmetic operations is $2N_{DTC}N_{ABP}(2N_{ZC} - 1)$.

In this chapter, we characterize the signaling overhead for tracking as the ratio between the number of OFDM symbols used for the DTCs (M_{DTC}) and the total number of symbols (M_{TOT}). We first assume that the beams in the auxiliary beam pairs are probed in the TDM manner. For a total of M_{ABP} auxiliary beam pairs, we can obtain $M_{DTC} = 2M_{ABP}$. We can then compute the corresponding overhead ratio as $2M_{ABP}/M_{TOT}$. For the CDM based design strategy, we have $M_{DTC} = M_{ABP}/N_{ABP}$, recalling that N_{ABP} is the number of simultaneously formed auxiliary beam pairs during one DTC.

127

In this case, we can derive the ratio as $M_{\text{ABP}}/N_{\text{ABP}}M_{\text{TOT}}$. Obviously, the CDM based method requires less signaling overhead than the TDM based strategy assuming the same M_{ABP}, but its tracking performance is subject to the inter-beam interference. For instance, if $M_{\text{TOT}} = 10^4$, $M_{\text{ABP}} = 100$ and $N_{\text{ABP}} = 1$, we can compute the corresponding signaling overhead as 1% for the CDM based design approach. This signaling overhead is similar to the frame timing synchronization design in LTE systems [86], in which one out of 70 OFDM symbols with normal CP length is used to carry the corresponding synchronization signal (1.4%). This 1% signaling overhead for tracking is equivalent to $\rho = 1\%$ assumed in the simulation section, which shows promising angle tracking performances under various deployment scenarios.

4.5 Impact of Radiation Pattern Impairments

Because of manufacturing inaccuracies, a variety of impairments such as geometrical and electrical tolerances cause non-uniform amplitude and phase characteristics of the individual antenna elements [88]. This results in phase and amplitude errors of the radiation patterns [89]. The angle tracking performance of the proposed auxiliary beam pair-assisted designs is subject to the radiation pattern impairments, which are neglected during the derivation of the ratio metric. If the radiation patterns of the beams in the auxiliary beam pair are impaired by the phase and amplitude errors, the monotonic and symmetric properties of the ratio metric may not hold, which in turn, results in large angle tracking errors. In the following, we first illustrate the impact

of the radiation pattern impairments on the proposed angle tracking designs. To calibrate the antenna array with the analog architecture, we custom design and evaluate an array calibration method. We then examine the impact of the residual calibration errors on the proposed angle tracking approaches.

4.5.1 Impact of phase and amplitude errors on proposed methods

Neglecting mutual coupling and matching effects, and denoting the phase and amplitude error matrices by $\boldsymbol{P}$ and $\boldsymbol{A}$, we have $\boldsymbol{P} = \mathrm{diag}\Big(\big[e^{\mathrm{j}p_0}, e^{\mathrm{j}p_1}, \cdots, e^{\mathrm{j}p_{N_{\mathrm{tot}}-1}}\big]^{\mathrm{T}}\Big)$ and $\boldsymbol{A} = \mathrm{diag}\Big(\big[a_0, a_1, \cdots, a_{N_{\mathrm{tot}}-1}\big]^{\mathrm{T}}\Big)$, where p_i and a_i correspond to the phase and amplitude errors on the i-th antenna element with $i = 0, \cdots, N_{\mathrm{tot}}-1$. Due to the UPA structure, we can decompose $\boldsymbol{P}$ and $\boldsymbol{A}$ as $\boldsymbol{P} = \boldsymbol{P}_{\mathrm{el}} \otimes \boldsymbol{P}_{\mathrm{az}}$ and $\boldsymbol{A} = \boldsymbol{A}_{\mathrm{el}} \otimes \boldsymbol{A}_{\mathrm{az}}$, where $\boldsymbol{P}_{\mathrm{el}} = \mathrm{diag}\Big(\big[e^{\mathrm{j}p_{\mathrm{el},0}}, e^{\mathrm{j}p_{\mathrm{el},1}}, \cdots, e^{\mathrm{j}p_{\mathrm{el},N_{\mathrm{x}}-1}}\big]^{\mathrm{T}}\Big)$ and $\boldsymbol{A}_{\mathrm{el}} = \mathrm{diag}\Big(\big[a_{\mathrm{el},0}, a_{\mathrm{el},1}, \cdots, a_{\mathrm{el},N_{\mathrm{x}}-1}\big]^{\mathrm{T}}\Big)$ correspond to the elevation domain, and $\boldsymbol{P}_{\mathrm{az}} = \mathrm{diag}\Big(\big[e^{\mathrm{j}p_{\mathrm{az},0}}, e^{\mathrm{j}p_{\mathrm{az},1}}, \cdots, e^{\mathrm{j}p_{\mathrm{az},N_{\mathrm{y}}-1}}\big]^{\mathrm{T}}\Big)$ and $\boldsymbol{A}_{\mathrm{az}} = \mathrm{diag}\Big(\big[a_{\mathrm{az},0}, a_{\mathrm{az},1}, \cdots, a_{\mathrm{az},N_{\mathrm{y}}-1}\big]^{\mathrm{T}}\Big)$ are for the azimuth domain. In this chapter, we model $p_{\mathrm{el},i_{\mathrm{el}}}$, $a_{\mathrm{el},i_{\mathrm{el}}}$ with $i_{\mathrm{el}} = 0, \cdots, N_{\mathrm{x}} - 1$ and $p_{\mathrm{az},i_{\mathrm{az}}}$, $a_{\mathrm{az},i_{\mathrm{az}}}$ with $i_{\mathrm{az}} = 0, \cdots, N_{\mathrm{y}} - 1$ as Gaussian distributed random variables with zero mean and certain variances. Note that other distributions of phase and amplitude errors are possible depending on array geometry, array size, and other array configurations. Our proposed array calibration strategy does not rely on specific phase and amplitude errors distributions. Further, the proposed calibration method is performed off-line assuming time-invariant phase and amplitude errors. If the phase and amplitude errors slowly change over time, we can still apply the

proposed off-line calibration method in a semi-static manner. If the phase and amplitude errors dynamically evolve over time, on-line array calibration methods are needed to frequently compensate for the phase and amplitude impairments in seconds, which are beyond the scope of this chapter.

We employ the beam pair example discussed in Section 4.4.1 to illustrate the impact of the phase and amplitude errors on the auxiliary beam pair design. Denote $C = AP$ and neglect the radiation pattern impairments at the UE side. Using the transmit analog beam $a_t(\eta_{el}, \eta_{az} - \delta_y)$ and the receive analog beam $a_r(\vartheta)$, we compute the corresponding noiseless received signal strength as

$$
\begin{aligned}
\chi_{az}^{\Delta} &= |g_{r^\star} \bar{\rho}_{\tau_{r^\star}}|^2 \, |a_r^*(\vartheta) a_r(\nu_{r^\star})|^2 \\
&\quad \times \ a_t^*(\eta_{el}, \eta_{az} - \delta_y) C^* a_t(\theta_{r^\star}, \psi_{r^\star}) a_t^*(\theta_{r^\star}, \psi_{r^\star}) C a_t(\eta_{el}, \eta_{az} - \delta_y) \qquad (4.13) \\
&= |g_{r^\star} \bar{\rho}_{\tau_{r^\star}}|^2 \, |a_r^*(\vartheta) a_r(\nu_{r^\star})|^2 \\
&\quad \times \ \left| \sum_{i_{el}=0}^{N_x-1} a_{el,i_{el}} e^{-j\left[i_{el}(\theta_{r^\star} - \eta_{el}) - p_{el,i_{el}}\right]} \right|^2 \left| \sum_{i_{az}=0}^{N_y-1} a_{az,i_{az}} e^{-j\left[i_{az}(\psi_{r^\star} - \eta_{az} + \delta_y) - p_{az,i_{az}}\right]} \right|^2 .
\end{aligned}
$$
$$(4.14)$$

We can similarly obtain the received signal strength χ_{az}^{Σ} with respect to the transmit and receive beams pair $a_t(\eta_{el}, \eta_{az} + \delta_y)$ and $a_r(\vartheta)$. Due to the phase and amplitude errors, the ratio metric calculated via $\zeta_{az} = \frac{\chi_{az}^{\Delta} - \chi_{az}^{\Sigma}}{\chi_{az}^{\Delta} + \chi_{az}^{\Sigma}}$ is therefore no longer a strict monotonic function of the angle to be estimated. By directly inverting the ratio metric function as according to (4.10), high angle estimation error probability could be incurred, which in turn, degrades the angle tracking performance of the proposed methods.

In Figures 4.4(a) and 4.4(b), we plot the azimuth radiation patterns with and without phase and amplitude errors for comparison. For a given ψ_0, we calculate $\left| \boldsymbol{a}_{\mathrm{ty}}^*(\psi) \boldsymbol{D}^* \boldsymbol{a}_{\mathrm{ty}}(\psi_0) \right|^2$ as a sample point corresponding to $\psi \in [-\pi/2, \pi/2]$, where $\boldsymbol{D} = \boldsymbol{I}_{N_{\mathrm{y}}}$ assuming no phase and amplitude errors, and $\boldsymbol{D} = \boldsymbol{A}_{\mathrm{az}} \boldsymbol{P}_{\mathrm{az}}$ assuming both phase and amplitude errors for the azimuth domain. We then form the radiation pattern by collecting all the sample points. Both the phase and amplitude errors for the azimuth domain are distributed according to $\mathcal{N}(0, 0.5)$ and $\mathcal{N}(0, 1)$ in Figures 4.4(a) and 4.4(b). Further, we employ a total of $N_{\mathrm{y}} = 16$ antennas for the azimuth domain. As can be seen from Figures 4.4(a) and 4.4(b), the azimuth radiation patterns are severely contaminated by the phase and amplitude errors such that the main lobe and side lobes can not be differentiated. In Figures 4.5(a) and 4.5(b), we plot the ratio metrics versus the angle to be estimated assuming ideal radiation pattern and impaired radiation pattern with $N_{\mathrm{y}} = 16$ and $\delta_{\mathrm{y}} = \pi/8$. It is observed from Figure 4.5(b) that with 0.5 phase and amplitude errors variances, the ratio metrics obtained via different impairment realizations are neither monotonic functions of the angle to be estimated nor symmetrical with respect to the origin. These observations are consistent with our analysis. Practical implementation of the proposed angle tracking designs therefore requires array calibration to compensate for the phase and amplitude errors.

Conventional array calibration methods such as those in [90] can not be directly applied to the hybrid array setup. This is because in the employed array architecture, all antenna elements are driven by a limited number of

RF chains such that only N_{RF}-dimensional measurements are accessible to calibrate all N_{tot} antenna elements. In this chapter, we develop and evaluate an off-line array calibration method for the employed array configurations assuming simple LOS channels and single-carrier setup.

In this method, we assume that a single calibration source transmitting the calibration reference signal (RS) is located at the origin with respect to the BS antenna array such that the calibration RS impinges on the antenna array at 0 degree in both the azimuth and elevation domains. At the BS, a set of receive combining vectors are formed in a TDM manner probing towards N_{tot} different angular directions in both the azimuth and elevation domains. The external calibration source can be placed close to the BS antenna array, and the channel between them is LOS. We can therefore express the signals received across all the N_{tot} receive probings as

$$y_0 \;=\; \boldsymbol{a}_{\mathrm{t}}^*(\eta_{\mathrm{el},0}, \eta_{\mathrm{az},0})\boldsymbol{C}\boldsymbol{a}_{\mathrm{t}}(\theta, \psi)x + \boldsymbol{a}_{\mathrm{t}}^*(\eta_{\mathrm{el},0}, \eta_{\mathrm{az},0})\boldsymbol{n}_0 \tag{4.15}$$

$$\vdots$$

$$y_{N_{\mathrm{tot}}-1} \;=\; \boldsymbol{a}_{\mathrm{t}}^*(\eta_{\mathrm{el},N_{\mathrm{x}}-1}, \eta_{\mathrm{az},N_{\mathrm{y}}-1})\boldsymbol{C}\boldsymbol{a}_{\mathrm{t}}(\theta, \psi)x + \boldsymbol{a}_{\mathrm{t}}^*(\eta_{\mathrm{el},N_{\mathrm{x}}-1}, \eta_{\mathrm{az},N_{\mathrm{y}}-1})\boldsymbol{n}_{N_{\mathrm{tot}}-1},$$

$$\tag{4.16}$$

where x represents the calibration RS, $\theta = \psi = 0$, $\eta_{\mathrm{el},i_{\mathrm{el}}}$ and $\eta_{\mathrm{az},i_{\mathrm{az}}}$ ($i_{\mathrm{el}} = 0, \cdots, N_{\mathrm{x}} - 1$ and $i_{\mathrm{az}} = 0, \cdots, N_{\mathrm{y}} - 1$) are the receive steering directions in the elevation and azimuth domains, and $\boldsymbol{n}_i$ ($i = 0, \cdots, N_{\mathrm{tot}} - 1$) is the corresponding noise vector. In this chapter, we assume the calibration RS $x = 1$ while it can be selected as a different symbol from 1 as long as it is known

a prior. By concatenating all the received signal samples $y_0, \cdots, y_{N_{\text{tot}}-1}$, we therefore have

$$\boldsymbol{y} = \begin{bmatrix} y_0 \\ \vdots \\ y_{N_{\text{tot}}-1} \end{bmatrix} = \boldsymbol{A}_{\text{t}}\boldsymbol{C}\boldsymbol{1}_{N_{\text{tot}}\times 1} + \boldsymbol{A}_{\text{t}}\boldsymbol{n}, \qquad (4.17)$$

with

$$\boldsymbol{A}_{\text{t}} = \begin{bmatrix} \boldsymbol{a}_{\text{t}}^*(\eta_{\text{el},0}, \eta_{\text{az},0}) \\ \vdots \\ \boldsymbol{a}_{\text{t}}^*(\eta_{\text{el},N_{\text{x}}-1}, \eta_{\text{az},N_{\text{y}}-1}) \end{bmatrix} \in \mathbb{C}^{N_{\text{tot}}\times N_{\text{tot}}}, \quad \boldsymbol{n} = \begin{bmatrix} \boldsymbol{n}_0 \\ \vdots \\ \boldsymbol{n}_{N_{\text{tot}}-1} \end{bmatrix} \in \mathbb{C}^{N_{\text{tot}}\times 1}.$$

$$(4.18)$$

According to (4.17), the phase and amplitude errors matrix can be estimated as

$$\hat{\boldsymbol{C}} = \text{diag}\left\{\boldsymbol{A}_{\text{t}}^{-1}\boldsymbol{y}\right\}, \qquad (4.19)$$

and the calibration matrix is determined as $\boldsymbol{K} = \hat{\boldsymbol{C}}^{-1}$. Note that with different receive steering directions and DFT-type receive steering vector structure, the square matrix $\boldsymbol{A}_{\text{t}}$ is invertible.

In Figure 4.6(a), we evaluate the impact of the residual calibration errors on the azimuth radiation pattern for the proposed calibration method. We set the calibration SNR as 0 dB. As can be seen from Figure 4.6(a), the calibrated radiation pattern almost matches with the ideal radiation pattern in the azimuth domain such that the main lobe and side lobes can be clearly differentiated. Note that with increase in the calibration SNR, the calibration performances can be further improved.

After the array calibration, the amplitude and phase errors become small and are approximately the same across all the antenna elements. The

corresponding ratio metric can therefore exhibit the same form as in the perfect radiation pattern case, implying that the channel directional information can be retrieved by inverting the ratio metric. In Figure 4.6(b), we plot the ratio metrics obtained after the array calibration with respect to the angle to be estimated in the azimuth domain. By comparing Figure 4.6(b) with Figure 4.6(a), it can be observed that the monotonic and symmetric properties of the ratio metric hold for most of the angle values.

4.5.2 ABPs, GoBs and compressive sensing

In this part, we compare our proposed ABPs, conventional GoBs and compressive sensing based methods in acquiring the angle information. We also analyze their differences and connections.

4.5.2.1 ABPs versus GoBs

As discussed before, the angle acquisition performance of the on-grid GoBs based approach is limited by the grid resolution, which depends on the beamwidth, and therefore, the number of employed antennas. Increasing the number of antennas will improve the angle acquisition performance of the GoBs based approach. Hence, without considering noise, the GoBs based method with infinite number of antennas (i.e., infinite grid resolution or without grid) is equivalent to our proposed off-grid ABPs based strategy (using finite number of antennas) in terms of the angle estimation/tracking performance. We can also interpret this comparison from two perspectives, i.e., (i) using the same array

134

size, the angle estimation/tracking performance of the ABPs based method is superior over that in the GoBs based approach, and (ii) targeting at the same angle acquisition performance, the GoBs based approach exhibits higher computational complexity and overhead than the ABPs. We have used several numerical examples presented in Figures 3.5(a) and 3.6(a) to validate the above statements. Note that the GoBs based approach, however, is more robust than the ABPs based method to the radiation pattern impairments [44].

Different from other off-grid channel estimation methods, our proposed auxiliary beam pairs are still constructed from a grid of beams. With necessary control signaling support, it becomes very flexible to switch between the ABPs and the GoBs based methods from a common beam codebook according to practical deployment scenarios. For instance, after the array calibration, if the residual phase and amplitude errors are still large, it is better to use the GoBs based approach. To better trade off the robustness, estimation/tracking accuracy and the complexity, a hybrid design of the ABPs and GoBs is also desired. For instance, in the multi-layer control channel beamforming discussed in Section 2.5.1, the ABPs and the GoBs can be implemented in different layers to reduce the initial access delay while at the same time covering as many users as possible.

4.5.2.2   ABPs versus compressive sensing

Our proposed ABPs based strategy primarily focused on estimating and tracking the angle information. Most of the compressive sensing based meth-

ods, however, can estimate both the angle information and the path gains, but the performance is still limited by the grid resolution. The design principle and procedure are also quite different between these two design options. In the compressive sensing based methods, correctly formulating the sparse channel estimation problem and developing efficient reconstruction algorithms are the design focus as long as the measurement matrices are Gaussian. In the ABPs based strategy, we actually focus on custom designing the measurement matrices such that the resulting ratio metrics are invertible with respect to the angle information. In Section 4.6, we numerically compare our proposed solution and the adaptive compressive sensing based approach developed in [91] in terms of the angle tracking performance. It is also of great interest to combine these two design options to facilitate the estimation process. For instance, the compressive sensing based methods can exploit the high-resolution angle estimates from the ABPs to optimize the dictionary matrices. By optimizing the dictionary matrices at both the BS and the UE, we expect to further improve the path gain estimation accuracy with reduced complexity and overhead. We leave the detailed procedure of jointly designing the ABPs and compressive sensing based methods for future research. We highlight here that it may be necessary to custom design the digital baseband precoding/combing matrices to enforce the Gaussian assumption on the measurement matrices.

4.6   Numerical Results

In this section, we evaluate the proposed BS-driven angle tracking design with the direct ratio metric feedback and the periodic DTC. Note that different angle tracking strategies developed in Section 4.4 exhibit similar tracking performances, though they have different requirements on the tracking triggering metric, feedback information, and information available at the UE side. We evaluate the proposed angle tracking method assuming ideal radiation pattern, impaired radiation pattern with phase and amplitude errors, and calibrated radiation pattern. For simplicity, we obtain the calibrated radiation pattern via the proposed single calibration source based strategy. We set the angle difference threshold for triggering the beam adjustment as $10°$. As the ratio metric is non-uniformly distributed within the interval of $[-1, 1]$ [41], we can employ the Lloyd's algorithm [92] to optimize the codebook for quantizing the ratio metric.

4.6.1   Narrowband single-path channels with single-carrier

In this part, we provide the numerical results in narrowband single-path channels with single-carrier modulation. We consider a single UE and two angular motion models shown in Figures 4.7(a) and 4.7(b) to reveal the moving trajectory of the UE. In the first model (angular motion model I), the ULA is employed at the BS, while in the second model (angular motion model II), the UPA is employed at the BS such that the tracking beams can steer towards both the elevation and azimuth domains. For both cases, the

137

ULA is assumed at the UE side. Note that we develop the angular motion models I and II to better characterize the angle variations in terms of the moving trajectory. In Section 4.6.3, we employ statistical temporal evolution tools to model practical channel variations. Other simulation assumptions and parameters follow those listed in [44, Table II]. We drop the path index here due to the single-path assumption. Note that we obtain the angle variations $\Delta\psi$ and $\Delta\theta$ according to the UE's azimuth and elevation velocities v_{az} and v_{el}, the BS-UE distance d, and the symbol duration. We further randomize the angle variations by incorporating a Gaussian distributed random variable w with zero mean and variance 1. In the simulations, we set $T = 1$. That is, each DTC comprises one time-slot (symbol), during which one auxiliary beam pair is formed. The two beams in the corresponding auxiliary beam pair are simultaneously transmitted, which are differentiated by the UE via the beam-specific pilot signal design. We can then define the tracking overhead as $\rho = 1/T_{\mathrm{d}}$. For instance, $T_{\mathrm{d}} = 1000$ results in less tracking overhead than $T_{\mathrm{d}} = 10$ as the corresponding tracking overheads are computed as $\rho = 0.1\%$ and $\rho = 10\%$.

In Figure 4.8(a), we provide snapshots of the angle tracking results over time for $\rho = 1\%$ and 0.05% in the proposed design. For comparison, we also provide the actual angle variations and the case without angle tracking. Further, we assume ideal radiation pattern. As can be seen from Figure 4.8(a), the proposed auxiliary beam pair-assisted angle tracking design can accurately track the angle variations under relatively high tracking overhead, i.e., 1%.

138

By reducing the tracking overhead to 0.05%, the tracking resolution becomes small, which in turn, degrades the angle tracking performances as shown in Figure 4.8(b). Under different tracking overhead assumptions, the trend of the angle variations can be well captured by the proposed angle tracking design.

We now evaluate the two-dimensional angle tracking performance for the proposed approach using calibrated radiation pattern. A total of $N_{\text{tot}} = 32$ antenna elements are equipped at the BS side with the UPA placed in the xy-plane. Further, we set $N_{\text{x}} = 4$ and $N_{\text{y}} = 8$. In Figure 4.9(a), we plot the cumulative density functions (CDFs) of the beamforming gains obtained from the anchor beam in the DDC. With calibrated radiation pattern, the proposed method shows close performance relative to the perfect case assuming various tracking overheads. In Figure 4.9(b), we evaluate the spectral efficiency performance using the anchor beam in the DDC. Specifically, denoting by $h_{\text{eff}} = g\boldsymbol{a}_{\text{r}}^*(\nu)\boldsymbol{a}_{\text{r}}(\nu)\boldsymbol{a}_{\text{t}}^*(\theta, \psi)\boldsymbol{a}_{\text{t}}(\hat{\theta}, \hat{\psi})$ for single-path channels, we can compute the spectral efficiency metric as $C = \mathbb{E}\left[\log_2\left(1 + \gamma h_{\text{eff}}^* h_{\text{eff}}\right)\right]$. Similar to Figure 4.9(a), the spectral efficiency performances obtained by using the proposed method with different tracking overheads are close to the perfect case. In Figures 4.9(a) and 4.9(b), we also evaluate the grid-of-beams based beam tracking design assuming various tracking overheads. For fair comparison, we employ the same number of tracking beams as in the auxiliary beam pair based angle tracking design. As can be seen from Figures 4.9(a) and 4.9(b), the proposed algorithm shows superior beamforming gain and spectral efficiency performances over the grid-of-beams based beam tracking strategy.

4.6.2   Narrowband multi-path channels with single-carrier

In this part, we employ the Rician multi-path channel model with various Rician K-factor values. We set the number of NLOS channel components to 5. Further, we evaluate the mean angle tracking error (MATE), which is calculated as $\mathbb{E}[|\xi_t - \hat{\xi}_t|]$, where ξ_t is the channel's azimuth/elevation angle at time t, and $\hat{\xi}_t$ is its tracked counterpart. We use the angular motion model I to characterize the angle variations of all paths, and the objective is to track the variations of the dominant path.

It is observed from Figure 4.10(a) that with increase in the number of channel paths, the MATE performance degrades because of the multi-path interference. Similar observation is obtained by reducing the Rician K-factor value from 13 dB to 6 dB. The performance differences between $N_{\mathrm{r}} = 2$ and $N_{\mathrm{r}} = 10$, and K = 6 dB and K = 13 dB, however, are marginal due to the fact that relatively narrow tracking beams are formed surrounding only the dominant path. Further, by increasing the total number of transmit antennas N_{tot} from 8 to 16, the MATE significantly decreases. At relatively high SNR, the multi-path interference would dominate the MATE performance. These observations are consistent with our approximation and analysis in Section 4.4.1. In Figure 4.10(b), we examine the impact of multiple auxiliary beam pairs probings on the MATE performance in a 6-path channel with 6 dB Rician K-factor. If the angle tracking is triggered, the MATE decreases with increase in the number of probings of identical auxiliary beam pairs, leveraging the spreading gain discussed in Section 4.4.2 to improve the angle tracking

performance especially in low to medium SNR regimes.

4.6.3 Wideband multi-path channels with OFDM

The temporal evolution effect of mmWave channels is not well characterized in current wideband mmWave channel models [93]. In this part of simulation, we therefore first implement the temporally correlated mmWave channels by considering both (i) the NYUSIM open source platform developed in [71] and (ii) the statistical temporal evolution model used in [93,94].

For the NYUSIM open source platform, we consider the UMi cellular scenario with NLOS components for the 28 GHz carrier frequency. We evaluate a 125 MHz RF bandwidth with $N = 512$ subcarriers. The corresponding CP lengths is $D = 64$. The employed ZC-type sequences occupy the central 63 subcarriers with the root indices $i_0 = 25$ and $i_1 = 34$. We set the subcarrier spacing and symbol duration as 270 KHz and 3.7 μs following the numerology provided in [1]. Detailed channel modeling parameters are given in [71, Table III]. Further, our design focus here is to track the strongest path's AoD by using the proposed approach.

Before proceeding with the temporal channel evolution model, we first rewrite the time-domain channel matrix in (5.10) in a more compact form. For time-slot t, denoting by $\boldsymbol{\varphi}_t = [\varphi_{1,t}, \varphi_{2,t}, \cdots, \varphi_{N_r,t}]^{\mathrm{T}}$, $\boldsymbol{\mu}_t = [\mu_{1,t}, \mu_{2,t}, \cdots, \mu_{N_r,t}]^{\mathrm{T}}$ and $\boldsymbol{\phi}_t = [\phi_{1,t}, \phi_{2,t}, \cdots, \phi_{N_r,t}]^{\mathrm{T}}$, we have $\boldsymbol{H}_t[d] = \boldsymbol{A}_{\mathrm{R}}(\boldsymbol{\varphi}_t)\boldsymbol{G}_t[d]\boldsymbol{A}_{\mathrm{T}}^*(\boldsymbol{\mu}_t, \boldsymbol{\phi}_t)$, where $\boldsymbol{A}_{\mathrm{R}}(\boldsymbol{\varphi}_t)$ and $\boldsymbol{A}_{\mathrm{T}}(\boldsymbol{\mu}_t, \boldsymbol{\phi}_t)$ represent the array response matrices for the

141

receiver and transmitter such that

$$\boldsymbol{A}_{\mathrm{R}}(\boldsymbol{\varphi}_t) = [\boldsymbol{a}_{\mathrm{r}}(\varphi_{1,t}) \quad \boldsymbol{a}_{\mathrm{r}}(\varphi_{2,t}) \quad \cdots \quad \boldsymbol{a}_{\mathrm{r}}(\varphi_{N_{\mathrm{r}},t})] \tag{4.20}$$

$$\boldsymbol{A}_{\mathrm{T}}(\boldsymbol{\mu}_t, \boldsymbol{\phi}_t) = [\boldsymbol{a}_{\mathrm{t}}(\mu_{1,t}, \phi_{1,t}) \quad \boldsymbol{a}_{\mathrm{t}}(\mu_{2,t}, \phi_{2,t}) \quad \cdots \quad \boldsymbol{a}_{\mathrm{t}}(\mu_{N_{\mathrm{r}},t}, \phi_{N_{\mathrm{r}},t})], \tag{4.21}$$

and $\boldsymbol{G}_t[d] = \mathrm{diag}\left([g_1 p\,(dT_{\mathrm{s}} - \tau_1), \cdots, g_{N_{\mathrm{r}}} p\,(dT_{\mathrm{s}} - \tau_{N_{\mathrm{r}}})]^{\mathrm{T}}\right)$. We model the temporal evolution of the path gains as the first-order Gauss-Markov process as [80]

$$\boldsymbol{G}_{t+1}[d] = \rho_{\mathrm{D}}\boldsymbol{G}_t[d] + \sqrt{1 - \rho_{\mathrm{D}}^2}\boldsymbol{B}_{t+1}, \tag{4.22}$$

where $\rho_{\mathrm{D}} = J_0\,(2\pi f_{\mathrm{D}} T_{\mathrm{s}})$ and $\boldsymbol{B}_{t+1}$ is a diagonal matrix with the diagonal entries distributed according to $\mathcal{N}_{\mathrm{c}}(0, 1)$. Here, $J_0(\cdot)$ denotes the zeroth-order Bessel function of first kind and f_{D} is the maximum Doppler frequency. The elevation and azimuth AoDs vary according to [94]

$$\boldsymbol{\mu}_{t+1} = \boldsymbol{\mu}_t + \Delta\boldsymbol{\mu}_{t+1}, \quad \boldsymbol{\phi}_{t+1} = \boldsymbol{\phi}_t + \Delta\boldsymbol{\phi}_{t+1}, \tag{4.23}$$

where $\Delta\boldsymbol{\mu}_{t+1}$ and $\Delta\boldsymbol{\phi}_{t+1}$ are distributed according to $\mathcal{N}_{\mathrm{c}}(\boldsymbol{0}_{N_{\mathrm{r}}}, \sigma_{\mu}^2\boldsymbol{I}_{N_{\mathrm{r}}})$ and $\mathcal{N}_{\mathrm{c}}(\boldsymbol{0}_{N_{\mathrm{r}}}, \sigma_{\phi}^2\boldsymbol{I}_{N_{\mathrm{r}}})$. We first determine the initial path gains, path delays, azimuth (elevation) AoDs, and AoAs through one simulation run using the NYUSIM open source platform. We then obtain the channels for the subsequent timeslots by using the initial channel results and the temporal evolution model presented in (4.22) and (4.23).

In Figure 4.11, we plot the beamforming gains against the employed OFDM symbols for $\rho = 0.1\%$ tracking overhead. We set $f_{\mathrm{D}} = 1.3$ KHz and $\sigma_{\mu}^2 = \sigma_{\phi}^2 = (\pi/180)^2$, which characterize relatively fast moving and angle

variation speeds [80,94]. In addition to the actual angle variations, we evaluate the proposed angle tracking and grid-of-beams based beam tracking designs with calibrated radiation patterns. Similar to the evaluation results shown in Section 4.6.1, the proposed algorithm shows close tracking performance to the perfect case, and outperforms the existing beam tracking approach for various system setups.

In Figures 4.12 and 4.13, we employ the channel results generated using QuaDRiGA Version 1.2.3-307 to evaluate our proposed method in tracking the angle variations of the LOS path. We set the number of clusters in the channel as 5, with a 3 dB Rician K-factor. The linear tracking model is used such that the UE moves away from the BS in a straight line having a 150 m length. Further, the UE of interest moves along the linear track with a constant 1 m/s (approximately 3.6 km/h) moving speed. Other simulation parameters including the carrier frequency, subcarrier spacing, and etc. are the same as those used in other wideband simulations. We evaluate the azimuth angle tracking results in Figures 4.12(a) and 4.12(b) with $\rho = 0.1\%$ and $\rho = 0.05\%$, and the elevation angle tracking results in Figures 4.13(a) and 4.13(b) with $\rho = 0.1\%$ and $\rho = 0.05\%$. Specifically, for a given tracking triggering time, the distance of the UE from the starting point (or equivalently, the position of the UE assuming the linear tracking model) is first computed. The corresponding channel condition can then be extracted, upon which our proposed angle tracking algorithms are performed. With this procedure, the spatial consistency such as the positions of the scattering clusters as a function

of the UE position can be maintained during the simulations. It is evident from these plots that our proposed method can accurately track the angle variations under a more practical varying model in contrast to the statistical temporal evolution model used in Figure 4.11. Further, our proposed solution performs better in the elevation domain than the azimuth domain because the actual angle variation in the elevation domain is less significant than that in the azimuth domain.

In Fig. 4.14, we examine the elevation MATE performance of our proposed method and the adaptive compressed sensing based strategy [91], using the same channel results as in Figures 4.12 and 4.13, generated by the QuaDRiGA platform. In contrast to the adaptive compressed sensing based strategy, the ABPs based tracking design shows better elevation MATE performance under $\rho = 0.1\%$. By reducing the tracking overhead from $\rho = 0.1\%$ to $\rho = 0.05\%$, however, our proposed solution becomes inferior relative to the adaptive compressed sensing based approach especially in the high SNR regime.

4.7 Conclusion

In this chapter, we developed and evaluated several new angle tracking design approaches for mobile wideband mmWave systems with antenna array calibration. The proposed methods are different in terms of tracking triggering metric, feedback information, and auxiliary beam pair setup required at the UE. These differences allow the proposed strategies to be adopted in

144

different deployment scenarios. We exposed the detailed design procedure of the proposed methods and showed that they can obtain high-resolution angle tracking results. The proposed methods neither depend on a particular angle variation model nor require the on-grid assumption. Since the proposed methods are sensitive to radiation pattern impairments, we showed by numerical examples that with appropriate array calibration, the angle variations can still be successfully tracked via the proposed methods under various angle variation models.
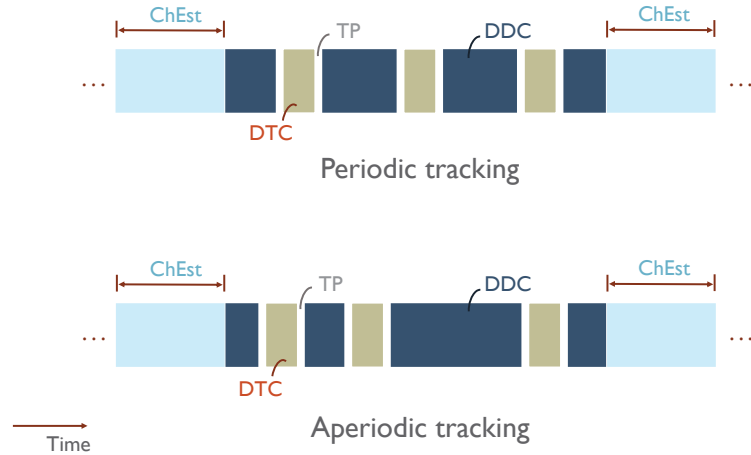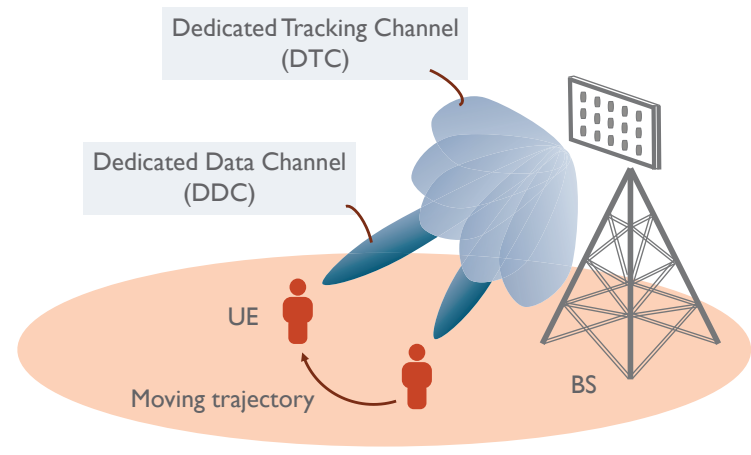
Figure 4.1: (a) Potential frame structures of the periodic and aperidoic beam/angle tracking designs. For the periodic beam/angle tracking design, the periodicity of the dedicated tracking channel (DTC) is fixed. For the aperiodic beam/angle tracking design, the DTC is flexibly triggered and configured by the BS. The channel estimation (ChEst), dedicated data channel (DDC) and DTC are multiplexed in the time-domain. A transition period (TP) may exist between the DTC and the DDC. (b) One conceptual example of the multiplexing between the DDC and DTC. The steering directions of the beams in the DDC are adjusted towards the UE's positions, which are obtained via the tracking beams in the DTC.
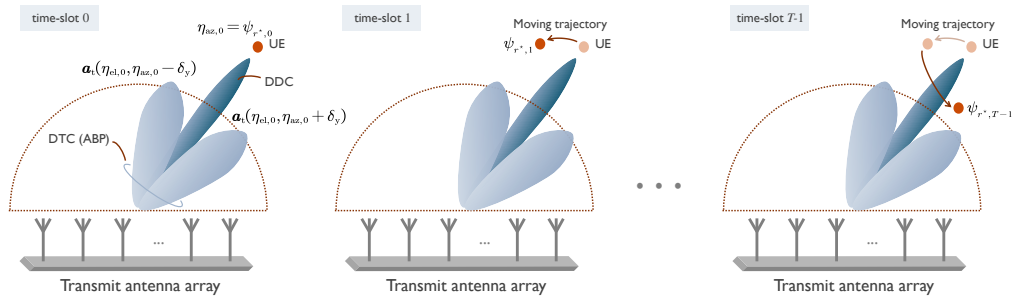
Figure 4.2: Conceptual examples of the relationship between the UE's moving trajectory (i.e., the angle variations) and the auxiliary beam pair based tracking beams in the DTC. As long as the relative position of the UE to the transmit antenna array is within the probing range of the auxiliary beam pair, it is expected to be tracked via the tracking beams in the DTC.

147
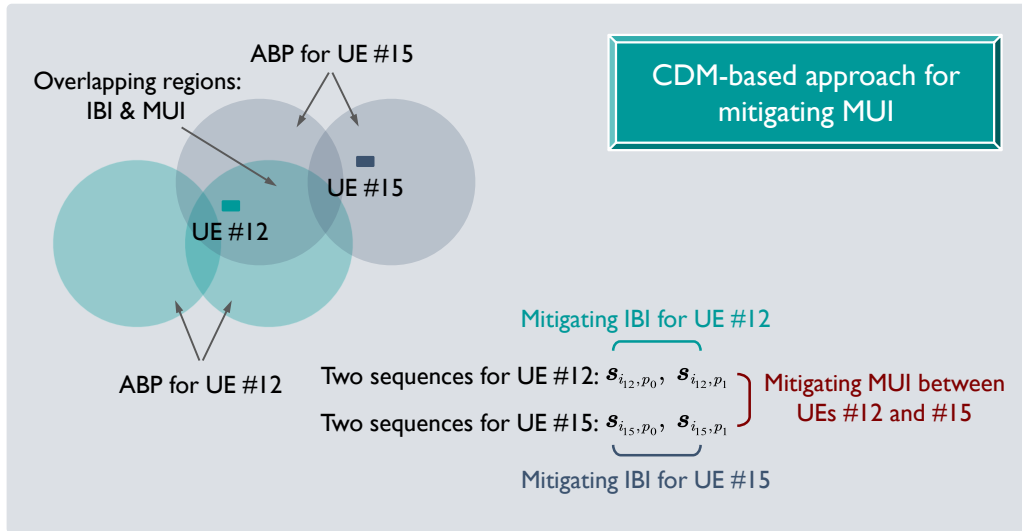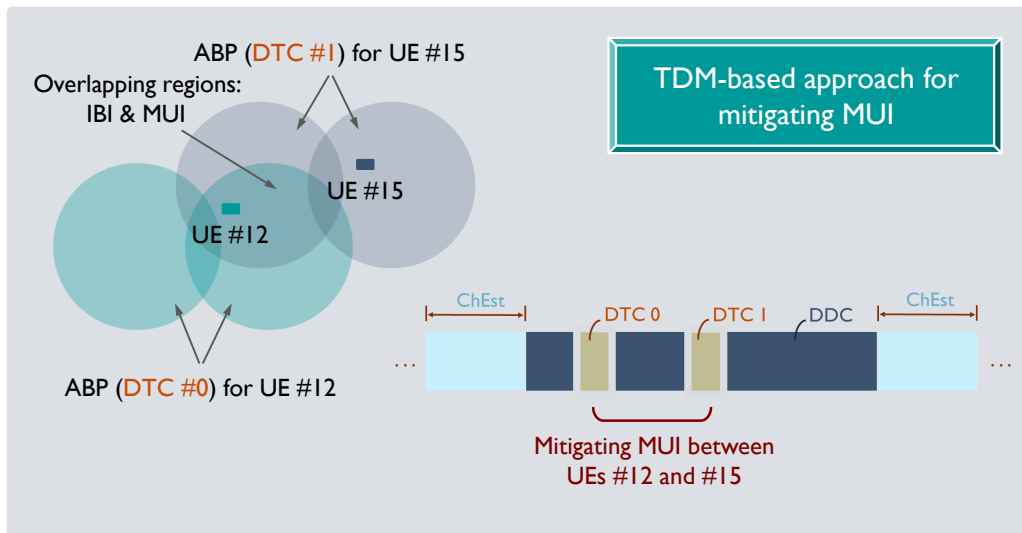
Figure 4.3: Bird's-eye view of the multi-user interference (MUI) between the DTCs and potential solutions. (a) CDM based multi-user interference mitigation strategy. (b) TDM based multi-user interference mitigation strategy.
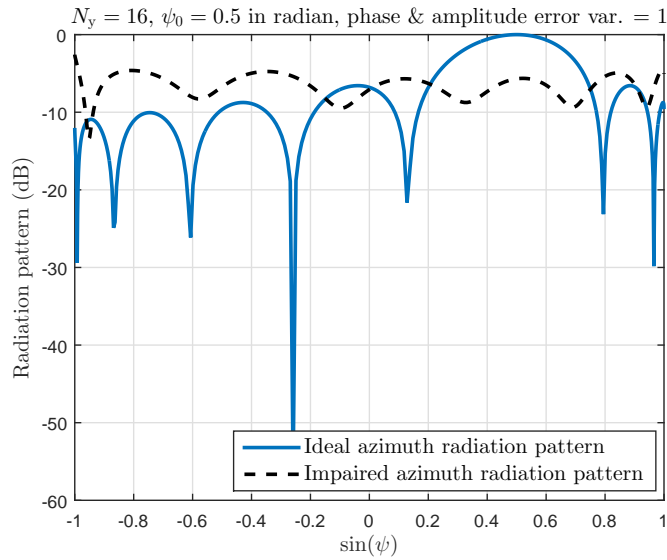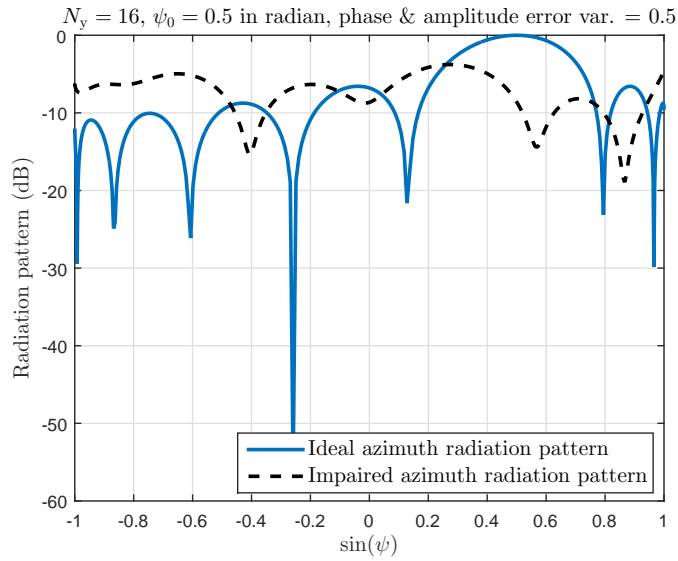
Figure 4.4: (a) Ideal azimuth radiation pattern and impaired azimuth radiation pattern with $N_\mathrm{y} = 16$ and the phase & amplitude errors variances 0.5. (b) Ideal azimuth radiation pattern and impaired azimuth radiation pattern with $N_\mathrm{y} = 16$ and the phase & amplitude errors variances 1.

149
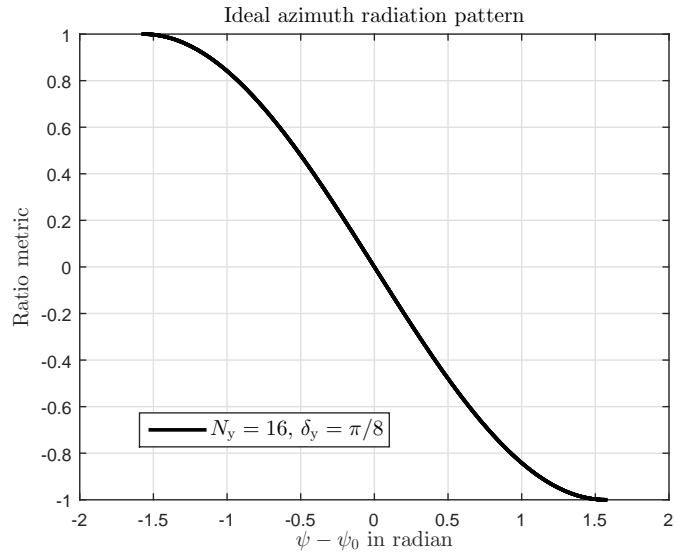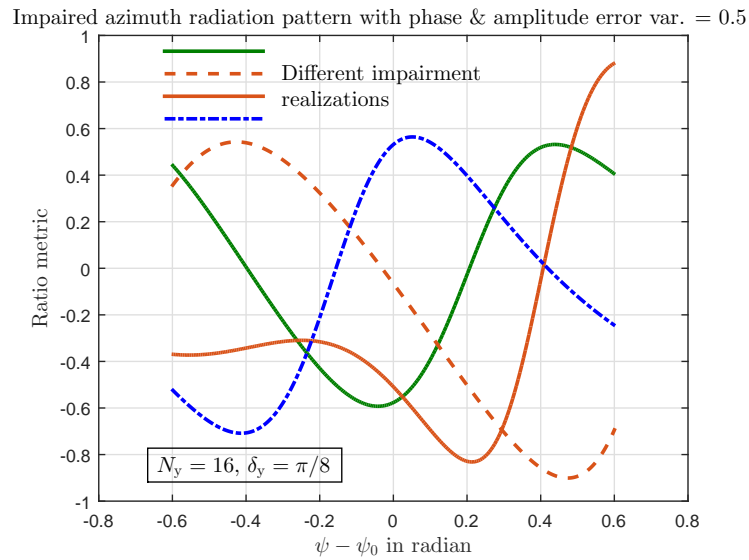
Figure 4.5: (a) Ratio metric versus angles to be estimated under ideal azimuth radiation pattern with $N_y = 16$ and $\delta_y = \pi/8$. (b) Ratio metrics versus angles to be estimated under different realizations of impaired azimuth radiation patterns with $N_y = 16$ and $\delta_y = \pi/8$. The phase & amplitude errors variances are 0.5.
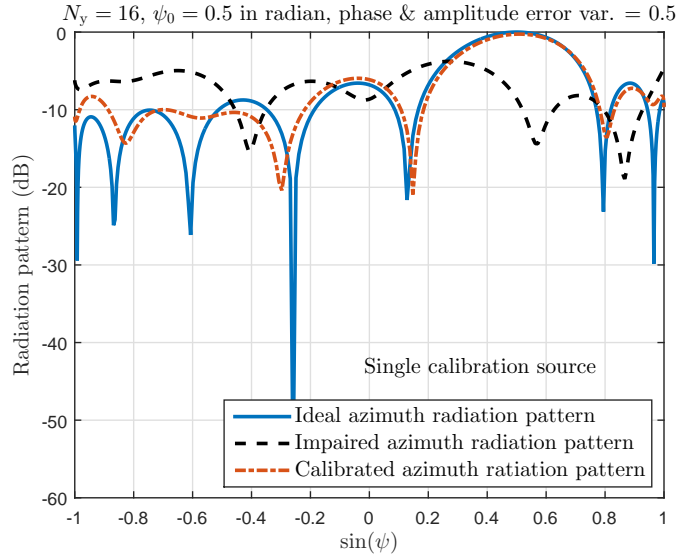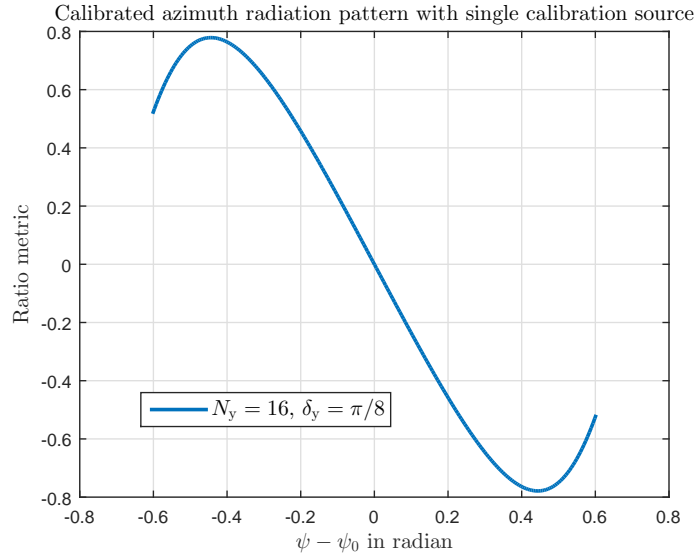
Figure 4.6: (a) Calibrated azimuth radiation pattern using the proposed single calibration source and receive combining based calibration method; $N_x = 1$, $N_y = 16$ with the phase & amplitude errors variances 0.5. (b) Ratio metric versus angles to be estimated under calibrated azimuth radiation pattern; $N_x = 1$, $N_y = 16$ and $\delta_y = \pi/8$; the phase & amplitude errors variances are 0.5.
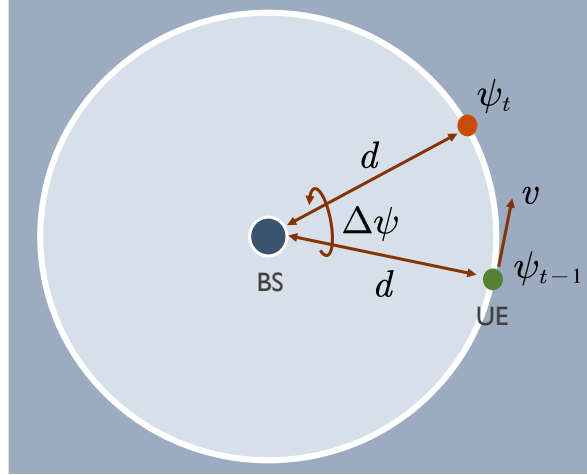
(a)
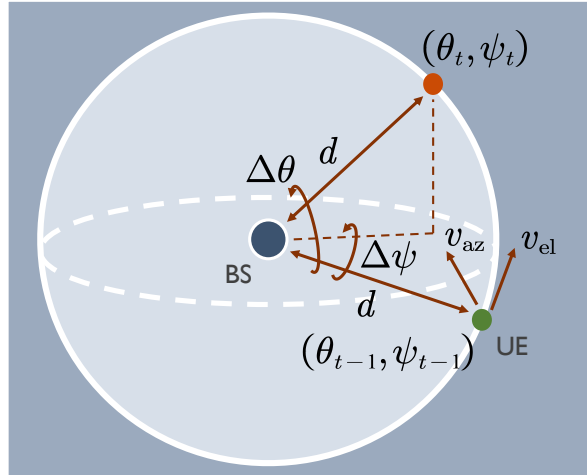
(b)

Figure 4.7: (a) Angular motion model I. The BS is located at the origin of a ring, and the UE is moving along the ring with certain absolute speed v. The radius of the ring is denoted by d. (b) Angular motion model II. The BS is located at the origin of a sphere, and the UE is moving on the surface with certain absolute speeds v_{az} and v_{el} towards the azimuth and elevation domains. The radius of the sphere is denoted by d.
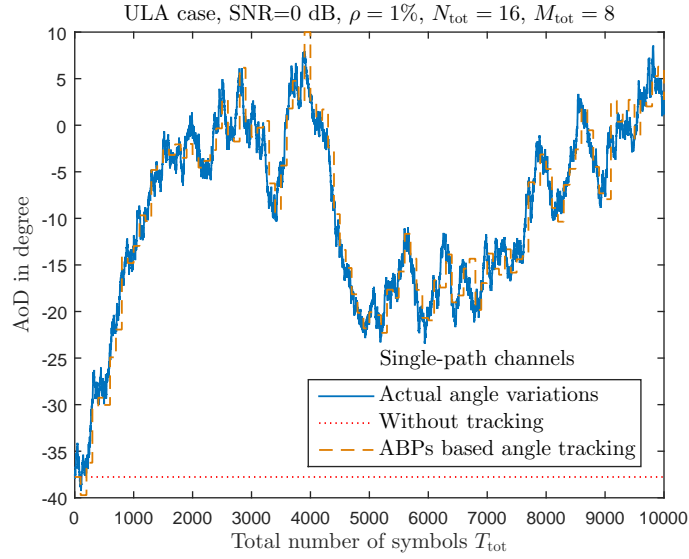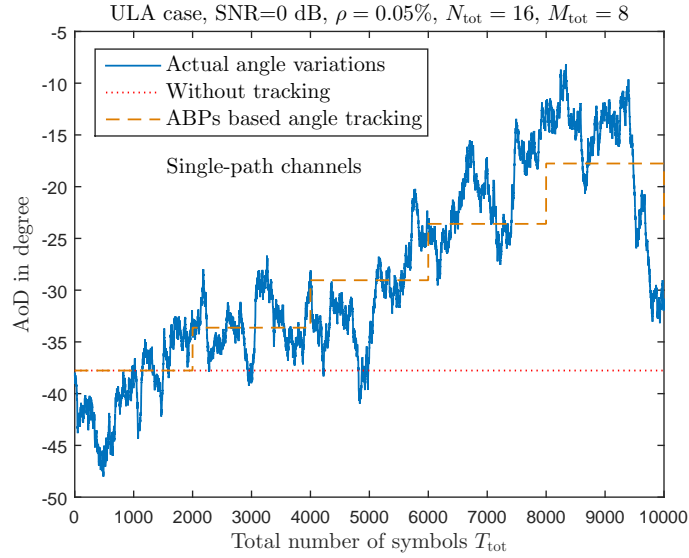
Figure 4.8: Examples of actual angle variations, angle tracking using the proposed method, and without angle tracking in single-path channels; $N_{\text{tot}} = 16$, $M_{\text{tot}} = 8$ and 0 dB SNR are assumed with the ULA equipped at the BS and ideal radiation pattern. (a) $\rho = 1\%$ tracking overhead. (b) $\rho = 0.05\%$ tracking overhead.
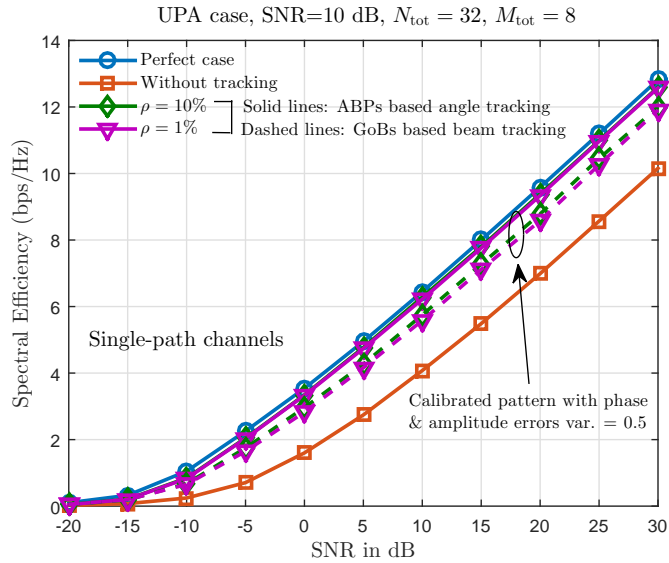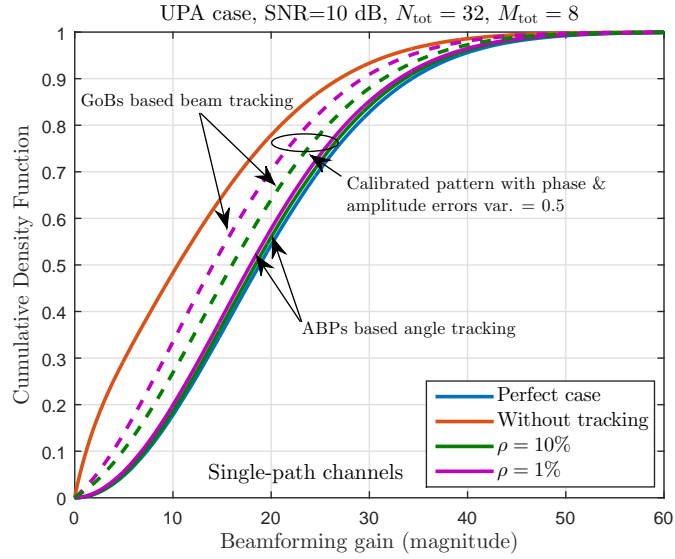
Figure 4.9: Angular motion model II. (a) CDFs of the beamforming gains obtained via the anchor beams in the DDC with $N_{\text{tot}} = 32$, $M_{\text{tot}} = 8$, 10 dB SNR and calibrated radiation pattern. (b) Spectral efficiency performance obtained via the anchor beams in the DDC with $N_{\text{tot}} = 32$, $M_{\text{tot}} = 8$, 10 dB SNR, and calibrated radiation pattern.
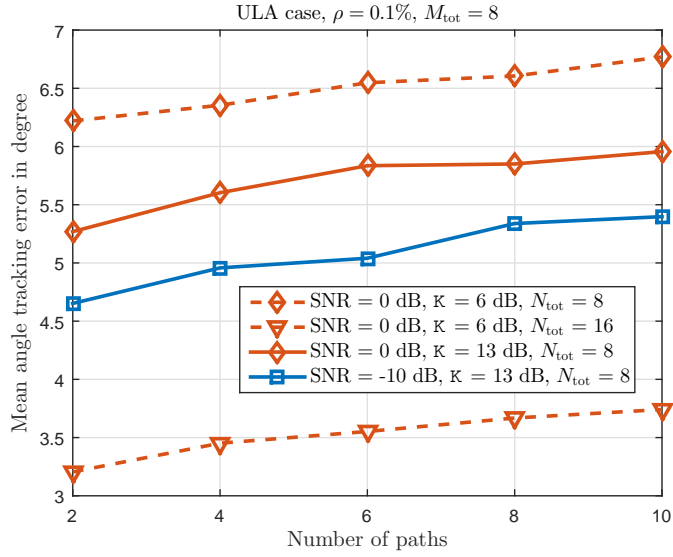
(a)
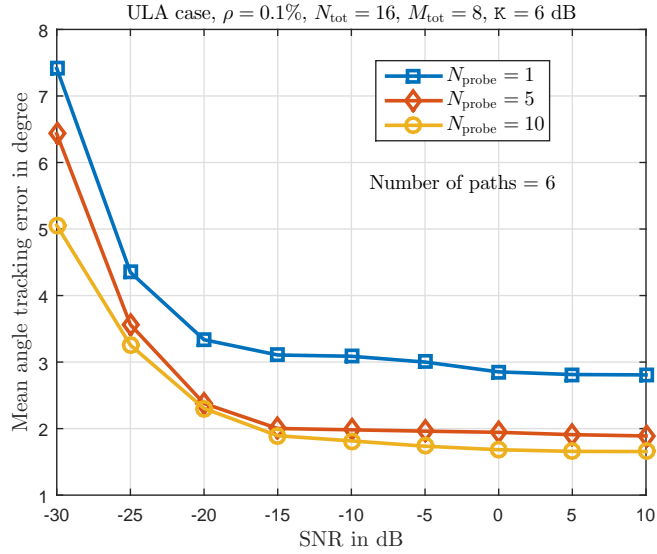
(b)

Figure 4.10: Angular motion model I with calibrated radiation patterns; phase and amplitude error variances are 0.5. (a) Mean angle tracking error (MATE) performance in narrowband Rician multi-path channels. (b) MATE performance in narrowband Rician multi-path channels with N_{probe} as the number of probings of identical auxiliary beam pairs to track a given angle's variations if the angle tracking is triggered.
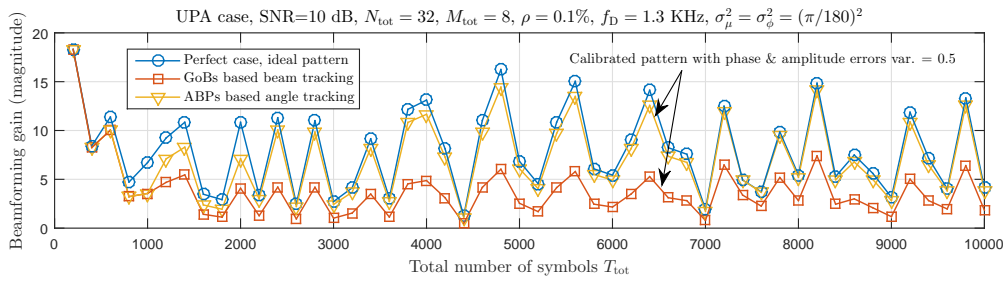
Figure 4.11: Beamforming gains obtained via the anchor beams in the DDC with $N_{\text{tot}} = 32$, $M_{\text{tot}} = 8$ and 10 dB SNR. The proposed approach and the grid-of-beams based beam tracking are evaluated assuming calibrated radiation pattern. $f_{\text{D}} = 1.3$ KHz and $\sigma_\mu^2 = \sigma_\phi^2 = (\pi/180)^2$. $\rho = 0.1\%$ tracking overhead.

(a)

(b)
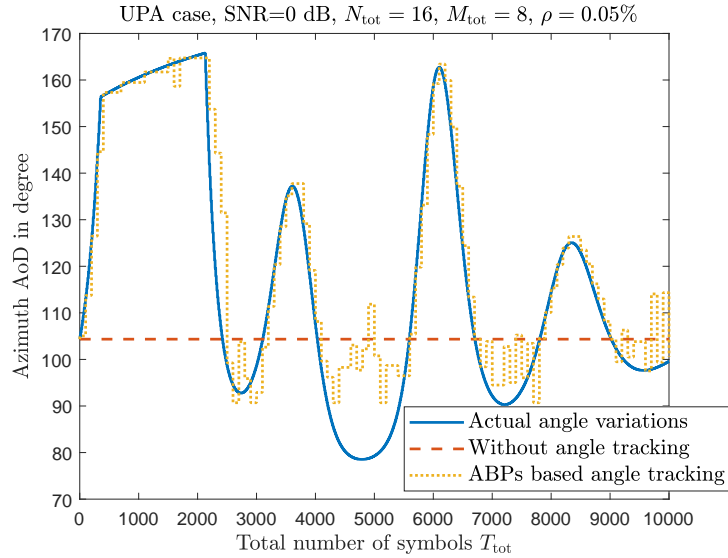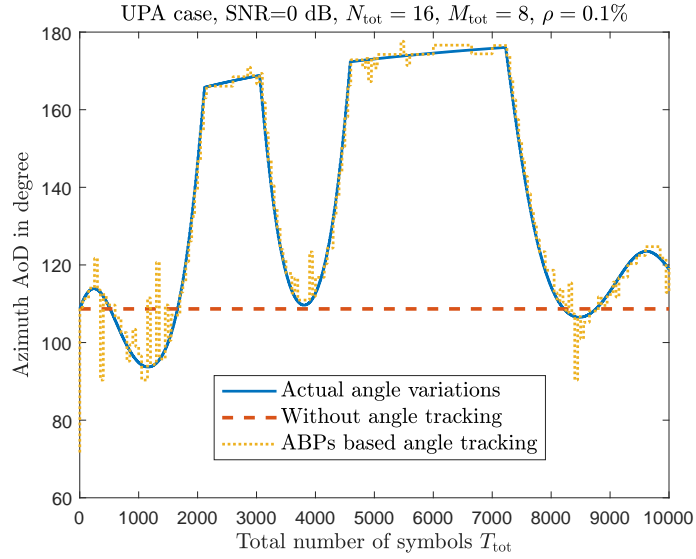
Figure 4.12: Examples of actual angle variations and angle tracking using the proposed method in the azimuth domain; the channel results are generated using QuaDRiGa Version 1.2.3-307 with linear varying model; $N_{\text{tot}} = 16$, $M_{\text{tot}} = 8$ and 0 dB SNR are assumed with ideal radiation pattern. (a) $\rho = 0.1\%$ tracking overhead. (b) $\rho = 0.05\%$ tracking overhead.
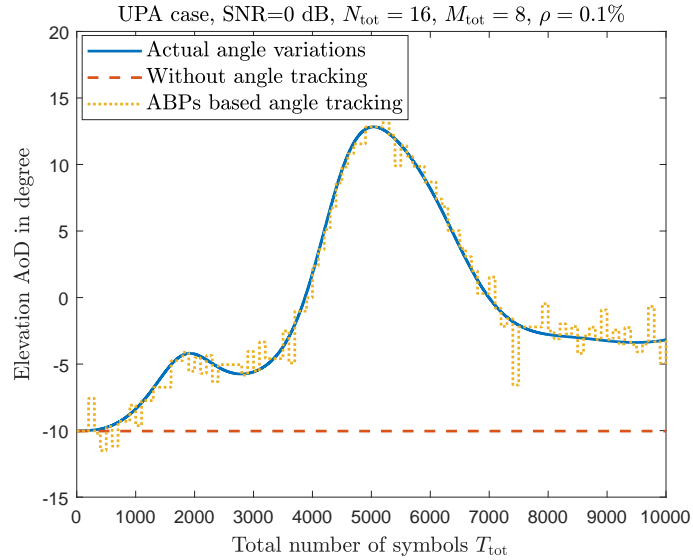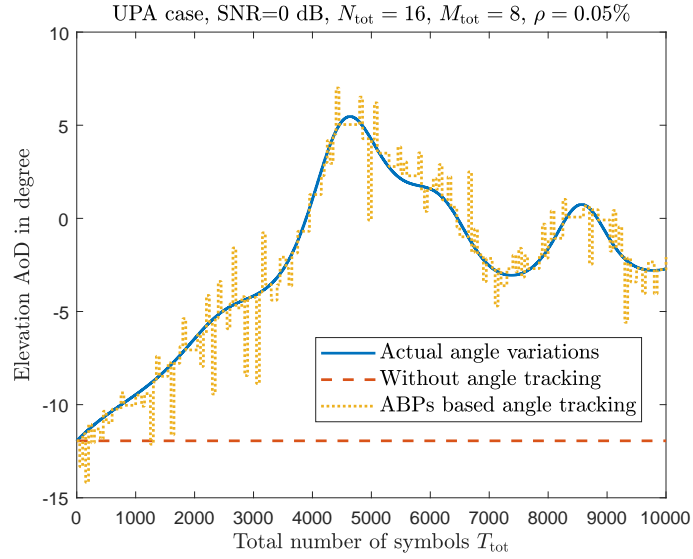
Figure 4.13: Examples of actual angle variations and angle tracking using the proposed method in the elevation domain; the channel results are generated using QuaDRiGa Version 1.2.3-307 with linear varying model; $N_{\text{tot}} = 16$, $M_{\text{tot}} = 8$ and 0 dB SNR are assumed with ideal radiation pattern. (a) $\rho = 0.1\%$ tracking overhead. (b) $\rho = 0.05\%$ tracking overhead.
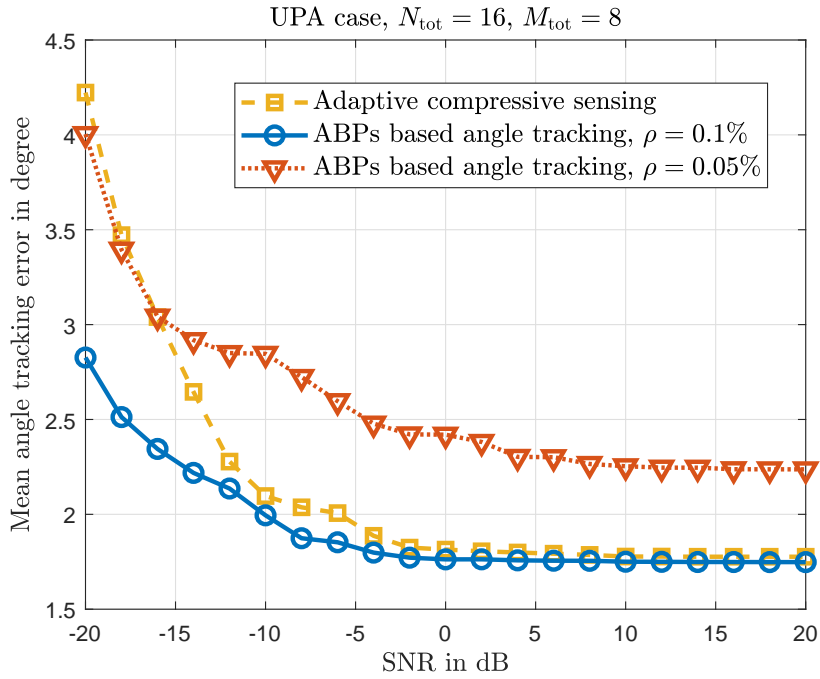
Figure 4.14: MATE performance comparison between the proposed ABPs based angle tracking design ($\rho = 0.1\%$ and $\rho = 0.05\%$) and the adaptive compressed sensing based approach in the elevation domain; the channel results are generated using QuaDRiGa Version 1.2.3-307 with linear varying model; $N_{\text{tot}} = 16$ and $M_{\text{tot}} = 8$ are assumed with the UPA equipped at the BS and ideal radiation pattern.

Chapter 5

Timing Synchronization in MmWave Cellular Systems with Low-Resolution ADCs

In this chapter, we propose and evaluate a novel beamforming strategy for directional frame timing synchronization in wideband mmWave systems operating with low-resolution ADCs. In the employed system model, we assume multiple radio frequency chains equipped at the base station to simultaneously form multiple synchronization beams in the analog domain. We formulate the corresponding directional frame timing synchronization problem as a max-min multicast beamforming problem under low-resolution quantization. We first show that the formulated problem cannot be effectively solved by conventional single-stream beamforming based approaches due to large quantization loss and limited beam codebook resolution. We then develop a new multi-beam probing based directional synchronization strategy, targeting at maximizing the minimum received synchronization signal-to-quantization-plus-noise ratio (SQNR) among all users. Leveraging a common synchronization signal structure design, the proposed approach synthesizes an effective composite beam from the simultaneously probed beams to better trade off the beamforming gain and the quantization distortion. Numerical results reveal that for wideband mmWave systems with low-resolution ADCs, the timing synchronization

160

performance of our proposed method outperforms the existing approaches due to the improvement in the received synchronization SQNR. This work has been submitted for possible publication [45], and part of it was published in [46].

5.1 Prior Work and Motivation

Current lower-frequency cellular networks such as long-term evolution systems [86] conduct frame timing synchronization with omni-directional transmission and reception. That is, the network broadcasts the synchronization signals in low-rate control channels to ensure both coverage and quality of reception. Directional transmission and detection of synchronization signals is interesting in mmWave systems due to the low SNR prior to beamforming. For directional synchronization, the network sends the synchronization signals towards predefined angular directions via analog-only beamforming, fully digital beamforming or hybrid precoding. In [95], a comprehensive overview and comparison between these options was presented. Some preliminary simulation results regarding the impact of low-resolution ADCs on the directional synchronization were also provided in [95]. The corresponding beamforming strategies, however, are not optimized for low-resolution ADCs. To obtain a quantizer model that can better characterize the beamforming effect, the spatial correlation induced by the directional transmission was incorporated in [96] when modeling the quantization distortion for rate and energy efficiency analysis. In [97], an energy-rate trade-off was developed for a generalized hybrid analog/digital beamforming and combining architecture with low-resolution

ADCs. The directional synchronization problem under low-resolution ADCs, however, was not addressed in either [96] or [97]. In [98], by exploiting the sparse nature of the mmWave channels, a new compressive sensing based beam training method was proposed and evaluated to track and compensate for the synchronization impairments; the impact of low-resolution ADCs on the synchronization performance was not included.

5.2 Contributions

In this chapter, we propose and evaluate a new beamforming strategy to improve the frame timing synchronization performance for mmWave cellular systems under low-resolution ADCs. Our proposed approach incorporates multiple users and optimizes the overall synchronization performance. In our system model, the BS deploys multiple RF chains and simultaneously forms multiple synchronization beams in the analog domain. Upon receiving the synchronization signals, the UE conducts cross-correlation based frame timing synchronization with fully digital front ends and low-resolution ADCs. We summarize the main contributions of the chapter as follows:

- For a single UE with low-resolution ADCs, we leverage Bussgang's decomposition theorem [99, 100] to formulate the corresponding received synchronization SQNR at zero-lag correlation. This formulation accounts for both the spatial correlation brought by the directional beamforming and the inherent correlation of the employed synchronization signals. Building on the derivation of a single UE's synchronization SQNR,

we extend the problem formulation of low-resolution synchronization to a multi-user scenario. In this case, we focus on maximizing the minimum received synchronization SQNR at zero-lag correlation among all UEs. We show that this type of max-min multicast problem cannot be effectively solved by existing single-stream beamforming based approaches due to large quantization distortion and limited beam codebook resolution.

- Without channel knowledge (a common assumption for synchronization), we first discretize the given angular range with a set of potential channel directions and transform the complex max-min multicast problem into a maximization problem. We then develop a new multi-beam probing based directional synchronization strategy to tackle this problem. Leveraging a common synchronization signal structure design, the simultaneously probed synchronization beams form an effective composite beam. We show that by optimizing the effective composite beam pattern, a good tradeoff between the beamforming gain and the resulted quantization distortion can be achieved, resulting in improved frame timing synchronization performance under low-resolution quantization.

In essence, optimizing the received synchronization SQNR at zero-lag correlation is a viable solution to improve the overall frame timing synchronization performance under low-resolution ADCs. This is because for well-structured synchronization signals, the non-zero-lag correlation values are small and barely

163

affected by the quantization, while the zero-lag peak correlation value is significantly distorted by the quantization. We use several analytical and numerical examples to reveal these observations. We also conduct simulations of wideband mmWave cellular systems, showing that the proposed design approach can achieve promising received synchronization SQNR, frame timing position estimation, and access delay performances assuming low-resolution quantization.

We organize the rest of this chapter as follows. In Section 5.3, we specify the system and channel models for the directional frame timing synchronization design in mmWave systems. In Section 5.4, we formulate the directional frame timing synchronization problem under low-resolution ADCs. In Section 5.5, we explicitly illustrate the design principle and procedure of the proposed multi-beam probing strategy. We evaluate the proposed synchronization method in Section 5.6 assuming both narrowband and wideband channels. We draw our conclusions in Section 5.7.

5.3 Models and Assumptions

In this section, we introduce the system model for the directional frame timing synchronization design in mmWave systems. We also summarize the common wideband channel model.

5.3.1 System model for directional frame timing synchronization in mmWave systems

In this chapter, we assume that the BS employs directional beams to transmit the downlink synchronization signals, providing sufficient link margin at mmWave frequencies. Note that the directional transmission of downlink synchronization signals will also be supported in the 3GPP 5G New Radio (NR) systems [74, 101]. In the following, we first present the assumed antenna array configurations and transceiver architecture along with the synchronization signal structure. We then develop the received synchronization signal model for our system. Finally, we explain the cross-correlation based frame timing synchronization design using the derived received signal model.

5.3.1.1 Transceiver architecture, array configurations and synchronization signal structure

We consider a precoded MIMO-OFDM system with N subcarriers and a hybrid precoding transceiver structure as shown in Figures 5.1(a) and 5.1(b), in which the BS deploys N_{tot} transmit antennas and N_{RF} RF chains, and the UE deploys M_{tot} receive antennas and M_{RF} RF chains. Both the BS and UE employ array-of-subarray architectures. As can be seen from Figure 5.1, in an array-of-subarray architecture, a single RF chain controls an antenna subarray. Denote the number of antenna elements in each transmit subarray by N_{A} and the number of antenna elements in each receive subarray by M_{A}. Then $N_{\text{tot}} = N_{\text{RF}}N_{\text{A}}$ and $M_{\text{tot}} = M_{\text{RF}}M_{\text{A}}$. For fully digital processing, $N_{\text{A}} = M_{\text{A}} = 1$, while for single-stream analog-only processing, $N_{\text{RF}} = M_{\text{RF}} = 1$.
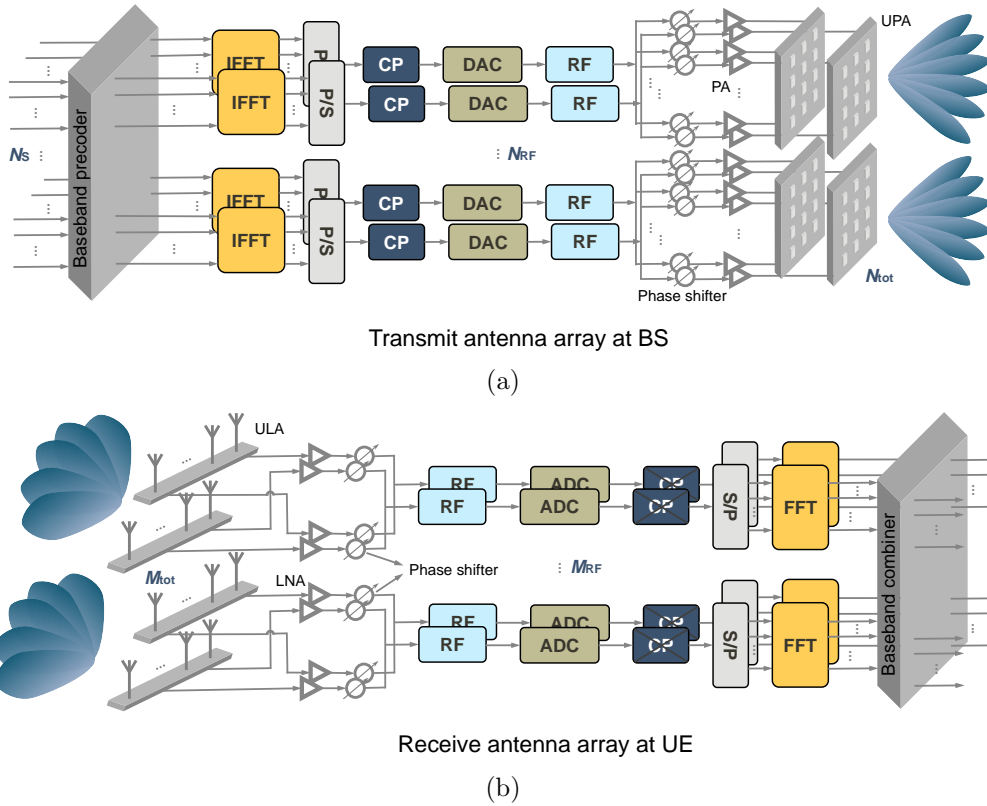
Figure 5.1: (a) Array-of-subarray architecture is employed at the BS with N_{RF} RF chains and N_{tot} transmit antenna elements. (b) Array-of-subarray architecture is employed at the UE with M_{RF} RF chains and M_{tot} receive antenna elements.

In this chapter, we employ ZC sequences for the downlink synchronization signals. Denote the length of the employed ZC sequence by N_{ZC} and the sequence root index by i ($i \in \{0, \cdots, N_{\mathrm{ZC}} - 1\}$). For $m = 0, \cdots, N_{\mathrm{ZC}} - 1$, the sequence can be represented as

$$s_i[m] = \exp\left\{-\mathrm{j}\frac{\pi m(m+1)i}{N_{\mathrm{ZC}}}\right\}. \tag{5.1}$$

The cyclic auto-correlation of the ZC sequence results in a single dirac-impulse

at zero-lag correlation, i.e.,

$$\chi[v] = \sum_{m=0}^{N_{\text{ZC}}-1} s_i[m] s_i^*[((m+v))_{N_{\text{ZC}}}] = \delta[v], \quad v = 0, \cdots, N_{\text{ZC}} - 1. \qquad (5.2)$$

The UE can therefore use this property to detect the correct frame timing position. In practice, the channel variations, noise power, and other impairments will affect the actual correlation values. Especially under low-resolution quantization, the good correlation properties of the ZC sequence are severely deteriorated by the quantization distortion. Besides the ZC-type sequences, Golay complementary sequences (GCSs) [102] exhibit a similar correlation property to (5.2). As a Golay complementary pair contains two sequences, both cyclic prefix and cyclic postfix are needed in the GCSs to prevent the inter-symbol interference, while only the cyclic prefix is appended to the ZC sequence when it is propagated through the multi-path channels. Nevertheless, the GCSs can also be employed for downlink synchronization. The corresponding problem formulation, however, would be different from that in the ZC sequence design when exploiting the complementary sequence structure.

Denote the frequency-domain modulated symbol on subcarrier $k = 0, \cdots, N - 1$ by $\mathsf{d}[k]$. We can then explicitly express the mapping between the ZC sequence and the subcarriers as

$$\mathsf{d}[\lfloor (N - N_{\text{ZC}} - 1)/2 \rfloor + m + 1] = \begin{cases} s_i[m], & m = 0, \cdots, N_{\text{ZC}} - 1, \\ 0, & \text{otherwise.} \end{cases} \qquad (5.3)$$

Note that (5.3) implies that in the frequency-domain, we map the ZC sequence onto the central N_{ZC} subcarriers (out of N subcarriers) surrounding the DC-carrier symmetrically. In this chapter, we set the DC-carrier as zero as in the
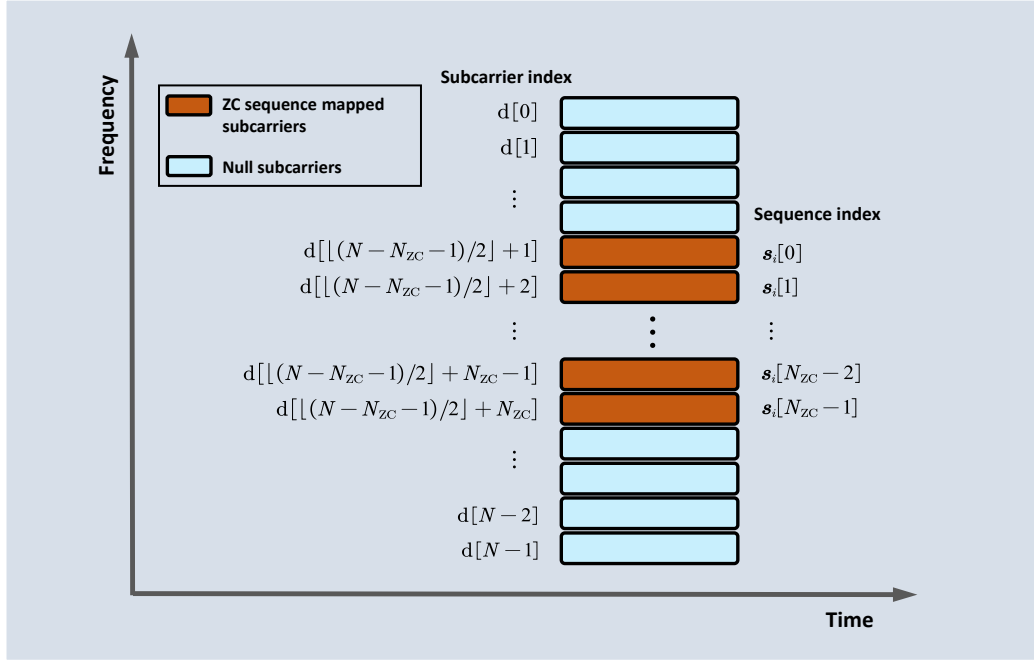
Figure 5.2: A conceptual example of the mapping between the ZC sequence and the subcarriers in the frequency-domain. A length-N_{ZC} ZC sequence is mapped onto the central N_{ZC} subcarriers out of a total N subcarriers.

LTE systems [86]; it is worth noting that no explicit DC-carrier is reserved for both the downlink and uplink in the 3GPP 5G NR systems (Release 15) [74]. We provide a conceptual example in Figure 5.2 to reveal this mapping relationship.

5.3.1.2 Synchronization frame structure and directional synchronization procedure

Now, we explain the directional frame timing synchronization procedure. We start by introducing a potential frame structure, which is shown in
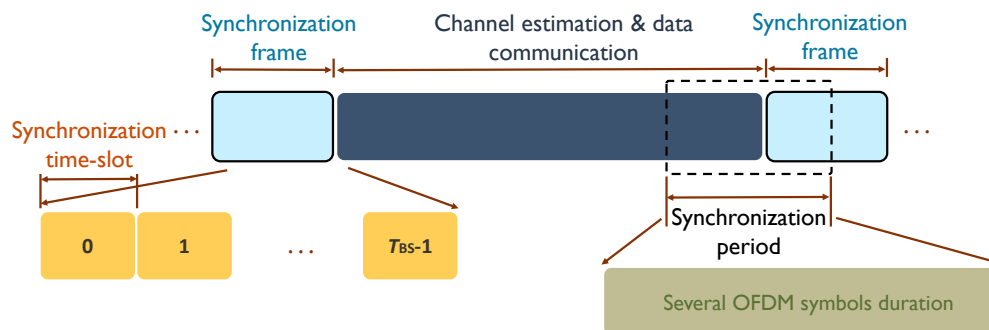
Figure 5.3: A conceptual example of a potential synchronization frame structure. The BS-wise synchronization frame consists of T_{BS} synchronization time-slots. The length of one UE-wise synchronization period is equivalent to T_{UE} OFDM symbols.

Figure 5.3. We define a time-slot, which may be one OFDM symbol duration (T_{s}). We also define a synchronization frame, in which the BS transmits the downlink synchronization signals to the UEs. As can be seen from Figure 5.3, each synchronization frame consists of T_{BS} synchronization time-slots. Different from uplink random access channels, the downlink multicast synchronization channels do not require guard intervals between the synchronization time-slots to deal with the propagation delay [86]. In conventional single-stream beamforming based approaches [74, 101], for a given synchronization time-slot, the BS probes one synchronization beam towards a predefined angular direction using a single RF chain. Across T_{BS} synchronization time-slots, the downlink synchronization beams fully scan the given angular range in a TDM manner.

Upon awakening from idle mode or power-up, the UE attempts to syn-

chronize to the network and then performs a random access procedure. We therefore define a UE-wise synchronization period here, which is shown on the right-hand side in Figure 5.3. For a given synchronization period, the UE employs fully digital front ends to detect the synchronization signal samples. In this chapter, the length of one synchronization period is equivalent to the duration of T_{UE} OFDM symbols.

In this dissertation, we use this hybrid transceiver architecture, i.e., analog-only structure at the BS and fully digital front ends at the UE, to formulate the optimization problems and develop the corresponding algorithms. This is mainly because: (i) the hybrid architecture is compatible with the current 3GPP 5G NR standards, (ii) the power consumption and implementation cost (e.g., brought by the quantization) are more crucial design aspects at the low-cost UE side than those at the BS side, and (iii) the major processing of the low-resolution timing synchronization happens at the UE side.

5.3.1.3 Received synchronization signal model

Based on the employed array configurations and synchronization signal structure, we develop the received synchronization signal model assuming $N_{\mathrm{RF}} = 1$, i.e., single-stream analog-only beamforming at the BS and $M_{\mathrm{RF}} = M_{\mathrm{tot}}$, i.e., fully digital baseband combining at the UE. Note that in Section 5.5, we will modify the received synchronization signal model by assuming $N_{\mathrm{RF}} > 1$. We consider a given UE $u \in \{1, \cdots, N_{\mathrm{UE}}\}$ in a single cell, where N_{UE} corresponds to the total number of UEs in the cell of interest. For

better illustration of the synchronization procedure, we assume $T_{\mathrm{BS}} = 1$, i.e., a single synchronization time-slot, say, synchronization time-slot 0. We further assume that all the synchronization signal samples $\{\mathsf{d}[0], \cdots, \mathsf{d}[N-1]\}$ sent during synchronization time-slot 0 are received by the UE across the synchronization period. Based on these assumptions, we now derive the received signal model for our system.

The symbol vector $\mathbf{d}$ in (5.3) is first transformed to the time-domain via N-point IFFTs, generating the discrete-time signals at symbol durations $n = 0, \cdots, N-1$ as

$$d[n] = \frac{1}{\sqrt{N}} \sum_{k=0}^{N-1} \mathsf{d}[k] e^{\mathsf{j}\frac{2\pi k}{N} n}. \tag{5.4}$$

Before applying an $N_{\mathrm{tot}} \times 1$ wideband analog beamforming vector, a CP is added to the symbol vector such that the length of the CP is greater than or equal to the maximum delay spread of the multi-path channels. Each sample in the symbol vector is then transmitted by a common wideband analog beamforming vector $\boldsymbol{f}_0$ probed from the BS, satisfying the power constraint $[\boldsymbol{f}_0 \boldsymbol{f}_0^*]_{a,a} = \frac{1}{N_{\mathrm{tot}}}$, where $a = 1, \cdots, N_{\mathrm{tot}}$. In this chapter, we use superscript (0) to denote variables obtained assuming $\boldsymbol{f}_0$.

Considering the b-th receive antenna ($b \in \{1, \cdots, M_{\mathrm{tot}}\}$) at UE u, we denote the time-domain received signal samples by $\boldsymbol{q}_{u,b}^{(0)} = \left[q_{u,b}^{(0)}[0], \cdots, q_{u,b}^{(0)}[N T_{\mathrm{UE}} - 1]\right]^{\mathrm{T}}$. Note that we ignore the CPs here because they do not affect our proposed frame timing synchronization strategy. The CPs will be discarded after the timing synchronization to mitigate the inter-symbol interference, and

the remaining samples are further processed for other initial access tasks. Denote the number of channel taps by L_u, the corresponding channel impulse response at tap $\ell \in \{0, \cdots, L_u - 1\}$ by $\boldsymbol{H}_u[\ell] \in \mathbb{C}^{M_{\text{tot}} \times N_{\text{tot}}}$, and the additive white Gaussian noise by $w_u[n] \sim \mathcal{N}_c(0, \sigma^2)$. We incorporate the effect of carrier frequency offset (CFO) in the received signal model. The CFO is a result of frequency mismatch between the transceiver's oscillators and the Doppler shift. Denote the frequency mismatch with respect to the subcarrier spacing by ε_u. As the UE employs fully digital baseband processing, each receive antenna first quantizes the received synchronization signals with dedicated ADCs. Denote $\mathcal{Q}(\cdot)$ as the quantization function. Further, denote the index of the first synchronization signal sample in the received signal by $t \in \{0, \cdots, N(T_{\text{UE}} - 1)\}$. For $n = 0, \cdots, N - 1$, the received samples are

$$q_{u,b}^{(0)}[t + n] = \mathcal{Q}\left(e^{j\frac{2\pi\varepsilon_u}{N}n} \sum_{\ell=0}^{L_u-1} [\boldsymbol{H}_u[\ell]]_{b,:} \, \boldsymbol{f}_0 d[((n - \ell))_N] + w_u[n]\right). \tag{5.5}$$

Practical cellular networks such as the LTE systems [86] perform the frame timing synchronization in the presence of CFO. After correctly detecting the frame timing, the UE then estimates the CFO and conducts the frequency synchronization. In this chapter, we set the offset $\varepsilon_u = 0$ ($u = 1, \cdots, N_{\text{UE}}$) in the following derivations. This is mainly because the CFO does not affect the development of the proposed frame timing synchronization algorithm in Section 5.5, though it affects the overall frame timing synchronization performance. In Section 5.6, we provide a simulation plot to characterize the CFO effect on the timing synchronization performance. Neglecting the CFO, we

rewrite (6.2) as

$$q_{u,b}^{(0)}[\mathrm{t}+n] = \mathcal{Q}\left(\underbrace{\sum_{\ell=0}^{L_u-1}[\boldsymbol{H}_u[\ell]]_{b,:}\,\boldsymbol{f}_0 d[((n-\ell))_N]+w_u[n]}_{y_{u,b}^{(0)}[\mathrm{t}+n]}\right). \qquad (5.6)$$

The received signal samples $\{q_{u,b}^{(0)}[0],\cdots,q_{u,b}^{(0)}[NT_{\mathrm{UE}}-1]\}$ also contain non-synchronization signal samples. Hence, we have

$$q_{u,b}^{(0)}[m'] = \begin{cases} \mathcal{Q}\left(\sum_{\ell=0}^{L_u-1}[\boldsymbol{H}_u[\ell]]_{b,:}\,\boldsymbol{f}_0 d[((m'-\mathrm{t}-\ell))_N]+w_u[m'-\mathrm{t}]\right), \\ \mathcal{Q}(w_u[m']),\ \ \text{otherwise,} \end{cases} \qquad (5.7)$$

for $m' = \mathrm{t},\cdots,\mathrm{t}+N-1$. As can be seen from (5.7), we model the received non-synchronization signal samples as noise, though they may contain deterministic data and/or control information.

By using the discrete-time received signal vector $\boldsymbol{q}_{u,b}^{(0)}$ and the known unquantized reference synchronization sequence, the frame timing synchronization can be conducted by UE u. According to (6.1), the unquantized reference synchronization sequence locally stored at the UE is $\boldsymbol{d} = \left[d[0],d[1],\cdots,d[N-1]\right]^{\mathrm{T}}$. The UE then calculates the time-domain cross-correlation between the received signal samples and the unquantized reference synchronization sequence for the b-th receive antenna as

$$\Gamma_{u,b}^{(0)}[\nu] = \sum_{n=0}^{N-1} q_{u,b}^{(0)}[n+\nu]d^*[n], \qquad (5.8)$$

where $\nu = 0,\cdots,N(T_{\mathrm{UE}}-1)$. Denote the index of the selected receive antenna by $\hat{b}$. The maximum likelihood detector [103] finds the estimate of the frame

173
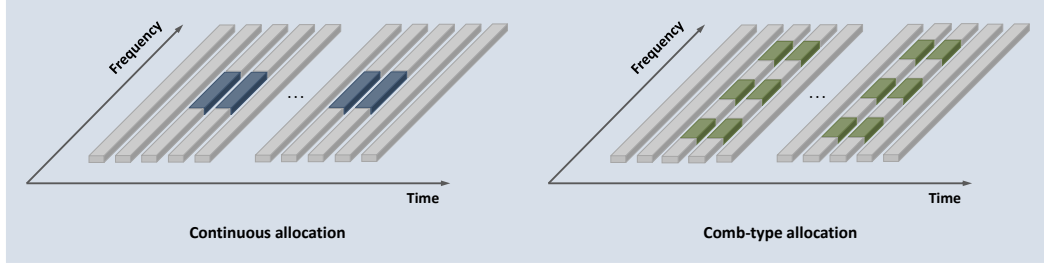
Figure 5.4: A conceptual example of continuous and comb-type subcarriers allocation methods for timing synchronization signal. In the continuous allocation strategy, the synchronization signal occupies a set of continuous subcarriers located in the center of the given frequency band. In the comb-type allocation strategy, the synchronization signal is sent across a set of discontinuous and equally spaced sub-signals in the frequency domain.

timing position $\hat{\nu}$ that corresponds to the peak in the correlation, i.e.,

$$\left(\hat{\nu}, \hat{b}\right) = \underset{\substack{\nu=0,\cdots,N(T_{\mathrm{UE}}-1) \\ b=1,\cdots,M_{\mathrm{tot}}}}{\mathrm{argmax}} \left|\Gamma_{u,b}^{(0)}[\nu]\right|^2. \tag{5.9}$$

If $\mathcal{Q}(\cdot)$ in (5.6) and (5.7) corresponds to low-resolution quantization (e.g., 1-4 bits), the corresponding quantization distortion will damage the good correlation properties of the employed synchronization sequences, leading to degraded timing synchronization performance.

5.3.1.4 Resource allocation for synchronization signal

In this dissertation, we consider two subcarrier and synchronization signal mapping strategies, which are (i) continuous subcarriers allocation, and (ii) comb-type subcarriers allocation. In Figure 5.4, we depict a conceptual example to characterize these two design options. As can be seen from Figure 5.4, in the continuous subcarriers allocation strategy, we map the synchronization

174

sequence onto a set of continuous subcarriers in the frequency domain, symmetrically surrounding the direct current (DC)-carrier. This mapping strategy is similar to the primary synchronization signal (PSS) structure in the LTE systems. In the comb-type subcarriers allocation method, we also assign a set of continuous subcarriers to a synchronization sequence (i.e., a sub-signal), but send multiple such sub-signals (N_{sub}) in a given synchronization time-slot (as shown in Figure 5.4). The comb-type PSS structure was originally proposed in [95] for cell discovery in mmWave systems. In this dissertation, we use this design for low-resolution timing synchronization. By configuring a minimum possible bandwidth for each sub-signal, the comb-type design can better enforce the flat channel and constant quantization distortion assumptions. Further, by exploiting frequency diversity of mmWave channels via the comb-type structure, good timing synchronization performance can be achieved. For simplicity, we employ the continuous subcarriers allocation strategy to illustrate the problem formulation, design principle, and implementation procedure of our proposed solution. Note that they can be extended to the comb-type assignment with moderate modifications. In the numerical evaluation section, we numerically compare the comb-type and continuous subcarriers allocation strategies in terms of the timing position estimation performance.

5.3.2 Channel model

Assume that the channel between the BS and UE $u \in \{1, \cdots, N_{\mathrm{UE}}\}$ has R_u paths, and each path r has azimuth and elevation AoDs $\phi_{u,r}$, $\theta_{u,r}$ and

AoA $\psi_{u,r}$. Let $p(\tau)$ denote the combined effect of filtering and pulse shaping for $T_{\rm s}$-spaced signaling at τ seconds. We then express the time-domain delay-ℓ MIMO channel matrix as

$$\boldsymbol{H}_u[\ell] = \sum_{r=1}^{R_u} \beta_{u,r} p\left(\ell T_{\rm s} - \tau_r\right) \boldsymbol{a}_{\rm rx}(\psi_{u,r}) \boldsymbol{a}_{\rm tx}^*(\theta_{u,r}, \phi_{u,r}), \tag{5.10}$$

where $\beta_{u,r}$ represents the complex path gain of path-r between the BS and UE u, and $\boldsymbol{a}_{\rm rx}(\cdot) \in \mathbb{C}^{M_{\rm tot} \times 1}$ and $\boldsymbol{a}_{\rm tx}(\cdot, \cdot) \in \mathbb{C}^{N_{\rm tot} \times 1}$ correspond to the receive and transmit array response vectors. For instance, if the BS employs a UPA in the xy-plane and the UE uses a ULA on the y axis, $\boldsymbol{a}_{\rm tx}(\cdot, \cdot)$ and $\boldsymbol{a}_{\rm rx}(\cdot)$ would exhibit the same structures as those in (3) and (4) in [43]. Note that the proposed design approach does not depend on array geometry. Define $\boldsymbol{A}_u^{\rm RX}$ and $\boldsymbol{A}_u^{\rm TX}$ as

$$\boldsymbol{A}_u^{\rm RX} = \left[\boldsymbol{a}_{\rm rx}(\psi_{u,1}) \; \boldsymbol{a}_{\rm rx}(\psi_{u,2}) \; \cdots \; \boldsymbol{a}_{\rm rx}(\psi_{u,R_u})\right], \tag{5.11}$$

$$\boldsymbol{A}_u^{\rm TX} = \left[\boldsymbol{a}_{\rm tx}(\theta_{u,1}, \phi_{u,1}) \; \boldsymbol{a}_{\rm tx}(\theta_{u,2}, \phi_{u,2}) \; \cdots \; \boldsymbol{a}_{\rm tx}(\theta_{u,R_u}, \phi_{u,R_u})\right], \tag{5.12}$$

which contain the receive and transmit array response vectors and a diagonal matrix $\boldsymbol{G}_u[\ell] = \mathrm{diag}\left([g_{u,1,\ell}, \cdots, g_{u,R_u,\ell}]^{\rm T}\right)$, where $g_{u,r,\ell} = \beta_{u,r} p\left(\ell T_{\rm s} - \tau_r\right)$ for $r \in \{1, \cdots, R_u\}$. We can then rewrite the channel matrix in (5.10) in a more compact form as $\boldsymbol{H}_u[\ell] = \boldsymbol{A}_u^{\rm RX} \boldsymbol{G}_u[\ell] \left(\boldsymbol{A}_u^{\rm TX}\right)^*$. Denote the corresponding channel frequency response on subcarrier $k = 0, \cdots, N-1$ by $\mathbf{G}_u[k]$. We have $\mathbf{G}_u[k] = \sum_{\ell=0}^{L_u-1} \boldsymbol{G}_u[\ell] e^{-{\rm j}2\pi\ell k/N}$ and $\mathbf{g}_{u,r,k} = [\mathbf{G}_u[k]]_{r,r} = \sum_{\ell=0}^{L_u-1} g_{u,r,\ell} e^{-{\rm j}2\pi\ell k/N}$. We can then express the corresponding frequency-domain channel matrix as $\mathbf{H}_u[k] = \boldsymbol{A}_u^{\rm RX} \mathbf{G}_u[k] \left(\boldsymbol{A}_u^{\rm TX}\right)^*$. In Sections 5.4 and 5.5, we use $\boldsymbol{H}_u[\ell]$ to develop

the received synchronization signal model in the time-domain and $\mathbf{H}_u[k]$ to illustrate the proposed algorithm in the frequency-domain.

5.4 Optimization Problem Formulation for Timing Synchronization with Few-Bit ADCs

In this section, we first formulate the directional frame timing synchronization problem for mmWave systems operating with low-resolution ADCs. We then show that the formulated problem is a max-min multicast optimization problem, which cannot be effectively solved under the framework of single-stream beamforming. For clarity, we conduct the problem formulation using the frequency-domain representations, though we first present the received signal model in the time-domain.

5.4.1 Optimization metric for low-resolution timing synchronization

To formulate the optimization problem for low-resolution timing synchronization, we need to first determine a proper optimization metric. Similar to Section 5.3.1, we assume a single synchronization time-slot, single-stream analog-only beamforming at the BS and fully digital baseband processing at the UE. By Bussgang's theorem [99, 100], the quantization output in (5.6) can be decoupled into a signal part and an uncorrelated distortion component. This decomposition is accurate in low and medium SNR ranges [95]. We first define $\boldsymbol{E}_{u,b}^{(0)} = \mathrm{diag}\left(\left[\eta_{u,b}^{(0)}[0], \cdots, \eta_{u,b}^{(0)}[N-1] \right]^{\mathrm{T}} \right)$ as the quantization distortion

matrix with

$$\eta_{u,b}^{(0)}[n] = \frac{\mathbb{E}\left[\left(q_{u,b}^{(0)}[t+n]\right)^* y_{u,b}^{(0)}[t+n]\right]}{\mathbb{E}\left[\left|y_{u,b}^{(0)}[t+n]\right|^2\right]}, \tag{5.13}$$

as the distortion factor of the quantization, which depends on the quantizer design, the number of quantization bits and the distribution of the input samples to the quantizer [104]. Rewriting

$$\boldsymbol{d}_\ell = [d[((-\ell))_N], d[((1-\ell))_N], \cdots, d[((N-1-\ell))_N]]^{\mathrm{T}}, \tag{5.14}$$

and $\boldsymbol{q}_{u,b}^{(0)} = \left[q_{u,b}^{(0)}[t], \cdots, q_{u,b}^{(0)}[t+N-1]\right]^{\mathrm{T}}$, we then decompose (5.6) as

$$\boldsymbol{q}_{u,b}^{(0)} = \boldsymbol{E}_{u,b}^{(0)} \underbrace{\left(\sum_{\ell=0}^{L_u-1} [\boldsymbol{H}_u[\ell]]_{b,:} \, \boldsymbol{f}_0 \boldsymbol{d}_\ell + \boldsymbol{w}_u \right)}_{\boldsymbol{v}_{u,b}^{(0)}} + \check{\boldsymbol{w}}_{u,b}^{(0)}. \tag{5.15}$$

Denote the quantization mean squared error by ξ_u assuming Gaussian signaling with unit variance [96]. We further denote the covariance matrix of the noiseless unquantized received signal $\boldsymbol{v}_{u,b}^{(0)}$ in (5.15) by $\boldsymbol{R}_{\boldsymbol{v}_{u,b}^{(0)}}$ and the additive quantization noise vector by $\check{\boldsymbol{w}}_{u,b}^{(0)} = \left[\check{w}_{u,b}^{(0)}[0], \cdots, \check{w}_{u,b}^{(0)}[N-1]\right]^{\mathrm{T}}$. As shown in [96], the quantization distortion matrix $\boldsymbol{E}_{u,b}^{(0)}$ can then be computed as

$$\boldsymbol{E}_{u,b}^{(0)} = (1 - \xi_u)\mathrm{diag}\left(\boldsymbol{R}_{\boldsymbol{v}_{u,b}^{(0)}} + \sigma^2 \boldsymbol{I}_N\right)^{-\frac{1}{2}}. \tag{5.16}$$

Denoting the unquantized received signal power matrix for the b-th receive antenna at UE u by $\boldsymbol{V}_{u,b}^{(0)}$, we can express the covariance matrix of the quantization noise vector $\check{\boldsymbol{w}}_{u,b}^{(0)}$ as [96, 97]

$$\boldsymbol{R}_{\check{\boldsymbol{w}}_{u,b}^{(0)}} = \boldsymbol{E}_{u,b}^{(0)}\left(\boldsymbol{I}_N - \boldsymbol{E}_{u,b}^{(0)}\right) \underbrace{\mathrm{diag}\left(\boldsymbol{R}_{\boldsymbol{v}_{u,b}^{(0)}} + \sigma^2 \boldsymbol{I}_N\right)}_{\boldsymbol{V}_{u,b}^{(0)}}. \tag{5.17}$$

178

As can be seen from (5.16) and (5.17), both $\boldsymbol{E}_{u,b}^{(0)}$ and $\boldsymbol{R}_{\check{\boldsymbol{w}}_{u,b}^{(0)}}$ depend on $\boldsymbol{R}_{\boldsymbol{v}_{u,b}^{(0)}}$, which depends on the effective beam-space channel.

In the following, we compute the zero-lag correlation between the received signal samples and the known unquantized reference synchronization sequence in the frequency-domain. We first express the frequency-domain quantized received signal $\mathbf{q}_{u,b}^{(0)} = \left[\mathsf{q}_{u,b}^{(0)}[0], \cdots, \mathsf{q}_{u,b}^{(0)}[N-1] \right]^{\mathrm{T}}$ as

$$\mathsf{q}_{u,b}^{(0)}[k] = \eta_{u,b}^{(0)}[k] \left[\boldsymbol{A}_u^{\mathrm{RX}} \mathbf{G}_u[k] \left(\boldsymbol{A}_u^{\mathrm{TX}} \right)^* \right]_{b,:} \boldsymbol{f}_0 \mathsf{d}[k] + \eta_{u,b}^{(0)}[k] \mathsf{w}_u[k] + \check{\mathsf{w}}_{u,b}^{(0)}[k],$$

(5.18)

where $\check{\mathsf{w}}_{u,b}^{(0)}[k] = \sum_{n=0}^{N-1} \check{w}_{u,b}^{(0)}[n] e^{-\mathrm{j}2\pi nk/N}$. We then calculate the zero-lag frequency domain correlation between $\mathbf{q}_{u,b}^{(0)}$ and the unquantized reference synchronization sequence $\mathbf{d}$ as

$$\begin{aligned}
\Lambda_{u,b}^{(0)}[0] &= \sum_{k=0}^{N-1} \mathsf{q}_{u,b}^{(0)}[k] \mathsf{d}^*[k] \qquad\qquad\qquad (5.19) \\
&= \sum_{k=0}^{N-1} \eta_{u,b}^{(0)}[k] \left[\boldsymbol{A}_u^{\mathrm{RX}} \mathbf{G}_u[k] \left(\boldsymbol{A}_u^{\mathrm{TX}} \right)^* \right]_{b,:} \boldsymbol{f}_0 \mathsf{d}[k] \mathsf{d}^*[k] \\
&\quad + \sum_{k=0}^{N-1} \eta_{u,b}^{(0)}[k] \mathsf{w}_u[k] \mathsf{d}^*[k] + \sum_{k=0}^{N-1} \check{\mathsf{w}}_{u,b}^{(0)}[k] \mathsf{d}^*[k]. \qquad (5.20)
\end{aligned}$$

Similar to (5.8), we have $\hat{b} = \underset{b=1,\cdots,M_{\mathrm{tot}}}{\operatorname{argmax}} \left| \Lambda_{u,b}^{(0)}[0] \right|^2$.

Different from high-rate data communications, the synchronization signals usually occupy a relatively small portion of the entire bandwidth with continuous subcarriers surrounding the DC-carrier. For instance, in the LTE systems [86], the synchronization signal samples occupy 62 subcarriers (out of

1024 for 10 MHz bandwidth, or 2048 for 20 MHz bandwidth) surrounding the DC-carrier. If the same design principle applies to mmWave systems, along with the sparse nature of the mmWave channels, the synchronization signals will most likely experience "flat" channels instead of severe frequency selectivity. It is also worth noting that the ZC-type sequences are robust to the frequency selectivity [105].

Leveraging the flat synchronization channels assumption and denoting the frequency-domain counterpart of the unquantized received signal power matrix $\boldsymbol{V}_{u,\hat{b}}^{(0)}$ in (5.17) by $\mathbf{V}_{u,\hat{b}}^{(0)}$, we can first obtain

$$
\begin{aligned}
\mathbf{V}_{u,\hat{b}}^{(0)} &= \mathsf{g}_u^2 \left| [\boldsymbol{a}_{\mathrm{rx}}(\psi_u)\boldsymbol{a}_{\mathrm{tx}}^*(\theta_u, \phi_u)]_{\hat{b},:} \, \boldsymbol{f}_0 \right|^2 \mathrm{diag}\,(\mathbf{dd}^*) + \sigma^2 \boldsymbol{I}_N \qquad (5.21) \\
&= \mathsf{g}_u^2 \left| [\boldsymbol{a}_{\mathrm{rx}}(\psi_u)\boldsymbol{a}_{\mathrm{tx}}^*(\theta_u, \phi_u)]_{\hat{b},:} \, \boldsymbol{f}_0 \right|^2 \\
&\quad \times \; \mathrm{diag}\,\left([\mathsf{d}[0]\mathsf{d}^*[0], \cdots, \mathsf{d}[N-1]\mathsf{d}^*[N-1]]^{\mathrm{T}} \right) + \sigma^2 \boldsymbol{I}_N, \quad (5.22)
\end{aligned}
$$

where the path and subcarrier indices are dropped. Also because of the flat synchronization channels assumption, we define $\underline{\eta}_{u,\hat{b}}^{(0)} = \eta_{u,\hat{b}}^{(0)}[0] = \cdots = \eta_{u,\hat{b}}^{(0)}[N-1]$ as a common quantization distortion factor. By exploiting the inherent correlation properties of the ZC sequence design in (5.2), we can compute the quantization noise power using (5.16), (5.17) and (5.22). We can then formulate the corresponding received synchronization SQNR at zero-lag correlation for UE u as

$$
\gamma_{u,\hat{b}}^{(0)} = \frac{\underline{\eta}_{u,\hat{b}}^{(0)} \mathsf{g}_u^2 \left| [\boldsymbol{a}_{\mathrm{rx}}(\psi_u)\boldsymbol{a}_{\mathrm{tx}}^*(\theta_u, \phi_u)]_{\hat{b},:} \, \boldsymbol{f}_0 \right|^2}{\underline{\eta}_{u,\hat{b}}^{(0)}\sigma^2 + \left(1 - \underline{\eta}_{u,\hat{b}}^{(0)}\right) \left(\mathsf{g}_u^2 \left| [\boldsymbol{a}_{\mathrm{rx}}(\psi_u)\boldsymbol{a}_{\mathrm{tx}}^*(\theta_u, \phi_u)]_{\hat{b},:} \, \boldsymbol{f}_0 \right|^2 + \sigma^2 \right)}. \qquad (5.23)
$$
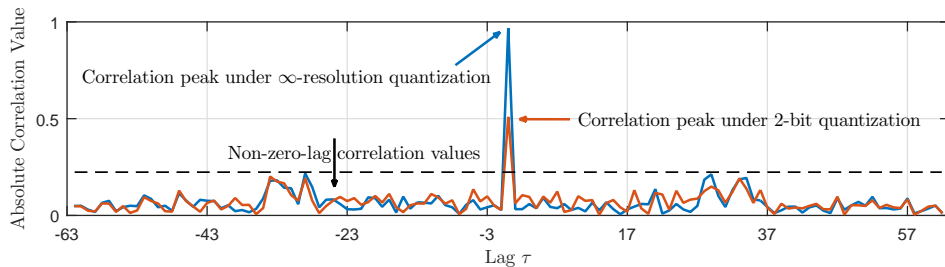
Figure 5.5: Absolute correlation values of the employed synchronization sequence under both infinite-resolution and 2-bit ADCs. To better characterize the impact of the quantization distortion on the absolute correlation values, a simple AWGN channel is considered with 0 dB SNR. The transmit beamforming is not incorporated. A length-62 ZC sequence with root index 34 is used.

Similar to the calculation of $\Lambda_{u,b}^{(0)}[0]$ in (5.19), we can also compute the non-zero-lag correlation values. In Figure 5.5, we plot the absolute correlation values of the employed synchronization sequence under both infinite-resolution and 2-bit ADCs. Both zero-lag and non-zero-lag correlations are revealed in this example. As can be seen from Figure 5.5, for both infinite-resolution and 2-bit ADCs, the non-zero-lag correlation values have small magnitudes and exhibit similar patterns. For the zero-lag correlation, however, the correlation peak obtained under 2-bit ADCs is much smaller than that under ∞-resolution quantization. Leveraging these observations, we employ the received synchronization SQNR at zero-lag correlation as the main optimization metric and formulate the corresponding optimization problems in Section 5.4.2.

5.4.2 Optimization problems for low-resolution timing synchronization

We first consider a single UE, e.g., UE u and a single synchronization time-slot, e.g., synchronization time-slot 0. Our design target here is to maximize the received synchronization SQNR at zero-lag correlation for UE u. Note that in (5.23), the only parameter that can be tuned is the beamforming vector. To better compensate for the quantization distortion, it is therefore desirable to custom design the synchronization beams as long as necessary information is available at the BS. This is different from traditional TDM probing based approaches [74, 101], where the synchronization beams are predetermined and fixed. According to (5.23), we can formulate this maximization problem as

$$\mathcal{P}0: \quad \max_{\boldsymbol{f}_0} \left\{ \gamma_{u,\hat{b}}^{(0)} \right\} \tag{5.24}$$
$$\text{s.t.} \quad [\boldsymbol{f}_0 \boldsymbol{f}_0^*]_{a,a} = \tfrac{1}{N_{\text{tot}}}, a = 1, \cdots, N_{\text{tot}}.$$

To simplify $\mathcal{P}0$, we assume that the BS uses a predefined analog beam codebook $\mathcal{F}$. We can then reformulate (5.24) as

$$\mathcal{P}1: \quad \max_{\boldsymbol{f}_0} \left\{ \gamma_{u,\hat{b}}^{(0)} \right\} \tag{5.25}$$
$$\text{s.t.} \quad \boldsymbol{f}_0 \in \mathcal{F}.$$

Solving $\mathcal{P}1$ does not increase the non-zero-lag correlation values at the same pace as the zero-lag peak correlation value. We verify this by the following lemma, which shows that maximizing the received synchronization SQNR at zero-lag correlation also maximizes the power difference between the zero-lag

peak correlation value and the non-zero-lag correlation values assuming low-resolution quantization.

Lemma 5.1. Consider the $\hat{b}$-th receive antenna at UE u equipped with low-resolution ADCs. Assume $\boldsymbol{f}_0$ and denote the corresponding power ratio between the zero-lag correlation value and a non-zero-lag correlation value by $\varsigma_{u,\hat{b}}^{(0)}$. For $\boldsymbol{f}_0^{\star}$, if the resulted received synchronization SQNR at zero-lag correlation $\gamma_{u,\hat{b}}^{(0)\star} = \max\left\{\gamma_{u,\hat{b}}^{(0)}, \boldsymbol{f}_0 \in \mathcal{F}\right\}$, then $\varsigma_{u,\hat{b}}^{(0)\star} = \max\left\{\varsigma_{u,\hat{b}}^{(0)}, \boldsymbol{f}_0 \in \mathcal{F}\right\}$.

The proof of Lemma 5.1 can be found in [45, Appendix].

Next, we extend the problem formulation to a single cell with multiple UEs. In this case, we expect that for a given synchronization time-slot, a group of UEs can simultaneously synchronize to the network with satisfying synchronization performance. This reduces the overall access delay of the network. The design target therefore becomes maximizing the minimum received synchronization SQNR at zero-lag correlation for all potential UEs. Assuming a total of N_{UE} UEs and synchronization time-slot 0, we formulate the following max-min optimization problem as

$$\mathcal{P}2: \quad \max_{\boldsymbol{f}_0} \ \min_{\forall u} \left\{\gamma_{u,\hat{b}}^{(0)}\right\} \tag{5.26}$$
$$\text{s.t. } \boldsymbol{f}_0 \in \mathcal{F}.$$

Denoting by $\lambda_u = \sigma^2/\mathrm{g}_u^2 \, |[\boldsymbol{a}_{\mathrm{rx}}(\psi_u)]_{\hat{b}}|^2$, we rewrite $\gamma_{u,\hat{b}}^{(0)}$ in (5.23) as

$$\gamma_{u,\hat{b}}^{(0)} \;\; = \;\; \frac{\underline{\eta}_{u,\hat{b}}^{(0)} \, |\boldsymbol{a}_{\mathrm{tx}}^*(\theta_u, \phi_u)\boldsymbol{f}_0|^2}{\underline{\eta}_{u,\hat{b}}^{(0)} \dfrac{\sigma^2}{\mathrm{g}_u^2 \, |[\boldsymbol{a}_{\mathrm{rx}}(\psi_u)]_{\hat{b}}|^2} + \left(1 - \underline{\eta}_{u,\hat{b}}^{(0)}\right)\left(|\boldsymbol{a}_{\mathrm{tx}}^*(\theta_u, \phi_u)\boldsymbol{f}_0|^2 + \dfrac{\sigma^2}{\mathrm{g}_u^2 \, |[\boldsymbol{a}_{\mathrm{rx}}(\psi_u)]_{\hat{b}}|^2}\right)}$$

$$(5.27)$$

$$= \;\; \frac{\underline{\eta}_{u,\hat{b}}^{(0)} \, |\boldsymbol{a}_{\mathrm{tx}}^*(\theta_u, \phi_u)\boldsymbol{f}_0|^2}{\underline{\eta}_{u,\hat{b}}^{(0)} \lambda_u + \left(1 - \underline{\eta}_{u,\hat{b}}^{(0)}\right)\left(|\boldsymbol{a}_{\mathrm{tx}}^*(\theta_u, \phi_u)\boldsymbol{f}_0|^2 + \lambda_u\right)}. \qquad (5.28)$$

We can interpret λ_u as the inverse of the received SNR at UE u. Denoting by $\lambda_{\max} = \max\{\lambda_1, \cdots, \lambda_{N_{\mathrm{UE}}}\}$ and replacing λ_u in (5.28) with $\lambda_{\max}$, we define a lower bound of $\gamma_{u,\hat{b}}^{(0)}$ as

$$\breve{\gamma}_{u,\hat{b}}^{(0)} = \frac{\underline{\eta}_{u,\hat{b}}^{(0)} \, |\boldsymbol{a}_{\mathrm{tx}}^*(\theta_u, \phi_u)\boldsymbol{f}_0|^2}{\underline{\eta}_{u,\hat{b}}^{(0)} \lambda_{\max} + \left(1 - \underline{\eta}_{u,\hat{b}}^{(0)}\right)\left(|\boldsymbol{a}_{\mathrm{tx}}^*(\theta_u, \phi_u)\boldsymbol{f}_0|^2 + \lambda_{\max}\right)}. \qquad (5.29)$$

For any given UE u, we therefore have

$$\breve{\gamma}_{u,\hat{b}}^{(0)} \leq \gamma_{u,\hat{b}}^{(0)}. \qquad (5.30)$$

By plugging the results of (5.16) and (5.22) into (5.29), we obtain

$$\breve{\gamma}_u^{(0)} = \frac{|\boldsymbol{a}_{\mathrm{tx}}^*(\theta_u, \phi_u)\boldsymbol{f}_0|^2}{\lambda_{\max} + \left[\dfrac{\left[\sigma^2\left(|\boldsymbol{a}_{\mathrm{tx}}^*(\theta_u,\phi_u)\boldsymbol{f}_0|^2/\lambda_{\max}+1\right)\right]^{1/2}}{1-\xi_u} - 1\right]\left(|\boldsymbol{a}_{\mathrm{tx}}^*(\theta_u, \phi_u)\boldsymbol{f}_0|^2 + \lambda_{\max}\right)}, \qquad (5.31)$$

which becomes irrelevant to the selected receive antenna index $\hat{b}$ for UE u. Denoting by $\xi_{\max} = \{\xi_1, \cdots, \xi_{N_{\mathrm{UE}}}\}$ and replacing ξ_u in (5.31) with $\xi_{\max}$, we can further define a lower bound of $\breve{\gamma}_u^{(0)}$ as

$$\acute{\gamma}_u^{(0)} = \frac{|\boldsymbol{a}_{\mathrm{tx}}^*(\theta_u, \phi_u)\boldsymbol{f}_0|^2}{\lambda_{\max} + \left[\dfrac{\left[\sigma^2\left(|\boldsymbol{a}_{\mathrm{tx}}^*(\theta_u,\phi_u)\boldsymbol{f}_0|^2/\lambda_{\max}+1\right)\right]^{1/2}}{1-\xi_{\max}} - 1\right]\left(|\boldsymbol{a}_{\mathrm{tx}}^*(\theta_u, \phi_u)\boldsymbol{f}_0|^2 + \lambda_{\max}\right)}. \qquad (5.32)$$

184

That is, for any given UE u, we have

$$\acute{\gamma}_u^{(0)} \leq \breve{\gamma}_u^{(0)}. \tag{5.33}$$

Note that $1/\lambda_{\max}$ and $1-\xi_{\max}$ represent the lowest received SNR and the lowest quantization resolution among all UEs, and they can be used to characterize the worst-case scenario of the network. Based on (5.30) and (5.33), we can therefore reformulate the optimization problem in (5.26) as

$$\mathcal{P}3: \max_{\boldsymbol{f}_0} \min_{\forall u} \left\{ \acute{\gamma}_u^{(0)} \right\} \tag{5.34}$$
$$\text{s.t. } \boldsymbol{f}_0 \in \mathcal{F}.$$

Solving (5.34) requires explicit knowledge of θ_u's, ϕ_u's, λ_u's ($\lambda_{\max}$), and ξ_u's ($\xi_{\max}$) for all UEs ($u = 1, \cdots, N_{\mathrm{UE}}$). In practice, $\lambda_{\max}$ and $\xi_{\max}$ can be replaced with predefined system-specific values that characterize the worst-case scenario of the network. The explicit channel directional information, however, is unavailable during the initial timing synchronization phase. In addition, a practical beam codebook $\mathcal{F}$ usually has a limited number of candidate beam codewords. Hence, for conventional single-stream multicast beamforming, the corresponding synchronization performance is highly limited by the beam codebook resolution especially under low-resolution quantization.

5.5 Proposed Low-Resolution Timing Synchronization

We develop a new multi-beam probing based low-resolution timing synchronization strategy to effectively solve the multicast problem. Along with a

common synchronization signal structure design, the proposed method exploits the spatial degrees of freedom arising from multiple RF chains to compensate for the quantization distortion without requiring explicit channel knowledge. Similar to Section 5.4, we explain the proposed algorithm using the frequency-domain representations, though we first present the received signal model in the time-domain.

5.5.1 Received signal model for multi-beam probing

We assume that for a given synchronization time-slot, the BS deploys multiple subarrays to simultaneously form multiple analog synchronization beams, through which a total of N_{UE} UEs synchronize to the network. This is different from the conventional directional synchronization design in Section 5.4.1, in which the BS sends one beam at a time. We set the corresponding baseband precoding matrix as identity matrix following the same methodology as in [106, 107]. Further, for the given synchronization time-slot, we assume that the BS transmits common synchronization signals (or identical synchronization sequences) across the simultaneously probed beams. This is also different from conventional MIMO communications, in which distinct signals are spatially multiplexed to boost the capacity.

For a given synchronization time-slot, we denote the employed analog

precoding matrix at the BS as

$$\boldsymbol{P} = \begin{bmatrix} \boldsymbol{p}_0 & \boldsymbol{0}_{N_A \times 1} & \cdots & \boldsymbol{0}_{N_A \times 1} \\ \boldsymbol{0}_{N_A \times 1} & \boldsymbol{p}_1 & \cdots & \boldsymbol{0}_{N_A \times 1} \\ \vdots & \vdots & \ddots & \vdots \\ \boldsymbol{0}_{N_A \times 1} & \boldsymbol{0}_{N_A \times 1} & \cdots & \boldsymbol{p}_{N_{RF}-1} \end{bmatrix}, \tag{5.35}$$

where for $j = 0, \cdots, N_{RF}-1$, the beam probed from the j-th transmit RF chain $\boldsymbol{p}_j \in \mathbb{C}^{N_A \times 1}$ satisfies the power constraint $\left[\boldsymbol{p}_j \boldsymbol{p}_j^* \right]_{a,a} = \frac{1}{N_A}$ with $a = 1, \cdots, N_A$. Denote the set of the analog synchronization beams by $\Omega = \{ \boldsymbol{p}_0, \cdots, \boldsymbol{p}_{N_{RF}-1} \}$. Similar to (6.2) and (5.6), we can then express the quantized time-domain received signal on the b-th receive antenna at UE $u \in \{1, \cdots, N_{UE}\}$ as

$$q_{u,b}^{\Omega}[t+n] = \mathcal{Q}\left(y_{u,b}^{\Omega}[t+n] \right) \tag{5.36}$$

$$= \mathcal{Q}\left(\left[\sum_{\ell=0}^{L_u-1} \sqrt{\frac{1}{N_{RF}}} \boldsymbol{H}_u[\ell] \boldsymbol{P} \left(d[((k-\ell))_N] \mathbf{1}_{N_{RF} \times 1} \right) \right]_b \right.$$

$$\left. + w_u[n] \right) \tag{5.37}$$

$$= \mathcal{Q}\left(\sum_{\ell=0}^{L_u-1} \sum_{j=0}^{N_{RF}-1} \sqrt{\frac{1}{N_{RF}}} \left([\boldsymbol{H}_u[\ell]]_{b,jN_A+1:(j+1)N_A} \boldsymbol{p}_j \right) d[((n-\ell))_N] \right.$$

$$\left. + w_u[n] \right), \tag{5.38}$$

where the transmit power is scaled by the number of streams, i.e., N_{RF}, to maintain the total power constraint. Note that $\mathbf{1}_{N_{RF} \times 1}$ in (37) indicates the common synchronization signal structure.

To express (5.38) in vector form, we first denote

$$h_{u,b}^{\Omega}[\ell] = \sum_{j=0}^{N_{RF}-1} [\boldsymbol{H}_u[\ell]]_{b,jN_A+1:(j+1)N_A} \boldsymbol{p}_j$$

187

as the time-domain composite effective transmit beam-space channel and $\boldsymbol{q}_{u,b}^{\Omega} = \left[q_{u,b}^{\Omega}[\mathrm{t}], \cdots, q_{u,b}^{\Omega}[\mathrm{t} + N - 1]\right]^{\mathrm{T}}$. By applying Bussgang's theorem, we then have

$$\boldsymbol{q}_{u,b}^{\Omega} = \boldsymbol{E}_{u,b}^{\Omega} \underbrace{\left(\sum_{\ell=0}^{L_u - 1} \sqrt{\frac{1}{N_{\mathrm{RF}}}} h_{u,b}^{\Omega}[\ell] \boldsymbol{d}_{\ell} + \boldsymbol{w}_u \right)}_{\boldsymbol{v}_{u,b}^{\Omega}} + \check{\boldsymbol{w}}_{u,b}^{\Omega}, \tag{5.39}$$

where the quantization distortion matrix

$$\boldsymbol{E}_{u,b}^{\Omega} = \mathrm{diag}\left(\left[\eta_{u,b}^{\Omega}[0], \cdots, \eta_{u,b}^{\Omega}[N - 1] \right]^{\mathrm{T}} \right),$$

and similar to (5.13), the corresponding quantization distortion factor is

$$\eta_{u,b}^{\Omega}[n] = \frac{\mathbb{E}\left[(q_{u,b}^{\Omega}[\mathrm{t} + n])^* y_{u,b}^{\Omega}[\mathrm{t} + n] \right]}{\mathbb{E}\left[\left| y_{u,b}^{\Omega}[\mathrm{t} + n] \right|^2 \right]}. \tag{5.40}$$

Denoting the covariance matrix of the noiseless unquantized received signal $\boldsymbol{v}_{u,b}^{\Omega}$ in (5.39) by $\boldsymbol{R}_{\boldsymbol{v}_{u,b}^{\Omega}}$, we can further express $\boldsymbol{E}_{u,b}^{\Omega}$ as

$$\boldsymbol{E}_{u,b}^{\Omega} = (1 - \xi_u) \mathrm{diag}\left(\boldsymbol{R}_{\boldsymbol{v}_{u,b}^{\Omega}} + \sigma^2 \boldsymbol{I}_N \right)^{-\frac{1}{2}}. \tag{5.41}$$

The covariance matrix of the quantization noise vector $\check{\boldsymbol{w}}_{u,b}^{\Omega}$ with respect to the b-th receive antenna at UE u now becomes

$$\boldsymbol{R}_{\check{\boldsymbol{w}}_{u,b}^{\Omega}} = \boldsymbol{E}_{u,b}^{\Omega} \left(\boldsymbol{I}_N - \boldsymbol{E}_{u,b}^{\Omega} \right) \underbrace{\mathrm{diag}\left(\boldsymbol{R}_{\boldsymbol{v}_{u,b}^{\Omega}} + \sigma^2 \boldsymbol{I}_N \right)}_{\boldsymbol{V}_{u,b}^{\Omega}}, \tag{5.42}$$

where $\boldsymbol{V}_{u,b}^{\Omega}$ represents the corresponding unquantized received signal power matrix.

5.5.2 Optimization problem formulation for multi-beam probing

Prior to formulating the low-resolution timing synchronization problem for the proposed multi-beam probing, we need to first derive the correlation between the frequency-domain quantized received synchronization signal $\mathbf{q}_{u,b}^{\Omega}$ and the known unquantized reference synchronization sequence $\mathbf{d}$. Denoting

$$\mathsf{h}_{u,b}^{\Omega}[k] = \sum_{j=0}^{N_{\mathrm{RF}}-1} \left[\boldsymbol{A}_u^{\mathrm{RX}} \mathbf{G}_u[k] \left(\boldsymbol{A}_u^{\mathrm{TX}} \right)^* \right]_{b, jN_{\mathrm{A}}+1:(j+1)N_{\mathrm{A}}} \boldsymbol{p}_j, \tag{5.43}$$

as the frequency-domain composite effective transmit beam-space channel relative to its time-domain counterpart $\mathsf{h}_{u,b}^{\Omega}[\ell]$, we can compute the zero-lag frequency-domain correlation for UE u as

$$\Lambda_{u,b}^{\Omega}[0] = \sum_{k=0}^{N-1} \mathsf{q}_{u,b}^{\Omega}[k] \mathsf{d}^*[k] \tag{5.44}$$

$$= \sum_{k=0}^{N-1} \eta_{u,b}^{\Omega}[k] \sqrt{\frac{1}{N_{\mathrm{RF}}}} \mathsf{h}_{u,b}^{\Omega}[k] \mathsf{d}[k] \mathsf{d}^*[k] + \sum_{k=0}^{N-1} \eta_{u,b}^{\Omega}[k] \mathsf{w}_u[k] \mathsf{d}^*[k]$$

$$+ \sum_{k=0}^{N-1} \check{\mathsf{w}}_{u,b}^{\Omega}[k] \mathsf{d}^*[k]. \tag{5.45}$$

Denoting by $\hat{b} = \operatorname*{argmax}_{b=1,\cdots,M_{\mathrm{tot}}} \left| \Lambda_{u,b}^{\Omega}[0] \right|^2$ and applying the same flat synchronization channels assumption as in (5.23), we can rewrite the frequency-domain composite effective transmit beam-space channel in (5.43) as

$$\mathsf{h}_u^{\Omega} = \sum_{j=0}^{N_{\mathrm{RF}}-1} \left[\boldsymbol{a}_{\mathrm{tx}}^*(\theta_u, \phi_u) \right]_{jN_{\mathrm{A}}+1:(j+1)N_{\mathrm{A}}} \boldsymbol{p}_j. \tag{5.46}$$

Further, denoting the frequency-domain counterpart of the unquantized received signal power matrix $\boldsymbol{V}_{u,\hat{b}}^{\Omega}$ in (5.42) by $\mathbf{V}_{u,\hat{b}}^{\Omega}$, we have

$$\mathbf{V}_{u,\hat{b}}^{\Omega} = \frac{\mathsf{g}_u^2 \left|[\boldsymbol{a}_{\mathrm{rx}}(\psi_u)]_{\hat{b}}\right|^2}{N_{\mathrm{RF}}} \left|\mathsf{h}_u^{\Omega}\right|^2 \mathrm{diag}\left(\left[\mathsf{d}[0]\mathsf{d}^*[0], \cdots, \mathsf{d}[N-1]\mathsf{d}^*[N-1]\right]^{\mathrm{T}}\right)$$
$$+ \sigma^2 \boldsymbol{I}_N. \tag{5.47}$$

By exploiting the inherent correlation properties of the common synchronization signal design and applying the common quantization distortion factor $\underline{\eta}_{u,\hat{b}}^{\Omega} = \eta_{u,\hat{b}}^{\Omega}[0] = \cdots = \eta_{u,\hat{b}}^{\Omega}[N-1]$, we can obtain the quantization noise power by using (5.41), (5.42) and (5.47), which results in the received synchronization SQNR at zero-lag correlation for UE u as

$$\gamma_{u,\hat{b}}^{\Omega} = \frac{\underline{\eta}_{u,\hat{b}}^{\Omega} \frac{\mathsf{g}_u^2 \left|[\boldsymbol{a}_{\mathrm{rx}}(\psi_u)]_{\hat{b}}\right|^2}{N_{\mathrm{RF}}} \left|\mathsf{h}_u^{\Omega}\right|^2}{\underline{\eta}_{u,\hat{b}}^{\Omega}\sigma^2 + \left(1 - \underline{\eta}_{u,\hat{b}}^{\Omega}\right)\left(\frac{\mathsf{g}_u^2 \left|[\boldsymbol{a}_{\mathrm{rx}}(\psi_u)]_{\hat{b}}\right|^2}{N_{\mathrm{RF}}} \left|\mathsf{h}_u^{\Omega}\right|^2 + \sigma^2\right)}. \tag{5.48}$$

For the given synchronization time-slot, we formulate the corresponding max-min optimization problem for the proposed multi-beam probing based multicast as

$$\mathcal{P}4: \ \max_{\Omega} \ \min_{\forall u} \left\{\gamma_{u,\hat{b}}^{\Omega}\right\} \tag{5.49}$$
$$\text{s.t. } \Omega \in (\mathcal{F})^{N_{\mathrm{RF}}}.$$

Denote by $\lambda_u' = N_{\mathrm{RF}}\sigma^2/\mathsf{g}_u^2 \left|[\boldsymbol{a}_{\mathrm{rx}}(\psi_u)]_{\hat{b}}\right|^2$ for $u = 1, \cdots, N_{\mathrm{UE}}$ and $\lambda_{\max}' = \max\{\lambda_1', \cdots, \lambda_{N_{\mathrm{UE}}}'\}$. Similar to (5.32), we obtain a lower bound of $\gamma_{u,\hat{b}}^{\Omega}$ as

$$\acute{\gamma}_u^{\Omega} = \frac{\left|\mathsf{h}_u^{\Omega}\right|^2}{\lambda_{\max}' + \left[\frac{\left[\sigma^2\left(\left|\mathsf{h}_u^{\Omega}\right|^2/\lambda_{\max}'+1\right)\right]^{1/2}}{1-\xi_{\max}} - 1\right]\left(\left|\mathsf{h}_u^{\Omega}\right|^2 + \lambda_{\max}'\right)}, \tag{5.50}$$

190
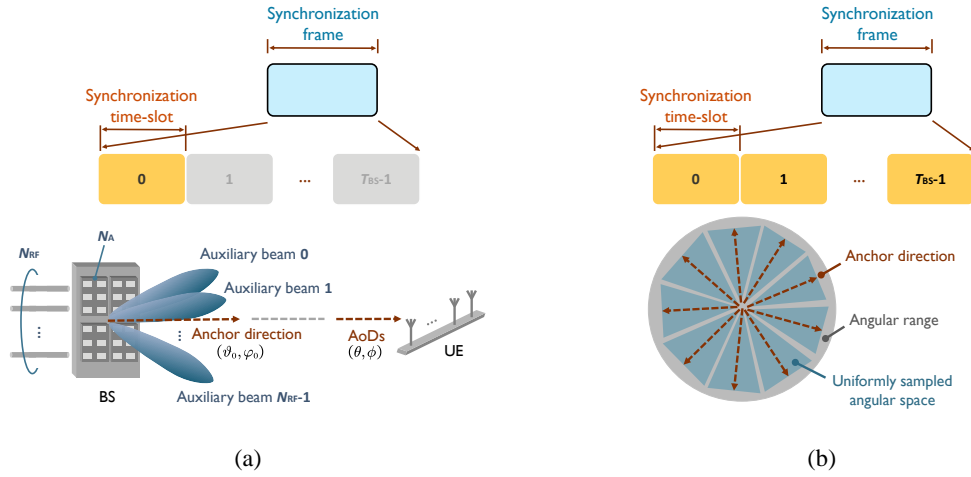
Figure 5.6: (a) Conceptual examples of anchor direction and auxiliary beams for synchronization time-slot 0. (b) Across T_{BS} synchronization time-slots, all T_{BS} anchor directions uniformly sample the given angular space.

such that

$$\acute{\gamma}_u^{\Omega} \leq \gamma_{u,\hat{b}}^{\Omega}, \;\; u \in \left\{ 1, \cdots, N_{\mathrm{UE}} \right\}. \tag{5.51}$$

Based on (5.51), we reformulate (5.49) as

$$\mathcal{P}5: \; \max_{\Omega} \; \min_{\forall u} \left\{ \acute{\gamma}_u^{\Omega} \right\} \tag{5.52}$$

$$\text{s.t. } \Omega \in (\mathcal{F})^{N_{\mathrm{RF}}}.$$

5.5.3 Proposed multi-beam probing based low-resolution synchronization design

Similar to $\mathcal{P}3$ in (5.34), solving $\mathcal{P}5$ in (5.52) also requires the BS to have explicit knowledge of the channel directional information of all UEs, which is unavailable during the initial frame timing synchronization phase. In our proposed design, the UEs with significantly different AoDs are not supposed to

191

synchronize to the network simultaneously, but instead via different synchronization time-slots. That is, for a given synchronization time-slot, we are only interested in a certain group of UEs that have similar AoDs. We therefore define an anchor direction to characterize those similar AoDs as much as possible for the synchronization time-slot of interest. As one synchronization frame contains T_{BS} synchronization time-slots, we define a set of T_{BS} anchor angular directions to represent the potential channel directions. We provide an example of the anchor direction for a given synchronization time-slot in Figure 5.6(a). The anchor directions and T_{BS} synchronization time-slots have one-to-one mapping, and all T_{BS} anchor directions uniformly sample the angular range of interest, which is shown in Figure 5.6(b). If the number of synchronization time-slots $T_{\mathrm{BS}} \to \infty$, the anchor directions fully sample the given angular space such that they characterize all possible channel directions. Note that other choices of the anchor directions are possible (e.g., non-uniformly sample the given angular space), depending on practical system requirements.

Based on the definition of anchor direction, we now reformulate the optimization problem in (5.52). We first define $\vartheta^\star$ and $\varphi^\star$ as the azimuth and elevation anchor directions for the synchronization time-slot of interest and use them to represent the potential channel's azimuth and elevation AoDs. Note that this representation becomes more accurate as T_{BS} increases. Similar to (5.46), we first define

$$
\mathsf{h}^{\Omega^\star} = \sum_{j=0}^{N_{\mathrm{RF}}-1} [\boldsymbol{a}_{\mathrm{tx}}^* (\vartheta^\star + \varphi^\star)]_{jN_{\mathrm{A}}+1:(j+1)N_{\mathrm{A}}}\, \boldsymbol{p}_j, \tag{5.53}
$$

192

where $\Omega^\star$ denotes the set of candidate beams with $\vartheta^\star$ and $\varphi^\star$ as the corresponding azimuth and elevation anchor directions. Similar to (5.50), we can then obtain

$$\acute{\gamma}^{\Omega^\star} = \frac{\left| h^{\Omega^\star} \right|^2}{\lambda'_{\max} + \left[\frac{\left[\sigma^2 \left(\left| h^{\Omega^\star} \right|^2 / \lambda'_{\max} + 1 \right) \right]^{1/2}}{1 - \xi_{\max}} - 1 \right] \left(\left| h^{\Omega^\star} \right|^2 + \lambda'_{\max} \right)}. \tag{5.54}$$

According to (5.52), we formulate the optimization problem as

$$\mathcal{P}6 : \max_{\Omega^\star} \left\{ \acute{\gamma}^{\Omega^\star} \right\} \tag{5.55}$$

$$\text{s.t. } \Omega^\star \in (\mathcal{F})^{N_{\mathrm{RF}}},$$

which transforms the complex max-min optimization problem into a maximization problem. To solve (5.55), the BS can execute the exhaustive search over all possible combinations among the candidate beam codewords in $\mathcal{F}$, resulting in

$$\Omega^\star_{\mathrm{opt}} = \underset{\Omega^\star \in (\mathcal{F})^{N_{\mathrm{RF}}}}{\operatorname{argmax}} \left\{ \acute{\gamma}^{\Omega^\star} \right\}, \tag{5.56}$$

for the given synchronization time-slot. We refer to the simultaneously probed beams in $\Omega^\star_{\mathrm{opt}}$ as auxiliary beams for the synchronization time-slot of interest as depicted in Figure 5.6(a).

From (5.43), (5.46) and (5.53), for the proposed multi-beam probing strategy with common synchronization signal structure, the simultaneously probed auxiliary beams actually form an effective composite beam. In Figure 5.7, we provide examples of the auxiliary beams and the corresponding effective composite beam pattern. The auxiliary beams are selected from a DFT

beam codebook with oversampling factor of 2. As evident from Figures 5.7(a) and 5.7(b), the effective composite beam may not yield the largest beamforming gain towards the corresponding anchor direction. In Figures 5.8(a) and 5.8(b), we plot the radiation patterns corresponding to the auxiliary beams and the composite beam in Figures 5.7(a) and 5.7(b). In summary, by optimizing the effective composite beam pattern via (5.56), we optimize the distribution/resolution of the input samples to the quantizer such that a better tradeoff between the beamforming gain and the resulted quantization distortion can be achieved.

In Figures 5.9 and 5.10, we examine the composite beam patterns for the same anchor angular direction assuming various target system settings such as different target ADC resolutions and SNRs, and different anchor angular directions under the same target system settings. It is evident from both plots that even for the same anchor angular direction, the corresponding composite beam patterns could be different due to different target system specific parameters, e.g., 2-bit ADCs and 0 dB SNR in Figure 5.9(a) versus 3-bit ADCs and -5 dB SNR in Figure 5.9(b). Hence, for varying system-specific parameters, it is difficult to conclude a one-to-one correspondence relationship between the multi-beam patterns and the anchor angular directions. For fixed target design parameters, however, it is possible to map a specific composite beam to a given anchor angular direction of interest. Similar observations can be obtained for different anchor angular directions by comparing Figure 5.9 and Figure 5.10.

Motivated by the composite beam pattern obtained from the multi-beam probing, we can also design a high-resolution limited-size beam codebook to support the single-beam based approach for low-resolution timing synchronization design. Each beam codeword in the custom designed beam codebook could be a linear combination of N_{RF} weighted beam codewords selected from the conventional DFT-type beam codebook. For instance, the beam codewords in the enhanced beam codebook may exhibit similar beam patterns to those shown in Figures 5.9 and 5.10. With the newly designed beam codebook, the phase shifter's resolution, and therefore the corresponding implementation cost will significantly increase, though a single RF chain is used to form the single synchronization beam for a given synchronization time-slot.

5.6 Numerical Results

In this section, we evaluate the proposed multi-beam directional frame timing synchronization design for mmWave systems operating with few-bit ADCs. The BS and UE employ a UPA and a ULA with inter-element spacing of $\lambda/2$ between the antenna elements. The BS covers three sectors, and each sector covers 120° angular range $[-60°, 60°]$ around azimuth boresight (0°) and 90° angular range $[-45°, 45°]$ around elevation boresight (0°). The UE monitors the entire 180° angular region $[-90°, 90°]$ around boresight (0°). We assume a 125 MHz RF bandwidth with $N = 512$ subcarriers. The corresponding CP length is $D = 64$. We set the subcarrier spacing and symbol duration as 270 KHz and 3.7 μs following the numerology provided in [1]. The

synchronization sequence occupies the central 63 subcarriers, and we set the DC-carrier as zero. We set the total number of receive antennas M_{tot} as 16 throughout the simulation section unless otherwise specified. For the multi-user setup, we let $1/\lambda'_{\max}$ be -20 dB. Further, we assume that the ADCs equipped at all UEs have identical quantization resolution (2 or 4 bits), which is used to determine $\xi_{\max}$.

In Figure 5.11(a), we plot the CDFs of the received synchronization SQNRs at zero-lag correlation for $N_{\mathrm{tot}} = 32$ with $N_{\mathrm{RF}} = 4$. We assume single-path frequency-flat channels. We set the transmit SNR as 0 dB, which is calculated before the transmit beamforming and receive processing. We also examine the single-stream beamforming based directional frame timing synchronization method described in Section 5.4 with infinite-resolution (∞) and low-resolution (2 and 4 bits) ADCs for comparison. We construct the employed synchronization signals according to (5.1) with root index 34. As can be seen from Figure 5.11(a), a significant performance gap can be observed between low-resolution quantization and infinite-resolution quantization for the existing strategy, though with increase in the quantization resolution, this performance difference decreases. By using the proposed multi-beam probing based design approach, the received synchronization SQNR performance is improved by several orders of decibels in contrast to the single-stream beamforming algorithm. In Figure 5.11(b), we provide the average received synchronization SQNRs at zero-lag correlation versus the quantization resolution of ADCs. In this example, we implement the statistical mmWave wideband channel model

developed in [71] using the NYUSIM open source platform. We assume the UMi scenario with NLOS components for 28 GHz carrier frequency. We evaluate both $N_{\text{tot}} = 32$ and $N_{\text{tot}} = 64$ for the proposed multi-beam probing and conventional single-stream beamforming based designs. Similar to the narrowband results shown in Figure 5.11(a), the proposed algorithm exhibits superior synchronization SQNR performance over the single-stream beamforming based design in wideband channels.

In Figure 5.12, we compare the two synchronization sequence allocation strategies in terms of the NMSE of the timing position estimate. Recall that N_{sub} represents the number of sub-signals in a given synchronization timeslot. At relatively high SNR, the comb-type subcarriers allocation design with $N_{\text{sub}} = 3$ shows better performance than the continuous allocation and exhibits significant diversity gain for both the single-stream and our proposed multi-beam probing based methods. The comb-type allocation method with $N_{\text{sub}} = 2$, however, shows similar performance to the continuous allocation strategy in this example. Note that the performance of the comb-type assignment depends on the frequency selectivity of the propagation channels, subcarrier spacing, N_{sub}, and the spacing between sub-signals. We also evaluate the random beamforming based design [108] in Figure 5.12 for comparison. For the random beamforming, we assume that the N_{RF} simultaneously formed beams are randomly chosen from the employed DFT beam codebook with continuous subcarriers allocation for the synchronization signal. As the synchronization beams are not optimized for low-resolution quantization, the

random beamforming based design even shows inferior NMSE performance of the timing position estimate relative to the single-stream beamforming based method.

In Figure 5.13(a), we evaluate the normalized MSE (NMSE) performance of the timing position estimate assuming a single UE. Denoting the NMSE of the timing position estimate by ω_{est}, we have

$$\omega_{\text{est}} = \mathbb{E}\left[\left|\frac{\kappa_{\text{true}} - \kappa_{\text{est}}}{\kappa_{\text{true}}}\right|^2\right], \qquad (5.57)$$

where κ_{true} denotes the first sample index of the probed synchronization signal, and κ_{est} corresponds to its estimated counterpart using various synchronization methods. We employ the wideband channels with 2-bit ADCs. It can be observed from Figure 5.13(a) that the performance gap between low-resolution quantization and infinite-resolution quantization is significant for the existing method especially at relatively high SNR. The proposed multi-beam directional synchronization method with common synchronization signal design approaches the infinite-resolution case for various SNR values. In Figure 5.13(b), we examine the NMSE performance of the timing position estimate in a single-cell multi-user scenario. In this example, we randomly drop a total of 10 UEs within a circular cell having a 150 m radius. We employ the same path loss model as in [71]. In this example, we obtain the NMSE performance of the timing position estimate over all UEs. Similar observations as in Figure 5.13(a) can be obtained, i.e., the proposed method exhibits better performance than the existing directional timing synchronization design.

For the last two examples, we numerically study the proposed method in a multi-cell scenario. Specifically, we assume 7 hexagonal cells and set the inter-site distance as 500 m. The root indices of the employed ZC sequences are 25, 29 and 34. The central cell corresponds to root index 25, and root indices 29 and 34 are reused among the other 6 surrounding cells such that the neighboring two cells are assigned two distinct root indices. Similar to the example provided in Figure 5.13(b), we randomly drop a total of 10 UEs within each cell sector, and we set the minimum distance between the BS and UE as 20 m. Performance statistics are obtained from the central cell of interest only. In Figure 5.14(a), we evaluate the probability of successful timing position detection. Different from the NMSE of the timing position estimate, we calculate the probability of successful detection as $\Pr(\kappa_{\text{est}} = \kappa_{\text{true}})$. It is observed that even at relatively low SNR, the proposed synchronization method with low-resolution ADCs can still achieve promising detection performance. For instance, at -10 dB SNR, the probability of successful detection is more than 0.8 for the proposed multi-beam probing with common synchronization signal design.

In Figure 5.14(b), we evaluate the synchronization time-slot access probability under low-resolution quantization. We calculate the synchronization time-slot access probability based on the following procedure. If a given UE successfully detects the frame timing position during synchronization time-slot τ_{t}, the algorithm stops for the UE of interest. Otherwise, the algorithm continues in synchronization time-slot $\tau_{\text{t}} + 1$ and repeats the previous proce-

199

dure. The synchronization time-slot access probability evaluates how fast a specific UE is capable of correctly detecting the frame timing position, which in turn implies the access delay for the given UE. Figure 5.14(b) shows that even with 2-bit ADCs, the UEs can correctly detect the frame timing position during the first several synchronization time-slots by using the proposed method. According to the 3GPP Technical Specification (TS) 36.101, the UE is expected to achieve a successful detection probability equal to 95% at -5 dB SNR for broadcast channel. Here, we use this metric to examine the effectiveness of our proposed multi-beam probing strategy in estimating the timing position under low-resolution ADC quantization. It is evident from Figure 5.14(b) that the successful detection probabilities for our proposed method are around 98% and 91% at -5 dB SNR assuming 4-bit and 2-bit ADCs. For the single-stream based method, the corresponding probabilities are approximately 80% and 65% at -5 dB SNR. We can conclude from these observations that our proposed low-resolution timing synchronization design is of great interest for practical implementation to achieve promising synchronization performance assuming few-bit ADCs.

5.7 Conclusion

In this chapter, we developed and evaluated a multi-beam probing-assisted directional frame timing synchronization method for mmWave systems with low-resolution ADCs. We first formulated the optimization problem as maximizing the minimum received synchronization SQNR at zero-lag

correlation among all UEs. We solved this problem by transforming the complex max-min multicast beamforming problem into a maximization problem. We then proposed a multi-beam probing strategy to tackle the maximization problem by optimizing the effective composite beam pattern. We showed via numerical examples that the effective composite beam can provide a good tradeoff between the beamforming gain and the quantization distortion and characterize the worst-case scenario of the network.
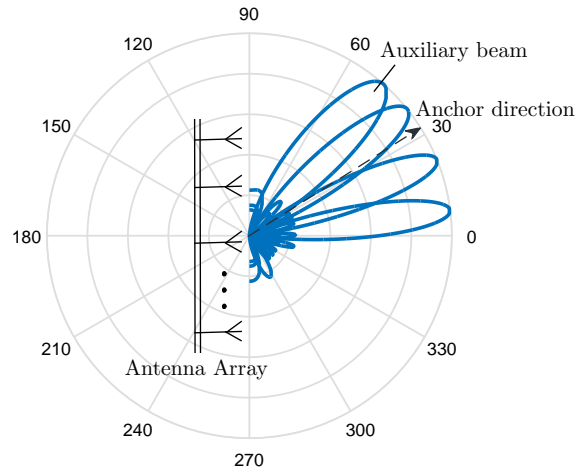
(a)
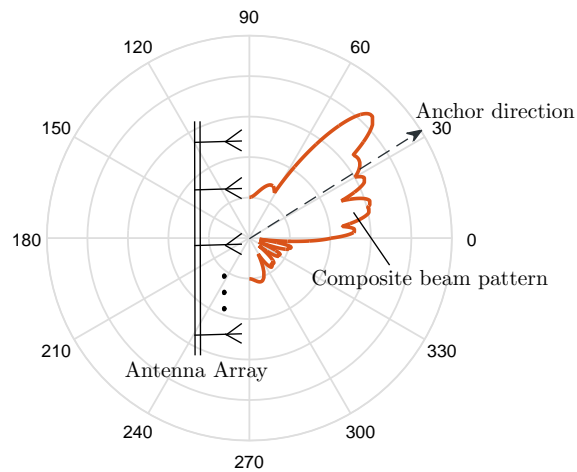
(b)

Figure 5.7: An example of auxiliary beams is provided in (a); the correspond-
ing composite beam is presented in (b). A ULA is assumed with $N_{\text{tot}} = 8$ and
$N_{\text{RF}} = 4$. A DFT beam codebook with oversampling factor of 2 is employed.
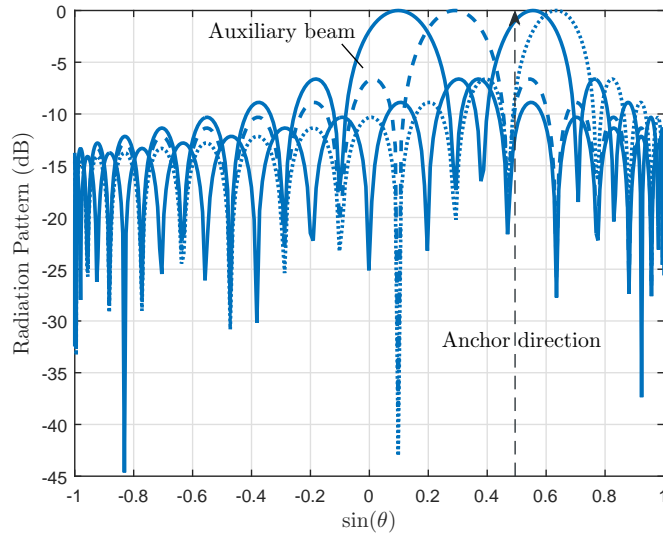
(a)
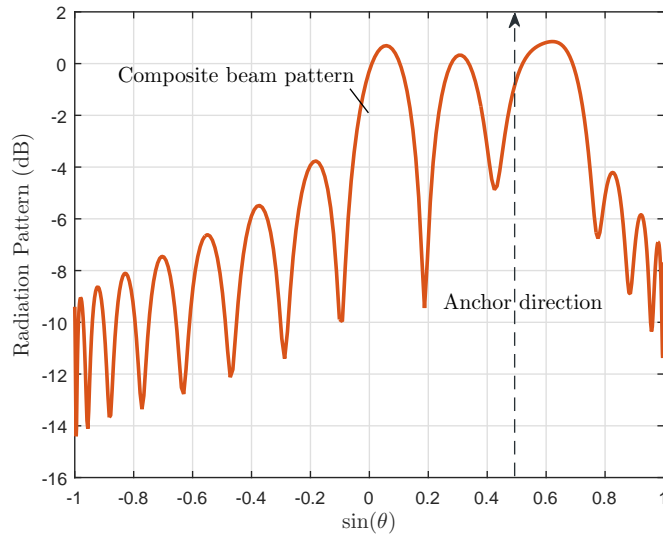
(b)

Figure 5.8: An example of radiation pattern of auxiliary beams is provided in (a); the corresponding radiation pattern of composite beam is presented in (b). A ULA is assumed with $N_{\text{tot}} = 8$ and $N_{\text{RF}} = 4$. A DFT beam codebook with oversampling factor of 2 is employed.
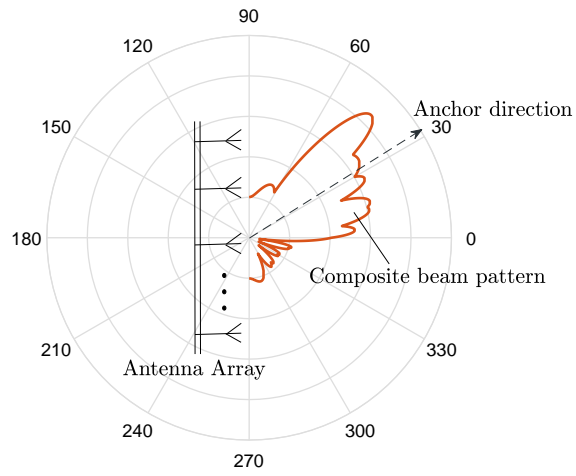
(a)
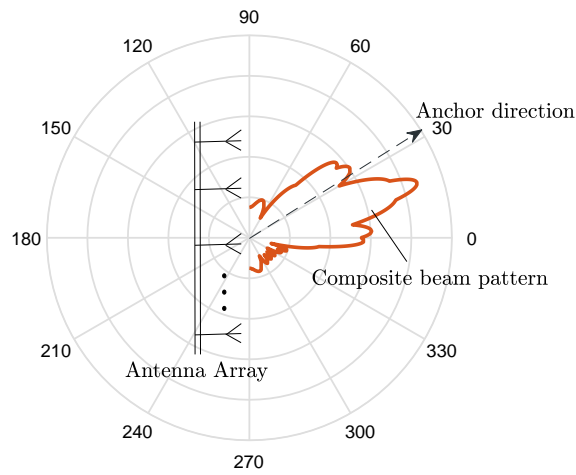
(b)

Figure 5.9: An example of a composite beam patten for a given anchor angular direction. A ULA is assumed with $N_{\text{tot}} = 8$ and $N_{\text{RF}} = 4$. A DFT beam codebook with oversampling factor of 2 is employed. (a) 2-bit ADCs and 0 dB SNR. (b) 3-bit ADC and -5 dB SNR.
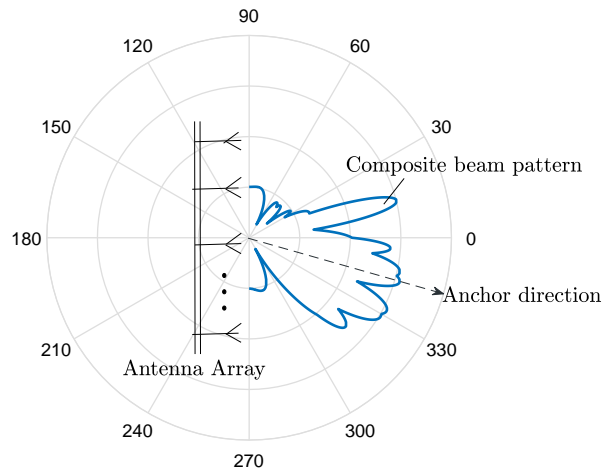
(a)
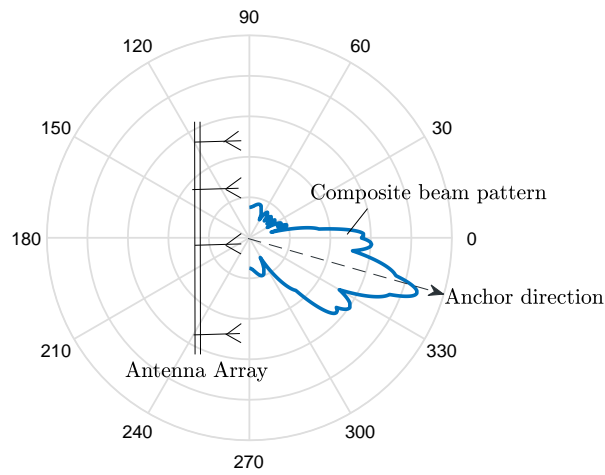
(b)

Figure 5.10: An example of a composite beam pattern for another anchor angular direction. A ULA is assumed with $N_{\text{tot}} = 8$ and $N_{\text{RF}} = 4$. A DFT beam codebook with oversampling factor of 2 is employed. (a) 2-bit ADCs and 0 dB SNR. (b) 3-bit ADC and -5 dB SNR.
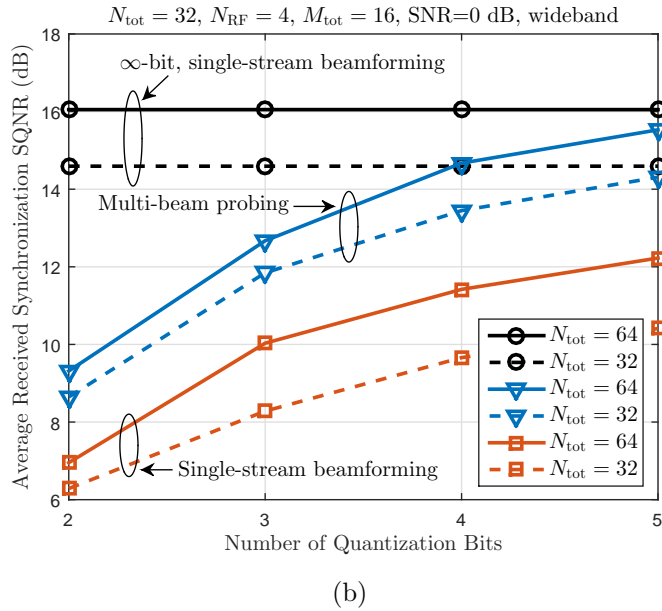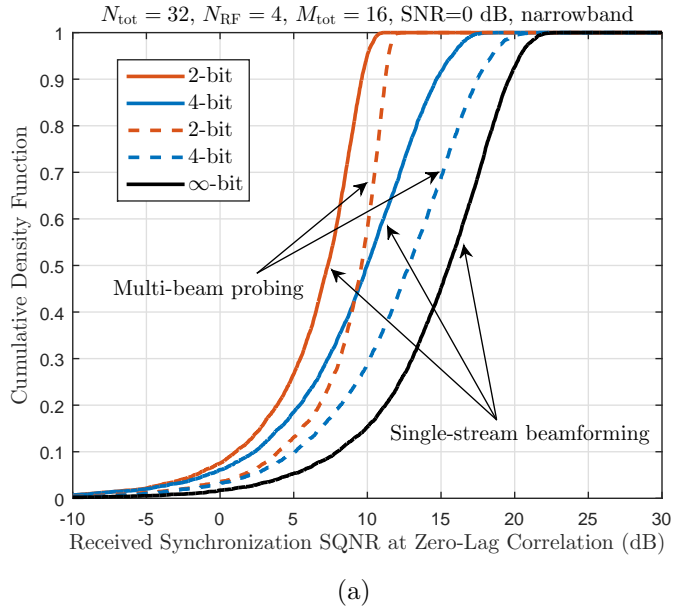
Figure 5.11: (a) CDFs of the received synchronization SQNRs in single-path frequency-flat channels; $N_{\text{tot}} = 32$ with $N_{\text{RF}} = 4$. (b) Average received synchronization SQNRs versus the number of quantization bits in multi-path frequency-selective channels; $N_{\text{tot}} = 32$ with $N_{\text{RF}} = 4$.
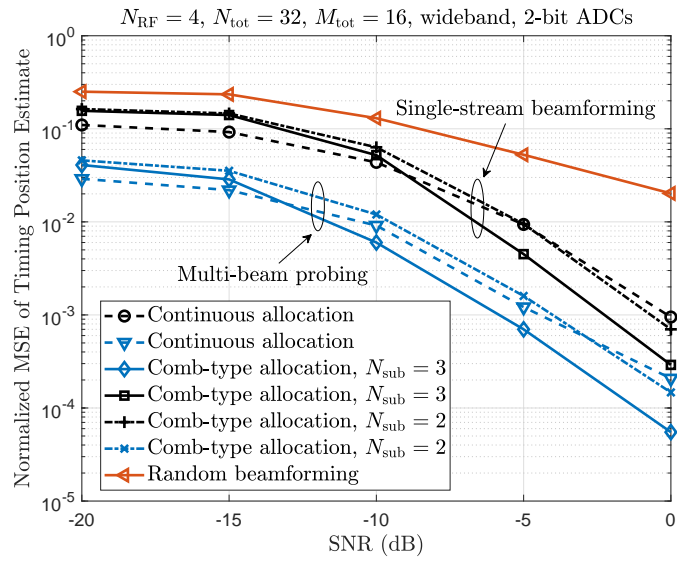
Figure 5.12: Normalized MSE of timing position estimate versus SNR assuming multiple UEs equipped with 2-bit ADCs receivers. Comparison among continuous and comb-type subcarriers allocation strategies, and the random beamforming based synchronization approach.
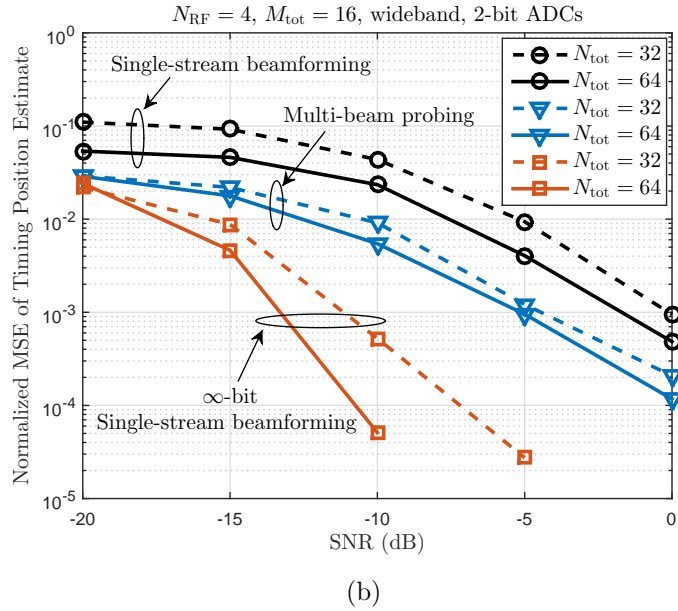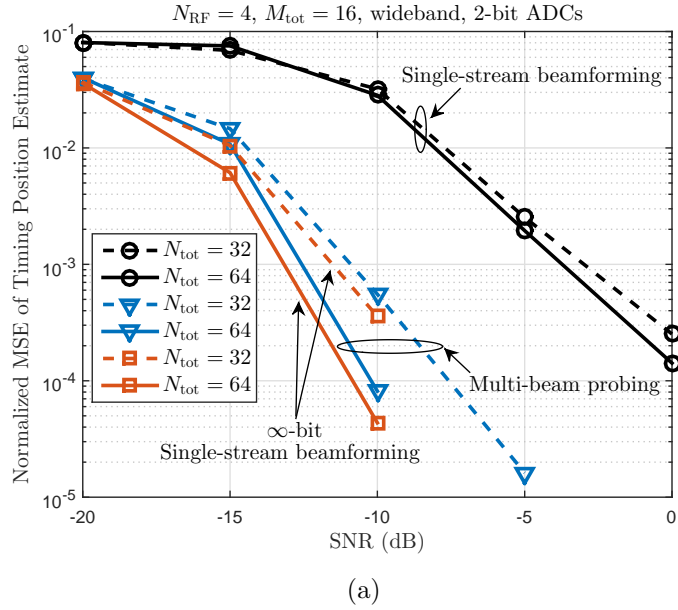
Figure 5.13: Normalized MSE of timing position estimate versus SNR. Multi-path frequency-selective channels are employed with $N_{\text{tot}} = \{32, 64\}$ and $N_{\text{RF}} = 4$. (a) a single UE equipped with a 2-bit ADCs receiver. (b) multiple UEs equipped with 2-bit ADCs receivers.

208
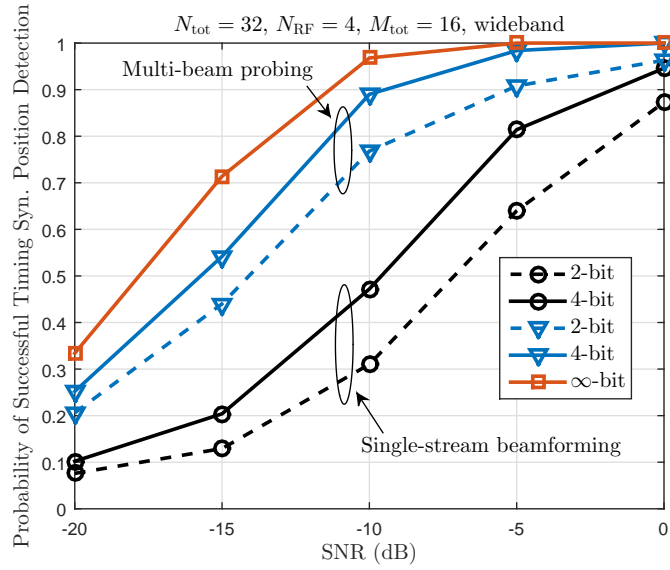
(a)
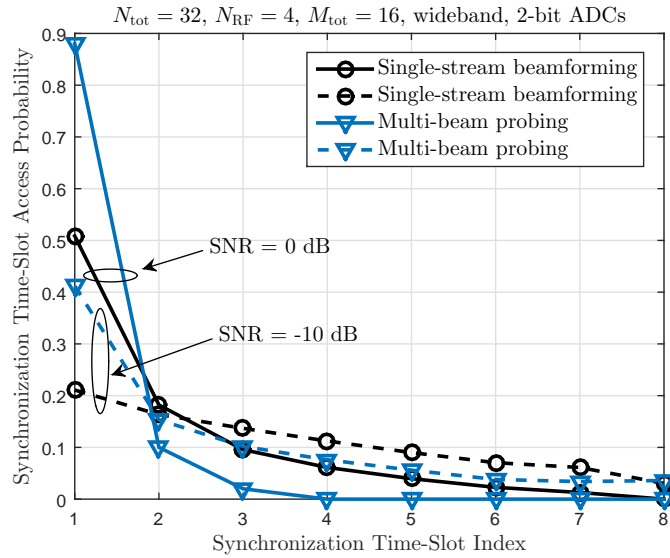
(b)

Figure 5.14: A multi-cell scenario is assumed with a total of 7 hexagonal cells. A number of 10 UEs are randomly distributed within each cell sector with 2 or 4-bit ADCs. (a) Probability of successful timing position detection versus SNR. (b) Synchronization time-slot access probability versus synchronization time-slot index. The performance is evaluated under both 0 dB and -10 dB SNRs.

Chapter 6

Frequency Synchronization in MmWave Cellular Systems with Low-Resolution ADCs

In this chapter, we propose and evaluate two novel double-sequence low-resolution frequency synchronization methods in downlink mmWave systems. In our system model, the base station uses analog beams to send the synchronization signal with infinite-resolution digital-to-analog converters (DACs). The user equipment employs a fully digital front end to detect the synchronization signal with low-resolution ADCs. The key ingredient of the proposed methods is the custom designed synchronization sequence pairs, from which there exists an invertible function (a ratio metric) of the CFO to be estimated. We use numerical examples to show that the ratio metric is robust to the quantization distortion. Further, we analytically characterize the CFO estimation performances of our proposed two design options assuming a single user and low-resolution ADCs. To implement our proposed methods in a multi-user scenario, we propose to optimize the double-sequence design parameters such that: (i) for each individual user, the impact of the quantization distortion on the CFO estimation accuracy is minimized, and (ii) the resulting frequency range of estimation can capture as many users' CFOs as possible. Numerical results reveal that under low-resolution ADCs, our proposed algorithms pro-

vide a flexible means to estimate CFO in a varies of settings, and outperform the Zadoff-Chu sequence based CFO estimation strategy. This work has been submitted for possible publication [47].

6.1   Prior Work and Motivation

There are many pilot/sequence-aided frequency synchronization methods for OFDM systems [109]-[114]. The Cox-Schmidl algorithm [109] and variants [110]-[113] is the classic pilot-aided CFO estimation approach. In the Cox-Schmidl algorithm, a first training sequence is used to estimate the CFO with an ambiguity identical to one subcarrier spacing, while a second training sequence is employed to resolve this ambiguity. In [114], the symmetry of the ZC sequences was exploited in the 3GPP LTE systems for frequency synchronization. Similar to the first training sequence in the Cox-Schmidl algorithm, the symmetry of the ZC sequences creates time-domain periodicity in one OFDM symbol duration to track the CFOs. That approach, however, only works for fractional CFO that is less than one subcarrier spacing. Of relevance in this chapter, prior work [109]-[114] did not consider the impact of few-bit ADCs. Their developed synchronization pilots/sequences are therefore sensitive to the quantization distortion. This motivates us to construct new synchronization sequences that are robust to the low-resolution quantization.

6.2   Contributions

In this chapter, we propose and evaluate two novel frequency synchronization methods for downlink mmWave systems operating with low-resolution ADCs. The proposed two strategies exhibit different frequency synchronization performances under various configurations, and can be applied in different deployment scenarios. In our system model, the BS forms directional beams in the analog domain to send the synchronization signal towards the UE. The UE employs a fully digital front end with low-resolution ADCs to detect the synchronization signal and conduct frequency synchronization. We focus on designing new synchronization sequences that are robust to the quantization distortion. We summarize the main contributions of this chapter as follows:

- We develop two double-sequence high-resolution CFO estimation methods for mmWave systems operating with low-resolution ADCs. In each method, we custom design two sequences (i.e., a sequence pair) for frequency synchronization. They are sent by the BS across two consecutive synchronization time-slots. We refer to the sequence pair as auxiliary sequences and sum-difference sequences in the proposed two methods. The key ingredient of the custom designed double-sequence structure (both auxiliary and sum-difference) is a ratio measure derived from the sequence pair, which is an invertible function of the CFO to be estimated. We use numerical examples to show that the ratio measures are robust to the quantization distortion brought by low-precision ADCs.

- We derive the CRLB of frequency estimation assuming 1-bit ADCs. We show that the MSEs of our estimated CFOs using 1-bit ADCs are close to the derived 1-bit CRLB. Leveraging Bussgang's decomposition theorem [99], we derive the variance of the CFO estimates obtained via the proposed auxiliary sequences and sum-difference sequences based methods operating with low-resolution (e.g., 2-4 bits) ADCs. These analytical results reveal that the CFO estimation performances highly depend on the double-sequence design parameters.

- Assuming multiple UEs, we formulate the corresponding low-resolution frequency synchronization problem as a min-max optimization problem. We first transform the min-max optimization problem into a minimization problem by exploiting certain measurements and system statistics. We then solve the minimization problem by fine tuning the double-sequence design parameters such that the CFO estimation accuracy and the frequency range of estimation are jointly optimized. To better realize our proposed algorithms in practical systems, we implement additional signaling support and procedure at both the BS and UE sides.

We organize the rest of this chapter as follows. In Section 6.3, we specify the signal model for frequency synchronization in mmWave systems. In Section 6.4, we present the design principle of the proposed auxiliary sequences and sum-difference sequences based CFO estimation strategies. We conduct performance analysis on our proposed methods in Section 6.5 assuming few-bit

213

ADCs. In Section 6.6, we address several practical issues of implementing the proposed double-sequence low-resolution frequency synchronization designs in communications systems. We evaluate our proposed methods in Section 6.7 assuming various channel models, quantization configurations and deployment scenarios. We draw our conclusions in Section 6.8.

6.3 Models and Assumptions

We consider a cellular system where synchronization and training data are sent periodically on directional beams, to support initial access [101, 107]. The direction module is important in a mmWave system because it enables favorable received signal power to overcome higher pathloss. This approach is used in the 3GPP 5G NR [74] and has been applied in other Wi-Fi standards [115]. We assume that the UEs use fully digital front ends to detect the synchronization signal samples, which is realistic because there will only be a few antennas.

To develop the received synchronization signal model, we assume: (i) a given UE $u \in \{1, \cdots, N_{\mathrm{UE}}\}$ in a single cell, where N_{UE} corresponds to the total number of serving UEs in the cell of interest, and (ii) a given synchronization time-slot, which may be one OFDM symbol duration (T_{s}). In Section 6.7, we simulate a more elaborate setting assuming multiple UEs and the frame structure adopted in the 3GPP LTE/NR.

The symbol vector $\mathbf{d}$ in (5.3) is transformed to the time-domain via N-point IFFTs, generating the discrete-time signals at symbol durations $n =$

$0, \cdots, N - 1$ as

$$d[n] = \frac{1}{\sqrt{N}} \sum_{k=0}^{N-1} \mathsf{d}[k] e^{\mathsf{j} \frac{2\pi k}{N} n}. \tag{6.1}$$

Before applying an $N_{\text{tot}} \times 1$ wideband analog beamforming vector, the CP is added to the symbol vector such that the length of the CP is greater than or equal to the maximum delay spread of the multi-path channels. Each sample in the symbol vector is then transmitted by a common wideband analog beamforming vector $\boldsymbol{f}$ from the BS, satisfying the power constraint $[\boldsymbol{f}\boldsymbol{f}^*]_{a,a} = \frac{1}{N_{\text{tot}}}$, where $a = 1, \cdots, N_{\text{tot}}$.

Consider the b-th receive antenna ($b \in \{1, \cdots, M_{\text{tot}}\}$) at UE u. After the timing synchronization and discarding the CP, the remaining time-domain received signal samples can be expressed as $\boldsymbol{q}_{u,b} = \left[q_{u,b}[0], \cdots, q_{u,b}[N-1]\right]^{\mathrm{T}}$. Denote the number of channel taps by L_u, the corresponding channel impulse response at tap $\ell \in \{0, \cdots, L_u - 1\}$ by $\boldsymbol{H}_u[\ell] \in \mathbb{C}^{M_{\text{tot}} \times N_{\text{tot}}}$, and additive white Gaussian noise by $w_u[n] \sim \mathcal{N}_{\mathrm{c}}(0, \sigma_u^2)$. Denote the frequency mismatch with respect to the subcarrier spacing by ε_u. As the UE employs fully digital baseband processing, each receive antenna first quantizes the received synchronization signal with dedicated ADCs. Denote $\mathcal{Q}(\cdot)$ as the quantization function. For $n = 0, \cdots, N - 1$, the time-domain received signal samples are

$$q_{u,b}[n] = \mathcal{Q}\left(e^{\mathsf{j} \frac{2\pi \varepsilon_u}{N} n} \sum_{\ell=0}^{L_u-1} [\boldsymbol{H}_u[\ell]]_{b,:} \boldsymbol{f} d[n - \ell] + w_u[n]\right). \tag{6.2}$$

Across all receive antennas, UE u selects the $\hat{b}$-th ($\hat{b} \in \{1, \cdots, M_{\text{tot}}\}$) receive antenna that exhibits the highest received signal strength. By exploiting the
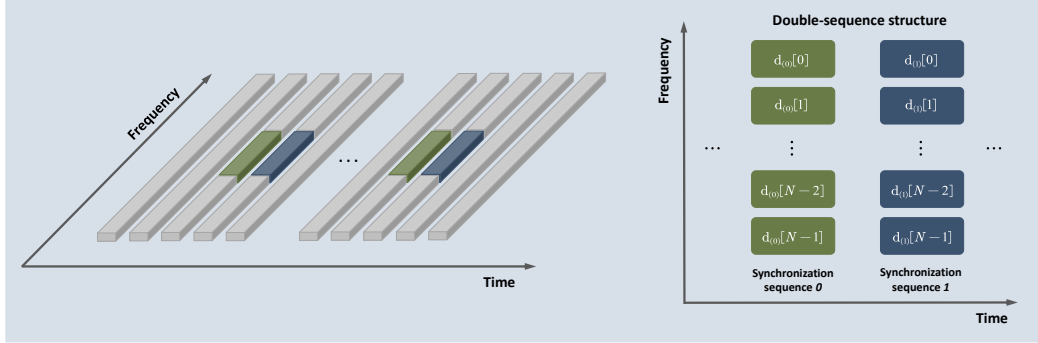
Figure 6.1: Time-frequency resource mapping of the proposed double sequence frequency synchronization. Synchronization sequences 0 and 1 in the double-sequence structure are transmitted by the BS across two consecutive synchronization time-slots.

symmetry of the employed ZC sequence and assuming perfect timing synchronization, the CFO can be estimated as

$$\hat{\varepsilon}_u = \frac{1}{\pi} \angle \left(\left[\sum_{n'=0}^{N/2-1} q_{u,\hat{b}}[n']d^*[n'] \right]^* \left[\sum_{n''=N/2}^{N-1} q_{u,\hat{b}}[n'']d^*[n''] \right] \right). \qquad (6.3)$$

UE u can then compensate the received signal samples with the estimated CFO as

$$\hat{q}_{u,b}[n] = e^{-\mathrm{j}\frac{2\pi\hat{\varepsilon}_u}{N}n} q_{u,b}[n]. \qquad (6.4)$$

If $\mathcal{Q}(\cdot)$ in (6.2) corresponds to low-resolution quantization (e.g., 1-4 bits), the corresponding quantization distortion would damage the symmetry of the ZC sequence, leading to degraded CFO estimation performance.

6.4 Proposed Double-Sequence Frequency Synchronization

We propose two novel double-sequence frequency synchronization methods. In this section, we explicitly explain the design principle of the proposed methods assuming infinite-resolution quantization. In later sections, we will illustrate the detailed implementation procedure of our proposed methods along with comprehensive performance evaluations assuming low-resolution quantization. In Figure 6.1, we depict the basic double-sequence structure and its time-frequency resource mapping. As can be seen from the right-hand side of Figure 6.1, two length-N sequences are periodically transmitted across two consecutive synchronization time-slots in the TDM manner.

6.4.1 Auxiliary sequences based frequency synchronization

We denote the time-domain samples of the two sequences by $\boldsymbol{d}_0 = \left[d_0[0], \cdots, d_0[N-1]\right]^{\mathrm{T}}$ and $\boldsymbol{d}_1 = [d_1[0], \cdots, d_1[N-1]]^{\mathrm{T}}$. Further, we construct $\boldsymbol{d}_0$ and $\boldsymbol{d}_1$ as

$$\boldsymbol{d}_0 = [d_0[0], d_0[1], \cdots, d_0[N-1]]^{\mathrm{T}} = \left[1, e^{-\mathrm{j}(\theta-\delta)}, \cdots, e^{-\mathrm{j}(N-1)(\theta-\delta)}\right]^{\mathrm{T}} \quad (6.5)$$

$$\boldsymbol{d}_1 = [d_1[0], d_1[1], \cdots, d_1[N-1]]^{\mathrm{T}} = \left[1, e^{-\mathrm{j}(\theta+\delta)}, \cdots, e^{-\mathrm{j}(N-1)(\theta+\delta)}\right]^{\mathrm{T}} \quad (6.6)$$

and they are sent by the BS using two consecutive synchronization time-slots, say, synchronization time-slots 0 and 1. For $k = 0, \cdots, N-1$, the frequency-domain samples that correspond to $\boldsymbol{d}_0$ and $\boldsymbol{d}_1$ are

$$\mathsf{d}_0[k] = \frac{1}{\sqrt{N}} \sum_{n=0}^{N-1} d_0[n] e^{-\mathrm{j}\frac{2\pi n}{N}k}, \quad \mathsf{d}_1[k] = \frac{1}{\sqrt{N}} \sum_{n=0}^{N-1} d_1[n] e^{-\mathrm{j}\frac{2\pi n}{N}k}. \quad (6.7)$$

217

For synchronization time-slot 0 and $n = 0, \cdots, N - 1$, we express the corresponding time-domain received signal samples as (similar to (6.2))

$$q_{u,b}^0[n] = \mathcal{Q}\left(e^{\mathrm{j}\frac{2\pi\varepsilon_u}{N}n}\sum_{\ell=0}^{L_u-1}[\boldsymbol{H}_u[\ell]]_{b,:}\,\boldsymbol{f}d_0[n-\ell] + w_u^0[n]\right). \tag{6.8}$$

Assuming infinite-resolution quantization and neglecting noise,

$$q_{u,b}^0[n] = e^{\mathrm{j}\frac{2\pi\varepsilon_u}{N}n}\sum_{\ell=0}^{L_u-1}[\boldsymbol{H}_u[\ell]]_{b,:}\,\boldsymbol{f}d_0[n-\ell]. \tag{6.9}$$

Defining the normalized CFO for UE u as $\mu_u = 2\pi\varepsilon_u/N$,

$$\begin{aligned}
q_{u,b}^0[n] &= e^{\mathrm{j}\mu_u n}\sum_{\ell=0}^{L_u-1}[\boldsymbol{H}_u[\ell]]_{b,:}\,\boldsymbol{f}d_0[n-\ell] \tag{6.10}\\[2mm]
&= e^{\mathrm{j}\mu_u n}\sum_{\ell=0}^{L_u-1}[\boldsymbol{H}_u[\ell]]_{b,:}\,\boldsymbol{f}e^{-\mathrm{j}(n-\ell)(\theta-\delta)} \tag{6.11}\\[2mm]
&= e^{\mathrm{j}\mu_u n}e^{-\mathrm{j}n(\theta-\delta)}\sum_{\ell=0}^{L_u-1}[\boldsymbol{H}_u[\ell]]_{b,:}\,\boldsymbol{f}e^{\mathrm{j}\ell(\theta-\delta)} \tag{6.12}\\[2mm]
&= e^{\mathrm{j}n(\mu_u-\theta+\delta)}\left[\mathbf{H}_u\left(e^{-\mathrm{j}(\theta-\delta)}\right)\right]_{b,:}\boldsymbol{f}. \tag{6.13}
\end{aligned}$$

Denote the selected receive antenna index by $\hat{b}$. Using the received signal samples $\boldsymbol{q}_{u,\hat{b}}^0 = \left[q_{u,\hat{b}}^0[0], \cdots, q_{u,\hat{b}}^0[N-1]\right]^{\mathrm{T}}$ from synchronization time-slot 0, UE u calculates

$$\begin{aligned}
p_{u,\hat{b}}^0 &= \left(\sum_{n=0}^{N-1}q_{u,\hat{b}}^0[n]\right)\left(\sum_{n=0}^{N-1}q_{u,\hat{b}}^0[n]\right)^* \tag{6.14}\\[2mm]
&= \left|\left[\mathbf{H}_u\left(e^{-\mathrm{j}(\theta-\delta)}\right)\right]_{\hat{b},:}\boldsymbol{f}\right|^2\left|\sum_{n=0}^{N-1}e^{\mathrm{j}n(\mu_u-\theta+\delta)}\right|^2 \tag{6.15}\\[2mm]
&\overset{(\star)}{=} \left|\left[\mathbf{H}_u\left(e^{-\mathrm{j}(\theta-\delta)}\right)\right]_{\hat{b},:}\boldsymbol{f}\right|^2\frac{\sin^2\left(\frac{N(\mu_u-\theta+\delta)}{2}\right)}{\sin^2\left(\frac{\mu_u-\theta+\delta}{2}\right)}, \tag{6.16}
\end{aligned}$$

218

where $(\star)$ is obtained via $\left| \sum_{m=1}^{M} e^{\mathrm{j}(m-1)x} \right|^2 = \frac{\sin^2\left(\frac{Mx}{2}\right)}{\sin^2\left(\frac{x}{2}\right)}$. Similarly, using the received signal samples $\boldsymbol{q}_{u,\hat{b}}^1 = \left[q_{u,\hat{b}}^1[0], \cdots, q_{u,\hat{b}}^1[N-1] \right]^{\mathrm{T}}$ from synchronization time-slot 1, UE u computes

$$p_{u,\hat{b}}^1 = \left(\sum_{n=0}^{N-1} q_{u,\hat{b}}^1[n] \right) \left(\sum_{n=0}^{N-1} q_{u,\hat{b}}^1[n] \right)^* \tag{6.17}$$

$$= \left| \left[\mathbf{H}_u \left(e^{-\mathrm{j}(\theta+\delta)} \right) \right]_{\hat{b},:} \boldsymbol{f} \right|^2 \frac{\sin^2\left(\frac{N(\mu_u-\theta-\delta)}{2} \right)}{\sin^2\left(\frac{\mu_u-\theta-\delta}{2} \right)}. \tag{6.18}$$

By letting $\delta = 2k'\pi/N$ $(k' = 1, \cdots, \frac{N}{4})$, we can rewrite (6.16) and (6.18) as

$$p_{u,\hat{b}}^0 = \left| \left[\mathbf{H}_u \left(e^{-\mathrm{j}(\theta-\delta)} \right) \right]_{\hat{b},:} \boldsymbol{f} \right|^2 \frac{\sin^2\left(\frac{N(\mu_u-\theta)}{2} \right)}{\sin^2\left(\frac{\mu_u-\theta+\delta}{2} \right)},$$

$$p_{u,\hat{b}}^1 = \left| \left[\mathbf{H}_u \left(e^{-\mathrm{j}(\theta+\delta)} \right) \right]_{\hat{b},:} \boldsymbol{f} \right|^2 \frac{\sin^2\left(\frac{N(\mu_u-\theta)}{2} \right)}{\sin^2\left(\frac{\mu_u-\theta-\delta}{2} \right)}. \tag{6.19}$$

Using $p_{u,\hat{b}}^0$ and $p_{u,\hat{b}}^1$ in (6.19), UE u calculates a ratio metric as

$$\alpha_u = \frac{p_{u,\hat{b}}^0 - p_{u,\hat{b}}^1}{p_{u,\hat{b}}^0 + p_{u,\hat{b}}^1} \tag{6.20}$$

$$= \frac{\sin^2\left(\frac{\mu_u-\theta-\delta}{2} \right) - \sin^2\left(\frac{\mu_u-\theta+\delta}{2} \right)}{\sin^2\left(\frac{\mu_u-\theta-\delta}{2} \right) + \sin^2\left(\frac{\mu_u-\theta+\delta}{2} \right)} \tag{6.21}$$

$$= -\frac{\sin(\mu_u-\theta)\sin(\delta)}{1 - \cos(\mu_u-\theta)\cos(\delta)}, \tag{6.22}$$

which does not depend on the selected receive antenna index $\hat{b}$. According to [41, Lemma 1], if $|\mu_u-\theta| < \delta$, the ratio measure α_u is a monotonic decreasing function of $\mu_u-\theta$ and invertible with respect to $\mu_u-\theta$. Via the inverse function, we can derive the estimated value of μ_u as

$$\hat{\mu}_u = \theta - \arcsin\left(\frac{\alpha_u \sin(\delta) - \alpha_u \sqrt{1 - \alpha_u^2} \sin(\delta)\cos(\delta)}{\sin^2(\delta) + \alpha_u^2 \cos^2(\delta)} \right). \tag{6.23}$$

219

We can then obtain the super-resolution CFO estimate for UE u as $\hat{\varepsilon}_u = \frac{N}{2\pi}\hat{\mu}_u$, comprising both the integer and fractional components. Note that if α_u is perfect, i.e., not impaired by noise and quantization distortion, the CFO can be perfectly recovered, i.e., $\hat{\varepsilon}_u = \varepsilon_u$.

6.4.2 Sum-difference sequences based frequency synchronization

In the proposed sum-difference sequences based approach, the time-domain synchronization sequences $\boldsymbol{d}_\Sigma$ and $\boldsymbol{d}_\Delta$ exhibit different forms from $\boldsymbol{d}_0$ and $\boldsymbol{d}_1$ in (6.5) and (6.6). Specifically, we construct $\boldsymbol{d}_\Sigma$ and $\boldsymbol{d}_\Delta$ as

$$
\begin{aligned}
\boldsymbol{d}_\Sigma &= [d_\Sigma[0], \cdots, d_\Sigma[N/2-1], d_\Sigma[N/2], \cdots, d_\Sigma[N-1]]^{\mathrm{T}} \\
&= \left[1, \cdots, e^{-\mathrm{j}(N/2-1)\eta}, e^{-\mathrm{j}(N/2)\eta}, \cdots, e^{-\mathrm{j}(N-1)\eta}\right]^{\mathrm{T}} \qquad (6.24)\\
\boldsymbol{d}_\Delta &= [d_\Delta[0], \cdots, d_\Delta[N/2-1], d_\Delta[N/2], \cdots, d_\Delta[N-1]]^{\mathrm{T}} \\
&= \left[1, \cdots, e^{-\mathrm{j}(N/2-1)\eta}, -e^{-\mathrm{j}(N/2)\eta}, \cdots, -e^{-\mathrm{j}(N-1)\eta}\right]^{\mathrm{T}}, \qquad (6.25)
\end{aligned}
$$

which are referred to as sum and difference synchronization sequences. They are transmitted via two consecutive synchronization time-slots. Their frequency-domain counterparts $\mathbf{d}_\Sigma$ and $\mathbf{d}_\Delta$ can be similarly obtained following (6.7). Note that the first halves of the sum and difference synchronization sequences $\boldsymbol{d}_\Sigma$ and $\boldsymbol{d}_\Delta$ are identical, while the second half of $\boldsymbol{d}_\Delta$ is the additive inverse of the second half of $\boldsymbol{d}_\Sigma$.

For synchronization time-slot 0, and therefore the corresponding sum synchronization sequence $\boldsymbol{d}_\Sigma$, we express the time-domain received signal sam-

ples as $(n = 0, \cdots, N - 1)$

$$q_{u,b}^{\Sigma}[n] = \mathcal{Q}\left(e^{\mathrm{j}\frac{2\pi\varepsilon_u}{N}n} \sum_{\ell=0}^{L_u-1} [\boldsymbol{H}_u[\ell]]_{b,:} \boldsymbol{f} d_\Sigma[n - \ell] + w_u^{\Sigma}[n]\right). \tag{6.26}$$

Neglecting noise and assuming $\mathcal{Q}(\cdot)$ as the infinite-resolution quantization function,

$$
\begin{aligned}
q_{u,b}^{\Sigma}[n] &= e^{\mathrm{j}\frac{2\pi\varepsilon_u}{N}n} \sum_{\ell=0}^{L_u-1} [\boldsymbol{H}_u[\ell]]_{b,:} \boldsymbol{f} d_\Sigma[n - \ell] & \tag{6.27} \\
&= e^{\mathrm{j}\mu_u n} \sum_{\ell=0}^{L_u-1} [\boldsymbol{H}_u[\ell]]_{b,:} \boldsymbol{f} d_\Sigma[n - \ell] & \tag{6.28} \\
&= e^{\mathrm{j}\mu_u n} \sum_{\ell=0}^{L_u-1} [\boldsymbol{H}_u[\ell]]_{b,:} \boldsymbol{f} e^{-\mathrm{j}(n-\ell)\eta} & \tag{6.29} \\
&= e^{\mathrm{j}n(\mu_u-\eta)} \sum_{\ell=0}^{L_u-1} [\boldsymbol{H}_u[\ell]]_{b,:} \boldsymbol{f} e^{\mathrm{j}\ell\eta} & \tag{6.30} \\
&= e^{\mathrm{j}n(\mu_u-\eta)} \left[\mathbf{H}_u\left(e^{-\mathrm{j}\eta}\right)\right]_{b,:} \boldsymbol{f}. & \tag{6.31}
\end{aligned}
$$

Assuming $\hat{b}$ as the selected receive antenna index for UE u, we sum $\boldsymbol{q}_{u,\hat{b}}^{\Sigma} = \left[q_{u,\hat{b}}^{\Sigma}[0], \cdots, q_{u,\hat{b}}^{\Sigma}[N-1]\right]^{\mathrm{T}}$ over all samples and obtain

$$
\begin{aligned}
p_{u,\hat{b}}^{\Sigma} &= \sum_{n=0}^{N-1} q_{u,\hat{b}}^{\Sigma}[n] & \tag{6.32} \\
&= \left[\mathbf{H}_u\left(e^{-\mathrm{j}\eta}\right)\right]_{\hat{b},:} \boldsymbol{f} \sum_{n=0}^{N-1} e^{\mathrm{j}n(\mu_u-\eta)} & \tag{6.33} \\
&= \left[\mathbf{H}_u\left(e^{-\mathrm{j}\eta}\right)\right]_{\hat{b},:} \boldsymbol{f} \left(1 + e^{\mathrm{j}(N/2)(\mu_u-\eta)}\right) \sum_{n'=0}^{N/2-1} e^{\mathrm{j}n'(\mu_u-\eta)} & \tag{6.34} \\
&= \left[\mathbf{H}_u\left(e^{-\mathrm{j}\eta}\right)\right]_{\hat{b},:} \boldsymbol{f} \left(1 + e^{\mathrm{j}(N/2)(\mu_u-\eta)}\right) e^{\mathrm{j}\frac{N/2-1}{2}(\mu_u-\eta)} \frac{\sin\left(\frac{N/2}{2}(\mu_u-\eta)\right)}{\sin\left((\mu_u-\eta)/2\right)}.
\end{aligned}
$$
$$\tag{6.35}$$

Similar to (6.35), for synchronization time-slot 1, we have

$$p_{u,\hat{b}}^{\Delta} = \left[\mathbf{H}_u\left(e^{-\mathrm{j}\eta}\right)\right]_{\hat{b},:} \boldsymbol{f} \left(1 - e^{\mathrm{j}(N/2)(\mu_u - \eta)}\right) \sum_{n'=0}^{N/2-1} e^{\mathrm{j}n'(\mu_u - \eta)} \tag{6.36}$$

$$= \left[\mathbf{H}_u\left(e^{-\mathrm{j}\eta}\right)\right]_{\hat{b},:} \boldsymbol{f} \left(1 - e^{\mathrm{j}(N/2)(\mu_u - \eta)}\right) e^{\mathrm{j}\frac{N/2-1}{2}(\mu_u - \eta)} \frac{\sin\left(\frac{N/2}{2}(\mu_u - \eta)\right)}{\sin\left((\mu_u - \eta)/2\right)}. \tag{6.37}$$

Using $p_{u,\hat{b}}^{\Sigma}$ and $p_{u,\hat{b}}^{\Delta}$, UE u calculates a ratio measure as

$$\beta_u = \mathrm{Im}\left\{\frac{p_{u,\hat{b}}^{\Sigma}}{p_{u,\hat{b}}^{\Delta}}\right\} = \frac{\sin\left(\frac{N}{2}(\mu_u - \eta)\right)}{1 - \cos\left(\frac{N}{2}(\mu_u - \eta)\right)} \tag{6.38}$$

$$= \cot\left(\frac{N}{4}(\mu_u - \eta)\right), \tag{6.39}$$

which does not depend on the selected receive antenna index $\hat{b}$. By exploiting some trigonometric identities, for $\mu_u - \eta \in \left(4i\pi/N, 4(i+1)\pi/N\right)$ with $i \in \mathbb{Z}$, we can invert the ratio measure β_u and obtain

$$\hat{\mu}_u = \eta + \frac{4}{N}\cot^{-1}(\beta_u), \tag{6.40}$$

which is then used by UE u to compute the CFO estimate as $\hat{\varepsilon}_u = \frac{N}{2\pi}\hat{\mu}_u$. If β_u is perfect, i.e., not impaired by noise and quantization distortion, the CFO can be perfectly recovered, i.e., $\varepsilon_u = \hat{\varepsilon}_u$. As μ_u ($\hat{\mu}_u$) and ε_u ($\hat{\varepsilon}_u$) are equivalent, we use the normalized CFO μ_u and its estimate $\hat{\mu}_u$ throughout the rest of this paper unless otherwise specified.

If $\mathcal{Q}(\cdot)$ in (6.8) and (6.26) corresponds to the low-resolution quantization function (e.g., 1-4 bits), the quantization distortion may damage the monotonic

properties of the ratio metrics, resulting in increased CFO estimation errors. In Sections 6.6 and 6.7, we use both analytical and numerical examples to show that our proposed approaches are robust to the low-resolution quantization; we further show that the proposed two design options exhibit different frequency synchronization performance under different settings (propagation condition, channel variation and etc.). Different cells may flexibly configure their employed synchronization sequences (either auxiliary or sum-difference) for frequency synchronization, depending on their own demands.

6.5 Low-Resolution Double-Sequence Frequency Synchronization

In Section 6.5.1, by exploiting Bussgang's theorem, we first derive the variance of the CFO estimates obtained via the proposed strategies assuming finite low-resolution (e.g., 2-4 bits) quantization. We then examine the robustness of our proposed methods to the quantization distortion. Leveraging the variance results derived in Sections 6.5.1 and 6.5.2, we provide design insights of implementing our proposed algorithms in practical cellular systems.

6.5.1 Performance analysis of auxiliary sequences under few-bit ADCs

Assuming that the input to the quantizer is IID Gaussian, we apply Bussgang's theorem and decompose the received synchronization signal samples in (6.8) (i.e., synchronization time-slot 0) into two uncorrelated compo-

nents, given as

$$q_{u,b}^0[n] \;=\; (1 - \kappa_u) \left(e^{\mathrm{j}\frac{2\pi\varepsilon_u}{N}n} \sum_{\ell=0}^{L_u-1} [\boldsymbol{H}_u[\ell]]_{b,:}\, \boldsymbol{f} d_0[n-\ell] + w_u^0[n] \right) + v_{u,b}^0[n]$$

$$(6.41)$$

$$= (1 - \kappa_u) \left(e^{\mathrm{j}n(\mu_u - \theta + \delta)} \left[\mathsf{H}_u\left(e^{-\mathrm{j}(\theta-\delta)}\right) \right]_{b,:} \boldsymbol{f} + w_u^0[n] \right) + v_{u,b}^0[n],$$

$$(6.42)$$

where $\boldsymbol{v}_{u,b}^0 = \left[v_{u,b}^0[0], \cdots, v_{u,b}^0[N-1] \right]^{\mathrm{T}}$ represents the quantization noise vector with covariance matrix $\sigma_{u,\mathrm{Q}}^2 \boldsymbol{I}_N$, and

$$\sigma_{u,\mathrm{Q}}^2 = \kappa_u(1 - \kappa_u) \left(\mathbb{E}\left[\left| \left[\mathsf{H}_u\left(e^{-\mathrm{j}(\theta-\delta)}\right) \right]_{b,:} \boldsymbol{f} \right|^2 \right] + \sigma_u^2 \right). \qquad (6.43)$$

Similarly, for auxiliary synchronization sequence 1 (synchronization time-slot 1), we express the corresponding quantized received synchronization signal samples as

$$q_{u,b}^1[n] = (1 - \kappa_u) \left(e^{\mathrm{j}n(\mu_u - \theta - \delta)} \left[\mathsf{H}_u\left(e^{-\mathrm{j}(\theta+\delta)}\right) \right]_{b,:} \boldsymbol{f} + w_u^1[n] \right) + v_{u,b}^1[n]. \quad (6.44)$$

The quantization noise vector $\boldsymbol{v}_{u,b}^1 = \left[v_{u,b}^1[0], \cdots, v_{u,b}^1[N-1] \right]^{\mathrm{T}}$ has covariance matrix $\sigma_{u,\mathrm{Q}}^2 \boldsymbol{I}_N$. Using the received signal samples from synchronization time-slots 0 and 1 and recalling that $\hat{b}$ is the selected receive antenna index at UE

u,

$$p^0_{u,\hat{b}} = \left(\sum_{n=0}^{N-1} q^0_{u,\hat{b}}[n]\right)\left(\sum_{n=0}^{N-1} q^0_{u,\hat{b}}[n]\right)^* \tag{6.45}$$

$$= \left[(1-\kappa_u)\left(\left[\mathbf{H}_u\left(e^{-\mathrm{j}(\theta-\delta)}\right)\right]_{\hat{b},:}\boldsymbol{f}\sum_{n=0}^{N-1} e^{\mathrm{j}n(\mu_u-\theta+\delta)} + \sum_{n=0}^{N-1} w^0_u[n]\right)\right.$$
$$\left. + \sum_{n=0}^{N-1} v^0_{u,b}[n]\right]$$
$$\times \left[(1-\kappa_u)\left(\left[\mathbf{H}_u\left(e^{-\mathrm{j}(\theta-\delta)}\right)\right]_{\hat{b},:}\boldsymbol{f}\sum_{n=0}^{N-1} e^{\mathrm{j}n(\mu_u-\theta+\delta)} + \sum_{n=0}^{N-1} w^0_u[n]\right)^*\right.$$
$$\left. + \left(\sum_{n=0}^{N-1} v^0_{u,b}[n]\right)^*\right] \tag{6.46}$$

$$p^1_{u,\hat{b}} = \left(\sum_{n=0}^{N-1} q^1_{u,\hat{b}}[n]\right)\left(\sum_{n=0}^{N-1} q^1_{u,\hat{b}}[n]\right)^* \tag{6.47}$$

$$= \left[(1-\kappa_u)\left(\left[\mathbf{H}_u\left(e^{-\mathrm{j}(\theta+\delta)}\right)\right]_{\hat{b},:}\boldsymbol{f}\sum_{n=0}^{N-1} e^{\mathrm{j}n(\mu_u-\theta-\delta)} + \sum_{n=0}^{N-1} w^1_u[n]\right)\right.$$
$$\left. + \sum_{n=0}^{N-1} v^1_{u,b}[n]\right]$$
$$\times \left[(1-\kappa_u)\left(\left[\mathbf{H}_u\left(e^{-\mathrm{j}(\theta+\delta)}\right)\right]_{\hat{b},:}\boldsymbol{f}\sum_{n=0}^{N-1} e^{\mathrm{j}n(\mu_u-\theta-\delta)} + \sum_{n=0}^{N-1} w^1_u[n]\right)^*\right.$$
$$\left. + \left(\sum_{n=0}^{N-1} v^1_{u,b}[n]\right)^*\right]. \tag{6.48}$$

Using $p^0_{u,\hat{b}}$ in (6.46) and $p^1_{u,\hat{b}}$ in (6.48) to calculate α_u via (6.20), the ratio measure is no longer a strict monotonic function of the CFO to be estimated due to the noise and quantization distortions. In this case, directly inverting the ratio metric may result in relatively large estimation error. In the following, we first analytically characterize the impact of low-resolution ADCs on the

proposed frequency synchronization methods. We then examine the robustness
of our proposed methods to the quantization distortion in Section 6.5.3.

By defining $c_{u,\hat{b}}^0 = p_{u,\hat{b}}^0 - p_{u,\hat{b}}^1$ as auxiliary channel 0 and $c_{u,\hat{b}}^1 = p_{u,\hat{b}}^0 + p_{u,\hat{b}}^1$
as auxiliary channel 1, we present the following lemma to characterize the
variance of the CFO estimate under low-resolution quantization.

Lemma 6.1. For the proposed auxiliary synchronization sequences based low-
resolution frequency synchronization, the variance of the corresponding CFO
estimate is

$$
\sigma_{\hat{\mu}_u,\text{ax}}^2 = \left[\frac{\sin^2\left(\frac{N(\mu_u-\theta+\delta)}{2}\right)\left[\sin^2\left(\frac{\mu_u-\theta-\delta}{2}\right) - \sin^2\left(\frac{\mu_u-\theta+\delta}{2}\right)\right]}{N\left(1-\kappa_u\right)\left(\kappa_u + 1/\gamma_{u,\text{ax}}\right)} \right]^{-2}
$$
$$
\times \quad \frac{[1-\cos(\delta)]^2}{\sin^2(\delta)}\left(1+\alpha_u^2\right), \tag{6.49}
$$

where

$$
\gamma_{u,\text{ax}} = \mathbb{E}\left[\left| \left[\mathbf{H}_u\left(e^{-\mathrm{j}(\theta\pm\delta)}\right)\right]_{\hat{b},:} \boldsymbol{f} \right|^2\right] / \sigma_u^2. \tag{6.50}
$$

Proof. For UE u, by denoting $\mathsf{h}_{u,\hat{b}}^{(\theta,\delta)} = \left[\mathbf{H}_u\left(e^{-\mathrm{j}(\theta-\delta)}\right)\right]_{\hat{b},:}\boldsymbol{f} = \left[\mathbf{H}_u\left(e^{-\mathrm{j}(\theta+\delta)}\right)\right]_{\hat{b},:}\boldsymbol{f}$,
we can first calculate $\mathbb{E}\left[p_{u,\hat{b}}^0\right]$ as

$$
\mathbb{E}\left[p_{u,\hat{b}}^0\right] = (1-\kappa_u)^2\left|\sum_{n=0}^{N-1}e^{\mathrm{j}n(\mu_u-\theta+\delta)}\right|^2\mathbb{E}\left[\left|\mathsf{h}_{u,\hat{b}}^{(\theta,\delta)}\right|^2\right]
$$
$$
+ \quad (1-\kappa_u)^2\sigma_u^2 + \kappa_u(1-\kappa_u)\left(\mathbb{E}\left[\left|\mathsf{h}_{u,\hat{b}}^{(\theta,\delta)}\right|^2\right] + \sigma_u^2\right). \tag{6.51}
$$

Similarly,

$$
\begin{aligned}
\mathbb{E}\left[p_{u,\hat{b}}^1\right] &= (1-\kappa_u)^2 \left|\sum_{n=0}^{N-1} e^{\jmath n(\mu_u - \theta - \delta)}\right|^2 \mathbb{E}\left[\left|\mathsf{h}_{u,\hat{b}}^{(\theta,\delta)}\right|^2\right] \\
&+ (1-\kappa_u)^2 \sigma_u^2 + \kappa_u(1-\kappa_u)\left(\mathbb{E}\left[\left|\mathsf{h}_{u,\hat{b}}^{(\theta,\delta)}\right|^2\right] + \sigma_u^2\right).
\end{aligned}
\tag{6.52}
$$

We can then express the auxiliary channel 0 $c_{u,\hat{b}}^0$ as

$$
\begin{aligned}
c_{u,\hat{b}}^0 &= \mathbb{E}\left[p_{u,\hat{b}}^0 - p_{u,\hat{b}}^1\right] \tag{6.53} \\
&= (1-\kappa_u)^2 \mathbb{E}\left[\left|\mathsf{h}_{u,\hat{b}}^{(\theta,\delta)}\right|^2\right] \left(\left|\sum_{n=0}^{N-1} e^{\jmath n(\mu_u - \theta + \delta)}\right|^2 - \left|\sum_{n=0}^{N-1} e^{\jmath n(\mu_u - \theta - \delta)}\right|^2\right)
\end{aligned}
$$

$$\tag{6.54}$$

$$
\begin{aligned}
&= (1-\kappa_u)^2 \mathbb{E}\left[\left|\mathsf{h}_{u,\hat{b}}^{(\theta,\delta)}\right|^2\right] \sin^2\left(\frac{N(\mu_u - \theta + \delta)}{2}\right) \\
&\times \frac{\sin^2\left(\frac{\mu_u - \theta - \delta}{2}\right) - \sin^2\left(\frac{\mu_u - \theta + \delta}{2}\right)}{\sin^2\left(\frac{\mu_u - \theta + \delta}{2}\right) \sin^2\left(\frac{\mu_u - \theta - \delta}{2}\right)}.
\end{aligned}
\tag{6.55}
$$

Denote the signal power of the auxiliary channel 0 output by S_u^0. According to (6.55), we can obtain

$$
\begin{aligned}
S_u^0 &= \left[(1-\kappa_u)^2 \mathbb{E}\left[\left|\mathsf{h}_{u,\hat{b}}^{(\theta,\delta)}\right|^2\right] \sin^2\left(\frac{N(\mu_u - \theta + \delta)}{2}\right)\right. \\
&\times \left.\frac{\sin^2\left(\frac{\mu_u - \theta - \delta}{2}\right) - \sin^2\left(\frac{\mu_u - \theta + \delta}{2}\right)}{\sin^2\left(\frac{\mu_u - \theta + \delta}{2}\right) \sin^2\left(\frac{\mu_u - \theta - \delta}{2}\right)}\right]^2.
\end{aligned}
\tag{6.56}
$$

Similarly, we can calculate the auxiliary channel 1 $c_{u,\hat{b}}^1$ as

$$
\begin{aligned}
c_{u,\hat{b}}^1 &= \mathbb{E}\left[p_{u,\hat{b}}^0 + p_{u,\hat{b}}^1\right] \tag{6.57} \\
&= (1-\kappa_u)^2 \mathbb{E}\left[\left|\mathsf{h}_{u,\hat{b}}^{(\theta,\delta)}\right|^2\right] \left(\left|\sum_{n=0}^{N-1} e^{\jmath n(\mu_u - \theta + \delta)}\right|^2 + \left|\sum_{n=0}^{N-1} e^{\jmath n(\mu_u - \theta - \delta)}\right|^2\right) \\
&+ 2N\left[(1-\kappa_u)^2 \sigma_u^2 + \sigma_{u,\mathrm{Q}}^2\right]. \tag{6.58}
\end{aligned}
$$

Denote the quantization-plus-noise power of the auxiliary channel 1 output for UE u by N_u^1. According to (6.58), we have

$$N_u^1 \;=\; 4N^2 \left[(1 - \kappa_u)^2 \, \sigma_u^2 + \sigma_{u,\mathrm{Q}}^2 \right]^2 \tag{6.59}$$

$$\;=\; 4N^2 \left[(1 - \kappa_u) \left(\kappa_u \mathbb{E} \left[\left| \mathsf{h}_{u,\hat{b}}^{(\theta,\delta)} \right|^2 \right] + \sigma_u^2 \right) \right]^2 . \tag{6.60}$$

Denote by $\gamma_{u,\mathrm{ax}} = \mathbb{E}\left[\left| \mathsf{h}_{u,\hat{b}}^{(\theta,\delta)} \right|^2 \right] / \sigma_u^2$. Using (6.51) and (6.52), we can express α_u as

$$\alpha_u =$$

$$\frac{\left| \sum_{n=0}^{N-1} e^{\mathrm{j}n(\mu_u - \theta + \delta)} \right|^2 - \left| \sum_{n=0}^{N-1} e^{\mathrm{j}n(\mu_u - \theta - \delta)} \right|^2}{\left(\left| \sum_{n=0}^{N-1} e^{\mathrm{j}n(\mu_u - \theta + \delta)} \right|^2 + \left| \sum_{n=0}^{N-1} e^{\mathrm{j}n(\mu_u - \theta - \delta)} \right|^2 \right) + 2/\gamma_{u,\mathrm{ax}} + \frac{2\kappa_u}{1 - \kappa_u}\left(1 + 1/\gamma_{u,\mathrm{ax}}\right)}. \tag{6.61}$$

Assuming high *received* SNR (high-power regime with very large N_{tot} and receive processing with antenna selection), we can approximate $1/\gamma_{u,\mathrm{ax}}$ as zero. Further, for low-resolution quantization ($2 \sim 4$ bits), we can also approximate $\kappa_u/(1 - \kappa_u)$ as zero. Hence,

$$\alpha_u \approx \alpha_{u,\mathrm{ideal}} = \frac{\left| \sum_{n=0}^{N-1} e^{\mathrm{j}n(\mu_u - \theta + \delta)} \right|^2 - \left| \sum_{n=0}^{N-1} e^{\mathrm{j}n(\mu_u - \theta - \delta)} \right|^2}{\left| \sum_{n=0}^{N-1} e^{\mathrm{j}n(\mu_u - \theta + \delta)} \right|^2 + \left| \sum_{n=0}^{N-1} e^{\mathrm{j}n(\mu_u - \theta - \delta)} \right|^2}. \tag{6.62}$$

Motivated by (6.23), we formulate the corresponding frequency estimator as

$$\breve{\mu}_u = \theta - \arcsin\left(\frac{\alpha_u \sin(\delta) - \alpha_u \sqrt{1 - \alpha_u^2} \sin(\delta)\cos(\delta)}{\sin^2(\delta) + \alpha_u^2 \cos^2(\delta)} \right). \tag{6.63}$$

Because $\alpha_u \approx \alpha_{u,\mathrm{ideal}}$, we can rewrite (6.63) as

$$\breve{\mu}_u \approx \theta - \arcsin\left(\frac{\alpha_{u,\mathrm{ideal}} \sin(\delta) - \alpha_{u,\mathrm{ideal}} \sqrt{1 - \alpha_{u,\mathrm{ideal}}^2} \sin(\delta)\cos(\delta)}{\sin^2(\delta) + \alpha_{u,\mathrm{ideal}}^2 \cos^2(\delta)} \right). \tag{6.64}$$

228

By plugging $\alpha_{u,\text{ideal}}$ in (6.22) into (6.64), we can obtain $\mathbb{E}\left[\breve{\mu}_u\right] \approx \mu_u$ such that the CFO estimator $\breve{\mu}_u$ in (6.63) in this response letter is approximately unbiased for a fixed pair (θ, μ_u) in the high-power regime.

The variance of the CFO estimate can then be expressed as [116, equation 3.26]

$$\sigma^2_{\hat{\mu}_u,\text{ax}} = \frac{1}{\varsigma^2_{\text{ax}} S^0_u / N^1_u} \left[1 + \mathcal{M}^2_{\text{ax}}(\mu_u)\right],\tag{6.65}$$

where $\mathcal{M}_{\text{ax}}(\mu_u) = \alpha_{u,\text{ideal}}$ for the proposed auxiliary sequences based method, and ς_{ax} represents the slope of $\mathcal{M}_{\text{ax}}(\cdot)$ at θ, i.e.,

$$\varsigma_{\text{ax}} = \mathcal{M}'_{\text{ax}}(\theta) = \frac{\sin(\delta)}{\cos(\delta) - 1}.\tag{6.66}$$

By plugging (6.56), (6.60) and (6.66) into (6.65), we can obtain (6.49), which completes the proof. □

As can be seen from (6.49), the CFO estimation performance of the proposed method depends on various design parameters such as the sequence length N, the quantization NMSE κ_u, the reference frequency set $\{\theta, \delta\}$, and the received SNR $\gamma_{u,\text{ax}}$.

6.5.2 Performance analysis of sum-difference sequences under few-bit ADCs

By Bussgang's theorem, we decouple the received signal samples corresponding to the sum synchronization sequence in (6.26) as

$$q_{u,b}^{\Sigma}[n] = (1 - \kappa_u) \left(e^{j\frac{2\pi\varepsilon_u}{N}n} \sum_{\ell=0}^{L_u-1} [\boldsymbol{H}_u[\ell]]_{b,:} \boldsymbol{f} d_{\Sigma}[n - \ell] + w_u^{\Sigma}[n] \right) + v_{u,b}^{\Sigma}[n] \tag{6.67}$$

$$= (1 - \kappa_u) \left(e^{jn(\mu_u - \eta)} \left[\mathbf{H}_u \left(e^{-j\eta}\right)\right]_{b,:} \boldsymbol{f} + w_u^{\Sigma}[n] \right) + v_{u,b}^{\Sigma}[n], \tag{6.68}$$

and the received signal samples for the difference synchronization sequence as

$$q_{u,b}^{\Delta}[n] = \begin{cases} (1 - \kappa_u) \left(e^{jn(\mu_u - \eta)} \left[\mathbf{H}_u \left(e^{-j\eta}\right)\right]_{b,:} \boldsymbol{f} + w_u^{\Delta}[n] \right) + v_{u,b}^{\Delta}[n], \\ \qquad\qquad\qquad\qquad\qquad n = 0, 1, \cdots, N/2 - 1 \\ (1 - \kappa_u) \left(-e^{jn(\mu_u - \eta)} \left[\mathbf{H}_u \left(e^{-j\eta}\right)\right]_{b,:} \boldsymbol{f} + w_u^{\Delta}[n] \right) + v_{u,b}^{\Delta}[n], \\ \qquad\qquad\qquad\qquad\qquad n = N/2, \cdots, N - 1. \end{cases} \tag{6.69}$$

The quantization noise vectors $\boldsymbol{v}_{u,b}^{\Sigma} = \left[v_{u,b}^{\Sigma}[0], \cdots, v_{u,b}^{\Sigma}[N - 1]\right]^{\mathrm{T}}$ and $\boldsymbol{v}_{u,b}^{\Delta} = \left[v_{u,b}^{\Delta}[0], \cdots, v_{u,b}^{\Delta}[N - 1]\right]^{\mathrm{T}}$ have the same covariance matrix $\sigma_{u,\mathcal{Q}}^2 \boldsymbol{I}_N$, and

$$\sigma_{u,\mathcal{Q}}^2 = \kappa_u (1 - \kappa_u) \left(\mathbb{E} \left[\left| \left[\mathbf{H} \left(e^{-j\eta}\right)\right]_{\hat{b},:} \boldsymbol{f} \right|^2 \right] + \sigma_u^2 \right). \tag{6.70}$$

For the selected $\hat{b}$-th receive antenna at UE u, we define $p_{u,\hat{b}}^{\Sigma} = \sum_{n=0}^{N-1} q_{u,\hat{b}}^{\Sigma}[n]$ and $p_{u,\hat{b}}^{\Delta} = \sum_{n=0}^{N-1} q_{u,\hat{b}}^{\Delta}[n]$ as the corresponding sum and difference channels. Based on (6.35) and (6.37), we obtain

$$p_{u,\hat{b}}^{\Sigma} = (1 - \kappa_u) \left(\left[\mathbf{H}_u \left(e^{-j\eta}\right)\right]_{\hat{b},:} \boldsymbol{f} \left(1 + e^{j(N/2)(\mu_u - \eta)}\right) e^{j\frac{N/2-1}{2}(\mu_u - \eta)} \right.$$
$$\left. \times \frac{\sin\left(\frac{N/2}{2}(\mu_u - \eta)\right)}{\sin\left((\mu_u - \eta)/2\right)} + \sum_{n=0}^{N-1} w_u^{\Sigma}[n] \right) + \sum_{n=0}^{N-1} v_{u,\hat{b}}^{\Sigma}[n] \tag{6.71}$$

230

$$p_{u,\hat{b}}^{\Delta} = (1 - \kappa_u) \left(\left[\mathbf{H}_u \left(e^{-\mathrm{j}\eta} \right) \right]_{\hat{b},:} \boldsymbol{f} \left(1 - e^{\mathrm{j}(N/2)(\mu_u - \eta)} \right) e^{\mathrm{j}\frac{N/2-1}{2}(\mu_u - \eta)} \right.$$

$$\left. \times \frac{\sin \left(\frac{N/2}{2}(\mu_u - \eta) \right)}{\sin \left((\mu_u - \eta)/2 \right)} + \sum_{n=0}^{N-1} w_u^{\Delta}[n] \right) + \sum_{n=0}^{N-1} v_{u,b}^{\Delta}[n]. \qquad (6.72)$$

Using $p_{u,\hat{b}}^{\Sigma}$ in (6.71) and $p_{u,\hat{b}}^{\Delta}$ in (6.72) to compute β_u via (6.38), the ratio metric is no longer a strict monotonic function of the CFO to be estimated. This observation is similar to that in Section 6.5.1 for the proposed auxiliary sequences based approach. According to (6.71) and (6.72), we first provide the following lemma to reveal the variance of the CFO estimate assuming low-resolution quantization.

Lemma 6.2. For the proposed sum-difference synchronization sequences based low-resolution frequency synchronization, the variance of the CFO estimate is given as

$$\sigma_{\hat{\mu}_u,\mathrm{sd}}^2 = \left[\frac{N \left(1 - \kappa_u \right) \left| 1 + e^{\mathrm{j}(N/2)(\mu_u - \eta)} \right|^2 \sin^2 \left(\frac{N/2}{2}(\mu_u - \eta) \right) \csc^4 \left(\frac{N}{4}\eta \right)}{16 \left(\kappa_u + 1/\gamma_{u,\mathrm{sd}} \right) \sin^2 \left((\mu_u - \eta)/2 \right)} \right]^{-1}$$

$$\times \left(1 + \beta_u^2 \right), \qquad (6.73)$$

where

$$\gamma_{u,\mathrm{sd}} = \mathbb{E} \left[\left| \left[\mathbf{H}_u \left(e^{-\mathrm{j}\eta} \right) \right]_{\hat{b},:} \boldsymbol{f} \right|^2 \right] / \sigma_u^2. \qquad (6.74)$$

As can be seen from Lemma 6.2, the variance of the CFO estimate depends on the sequence length N, the quantization NMSE κ_u, the frequency difference $\triangle_u = |\mu_u - \eta|$, and the received SNR $\gamma_{u,\mathrm{sd}}$.

6.5.3 Robustness to low-resolution quantization

It is still difficult to analytically characterize the robustness of the proposed frequency synchronization methods to the quantization distortion, though their closed-form CFO estimation performances are presented in (6.49) and (6.73). We therefore focus on empirical evaluations and plot the ratio metrics in Figures 6.2(a) and 6.2(b) for various quantization resolutions. As shown in Figure 6.2, the monotonic properties do not hold for the ratio measures in the ambiguity regions such that directly inverting these ratio measures may result in large estimation errors. The ambiguity regions, however, are relatively small under various quantization resolutions. Further, except the ambiguity regions, the actual ratio values under few-bit ADCs are close to those under infinite-resolution ADCs. Hence, by inverting the ratio measures obtained through few-bit ADCs, we can still expect promising CFO estimation performances for our proposed methods, which are numerically verified in Section 6.7.

As shown in (6.49) and (6.73), the CFO estimation performances of our proposed methods also depend on certain double-sequence design parameter(s). For the auxiliary sequences based strategy, these parameters correspond to the reference frequency set $\{\theta, \delta\}$; for the sum-difference sequences based strategy, this parameter becomes η (or the frequency difference $\triangle$). In addition to the sequence length N and the received SNR, the double-sequence design parameter(s) can be further optimized to compensate for the quantization distortion. In Section 6.6, we first use (6.49) (or equivalently, (6.73)) to

formulate the optimization problems; we then conclude from the corresponding solutions that in contrast to conventional pilot/sequence-aided frequency synchronization methods, our proposed strategies are capable of exploiting more design degrees of freedom to further improve the low-resolution frequency synchronization performance.

6.6 Practical Implementation of Double-Sequence Frequency Synchronization

In this section, we explain the implementation procedure of our proposed double-sequence low-resolution frequency synchronization methods in practical cellular networks. We focus on a multi-user scenario with various quantization configurations. We exploit the analytical performance assessments to configure the double-sequence design parameters such that for different deployment scenarios, the impact of low-resolution quantization distortion on the overall frequency synchronization performance can be minimized.

6.6.1 Basic system setup and assumption

In this chapter, we consider a single cell serving multiple UEs. Note that our proposed designs can be extended to multiple cells by scrambling the synchronization channels with different physical cell identities (PCIs) to avoid inter-cell interference. All serving UEs are equipped with fully digital front ends and low-resolution ADCs. The ADC resolutions could be different for different UEs. The BS transmits common synchronization signal to all serving

UEs via directional analog beamforming. The design target here is to track all serving UEs' CFOs without compromising much on each individual UE's CFO estimation performance. This can be accomplished by adjusting the frequency range of estimation of the common synchronization signal according to the distribution of all potential CFOs. In the following, we first formulate the multicast frequency synchronization problem as a min-max optimization problem assuming low-resolution quantization. By leveraging certain predefined system specific parameters, we transform the min-max problem into a minimization problem, and develop an adaptive algorithm to solve it. For the rest of this section, we employ the auxiliary sequences based method to illustrate the basic design procedure, which applies to the sum-difference sequences based design as well with moderate modifications.

6.6.2 Optimization problem formulation of proposed low-resolution frequency synchronization

To accommodate many UEs with satisfying low-resolution frequency synchronization performance, we need to incorporate the frequency range of estimation (e.g., $[\theta - \delta, \theta + \delta]$ in the auxiliary sequences based method and $\triangle$ in the sum-difference sequences based approach) into the optimization problem formulation. Define Θ as a codebook containing discrete values distributed within $[-1, 1]$. Using (6.49) and accounting for all N_{UE} serving UEs, we can therefore formulate the corresponding low-resolution frequency synchroniza-

tion problem as

$$\min_{\{\theta,\delta\}} \max_{\forall u} \quad \left\{\sigma^2_{\hat{\mu}_u,\text{ax}}\right\} \tag{6.75}$$

$$\text{subject to} \quad \theta \in \Theta$$

$$\delta = 2k'\pi/N, k' = 1, \cdots, \frac{N}{4}$$

$$u \in \{1, \cdots, N_{\text{UE}}\},$$

which is a min-max optimization problem and difficult to solve. To simplify (6.75), we first define κ_{ax}, μ_{ax}, α_{ax} and γ_{ax} as system specific parameters. They are predefined and can be flexibly configured by the network controller according to long-term measurements and system statistics. We use κ_{ax}, μ_{ax}, α_{ax} and γ_{ax} to replace κ_u, μ_u, α_u and $\gamma_{u,\text{ax}}$ in (6.49) and obtain

$$\sigma^2_{\hat{\mu}_{\text{ax}}} = \left[\frac{\sin^2\left(\frac{N(\mu_{\text{ax}}-\theta+\delta)}{2}\right)\left[\sin^2\left(\frac{\mu_{\text{ax}}-\theta-\delta}{2}\right) - \sin^2\left(\frac{\mu_{\text{ax}}-\theta+\delta}{2}\right)\right]}{N(1-\kappa_{\text{ax}})(\kappa_{\text{ax}}+1/\gamma_{\text{ax}})}\right]^{-2}$$

$$\times \frac{[1-\cos(\delta)]^2}{\sin^2(\delta)}\left(1+\alpha^2_{\text{ax}}\right). \tag{6.76}$$

We can then rewrite the optimization problem as

$$\min_{\{\theta,\delta\}} \quad \left\{\sigma^2_{\hat{\mu}_{\text{ax}}}\right\} \tag{6.77}$$

$$\text{subject to} \quad \theta \in \Theta$$

$$\delta = 2k'\pi/N, k' = 1, \cdots, \frac{N}{4}.$$

We formulate (6.77) by treating all serving UEs as a single virtual UE with common system specific parameters κ_{ax}, μ_{ax}, α_{ax} and γ_{ax}. We need to carefully select κ_{ax}, μ_{ax}, α_{ax} and γ_{ax} such that $\sigma^2_{\hat{\mu}_{\text{ax}}}$ for the virtual UE can represent each

235

individual UE's error variance, i.e., $\sigma^2_{\hat{\mu}_u,\mathrm{ax}}$ ($u \in \{1, \cdots, N_{\mathrm{UE}}\}$), as much as possible. We present one example of how to determine the system specific parameters in Section 6.6.3. Note that if κ_u, μ_u, α_u and $\gamma_{u,\mathrm{ax}}$ ($u \in \{1, \cdots, N_{\mathrm{UE}}\}$) vary significantly from UE to UE, the problem formulation in (6.76) and (6.77) may not be accurate. This in turn, may result in poor frequency synchronization performance in the multi-user scenario. In Section 6.7, we use several numerical examples to characterize this aspect. Finally, we solve (6.77) by optimizing the double-sequence parameters such that the estimation error variance of the virtual UE is minimized.

6.6.3 Design procedure of proposed low-resolution frequency synchronization

According to (6.76), solving (6.77) requires the BS to have explicit knowledge of κ_{ax}, μ_{ax} (α_{ax}) and γ_{ax}. Though different UEs may have different ADC resolutions, we use a single κ_{ax} to characterize all serving UEs. In Section 6.7, we set $\kappa_{\mathrm{ax}} = 0.1175$ (i.e., 2-bit ADCs) when simulating the multi-user scenario. Further, γ_{ax} can be obtained by averaging over the received signal-to-interference-plus-noise ratios (SINRs) of all UEs. Selecting a good μ_{ax} is also important for the BS to determine a proper frequency range of estimation that can capture as many UEs' CFOs as possible. In this paper, we assume that the BS or the network controller configures μ_{ax} using long-term system statistics such as those from previously connected UEs.

We summarize the detailed design procedure in Algorithm 6.1. As

---
Algorithm 6.1 Auxiliary sequences based low-resolution frequency synchronization design

---

BS-SIDE PROCESSING

    1 : Configuring κ_{ax}, μ_{ax}, α_{ax} and γ_{ax} based on long-term measurements and system statistics.

    2 : Computing $\sigma^2_{\hat{\mu}_{\mathrm{ax}}}$ according to (6.76) and finding θ_{opt} and δ_{opt} that minimizes $\sigma^2_{\hat{\mu}_{\mathrm{ax}}}$ following (6.77).

    3 : If necessary, conveying the selected θ_{opt} and δ_{opt} to UEs after their timing synchronization.

    4 : Constructing $\boldsymbol{d}_0$ and $\boldsymbol{d}_1$ according to (6.5) and (6.6), and maps their frequency-domain counterparts on given subcarriers.

    5 : Probing the synchronization signal at given synchronization time-slots.

UE-SIDE PROCESSING (UE u, $u \in \{1, \cdots, N_{\mathrm{UE}}\}$)

    i : Preprocessing: timing synchronization and discarding the CP.

    ii : Computing the received synchronization signal strengths $p^0_{u,\hat{b}}$, $p^1_{u,\hat{b}}$ and the ratio measure α_u according to (6.20).

    iii : Inverting the ratio measure α_u according to (6.22) to obtain the CFO estimate $\hat{\mu}_u$.

    iv : Compensating the received signal samples with the estimated CFO.

---

can be seen from Algorithm 6.1, the BS needs to convey the optimized double-sequence design parameters (e.g., θ_{opt} and δ_{opt} in the auxiliary sequences based method) to the UE so that the UE can execute the ratio metric inversion. This requires additional signaling support from the BS to the UE, which can still be implemented in the initial access process after the UE completes the symbol/frame timing synchronization and PCI detection. To reduce this signaling overhead, the BS can optimize the double-sequence design parameters in a semi-static manner, using long-term measurements and system statistics.

6.7   Numerical Results

In this section, we evaluate our proposed auxiliary and sum-difference sequences based frequency synchronization methods assuming low-resolution (e.g., 1-4 bits) ADCs. Both the BS and UE employ a ULA with inter-element spacing $\lambda/2$, where λ represents the wavelength corresponding to the operating carrier frequency. Throughout the simulation section, we assume that $N_{\mathrm{tot}} = 16$ and $M_{\mathrm{tot}} = 8$. The BS covers $120°$ angular range $[-60°, 60°]$ around boresight ($0°$), and the UE monitors the entire $180°$ angular region $[-90°, 90°]$ around boresight ($0°$). We consider both narrowband and wideband mmWave channels to evaluate our proposed algorithms, incorporating a single UE or multiple UEs.

6.7.1 Narrowband mmWave channels with a single UE

In Figure 6.3, we evaluate our proposed strategies in narrowband channels with a single UE. Specifically, we employ the Rician channel model. We set the number of NLOS channel components as 5 and the Rician K-factor value as 13.2 dB. We also simulate the conventional ZC sequence based CFO estimation approach for comparison. We set the root index as 24 for the employed ZC sequence.

We plot the MSEs of the CFO estimates in Figures 6.3(a) and 6.3(b), in which we set the normalized CFOs as 0.6 and 0.95. It can be observed from Figures 6.3(a) and 6.3(b) that under various quantization resolutions, our proposed auxiliary sequences and sum-difference sequences based methods exhibit superior CFO estimation performances over the ZC sequence based design. For 0.95 normalized CFO in Figure 6.3(b), the sum-difference sequences based approach shows better performance than the auxiliary sequences based method under various SNRs.

6.7.2 Wideband mmWave channels with a single UE

Now, we evaluate the frame error rate (FER) of our proposed methods assuming few-bit ADCs. We present the block diagram of the developed link-level simulator in Figure 6.4, which includes a complete chain of Turbo coding/decoding, OFDM and DAC/ADC modules. We assume perfect channel estimation, frame timing synchronization and infinite-resolution DACs. We adopt the 3GPP 5G tapped delay line (TDL-A) wideband channel model

Table 6.1: Simulation assumptions and parameters for low-resolution frequency synchronization in wideband mmWave channels.

SYSTEM PARAMETERS	SIMULATION ASSUMPTIONS
Carrier frequency	30 GHz
System bandwidth	80 MHz
FFT size	1024
Subcarrier spacing	120 KHz
OFDM symbol duration (μs)	8.33
CP length (μs)	0.82
Channel coding	Turbo
MCS	QPSK 1/2
Channel model	3GPP 5G NR TDL-A
Channel estimation	Ideal

into the link-level simulation assuming 30 GHz carrier frequency and a 80 MHz RF bandwidth. We provide other simulation assumptions such as the assumed OFDM numerology and the modulation and coding scheme (MCS) in Table 6.1. Note that we do not incorporate the phase noise and channel estimation error in evaluating our proposed low-resolution frequency synchronization methods. This is because these two design aspects, especially the channel estimation, are less relevant to the considered CFO estimation problem under low-resolution ADCs. It may be interesting though to include all the impairments for future numerical evaluations of our proposed strategies. According to these settings, a 0.1 normalized CFO corresponds to a 1.95 MHz time-domain CFO or 65 ppm of the 30 GHz carrier frequency. In Figures 6.5(a) and 6.5(b), we plot the FER performances assuming both 2-bit and 3-bit ADCs. As can be seen from Figure 6.5(b), our proposed auxiliary and sum-difference sequences based frequency synchronization strategies significantly outperform the ZC se-

quence based CFO estimation method. Further, in the low-to-medium SNR regime (e.g., -10 dB ~ 10 dB), our proposed methods show close error rate performances to the ideal case without CFO. For our proposed methods and the ZC sequence based strategy, we can observe error floors at high SNRs. In contrast to the narrowband results shown in Figure 6.3, we can conclude from Figure 6.5 that the auxiliary sequences based method is more robust to the frequency selectivity than the sum-difference sequences based strategy.

In Figure 6.6, we evaluate the throughput performances for our proposed methods assuming various quantization resolutions. We compare 1-bit and 2-bit ADCs in Figure 6.6(a) and observe that our proposed methods outperform the ZC sequence based strategy (similar to Figure 6.5) for 0.05 normalized CFO. For instance, at 20 dB SNR, the throughput of our proposed sum-difference sequences based method is 3 bit/s/Hz higher than that of the ZC sequence based strategy assuming 1-bit ADCs. The corresponding throughput gain is 150%. With increase in the quantization resolution, their performance gap reduces. In Figure 6.6(b), we examine our proposed approaches under 4-bit and infinite-resolution ADCs. The performance differences between 4-bit quantization and infinite-resolution quantization are marginal.

In Figure 6.7, we examine the impact of the overall synchronization sequence length on the low-resolution frequency synchronization performance. Here, the overall sequence length L_{seq} corresponds to $2N$ for the double-sequence structure, and N_{ZC} for the ZC symmetry based strategy. It can be

seen from Figure 6.7(a) that a longer overall sequence length does not necessarily result in a better CFO estimation performance for the ZC sequence based method assuming low-resolution quantization. At relatively high SNR, e.g., 20 dB in this example, the quantization distortion dominates the performance, and may severely corrupt the symmetry of the ZC sequence especially when a longer overall sequence length is assumed. With increase in L_{seq}, however, the low-resolution frequency synchronization performance improves for both our proposed auxiliary sequences and sum-difference sequences based methods. In Figure 6.7(b), we compute the resource overhead in percentile by assuming a total of 128 resource elements available for transmitting the synchronization sequence. It is evident from Figure 6.7(b) that except for $L_{\text{seq}} = 32$ at relatively high SNR, our proposed methods even exhibit a better low-resolution CFO estimation performance than the ZC symmetry based strategy with a reduced resource overhead.

6.7.3 Wideband mmWave channels with multiple UEs

In this part of simulation, we consider multiples UEs with 2-bit ADCs equipped each. Other simulation parameters and wideband channel model are the same as those in Section 6.7.2. In Figure 6.8, we evaluate our proposed methods assuming a total of 10 UEs. Their normalized CFOs are randomly distributed within given intervals $[-0.02, 0.02]$, $[-0.03, 0.03]$, $[-0.05, 0.05]$, $[-0.07, 0.07]$ and $[-0.1, 0.1]$.

In Figure 6.8(a), we compare the CFO estimation MSEs between our

proposed strategies and the ZC sequence based approach under various frequency ranges of CFOs. For the auxiliary and sum-difference sequences, we set the frequency range of estimation as $[-0.01, 0.01]$ by configuring the double-sequence design parameters. As can be seen from Figure 6.8(a), our proposed methods can provide better CFO estimation performances for a wide range of frequencies in the multi-user setup.

In Figure 6.8(b), we examine the impact of frequency range of estimation on the frequency synchronization performances. In this plot, we only consider the auxiliary sequences based method. It is evident from Figure 6.8(b) that by increasing the frequency range of estimation from $[-0.01, 0.01]$ to $[-0.03, 0.03]$, the CFO estimation MSEs reduce. By further enlarging the frequency range of estimation to accommodate even more UEs (e.g., from $[-0.03, 0.03]$ to $[-0.08, 0.08]$), however, the overall CFO estimation performance degrades. These performance variations are resulted from the fact that the frequency range of estimation ($[\theta - \delta, \theta + \delta]$ in this example) is not optimized according to the CFOs distribution and the received SNRs. Finally, we plot the optimal case that uses θ_{opt} and δ_{opt} (obtained via (6.77)) to construct the auxiliary sequences in Figure 6.8(b). It can be observed that the corresponding CFO estimation performance is the best among all configurations and consistent across all frequency ranges of CFOs.

6.8   Conclusion

In this chapter, we custom designed two double-sequence structures, i.e., auxiliary sequences and sum-difference sequences, for frequency synchronization in mmWave systems operating with low-resolution ADCs. The proposed two design options are different in terms of the ratio metric formulation, the double-sequence design parameters, and the achievable CFO estimation performance. We used analytical and numerical examples to show that our proposed methods are robust to the low-resolution quantization for a various of network settings. We concluded from extensive empirical results that under low-resolution ADCs: (i) our proposed strategies provide promising overall frequency synchronization performance that can better trade off the CFO estimation accuracy and the frequency range of estimation, and (ii) our custom designed auxiliary and sum-difference sequences outperform the ZC sequences in estimating the frequency offset.
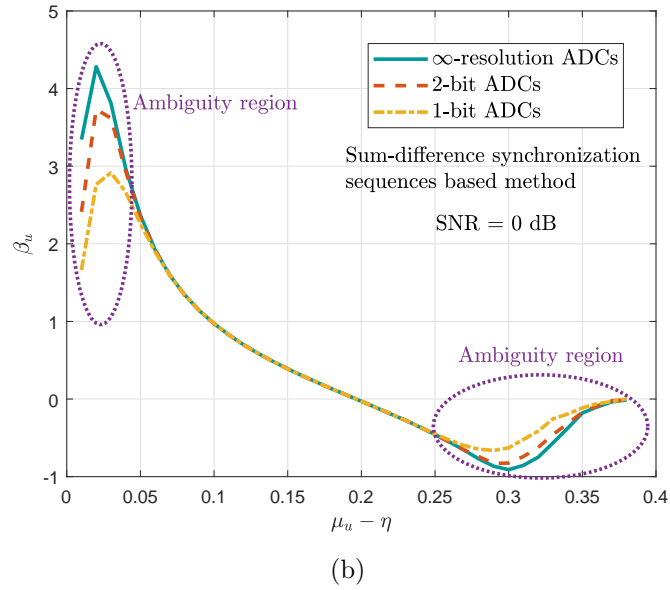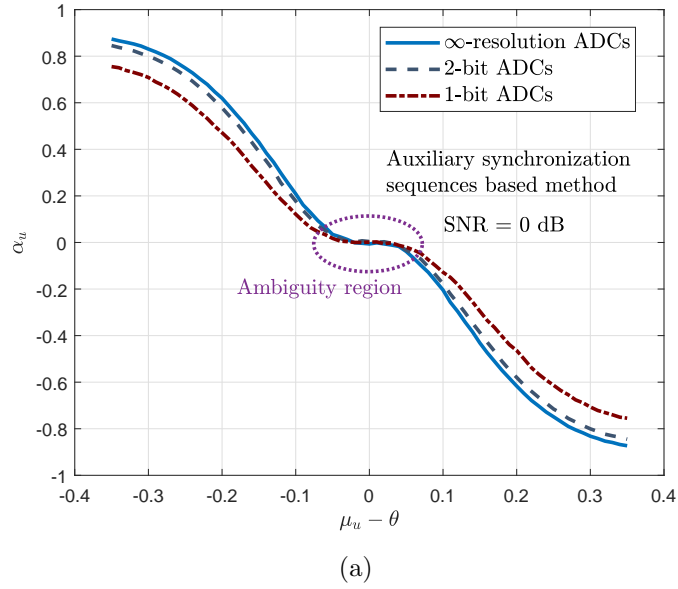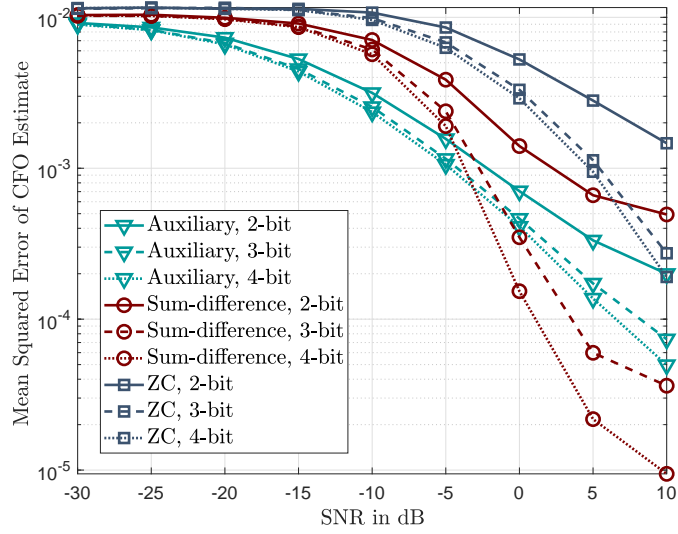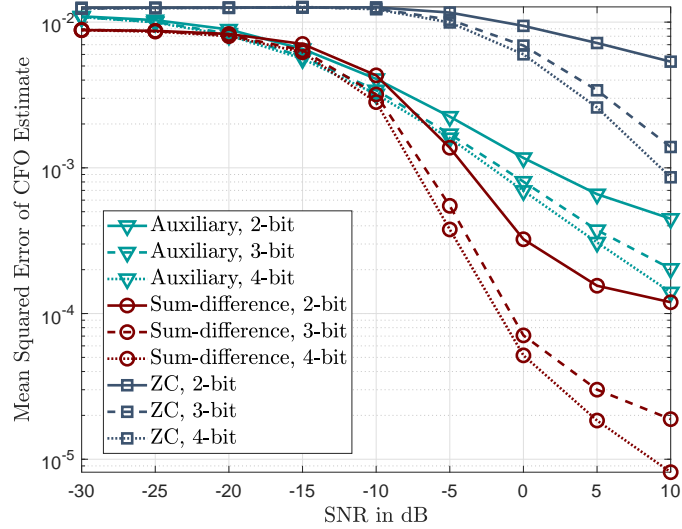
(a)

(b)

Figure 6.2: (a) Ratio metric versus $\mu_u - \theta$ for the proposed auxiliary sequences based double-sequence design. The ratio metric is no longer a monotonic function of the CFO to be estimated in the ambiguity region(s). (b) Ratio metric versus $\mu_u - \eta$ for the proposed sum-difference sequences based design.

245

Figure 6.3: Mean squared errors of the CFO estimates obtained via the ZC sequence based method and our proposed auxiliary and sum-difference sequences based methods are plotted against various SNRs. Narrowband Rician channels are assumed with 13.2 dB Rician K-factor and a single UE. (a) 0.6 normalized CFO. (b) 0.95 normalized CFO.
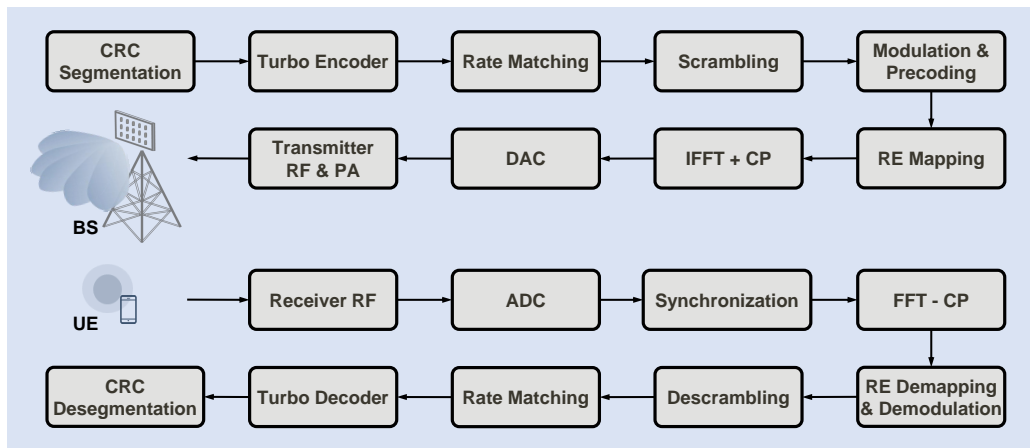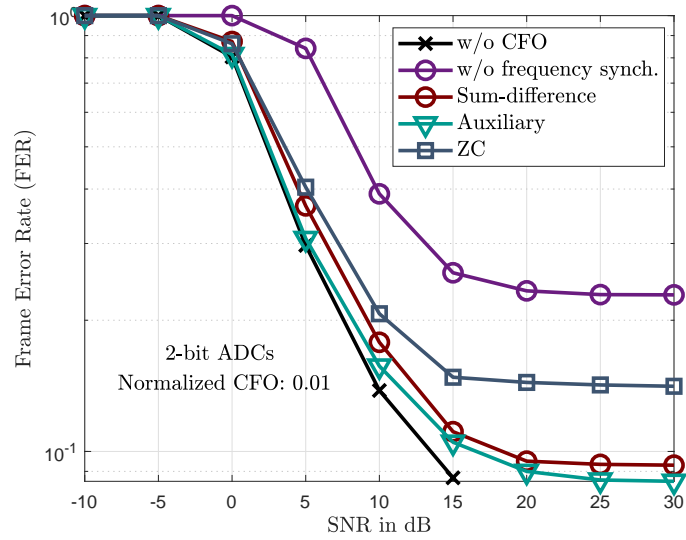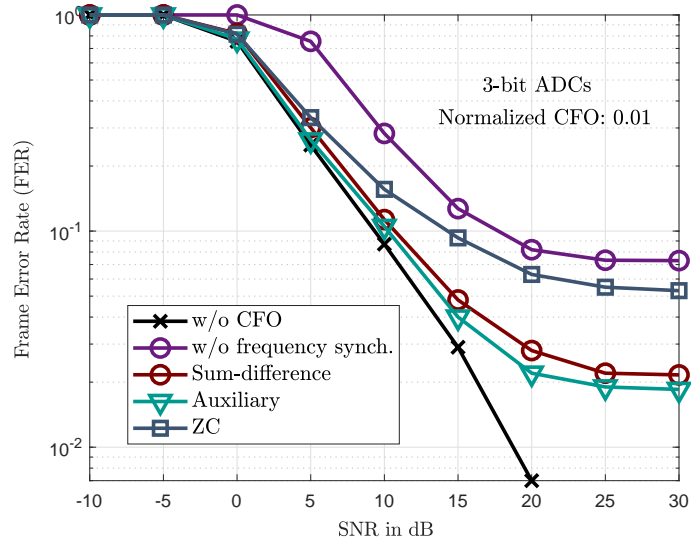
Figure 6.4: Block diagram of employed link-level simulator for evaluating our proposed low-resolution frequency synchronization methods in wideband mmWave channels.
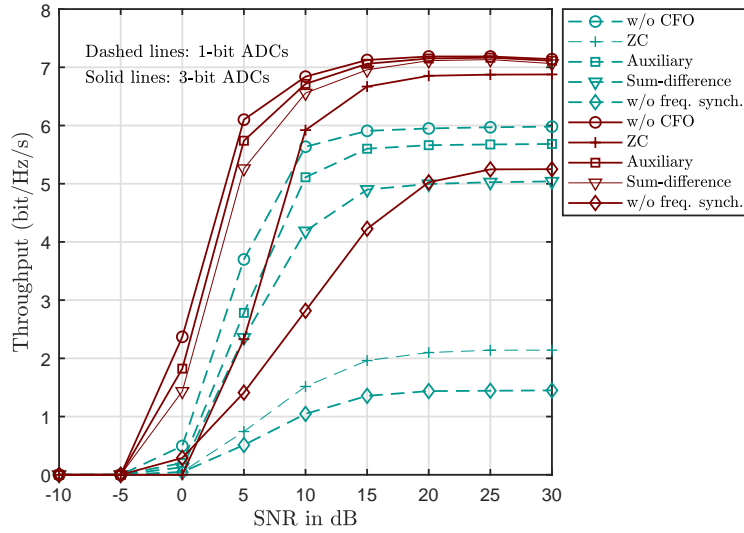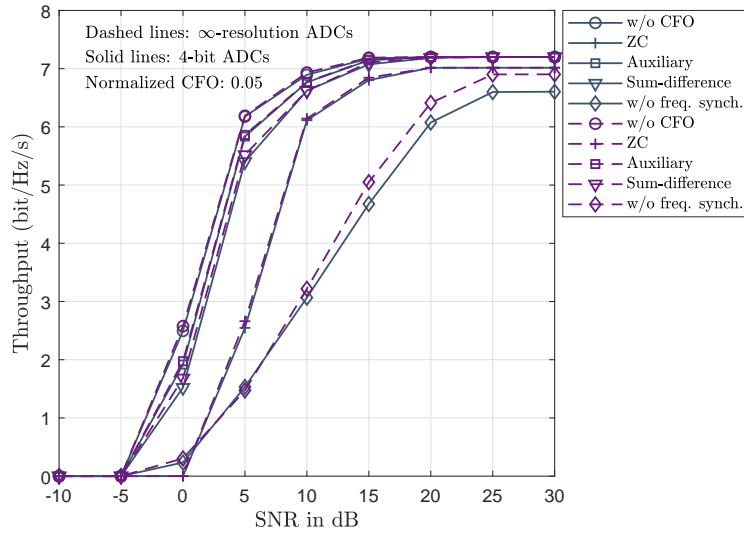
Figure 6.5: Frame error rate performances of our proposed auxiliary and sum-difference sequences based low-resolution frequency synchronization methods. The normalized CFO is set to 0.01. Other simulation assumptions are given in Table 6.1. (a) 2-bit ADCs. (b) 3-bit ADCs.

(a)

(b)

Figure 6.6: Throughput performances versus SNRs of our proposed auxiliary and sum-difference sequences based low-resolution frequency synchronization methods. The normalized CFO is set to 0.05. Other simulation assumptions are given in Table 6.1. (a) 1 bit and 2 bits ADCs. (b) 4 bits and infinite resolution ADCs.
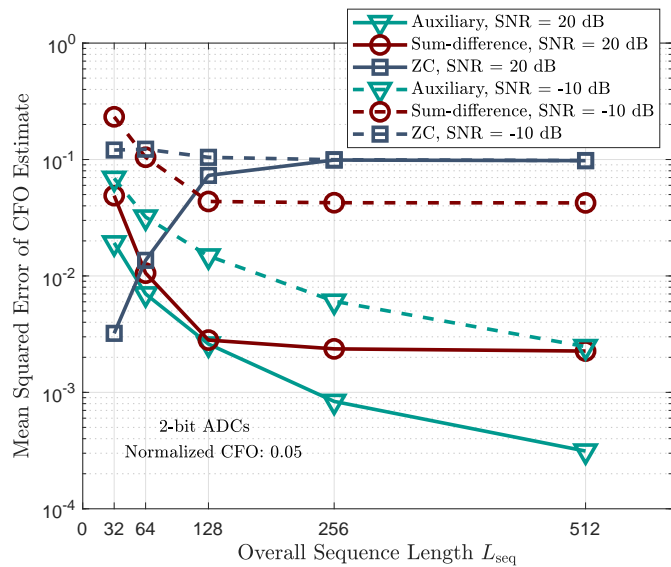
(a)
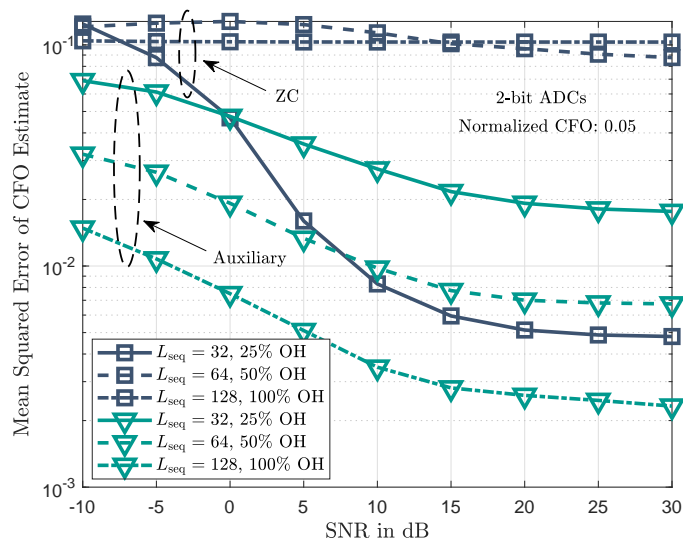
(b)

Figure 6.7: The assumed quantization resolution for the ADCs is 2 bits. (a) Mean squared errors of the CFO estimates are plotted against various sequence lengths assuming -10 dB and 20 dB SNRs. (b) Mean squared errors of the CFO estimates are plotted against various SNRs. The assumed overall sequence lengths are 32 and 64.
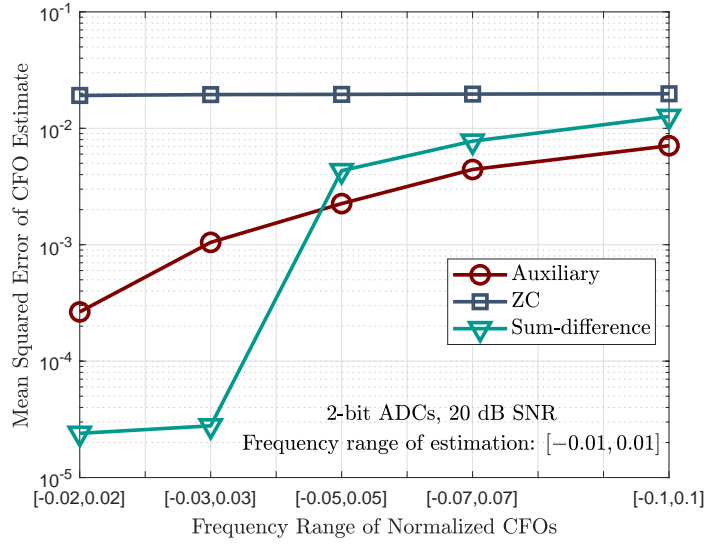
(a)
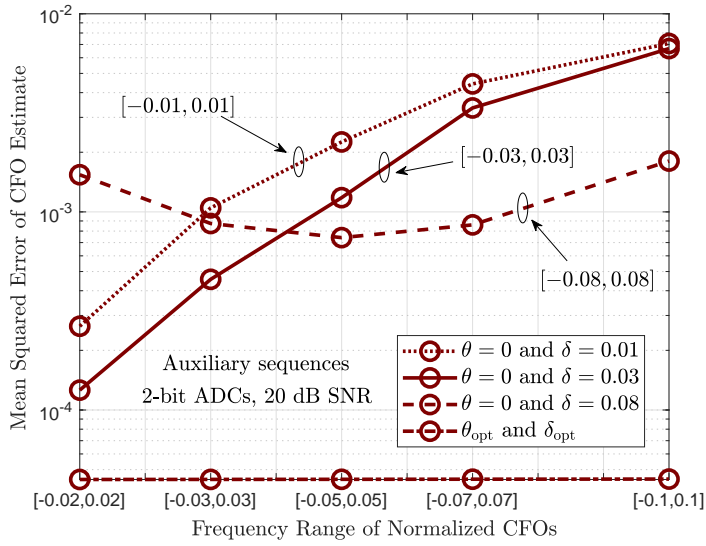
(b)

Figure 6.8: Low-resolution frequency synchronization performance evaluations in a multi-user scenario. A total of 10 UEs are assumed with each of them having a 2-bit ADCs receiver. (a) Mean squared errors of the CFO estimates against various frequency ranges of normalized CFOs. (b) Mean squared errors of the CFO estimates under various frequency ranges of estimation.

251

Chapter 7

Conclusion

With accurate channel directional information available at both the transmitter and receiver, a mmWave system can form highly directional beams towards the channel's AoD/AoA, enabling favorable received signal power. Most of the prior work on estimating mmWave channel's AoD/AoA either relies on the on-grid assumption, which depends onthe beam codebook resolution, or requires a large number of training samples, resulting in prohibitive complexity and overhead. In the first part of this dissertation, we focused on designing high-resolution low-overhead angle information acquisition (both angle estimation and tracking) strategies for mmWave systems. We custom designed a beam pair structure, from which there exists an invertible function of the channel's AoD/AoA to be estimated. We not only illustrated the detailed design principle of our proposed methods, but also addressed several issues of implementing the proposed algorithms in practical cellular systems. We concluded from extensive numerical and analytical examples that our developed auxiliary beam pair is viable in providing accurate AoD/AoA estimates under various channel models, mobility conditions, and transceiver configurations.

Reducing ADC quantization resolution is a promising solution to reduce

the power consumption and hardware complexity of a mmWave system. There is little work on time-frequency synchronization under low-resolution ADCs, though the initial access is one of the most important procedures in many cellular network standards. In the second part of this dissertation, we first revealed the impact of low-resolution quantization on the time-frequency synchronization performance; we then developed new synchronization strategies that are suited for few-bit ADCs. For frame timing synchronization, we focused on improving the received synchronization SQNR at zero-lag by optimizing the transmit beam pattern. For frequency synchronization, we constructed new synchronization sequences that are robust to the quantization distortion. We evaluated our proposed algorithms in realistic channel setup, and the results validated the effectiveness of our developed low-resolution synchronization solutions.

We present a summary of the main contributions in this dissertation as follows.

7.1 Summary

- **Chapter 2**: We custom designed pairs of auxiliary beams and derived a set of ratio measures by comparing the received signal strengths of the auxiliary beam pairs. We showed that the derived ratio metrics characterize the channel's AoDs and AoAs, and can be inverted to retrieve the corresponding angle information. We proposed two quantization and feedback options for implementing the proposed strategy in FDD

253

systems. We also derived the variance of the angle estimate, which analytically characterizes the achievable angle estimation performance of the proposed method. Extending our proposed single-path solution to estimate multi-path's angle components, however, are not straightforward, which required asymptotic assumption on the number of employed antennas and channel sparsity. We observed from numerical examples that if the channel has many paths with small Rician K-factor, the performance of our proposed solution would be highly limited by the multi-path interference. Further, the system needs to properly configure the beam width to achieve a better trade-off between the angle estimation accuracy and the computational complexity in multi-path channels.

- **Chapter 3**: We focused on estimating two-dimensional (azimuth and elevation) angle information via the auxiliary beam pair design. We developed a multi-layer pilot structure to better support the implementation of the proposed algorithm in wideband channels with multi-carrier transmission. We incorporated dual-polarized MIMO structure into the design of our proposed algorithm. We developed various mapping strategies between auxiliary beams and polarization domains (vertical and horizontal). The obtained results show that the proposed technique is robust to the angle mismatch and power imbalance in dual-polarized MIMO. Via both analytical and numerical results, we found that the proposed multi-layer pilot structure highly depends on the fluctuations of the channel gains across the occupied subcarriers. For practical imple-

254

mentation, it is therefore necessary to optimize the employed sequence length such that it fits for the minimum possible bandwidth of a given wideband system.

- **Chapter 4**: Building on the angle estimation results, we developed several auxiliary beam pair-assisted high-resolution angle tracking strategies for wideband mmWave systems in fast-varying environments. We proposed a beam-specific pilot signal structure for tracking and several feedback strategies to better adopt the proposed methods in different deployment scenarios. We also characterized the impact of the impaired radiation pattern with phase and amplitude errors on the proposed designs. We observed from our extensive simulations that the proposed solution is sensitive to the beam pattern impairments. Hence, array calibration is required prior to performing our proposed tracking algorithm. Note that in this dissertation, we did not model the mutual coupling effect and other non-linear impairments for either the algorithm development or the numerical evaluation. If we consider all these impairments and assume that they evolve over time, we need to further optimize the beam pair structure and the corresponding tracking procedure, making our solution more robust to these impairments.

- **Chapter 5**: We first exhibited that optimizing the received synchronization SQNR at zero-lag correlation is a viable solution to improve the overall frame timing synchronization performance under low-resolution

ADCs. We then formulated the corresponding optimization problem as maximizing the minimum received synchronization SQNR at zero-lag correlation among all serving UEs. We solved the formulated problem by optimizing the combination of the synchronization beams such that the resulted composite beam maximizes the received synchronization SQNR at zero-lag correlation, while at the same time characterizing the worst-case scenario of the network. The multi-beam probing has been supported in MIMO for spatial multiplexing, but we showed that along with the common synchronization signal structure, it is still a novel solution specific to our formulated low-resolution timing synchronization problem. We also found that optimizing the transmit beam pattern is an effective solution to compensate for the quantization loss for directional communications in mmWave systems.

- **Chapter 6**: We developed two double-sequence high-resolution CFO estimation methods for mmWave systems operating with low-resolution ADCs. In each method, we custom design two sequences (i.e., a sequence pair) for frequency synchronization. We also proposed to fine tune the double-sequence design parameters such that the CFO estimation accuracy and the frequency range of estimation are jointly optimized. Via extensive simulations using 5G NR channel model, we proved that our proposed low-resolution frequency synchronization strategies are effective in estimating and correcting the CFO under few-bit ADCs. In contrast to the timing synchronization, the frequency synchronization is more sensi-

tive to the low-resolution quantization distortion. Custom designing new sequences for low-resolution frequency synchronization showed promising performance, but it is still of great implementation interest to make the sequences compatible with the existing system as much as possible.

7.2 Future Research Directions

In this section, we discuss several future research directions related to the work in this dissertation.

7.2.1 Performance tradeoff between estimation accuracy and overhead for auxiliary beam pair based methods

In this dissertation, we presented novel auxiliary beam pair based high-resolution AoD/AoA estimation and tracking strategies for mmWave systems. We explicitly explained the design principle, procedure, and several practical implementation issues of our proposed methods. We pointed out that the angle estimation accuracy and the corresponding estimation overhead are two key indicators to evaluate our proposed algorithms. In this dissertation, we separately considered these two design aspects. We showed that under the same computational complexity and pilot overhead, the MSEs of our estimated AoD/AoA are much smaller than those obtained via the grid-of-beams based approach; we also showed that for a given level of angle estimation error, our proposed methods require less number of training beams and iterations than the conventional approach. Hence, there is an opportunity to jointly con-

sider the angle estimation accuracy and the corresponding overhead to further optimize the auxiliary beam pair structure, and analytically characterize the performance tradeoff between these two design aspects. One could leverage the performance tradeoff to determine appropriate beam codebook and optimize the frequency to form the auxiliary beams according to specific system settings. For example, we can implement a look-up table at both the BS and UE, carefully mapping the estimation accuracy and overhead related parameters based on the tradeoff analysis. For a given performance metric, e.g., a $5°$ angle estimator error, the system can quickly configure the appropriate parameters according to the look-up table to conduct the angle estimation and tracking. In Chapter 2, we compared the error variance performances between our proposed auxiliary beam pair, grid-of-beam and compressed sensing based strategies under the large system assumption. For finite size beam codebook and/or dictionary, it is also interesting to derive the CRLBs of these design options under the same setup. Using the CRLBs, we can justify the achievable performance of each method, and identify their potential deployment scenarios.

7.2.2 New beam pair structures robust to various impairments

In this dissertation, we leveraged the DFT beam structure to custom design the auxiliary beam pair for mmWave communications systems. Radar systems use a different beam pair structure, containing a sum beam and a difference beam, to detect the target's position. Other than the sum-difference

beam pair and our constructed auxiliary beam pair, there are opportunities in developing new beam pair structures for a variety of deployment scenarios. We highlight here that though the exact beam pair structure could be different, the same principle that the beam pair generates an invertible function of the AoD/AoA to be estimated should still hold. For instance, for high-speed rail-way communications, we can design a new beam pair structure robust to high mobility and Doppler spread to capture the angle variations. For another example, we can specifically design the beam pair suited for low-resolution quantization, e.g., 1-bit ADCs/DACs, targeting at minimizing the power consumption and hardware complexity at mmWave frequencies.

7.2.3 Adaptive auxiliary beam pair design based on feedback

Implementing the look-up table as introduced in Section 7.2.1 may require extensive measurements to obtain accurate system statistics. Using completely different beam pair structures for different deployment scenarios as described in Section 7.2.2 may complicate the system design. One alternative design to deal with various deployment scenarios is to configure the beam pair setup and probing strategy according to necessary feedback information. This idea is similar to the link adaptation design in the 3GPP LTE systems. For instance, the UE can continuously measure and monitor the received SINR from the beam pairs probed by the BS. If the received SINR is below a given threshold, the UE can send the quantized version of the received SINR back to the BS. Upon receiving the feedback, the BS can transmit the same auxiliary

259

beam pairs multiple times towards the UE to exploit the SINR variations in the TDM manner. There are opportunities in specifying the detailed implementation procedure such as the performance metric, feedback information, and triggering threshold for the beam pair adaptation. There are also opportunities in analytically characterizing the adaptive beam pair design such that one could have a better understanding of the achievable performance and the performance tradeoff.

7.2.4   Joint design of auxiliary beam pair and compressive sensing based methods

In this dissertation, we focused on angle information acquisition (both estimation and tracking) without considering the estimation of other channel parameters, such as the path gains and angular spread. As discussed in Section 4.5.2.2 Chapter 4, there is an opportunity to combine our proposed auxiliary beam pair design with the compressive sensing based method for mmWave channel estimation. For instance, the compressive sensing based methods can exploit the high-resolution angle estimates obtained via the ABPs to optimize the dictionary matrices. By optimizing the dictionary matrices at both the BS and UE sides, we expect to further improve the estimation accuracy of path gains with reduced complexity and overhead. For practical implementation, it may also be necessary to custom design the digital baseband precoding/combing matrices to enforce the Gaussian assumption on the measurement matrices. There are also opportunities in specifying the corresponding design procedure such as the detailed algorithm and signaling flow,

complexity analysis, feedback strategy and multi-path estimation.

7.2.5 Impact of low-resolution DACs on time-frequency synchronization

In this dissertation, we focused on designing new time-frequency synchronization strategies assuming few-bit ADCs at the UE and infinite-resolution DACs at the BS. That is, our constructed beam pattern and synchronization sequences did not suffer from any quantization distortion at the BS. With massive MIMO, however, it becomes necessary to employ low-resolution DACs to further reduce the power consumption and implementation complexity. Assuming low-resolution or even 1-bit DACs at the BS, our proposed sequences in Chapter 6 would be distorted before they are sent through the wireless channels, resulting in degraded overall synchronization performance. To address this issue, we need to first understand the impact of low-resolution DACs on the time-frequency synchronization performance. Some related future research topics may include formulating the synchronization optimization problem under low-resolution DACs, simplifying the optimization problem by leveraging long-term system statistics, and characterizing the performance tradeoff between the quantization resolution and the achievable synchronization performance. To solve the optimization problem, we propose to focus on digital precoder optimization to pre-compensate for the quantization distortion on the synchronization sequences, constructing new synchronization sequences that are robust to low-resolution DAC quantization, and new pulse shaping design. These directions not only will have significant impact on the system design,

but also are important from the perspective of practical implementation. It would also be interesting to investigate the impact of low-resolution, or even 1-bit DACs on general broadcast/multicast channel design. Optimizing the time-frequency synchronization process or the multicasting strategy assuming a fully digital low-resolution transceiver, i.e., low-resolution DACs at the BS and low-resolution ADCs at the UE, is of great practical interest for future research.

7.2.6 Joint low-resolution time-frequency synchronization optimization

In Chapters 5 and 6 of this dissertation, we separately developed frame timing synchronization and frequency synchronization (CFO estimation and correction) methods under low-resolution ADCs. For frame timing synchronization, we focused on optimizing the beam pattern, and therefore the input samples to the quantizer, to improve the received synchronization SQNR at zero-lag correlation. For frequency synchronization, we proposed to construct new synchronization sequences to combat with the quantization distortion. It would be of great research interest to jointly consider low-resolution time-frequency synchronization in mmWave systems. Potential research topics may include formulating the optimization problem accounting for both time and frequency offsets, simplifying the optimization problem by leveraging long-term system statistics, and analytically characterizing the achievable synchronization performance by leveraging Bussgang's decomposition theorem. There is an opportunity to construct generic synchronization sequences robust to low-

resolution quantization to jointly estimate the time and frequency offsets. The synchronization sequences could be custom designed for a target quantization resolution level, e.g., 1-bit, to characterize the worst-case scenario of the network. For 1-bit quantization, binary sequences such as Golay complementary sequences or m-sequences other than the ZC-type sequences can be optimized to better support the time-frequency synchronization. We expect that the sequences constructed for a given quantization resolution, e.g., 1-bit, can provide promising synchronization performances for other quantization resolutions as well. To reduce resource overhead, different synchronization sequences could be multiplexed in a code-domain multiplexing manner.

7.2.7 Beam codebook design and performance analysis for single-beam based low-resolution timing synchronization

In Chapter 5, we showed the effective composite beam pattern obtained from the proposed multi-beam structure for a given anchor angular direction. As our proposed multi-beam probing based strategy targeted at increasing the spatial design degrees of freedom for a given limited-size low-resolution beam codebook, the effective composite beam exhibits higher resolution than the DFT-type beams, and does not necessarily yield the largest beamforming gain towards the anchor angular direction. If the resolution of the beam codebook itself can be enhanced, e.g., by optimizing the beam codewords without any power constraint, the single-beam based method can be supported as well. For instance, each beam codeword in the enhanced beam codebook can be designed as a linear combination of a certain number of weighted beam codewords

263

from the conventional DFT beam codebook. Hence, it would be interesting for future research to quantify such beam codebooks and the corresponding achievable performance with the single-beam based timing synchronization method under low-resolution quantization.

Bibliography

[1] Z. Pi and F. Khan, "An introduction to millimeter-wave mobile broadband systems," *IEEE Commun. Mag.*, vol. 49, no. 6, pp. 101–107, Jun. 2011.

[2] R. W. Heath Jr., N. Gonzalez-Prelcic, S. Rangan, W. Roh, and A. Sayeed, "An overview of signal processing techniques for millimeter wave MIMO systems," *IEEE J. Sel. Top. Signal Process.*, vol. 10, no. 3, pp. 436–453, Feb. 2016.

[3] F. Boccardi, R. W. Heath Jr., A. Lozano, T. L. Marzetta, and P. Popovski, "Five disruptive technology directions for 5G," *IEEE Commun. Mag.*, vol. 52, no. 2, pp. 74–80, Feb. 2014.

[4] T. S. Rappaport, R. W. Heath Jr., R. C. Daniels, and J. N. Murdock, *Millimeter wave wireless communications*, Prentice Hall, 2014.

[5] C. Oestges, B. Clerckx, M. Guilaud, and M. Debbah, "Dual-polarized wireless communications: from propagation models to system performance evaluation," *IEEE Trans. Wireless Commun.*, vol. 7, no. 10, pp. 4019–4031, Oct. 2008.

[6] T. Kim, B. Clerckx, D. J. Love, and S. J. Kim, "Limited feedback beamforming systems in dual-polarized MIMO channel," *IEEE Trans.*

Commun., vol. 11, no. 9, pp. 3425–3439, Oct. 2010.

[7] J. Park and B. Clerckx, "Multi-user linear precoding for multi-polarized massive MIMO system under imperfect CSIT," *IEEE Trans. Wireless Commun.*, vol. 14, no. 5, pp. 2532–2547, May 2015.

[8] A. Alkhateeb, O. E. Ayach, G. Leus, and R. W. Heath Jr., "Channel estimation and hybrid precoding for millimeter wave cellular systems," *IEEE J. Sel. Top. Signal Process.*, vol. 8, no. 5, pp. 831–846, Oct. 2014.

[9] R. Mendez-Rial, C. Rusu, N. Gonzalez-Prelcic, A. Alkhateeb, and R. W. Heath Jr., "Hybrid MIMO architectures for millimeter wave communications: phase shifters or switches?," *IEEE Access*, vol. 4, pp. 247–267, Jan 2016.

[10] R. Mendez-Rial, N. Gonzalez-Prelcic, and R. W. Heath Jr., "Adaptive hybrid precoding and combining in mmWave multiuser MIMO systems based on compressed covariance estimation," in *Proc. of IEEE Intern. Workshop on Computational Advances in Multi-Sensor Adaptive Processing*, Dec. 2015, pp. 213–216.

[11] L. Dai, X. Gao, S. Han, C.-L. I, and X. Wang, "Beamspace channel estimation for millimeter-wave massive MIMO systems with lens antenna array," in *Proc. of IEEE/CIC Intern. Conf. on Commun. in China*, Jul. 2016.

[12] T. E. Bogale, L. B. Le, and X. Wang, "Hybrid analog-digital channel estimation and beamforming: training-throughput tradeoff," *IEEE Trans. Commun.*, vol. 63, no. 12, pp. 5235–5249, Oct. 2015.

[13] J. Singh and S. Ramakrishna, "On the feasibility of codebook-based beamforming in millimeter wave systems with multiple antenna arrays," *IEEE Trans. Wireless Commun.*, vol. 14, no. 5, pp. 2670–2683, May 2015.

[14] J. Wang, Z. Lan, C. Pyo, T. Baykas, C. Sum, M. Rahman, J. Gao, R. Funada, F. Kojima, H. Harada, and S. Kato, "Beam codebook based beamforming protocol for multi-Gbps millimeter-wave WPAN systems," *IEEE J. Sel. Areas Commun.*, vol. 27, no. 8, pp. 1390–1399, Oct. 2009.

[15] S. Hur, T. Kim, D. J. Love, J. Krogmeier, T. Thomas, and A. Ghosh, "Millimeter wave beamforming for wireless backhaul and access in small cell networks," *IEEE Trans. Commun.*, vol. 61, no. 10, pp. 4391–4403, Oct. 2013.

[16] K. Venugopal, A. Alkhateeb, R. W. Heath Jr., and N. Gonzalez-Prelcic, "Time-domain channel estimation for wideband millimeter wave systems with hybrid architecture," in *Proc. of IEEE Int. Conf. Acoust. Speech Signal Process.*, Mar. 2017, pp. 6493–6497.

[17] K. Venugopal, A. Alkhateeb, N. Gonzalez-Prelcic, and R. W. Heath Jr., "Channel estimation for hybrid architecture based wideband millimeter

wave systems," *IEEE J. Sel. Areas Commun.*, vol. 35, no. 9, pp. 1996–2009, Sep. 2017.

[18] J. Rodriguez-Fernandez, K. Venugopal, N. Gonzalez-Prelcic, and R. W. Heath Jr., "A frequency-domain approach to wideband channel estimation in millimeter wave systems," in *Proc. of IEEE Intern. Conf. Commun.*, May 2017, pp. 1–7.

[19] S. Liu, F. Yang, W. Ding, X. Wang, and J. Song, "Two-dimensional structured-compressed-sensing-based NBI cancelation exploiting spatial and temporal correlations in MIMO systems," *IEEE Trans. Veh. Technol.*, vol. 65, no. 11, pp. 9020–9028, Nov. 2016.

[20] Z. Gao, L. Dai, and Z. Wang, "Channel estimation for mmWave massive MIMO based access and backhaul in ultra-dense network," in *Proc. of IEEE Intern. Conf. Commun.*, May 2016, pp. 1–6.

[21] Z. Cao, C. Hu, L. Dai, and Z. Wang, "Channel estimation for millimeter-wave massive MIMO with hybrid precoding over frequency-selective fading channels," *IEEE Commun. Lett.*, vol. 20, no. 6, pp. 1259–1262, Jun. 2016.

[22] J. Rodriguez-Fernandez, N. Gonzalez-Prelcic, K. Venugopal, and R. W. Heath Jr., "Frequency-domain compressive channel estimation for frequency selective hybrid mmWave MIMO systems," *IEEE Trans. Wireless Commun.*, vol. 17, no. 5, pp. 2946–2960, May 2018.

[23] J. Gonzalez-Coma, J. Rodriguez-Fernandez, N. Gonzalez-Prelcic, L. Castedo, and R. W. Heath Jr., "Channel estimation and hbyrid precoding for frequency selective multiuser mmWave MIMO systems," *IEEE J. Sel. Top. Signal Process.*, vol. 12, no. 2, pp. 353–367, May 2018.

[24] Z. Zhou, J. Fang, L. Yang, H. Li, Z. Chen, and R. S. Blum, "Low-rank tensor decomposition-aided channel estimation for millimeter wave MIMO-OFDM systems," *IEEE J. Sel. Areas Commun.*, vol. 35, no. 7, pp. 1524–1538, Apr. 2017.

[25] A. Ahmed, J. Mo, N. G. Prelcic, and R. W. Heath Jr., "MIMO precoding and combining solutions for millimeter-wave systems," *IEEE Commun. Mag.*, vol. 52, no. 12, pp. 122–131, Dec. 2014.

[26] A. Mezghani and J. A. Nossek, "Analysis of Rayleigh-fading channels with 1-bit quantized output," in *Proc. of IEEE Intern. Symp. on Info. Theory*, Jul. 2008.

[27] J. Singh, O. Dabeer, and U. Madhow, "On the limits of communications with low-precision analog-to-digital conversion at the receiver," *IEEE Trans. Commun.*, vol. 57, no. 12, pp. 3629–2639, Dec. 2009.

[28] A. Mezghani and J. A. Nossek, "On ultra-wideband MIMO systems with 1-bit quantized outputs: performance analysis and input optimization," in *Proc. of IEEE Intern. Symp. on Info. Theory*, Jun. 2007.

[29] J. Mo and R. W. Heath Jr., "Capacity analysis of one-bit quantized MIMO systems with transmitter channel state information," *IEEE Trans. Signal Process.*, vol. 63, no. 20, pp. 5498–5512, Oct. 2015.

[30] M. T. Ivrlac and J. A. Nossek, "Challenges in coding for quantized MIMO systems," in *Proc. of IEEE Intern. Symp. on Info. Theory*, Jul. 2006.

[31] B. M. Murray and I. B. Collings, "AGC and quantization effects in a zero-forcing MIMO wireless system," in *Proc. of IEEE Veh. Tech. Conf.*, May 2006.

[32] T. Lok and V.-W. Wei, "Channel estimation with quantized observations," in *Proc. of IEEE Intern. Symp. on Info. Theory*, Aug. 1998.

[33] G. Zeitler, G. Kramer, and A. Singer, "Bayesian parameter estimation using single-bit dithered quantization," *IEEE Trans. Signal Process.*, vol. 60, no. 6, pp. 2713–2726, Jun. 2012.

[34] O. Dabeer and U. Madhow, "Channel estimation with low-precision analog-to-digital conversion," in *Proc. of IEEE Intern. Conf. Commun.*, Jun. 2010.

[35] J. Choi, D. J. Love, and D. R. Brown III., "Channel estimation techniques for quantized distributed reception in MIMO systems," in *Proc. of IEEE Asilomar Conf. on Signals, Systems, and Computers*, Nov. 2014.

[36] J. Mo, P. Schniter, N. G. Prelcic, and R. W. Heath Jr., "Channel esti-
mation in millimeter wave MIMO systems with one-bit quantization,"
in *Proc. of IEEE Asilomar Conf. on Signals, Systems, and Computers*,
Nov. 2014.

[37] S. Wang, Y. Li, and J. Wang, "Multiuser detection for uplink large-scale
MIMO under one-bit quantization," in *Proc. of IEEE Intern. Conf.
Commun.*, Jun. 2014.

[38] J. Choi, J. Mo, and R. W. Heath Jr., "Near maximum-likelihood detec-
tor and channel estimator for uplink multiuser massive MIMO systems
with one-bit ADCs," *IEEE Trans. Commun.*, vol. 64, no. 5, pp.
2005–2018, May 2016.

[39] C. Mollen, J. Choi, E. G. Larsson, and R. W. Heath Jr., "Uplink perfor-
mance of wideband massive MIMO with one-bit ADCs," *IEEE Trans.
Wireless Commun.*, vol. 16, no. 1, pp. 87–100, Jan. 2017.

[40] D. Zhu, J. Choi, and R. W. Heath Jr., "Auxiliary beam pair design in
mmWave cellular systems with hybrid precoding and limited feedback,"
in *Proc. of IEEE Int. Conf. Acoust. Speech Signal Process.*, Mar. 2016,
pp. 3391–3395.

[41] D. Zhu, J. Choi, and R. W. Heath Jr., "Auxiliary beam pair enabled
AoD and AoA estimation in closed-loop large-scale mmWave MIMO
system," *IEEE Trans. Wireless Commun.*, vol. 16, no. 7, pp. 4770–
4785, Jul. 2017.

[42] D. Zhu, J. Choi, and R. W. Heath Jr., "Auxiliary beam pair enabled AoD and AoA estimation in mmWave FD-MIMO systems," in *Proc. of IEEE Global Telecomm. Conf.*, Dec. 2016.

[43] D. Zhu, J. Choi, and R. W. Heath Jr., "Two-dimensional AoD and AoA acquisition for wideband mmWave systems with dual-polarized MIMO," *IEEE Trans. Wireless Commun.*, vol. 16, no. 12, pp. 7890–7905, Dec. 2017.

[44] D. Zhu, J. Choi, Q. Cheng, W. Xiao, and R. W. Heath Jr., "High-resolution angle tracking for mobile wideband millimeter-wave systems with antenna array calibration," *IEEE Trans. Wireless Commun.*, vol. 17, no. 11, pp. 7173–7189, Nov. 2018.

[45] D. Zhu, R. Bendlin S. Akoum, A. Ghosh, and R. W. Heath Jr., "Directional frame timing synchronization in wideband mmWave systems with low-resolution ADCs," *submitted to IEEE Trans. Wireless Commun., arXiv preprint arXiv:1809.02890*, Sep. 2018.

[46] D. Zhu and R. W. Heath Jr., "Directional timing synchronization in wideband millimeter wave cellular systems with low-resolution ADCs," in *Proc. of 51st Asilomar Conf. on Signals, Systems, and Computers*, Nov. 2017.

[47] D. Zhu, R. Bendlin S. Akoum, A. Ghosh, and R. W. Heath Jr., "Double-sequence frequency synchronization for wideband mmWave systems with

few-bit ADCs," *submitted to IEEE Trans. Wireless Commun., arXiv preprint arXiv:1812.03629*, Dec. 2018.

[48] R. O. Schmidt, *A signal subspace approach to multiple emitter location and spectral estimation*, Stanford University, 1981.

[49] R. Roy and T. Kailath, "ESPRIT-estimation of signal parameters via rotational invariance techniques," *IEEE Trans. on Acoustics, Speech and Signal Processing*, vol. 32, no. 7, pp. 984–995, Jul. 1989.

[50] H. Krim and M. Viberg, "Two decades of array signal processing research: the parametric approach," *IEEE Signal Process. Mag.*, vol. 13, no. 4, pp. 67–94, Jul. 1996.

[51] T. Wang, B. Ai, R. He, and Z. Zhong, "Two-dimension direction-of-arrival estimation for massive MIMO systems," *IEEE Access*, vol. 3, pp. 2122–2128, Nov. 2015.

[52] A. Hu, T. Lv, H. Gao, Z. Zhang, and S. Yang, "An ESPRIT-based approach for 2-D localization of incoherently distributed sources in massive MIMO systems," *IEEE J. Sel. Topics Signal Process.*, vol. 8, no. 5, pp. 996–1011, Oct. 2014.

[53] A. Wang, L. Liu, and J. Zhang, "Low complexity direction of arrival (DOA) estiamtion for 2D massive MIMO systems," in *Proc. of IEEE Global Telecomm. Conf.*, Dec. 2012, pp. 703–707.

[54] L. Cheng, Y.-C. Wu, J. Zhang, and L. Liu, "Subspace identification for DOA estimation in massive/full-dimension MIMO systems: bad data mitigation and automatic source enumeration," *IEEE Trans. Signal Process.*, vol. 63, no. 22, pp. 5897–5909, Nov. 2015.

[55] R. Shafin, L. Liu, and J. Zhang, "DoA estimation and capacity analysis for 3D massive-MIMO/FD-MIMO OFDM system," in *Proc. of IEEE Global Conf. on Signal and Information Process.*, Dec. 2015, pp. 181–184.

[56] V. Raghavan, J. Cezanne, S. Subramanian, A. Sampath, and O. Koymen, "Beamforming tradeoffs for initial UE discovery in millimeter-wave MIMO systems," *IEEE J. Sel. Top. Signal Process.*, vol. 10, no. 3, pp. 543–559, Jan. 2016.

[57] E. M. Hofstetter and D. Delong, "Detection and parameter estimation in an amplitude-comparison monopulse radar," *IEEE Trans. Inf. Theory*, vol. 15, no. 1, pp. 22–30, Jan. 1969.

[58] J. S. Orfanidis, *Electromagnetic waves and antennas*, [Online]. Available: www.ece.rutgers.edu/orfanidi/ewa, Rutgers University, 2004.

[59] E. Torkildson, H. Zhang, and U. Madhow, "Channel modeling for millimeter wave MIMO," in *IEEE Info. Theory and App. Workshop*, Feb. 2010, pp. 1–8.

[60] T. S. Rappaport, F. Gutierrez, E. Ben-Dor, J. N. Murdock, Y. Qiao, and J. I. Tamir, "Broadband millimeter-wave propagation measurements and models using adaptive-beam antennas for outdoor urban cellular communications," *IEEE Trans. Antennas Propag.*, vol. 61, no. 4, pp. 1850–1859, Apr. 2013.

[61] O. E. Ayach, R. W. Heath Jr., S. Abu-Surra, S. Rajagopal, and Z. Pi, "The capability optimality of beam steering in large millimeter wave MIMO systems," in *IEEE Intern. Workshop Signal Process. Adv. Wireless Commun.*, Jun. 2012, pp. 100–104.

[62] F. Gomez-Cuba and A. J. Goldsmith, "Sparse mmWave OFDM channel estimation using compressed sensing in OFDM systems," in *to appear in IEEE Intern. Conf. Commun.*, May 2019.

[63] Z. Muhi-Eldeen, L. Ivrissimtzis, and M. Al-Nuaimi, "Modelling and measurements of millimeter wavelength propagation in urban environments," *IET Microwaves, Antennas & Propagation*, vol. 4, no. 9, pp. 1300–1309, Sep. 2010.

[64] J. Song, S. G. Larew, D. J. Love, T. A. Thomas, and A. Ghosh, "Millimeter wave beam-alignment for dual-polarized outdoor MIMO systems," in *IEEE Global Telecomm. Conf. Workshops*, Dec. 2013, pp. 356–361.

[65] G. Calcev, D. Chizhik, B. Goransson, S. Howard, H. Huang, A. Kogiantis, A. F. Molish, A. L. Moustakas, and H. X. Reed, "A wideband

spatial channel model for system-wide simulations," *IEEE Trans. Veh. Technol.*, vol. 56, no. 2, pp. 389–403, Mar. 2007.

[66] J. Song, J. Choi, S. G. Larew, D. J. Love, T. A. Thomas, and A. Ghosh, "Adaptive millimeter wave beam alignment for dual-polarized MIMO systems," *IEEE Trans. Wireless Commun.*, vol. 14, no. 11, pp. 6283–6296, Nov. 2015.

[67] B. M. Popovic, "Generalized chirp-like polyphase sequences with optimum correlation properties," *IEEE Trans. Inf. Theory*, vol. 38, no. 4, pp. 1406–1409, Jul. 1992.

[68] B. C. Berndt, R. J. Evans, and K. S. Williams, *Gauss and Jacobi sums*, Joh Wiley and Sons, 1998.

[69] B.-W. Ku, D.-G. Han, and Y.-S. Cho, "Efficient beam-training technique for millimeter-wave cellular communications," *ETRI Journal*, vol. 38, no. 1, pp. 81–89, Feb. 2016.

[70] O. E. Ayach, S. Rajagopal, S. Abu-Surra, Z. Pi, and R. W. Heath Jr., "Spatially sparse precoding in millimeter wave MIMO systems," *IEEE Trans. Wireless Commun.*, vol. 13, no. 3, pp. 1499–1513, Mar. 2014.

[71] M. K. Samimi and T. S. Rappaport, "3-D millimeter-wave statistical channel model for 5G wireless system design," *IEEE Transactions on Microwave Theory and Techniques*, vol. 64, no. 7, pp. 2207–2225, Jul. 2016.

[72] A. Alkhateeb and R. W. Heath Jr., "Frequency selective hybrid precoding for limited feedback millimeter wave systems," *IEEE Trans. Commun.*, vol. 64, no. 5, pp. 1801–1818, May 2016.

[73] "Wireless LAN Medium Access Control (MAC) and Physical Layer (PHY) Specifications - Amendment 4: Enhancements for Very High Throughput in the 60 GHz Band," IEEE P802.11ad/D9.0, Oct. 2012.

[74] "NR; Physical Channels and Modulation," 3GPP TS 38.211, Jun. 2018. [Online]. Available: http://www.3gpp.org/ftp//Specs/archive/ 38 series/38.211/.

[75] J. Palacios, D. D. Donno, and J. Widmer, "Tracking mm-Wave channel dynamics: fast beam training strategies under mobility," in *Proc. of IEEE Conf. on Computer Commun. (INFOCOM 2017)*, Oct. 2017.

[76] J. Bae, S.-H. Lim, J.-H. Yoo, and J.-W. Choi, "New beam tracking technique for millimeter wave-band communications," *arXiv preprint arXiv:1702.00276*, Feb. 2017.

[77] L. Dai and X. Gao, "Priori-aided channel tracking for millimeter-wave beamspace massive MIMO systems," in *Proc. of IEEE URSI Asia-Pacific Radio Science Conference (URSI AP-RASC)*, Aug. 2016.

[78] X. Gao, L. Dai, T. Xie, X. Dai, and Z. Wang, "Fast channel tracking for Terahertz beamspace massive MIMO systems," *IEEE Trans. Veh. Technol.*, vol. 66, no. 7, pp. 5689–5696, Oct. 2016.

[79] Y. Zhou, P. C. Yip, and H. Leung, "Tracking the direction-of-arrival of multiple moving tragets by passive arrays: asymptotic performance analysis," *IEEE Trans. Signal Process.*, vol. 47, no. 10, pp. 2644–2654, Oct. 1999.

[80] C. Zhang, D. Guo, and P. Fan, "Mobile millimeter wave channel acquisition, tracking, and abrupt change detection," *arXiv preprint arXiv:1610. 09626*, Oct. 2016.

[81] V. Va, H. Vikalo, and R. W. Heath Jr., "Beam tracking for mobile millimeter wave communication systems," in *Proc. of IEEE Global Conf. on Signal and Information Process.*, Dec. 2016.

[82] V. Rabinovich and N. Alexandrov, *Antenna arrays and automotive applications*, Springer New York, 2013.

[83] "Study on channel model for frequency spectrum above 6 GHz," 3GPP TR 38.900 V14.2.0, Dec. 2016.

[84] A. Sayeed, J. Brady, P. Cheng, and U. Tayyab, "Indoor channel measurements using a 28 GHz multi-beam MIMO prototype," in *IEEE Veh. Tech. Conf.*, Sep. 2016, pp. 1–5.

[85] A. Sayeed and J. Brady, "Beamspace MIMO channel modeling and measurement: methodology and results at 28 GHz," in *IEEE Global Telecomm. Conf.*, Dec. 2016.

[86] "Technical Specification Group RAN: Evolved Universal Terrestrial Radio Access (E-UTRA); Physical Channels and Modulation," 3GPP, Dec. 2011. [Online]. Available: http://www.3gpp.org/ftp/Specs/html-info/36211.htm.

[87] M. Hyder and K. Mahata, "Zadoff-Chu sequence design for random access initial uplink synchronization in LTE-like systems," *IEEE Trans. Wireless Commun.*, vol. 16, no. 1, pp. 503–511, Jan. 2017.

[88] G. Sommerkorn, D. Hampicke, R. Klukas, A. Richter, A. Schneider, and R. Thoma, "Reduction of DoA estimation errors caused by antenna array imperfections," in *Proc. of IEEE European Microwave Conf.*, Oct. 1999, pp. 287–290.

[89] B. Ng and C. See, "Sensor-array calibration using a maximum-likelihood approach," *IEEE Trans. Antennas Propag.*, vol. 44, no. 6, pp. 827–835, Jun. 1996.

[90] K. Sakaguchi, K. Kuroda, J.-I. Takada, and K. Araki, "Comprehensive calibration for MIMO system," in *Proc. of IEEE WPMC 2002*, Oct. 2002.

[91] S. Sun and T. S. Rappaport, "Millimeter wave MIMO channel estimation based on adaptive compressed sensing," in *Proc. of IEEE Intern. Conf. Commun.*, May 2017.

[92] S. Lloyd, "Least squares quantization in PCM," *IEEE Trans. Info. Theory*, vol. 28, no. 2, pp. 129–137, Mar. 1982.

[93] T. S. Rappaport, S. Sun, and M. Shafi, "Investigation and comparison of 3GPP and NYUSIM channel models for 5G wireless communications," *arXiv preprint arXiv:1707.00291*, Jul. 2017.

[94] J. He, T. Kim, H. Ghauch, K. Liu, and G. Wang, "Millimeter wave MIMO channel tracking systems," in *Proc. of IEEE Global Telecomm. Conf.*, Dec. 2014, pp. 1–5.

[95] C. N. Barati, S. A. Hosseini, S. Rangan, P. Liu, T. Korakis, S. S. Panwar, and T. S. Rappaport, "Directional cell discovery in millimeter wave cellular networks," *IEEE Trans. Wireless Commun.*, vol. 14, no. 12, pp. 6664–6678, Dec. 2015.

[96] K. Roth and J. A. Nossek, "Achievable rate and energy efficiency of hybrid and digital beamforming receivers with low resolution ADC," *IEEE J. Sel. Areas Commun.*, vol. 35, no. 9, pp. 2056–2068, Sep. 2017.

[97] J. Mo, A. Alkhateeb, S. Abu-Surra, and R. W. Heath Jr., "Hybrid architectures with few-bit ADC receivers: achievable rates and energy-rate tradeoffs," *IEEE Trans. Wireless Commun.*, vol. 16, no. 4, pp. 2274–2287, Apr. 2017.

[98] H. Yan and D. Cabria, "Compressive sensing based initial beamforming training for massive MIMO millimeter-wave systems," in *Proc. of IEEE*

Global Conf. on Signal and Information Process., Dec. 2016.

[99] J. J. Bussgang, "Crosscorrelation functions of amplitude-distorted Gaussian signals," *MIT Research Laboratory Technical Report*, Mar. 1952.

[100] A. Mezghani and J. Nossek, "Capacity lower bound of MIMO channels with output quantization and correlated noise," in *IEEE Intern. Symp. on Info. Theory*, Jul. 2012.

[101] M. Giordani, M. Polese, A. Roy, D. Castor, and M. Zorzi, "A tutorial on beam management for 3GPP NR at mmWave frequencies," *arXiv preprint arXiv:1804.01908*, Apr. 2018.

[102] M. J. Golay, "Complementary series," *IRE Trans. on Inf. Theory*, vol. 7, no. 2, pp. 82–87, Apr. 1961.

[103] Y. Tsai and G. Zhang, "Time and frequency synchronization for 3GPP long term evolution systems," in *IEEE Veh. Tech. Conf.*, May 2007.

[104] C. Mollen, J. Choi, E. G. Larsson, and R. W. Heath Jr., "Uplink performance of wideband massive MIMO with one-bit ADCs," *IEEE Trans. Wireless Commun.*, vol. 16, no. 1, pp. 87–100, Jan. 2017.

[105] K. Manolakis, D. M. Estevez, V. Jungnickel, W. Xu, and C. Drewes, "A closed concept for synchronization and cell search in 3GPP LTE systems," in *IEEE Wireless Commun. Netw. Conf.*, Apr. 2009, pp. 1–6.

[106] W. Roh et al., "Millimter-wave beamforming as an enabling technology for 5G cellular communications: theoretical feasibility and prototype results," *IEEE Commun. Mag.*, vol. 52, no. 2, pp. 106–113, Feb. 2014.

[107] T. A. Thomas, F. W. Vook, R. Ratasuk, and A. Ghosh, "Broadcast control strategies for mmWave massive MIMO leveraging orthogonal basis functions," in *IEEE Global Telecomm. Conf.*, Dec. 2015.

[108] Y. Yang, H. S. Ghadikolaei, C. Fischione, M. Petrova, and K. W. Sung, "Fast and reliable initial access with random beamforming for mmWave networks," *arXiv preprint arXiv:1802.06450*, Nov. 2018.

[109] T. M. Schmidl and D. C. Cox, "Robust frequency and timing synchronization for OFDM," *IEEE Trans. Commun.*, vol. 45, no. 12, pp. 1613–1621, Dec. 1997.

[110] H. Minn, V. K. Bhargava, and K. B. Letaief, "A robust timing and frequency synchronization for OFDM systems," *IEEE Trans. Wireless Commun.*, vol. 2, no. 4, pp. 822–839, Jul. 2003.

[111] Z. Zhang, W. Jiang, H. Zhou, Y. Liu, and J. Gao, "High accuracy frequency offset correction with adjustable acquisition range in OFDM systems," *IEEE Trans. Wireless Commun.*, vol. 4, no. 1, pp. 228–237, Jan. 2005.

[112] M. Ghogho, P. Ciblat, A. Swami, and P. Bianchi, "Training design for repetitive-slot-based CFO estimation in OFDM," *IEEE Trans. Signal*

Process., vol. 57, no. 12, pp. 4958–4964, Dec. 2009.

[113] M. Morelli and M. Moretti, "Carrier frequency offset estimation for OFDM direct-conversion receivers," *IEEE Trans. Wireless Commun.*, vol. 11, no. 7, pp. 2670–2679, Jul. 2012.

[114] Y. Tsai and G. Zhang, "Time and frequency synchronization for 3GPP long term evolution systems," in *IEEE Veh. Tech. Conf.*, Apr. 2007, pp. 1727–1731.

[115] P. Zhou, K. Cheng, X. Han, X. Fang, Y. Fang, R. He, Y. Long, and Y. Liu, "IEEE 802.11ay-based mmWave WLANs: design challenges and solutions," *IEEE Communications Surveys & Tutorials*, vol. 20, no. 3, pp. 1654–1681, Mar. 2018.

[116] Y. Seliktar, "Space-time adaptive monopulse processing," *Ph.D. dissertation, Dept. Elect. Eng., Georgia Inst. of Tech., Atlanta, GA,*, Dec. 1998.

Vita

Dalin Zhu received his B.Eng. in Information Engineering from Beijing University of Posts and Telecommunications (BUPT) and M.S. in Electrical and Computer Engineering from Kansas State University in 2007 and 2009, respectively. He is a Ph.D. candidate in the Department of Electrical and Computer Engineering at the University of Texas at Austin, advised by Professor Robert W. Heath, Jr. in Wireless Networking & Communications Group (WNCG). From 2010 to 2014, he worked as a research staff member and project manager in the Dept. of Wireless Communications at NEC Laboratories China (NLC). From 2014 to 2015, he worked at Samsung R&D Institute China - Beijing (SRC-B) as a staff engineer working towards 5G New Radio (NR). During the summers of 2018, 2017 and 2016, he worked as an intern at AT&T Labs, Austin, TX and Huawei Technologies, Rolling Meadows, IL focusing on 5G NR simulation and research. He was the recipient of the University Graduate Continuing Fellowship (2018-2019) and Cullen M. Crain Endowed Scholarship in Engineering (2017-2018) from the University of Texas at Austin, Award of Excellence (2015/Q1) from Samsung R&D Institute China - Beijing, best paper award from Chinacom 2013 (Green Communications Symposium), and Dean's Special Award of Merit (2010-2011) from NEC Laboratories China.

Permanent address: 3607 Greystone Drive
Austin, Texas 78731

This dissertation was typeset with LaTeX† by the author.